PRESSURE IMPULSES CAUSED BY WAVE IMPACT

A thesis
submitted to the School of Mathematics
of the University of East Anglia
in partial fulfilment of the requirements
for the degree of
Doctor of Philosophy

By

Simon John Cox

September 1998

Abstract

Coastal sea defences fail when the impact pressures due to breaking waves cause their constitutive elements to move. This situation is modelled in an idealised domain by solving a boundary value problem for the Pressure Impulse, the integral of pressure over the short time of the impact. The relative insensitivity of this model to the velocity profile chosen when representing the impacting wave, compared to variables such as the wave's height and speed, is demonstrated explicitly for three profiles. In order to analyse further the impulse on a vertical wall, a class of awkward summations of trigonometric terms is approximated with a rapidly convergent series.

The impulsive forces on a body resting on the sea bed are calculated using two different methods, and shown to be dependent on its added mass and volume. A number of different classes of body are examined and larger objects are found to be more prone to movement away from a wall, due to the pressure impulse gradient along the sea bed. The case of a sphere, where the problem is equivalent to finding the potential flow perpendicular to the line joining two touching spheres, is solved with a very accurate numerical method and the distance moved by a near-spherical boulder on a beach subjected to wave impact is calculated. Similarly, a surface-piercing body experiences a vertical impulse when a wave breaks against a nearby vertical wall. The velocity at which a body will initially move is calculated for several different shaped bodies.

The pressure impulse in a fluid filled crack in a wall which is exposed to wave impact is calculated for several different crack geometries allowing the force on an element of a breakwater to be calculated, showing that these impact pressures are the probable cause of failure.

Acknowledgements

My thanks go to my parents, for their continued support and interest, and to my supervisor, Dr. Mark Cooker, for his guidance and friendship. Professor A. Korobkin deserves mention for correcting an earlier mistake in the work of Chapter 4.

Thanks also to all my friends and colleagues in the School of Mathematics for making the last three years so enjoyable, in particular BB, The Cube and the members of SportsMTH. Other friends at UEA, especially the Murthsoccers, the Taizé group and fellow birders, I thank for their distractive talents. My commiserations to anyone to whom I've tried to explain this material, probably incoherently.

Financial support from both the School of Mathematics at UEA and the UK Engineering and Physical Sciences Research Council, award number 96000215, is gratefully acknowledged.

Break, break, break,
On thy cold gray stones, O Sea!
And I would that my tongue could utter
The thoughts that arise in me.

Alfred Lord Tennyson.

Contents

3 The Pressure Impulse on a Body on the Sea Floor 40

Chapter 1

Introduction

1.1 Wave Breaking on Coastal Structures

Waves crashing against breakwaters and causing huge sheets of spray to erupt into the air are a popular image, being visually arresting. But the breaking process is not understood at all well. Many of the world's coastal areas, especially harbours, are protected by sea walls, but not always successfully. Coastal engineers need to predict the high, short-lived pressures which breaking waves can exert on these walls, with the aim of determining what causes them to fail. We are interested in the highest pressures, which give rise to the greatest forces and therefore usually cause the most damage. One of our aims is to construct a theory which gives coastal engineers reliable, straightforward information on the movement of objects in the zone where breaking waves occur. But there are many variables in a physical model which are hard to include in a mathematical treatment, so we concern ourselves only with those waves which generate high pressures over short times as they slam into sea walls. These are known as impact pressures, being very high pressures of brief duration which are associated with a delta-function-like pressure versus time graph.

It has long been known that large and sudden impulsive pressures occur (see

Bagnold (1939) and Denny (1951) who discuss the work of French and Italian experimenters towards the beginning of this century) but there are still no definitive rules relating the parameters associated with the incident wave (e.g. height, velocity) and the geometry of the area where it breaks (e.g. water depth) to the pressures recorded on the wall.

Evidence for these huge impulsive forces includes observations such as those by Stevenson (1864) of the “remarkable destructive effects at Whalsey Skerries” in Scotland, where “blocks of 6 tons weight have been quarried or broken out of their beds in situ ... [by] aqueous action”. He also records the passage of a rock, weighing $7\frac{1}{2}$ tons, across 73 feet of rugged ledges, at a height of 20 feet above the sea. This feat is remarkable, even if we assume that it occurred in many small successive motions over a long period of time. Blocks of stone of a hundred tons in weight have been disturbed by heavy seas (Cunningham 1928). Gaillard (1904, §8) gives many instances of the destructive forces exerted by waves, including that of a 20 ton block being lifted vertically to land atop a pier of 12 feet in height, almost 5 feet above the level of high water. At the same site, the entrance to the Amsterdam Canal in the Netherlands, a block weighing 7 tons was pushed forward out of its position in the wall. Gaillard surmises that this is due to the air at the back of the stone being compressed by the incoming wave, so that the block moves in a direction opposite to the direction of impact. These events also occur in smaller expanses of water, for instance in the great lakes of America, where Stevenson (1849) quotes observations of stones “weighing upwards of half-a-ton [being] completely turned over”.

Breakwaters are usually constructed from a series of huge rectangular concrete ‘buckets’ or caissons which are filled with rubble and then sunk in the required position. They have a vertical face and are then often surrounded by a pile of armour protection units designed to break up incoming waves and therefore reduce impact pressures. These are made in various shapes (see the Shore Protection Manual, U.S. Army 1973), and the breakwaters employing them are known as composite. We follow Lundgren (1969) in considering two sorts of breakwater: (i) where the caisson extends almost to the sea floor on a small rubble foundation so that the depth of water in front of the caisson is large and (ii) where the caisson sits on top of a high rubble foundation, with relatively shallow water in front. This latter is more likely to cause waves to break right in front of the structure (although this does depend to some extent on the wave height), and it is breakwaters of type (ii) that we expect will receive very high pressures. These pressures will cause large forces to act on the breakwater, in addition to the frictional forces holding the blocks in place and the drag forces due to the passage of waves near the structure.

Occasions when the sea has caused large scale damage to man-made coastal structures include the failures of both the Mutsu-Ogawara Port in Japan and the Sines breakwater in Portugal, which are documented by Hitachi (1994) and Baird, Caldwell, Edge, Magoon, and Treadwell (1980) respectively. The damage at Mutsu-Ogawara, in 1991, occurred while the construction of the caisson-type composite breakwater was still in progress (although 8 years after construction had begun!). The huge concrete caissons were struck by waves of up to fifteen metres in height and some of the armour blocks found their way inside the caissons. However, the worst damage was characterised by the caissons sliding away from the wall, in some cases by distances of almost 5 metres (his figure 3), and scattering the armour blocks at the base of the wall. At Sines, in 1978, the majority of the damage was caused by the movement and loss of the ‘dolos’ armour units - those units that broke free then proceeded to batter the wall further. The breakwater was again of a composite type and the armour units were placed so as to attempt to protect the concrete wall. It is noteworthy that the sea floor shelves very steeply away from the wall, so that large waves were to be expected. Lamberti and Franco (1994) reproduce an old photograph showing parts of the rubble mound scattered across the remains of the breakwater at Galliera. In 1898 a severe storm, with waves of almost 7 metres in height, destroyed 140 metres of the wall.

Further evidence of the magnitude of the impulsive forces around the impact zone (by which we mean that area of the wall over which the wave breaks - the part which goes from being in contact with air to being in contact with fluid, ignoring the presence of entrained air) is seen in the failure of the breakwater at Sakata Port in Japan during the winter of 1973/74 due to sliding of the caissons, as at Mutsu-Ogawara Port. Tanimoto and Takahashi (1994) record the sliding distances of eight metre high caissons due to the impact of large waves, showing movements of almost 4 metres away from their initial position. On this occasion there were no armour protection units around the caissons to protect them (or cause further damage by solid body impact). Since the frictional forces opposed the motion of the caissons, this observation suggests that the impulsive forces were very large.

In order to understand the wave damage, many researchers study scale modelling of waves impinging on both vertical and sloping walls under controlled conditions. However, they are all faced with the inherent problem of unrepeatability in their experiments. Chan and Melville (1988) measured the impact dynamics of deep-water plunging waves hitting a vertical wall and conclude that "at each wall location, identical incident wave conditions could yield significantly different impact pressures". To overcome the problem of unrepeatability, Bagnold (1939) showed that while the peak pressure varied between apparently similar impacts, the pressure impulse, which is the integral of pressure over the duration of the impact, remained fairly constant. This conclusion is not supported by the experiments of Richert (1968), however, who finds that "the pressure and impulse distributions are fairly congruent". That is, the pressure impulse varied just as much as the pressure itself. However, as the pressure peak becomes larger, and the pressure rise time smaller, the pressure impulse becomes a better approximation, providing that one can measure the start and finish times of the pressure peak. (Due to the oscillatory nature of the pressure-time trace, it is not always evident where the impact starts and finishes, a problem encountered by Wood 1997, §2.)

Waves are generally classified into three types, each giving different sorts of pressure response when they hit a wall. Oumeraci, Klammer, and Partenscky (1993) find that *plunging* breakers give the highest impact pressures. These are waves where the top of the wave curls over to entrap air prior to impact. Less air being trapped leads to higher pressures. In fact, the largest pressures occur when the forward face of the wave is vertical as it hits the wall. Bagnold (1939) modelled this as due to a column of fluid hitting the wall, whose momentum can be correlated with the measured impulse. The length of column causing that impulse is the momentum length of the wave. An *upward deflected* breaker gives the next highest pressures, and is due to the wave meeting the wall before it can break, so that the free surface rises very quickly up the wall. A thin jet is formed, although the pressure on the wall due to the jet is negligible, and vertical fluid particle accelerations of over $10,000g$ (where g is the acceleration due to gravity) have been predicted by Cooker (1997). These calculations agree with the experiments of Chan and Melville (1988) and Chan (1994) and this mechanism has been called *flip through* by Cooker and Peregrine (1992). The third, and final, type of wave, which generally causes the lowest impact pressures, is the turbulent bore or *spilling* breaker, when the broken wave moves towards the wall in a welter of foam. There is a large volume of bubbly mixture, of low density and lower speed, which helps to explain the low recorded pressures. Usually a particular wave will not show features of any one type, and this classification is more a rule of thumb than a definitive guide. For instance, the position of the wall in relation to the position at which a wave breaks is critical in how it is classified, as shown by Hattori, Arami, and Yui (1994). These authors present stills from video footage of breaking waves in a tank, showing in detail how the breaking wave deforms. Their measurements confirm that the highest pressures (of brief duration) occur when the front of the wave is vertical. Further, these maximum impact pressures usually occur around the still water level.

Blackmore and Hewson (1984) recorded full-scale prototype pressures at a sea wall in Ilfracombe, England. The wall is not quite vertical and an array of nine pressure transducers was used to allow comparison between real data and the "semi-empirical equations" used to estimate pressures at that time. The correlation is shown to be poor, and from their data we can estimate values of peak pressure (the greatest pressure recorded at any one point as a function of time) and pressure rise time with which to compare theory. The pressure rise time is the time taken for the pressure to rise to its peak value from hydrostatic pressure, $\rho g h$, where ρ is the density of the water, g the acceleration due to gravity and h the depth of water.

To give an idea of the magnitude of impact pressures and pressure rise times involved in wave breaking, we review some of the pressures recorded in experiments at different wave scales. The small scale experiments of Hattori *et al* (1994), with wave heights of about 5 cm, showed that for flip through type breaking the peak pressures recorded on the vertical wall were fairly small, although the free surface motion was large. However, breaking waves enclosing a thin cushion of air gave the highest peak pressures of the order of 5×10^4 N m^{-2}. These large pressures were associated with pressure rise times of the order of 1×10^{-3} sec. At a slightly larger laboratory scale, the impact pressures measured by Chan (1994) for deep water plunging breakers of about 12 cm in height had much larger amounts of entrained air. The peak pressures recorded when the waves impacted on a vertical wall were much less than those found by Hattori *et al*, with a maximum of about 3×10^3 N m^{-2}. However the pressure rise time was similar, 1×10^{-3} sec. At full scale, the analysis of Blackmore and Hewson (1984) for wave impact pressures on sea walls found maximum impact pressures similar to those of Hattori *et al*, 5×10^4 N m^{-2}, but rather slower rise times of the order of 0.1 sec. This shows how difficult it is to scale laboratory measurements to try and predict full scale pressures on breakwaters.

One of the reasons that scaling from model experiments to prototype is difficult is the presence of air, which is entrained in the wave during breaking. Walkden, Hewson, and Bullock (1997) obtain reasonably good results when they scale their results from a small wave tank up to those obtained in a large one. Rather than repeating the physical boundary conditions in each tank, they tried to create the same breaking wave profile at the vertical wall so that the fraction of entrained air was the same. The experiments of Kortenhaus, Oumeraci, Kohlhase, and Klammer (1994) showed that the effect of trapped air is to extend the pressure rise time and reduce the peak pressures. These authors were concerned with finding the uplift forces on a breakwater caisson resulting from different types of impinging wave. The greatest forces occurred for plunging breakers without entrained air, when the caisson tended to move horizontally rather than rotating about a point on its underside. As the amount of air in the wave decreases, we are led to consider the flat faced wave that Bagnold (1939) says is responsible for the highest pressures. Lundgren (1969), in his summary of wave impact dynamics, indicates that Froude scaling can be used when there is little air trapped, which means that impact pressures are directly proportional to wave height.

Until recently, theoretical simulations of waves breaking against coastal structures have involved large scale computational schemes. Cauchy's integral theorem and Green's identity are invoked to solve Laplace's equation in a domain whose free-surface boundary deforms in time. For example, Dold and Peregrine (1986) and Dold (1992) solve for the exact non-linear boundary condition on the free surface with a method that is stable and does not require smoothing, even when the computed flow is violent or continued for many wave periods (unlike previous methods, e.g. New, McIver, and Peregrine 1986). The method works for waves which are breaking, and, with a sufficiently small time step, can cope with the jet which is formed at the tip of the breaker. Cooker and Peregrine (1992) use a similar numerical scheme, which allows them to show that high pressure gradients act along the sea bed away from the wall.

Peregrine and Kalliadasis (1996) investigate analytically the effect of a wave breaking into a crack in a sea wall. This two-dimensional *filling flow*, where the fluid moves rapidly along the base of the crack and then returns along the top, may have enough force to dislodge material from the interior of the crack, thereby deepening it. The fluid also exerts an impulse on the boundaries of the crack which may be large enough to move parts of the surrounding structure. Peregrine and Kalliadasis give this impulse as

$$I = \frac{\rho k V_1 L^2}{2(2k-1)} \tag{1.1.1}$$

where L is the length of the crack, V_1 the speed of the incoming fluid and k^2 is the ratio of the height of the incoming water jet to the height of the crack (with $k > \frac{1}{2}$).

The analysis of Peregrine and Kalliadasis (1996) is extended by Peregrine and Thais (1996) to include the effect of the compressibility of the fluid. They find that a small amount of entrained air significantly reduces the impact pressures. Indeed, this statement is true for all impacts, since the entrained air reduces the sound speed in the bubbly mixture. They conclude that the volume reduction of the fluid at high pressures reduces the speed of filling so that the pressures are reduced.

The theoretical analysis in our work uses the concept of a Pressure Impulse, which allows estimates of the peak pressures associated with wave breaking to be made, without recourse to complicated numerical schemes. We will first derive Pressure Impulse Theory, and then review the literature which uses it. In Chapter 2 we examine three different velocity profiles for the impact of a wave against a vertical wall. A boundary value problem for the pressure impulse in a semi-infinite domain is solved to analyse the sensitivity of the pressure impulse distribution to changes in the way the impacting wave is modelled. This extends the simple model of Cooker and Peregrine (1995), where the wave is assumed to have a flat forward face with all points moving towards the wall at the same, constant, velocity. Their case is included for comparison. The expressions for the pressure impulse are found as infinite sums, so we derive an approximation to some awkward trigonometric sums to allow the pressure impulse on the wall to be found more easily.

We follow Cooker and Peregrine (1992) in using the model of Chapter 2, for the whole domain, to supply a far-field boundary condition for the problem of finding the impulse on a body which is at rest on the sea bed. Information gained from this analysis is of use in determining mechanisms by which armour units around breakwaters are moved by storm waves. This is explored in Chapter 3, where we give two methods of finding the pressure impulse distribution around a body. The first is to construct a periodic surface using a Fourier series. This requires a rather complicated way of finding the impulse on a body consisting of one period of the series. Secondly, we show how to use a conformal map to generate an isolated body on the bed. Formulae for both the horizontal and vertical impulses are given, and several examples are shown in order to ascertain the effect of shape and size on the magnitude of the impulse.

If a body is held so that it pierces the free surface, we can again use the results of Chapter 2 to give a far-field boundary condition for the motion of the body when a wave impacts against a nearby wall. An object is given a vertical velocity by the impulsive upthrust associated with the impact, which can be found by solving Laplace's equation for the pressure impulse, P, subject to mixed boundary conditions. In Chapter 4 we show that this is related to the solution for the pressure impulse around a body on the sea bed and this enables P below a flat plate on the free surface to be found. We then conformally map the solution around this plate to find the different velocities and impulses associated with other two-dimensional bodies, and derive some general formulae. This analysis is detailed in Cox and Cooker (1998). We also examine some three-dimensional bodies, and find that the same formulae are applicable.

Chapter 5 shows how the pressure impulse in a thin crack in the wall of the above domain can be found. Integrating the pressure impulse over the (small) height of the crack gives a modified Laplace's equation for the pressure impulse in the crack. We solve this for several geometries relating, for instance, to cracks between constituent blocks of sea walls. Our aim is to try and find ways in which these blocks will be loosened by the effect of wave impact, to explain the failures of coastal structures, noted in §1.1, such as that at Sakata Port in Japan. The equation is also applied to the flow in the crack around the base of an axisymmetric body which has point contact with a horizontal plane. In particular, this solution is valid around the point of contact of a sphere with a plane. The method of conformal mapping, from Chapter 3, is also used to find the pressure impulse in a crack in the sea wall, enabling qualitative comparison with the solutions of our modified Laplace's equation.

A particularly interesting body on the sea bed, on which we were unable to find the impulse using the methods of Chapter 3, is a sphere, which has a singularity in the velocity around the point of contact. We solve this problem in Chapter 6, much of the contents of which are in Cox and Cooker (2000), using tangent sphere coordinates to express the pressure impulse as an integral, up to an unknown function α. An ordinary differential equation for α is solved numerically and we then match P with the crack solution from Chapter 5, near to the contact point. This calculation allows the velocity potential and added mass of a sphere on its tangent plane to be found, or, what is equivalent, the velocity potential and added mass for two spheres in ideal flow perpendicular to the line joining their centres. With this solution for P we show that large boulders on a beach exposed to wave impact are likely to move farther up the beach than small ones.

Finally, some conclusions are drawn and we suggest some areas for further work, and for further experimentation to allow verification of our theoretical results.

1.2 Pressure Impulse Theory

We now describe Pressure Impulse Theory, hereafter referred to as PIT. Measurements on both real coastal structures and scale models show that breaking waves produce a pressure response such as that shown in figure 1.2.1. In the majority of 'impact pressure' traces, there is an initial large pressure rise, then a rapid descent. This is followed by a period of oscillation between relatively small pressures, thought to be due to compression and expansion of the entrapped air bubble (see Topliss 1994), before the pressure returns to hydrostatic. An impulsive pressure is defined by the limiting process of an infinitely great pressure acting for an infinitely short time and we consider twice the pressure rise time to be the short time scale over which the pressure is very large and then the Pressure Impulse, P, is defined to be the integral of pressure over time, following Batchelor (1973, §6.10). That is,

$$P = \int_{t_b}^{t_a} p(x, y, t) \mathrm{d}t, \tag{1.2.1}$$

where the subscripts b and a refer to before and after the impact, i.e. t_b and t_a are the start and finish times of the impact. Then it is evident that P is the area under the pressure spike in figure 1.2.1. The empirical observation of Bagnold (1939) was that, whilst the peak pressure, p_{peak}, varied, the product $\frac{1}{2} p_{peak} \Delta t$ remained fairly constant (where $\Delta t = t_a - t_b$ is the time taken for the impact to occur). If Δt is taken as twice the pressure rise time (normally of the order of 1×10^{-3}sec, at least at laboratory scales) this product approximates the pressure impulse. That is,

$$P \approx \frac{1}{2} p_{peak} \Delta t \quad \text{or, alternatively,} \quad p_{peak} \approx \frac{2P}{\Delta t}. \tag{1.2.2}$$

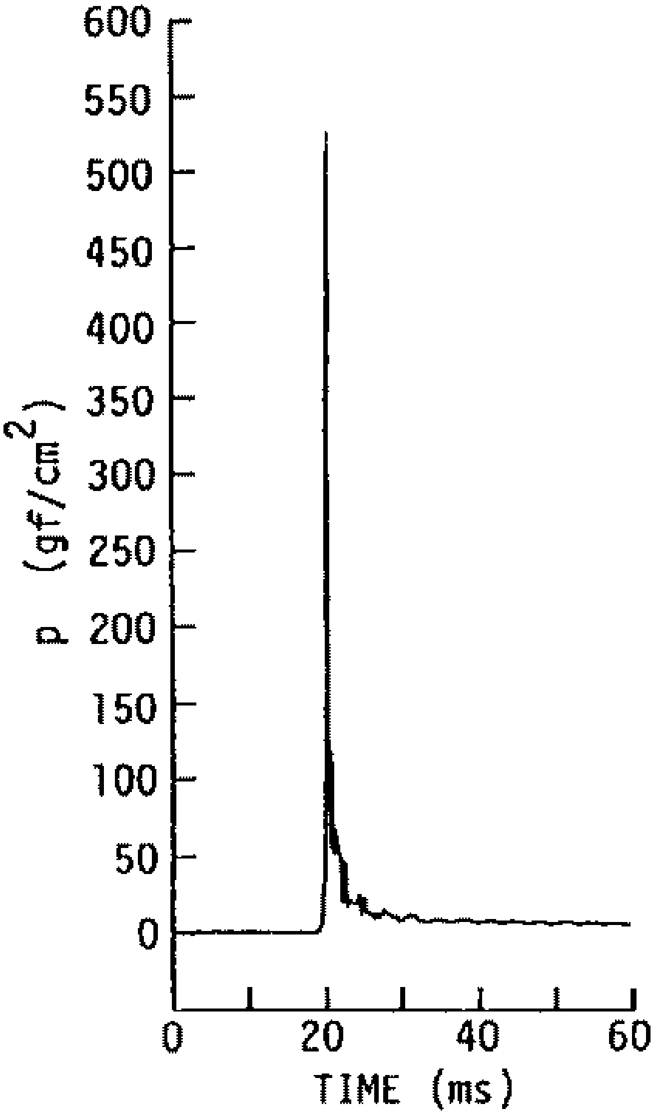

Figure 1.2.1: A pressure-time trace for a wave which impacts with an almost vertical front surface, recorded on a vertical wall at still water level by Hattori *et al* (1994, fig 15). The wave entrains little or no air and the pressure peak occurs over a short time and has large magnitude ($p_{peak} \approx 530\text{gf cm}^{-2} \approx 5 \times 10^4\text{N m}^{-2}$). It is not clear how we define the end of the impulsive pressure for the purposes of PIT but $t_b = 20 \times 10^{-3}$sec and t_a lies somewhere in the range $22 - 30 \times 10^{-3}$sec so Δt is at most 0.01sec. Notice also that the pressure doesn't rapidly decrease back to zero after the impact.

Thus P, as defined by (1.2.1), is a more convenient concept to study, and we can use the knowledge gained about P to estimate corresponding peak pressures.

We derive the equations of motion from the Navier Stokes equations:

$$\frac{\partial \underline{u}}{\partial t} + (\underline{u}.\nabla)\,\underline{u} = -\frac{1}{\rho}\nabla p + \nu \nabla^2 \underline{u} - g\underline{k} \qquad (1.2.3)$$

where $\underline{u}$ is the velocity, p the pressure, ρ the density and ν the kinematic viscosity of the fluid, g the acceleration due to gravity and $\underline{k}$ is a unit vector pointing vertically up. We non-dimensionalise the variables with a time scale Δt, a length scale L, a velocity scale u_0 and a pressure scale p_0. The length scale L is associated with the depth of water prior to the impact and u_0 is pertinent to the speed of waves approaching the wall. Then, after some manipulation, with primes denoting dimensionless variables,

$$\frac{\partial \underline{u}'}{\partial t'} + S\,(\underline{u}'.\nabla')\,\underline{u}' = -\frac{\Delta t p_0}{\rho u_0 L}\nabla' p' + N\nabla'^2 \underline{u}' - \frac{\Delta t}{u_0} g\underline{k} \qquad (1.2.4)$$

where $S = \Delta t u_0 / L$ and $N = \Delta t\,\nu / L^2$. Typically, if $L \sim 10$ m, $u_0 \sim 10 \text{ m sec}^{-1}$ and $\Delta t \sim 0.01$ sec then $S = 0.01$, $N = 1 \times 10^{-10}$ for water and the quantity scaling gravity is 0.001. So we seek a balance between the first term and the pressure term in (1.2.4) by scaling pressure according to $p_0 = \rho u_0 L / \Delta t$, which is very large (1×10^7). These two terms are those which relate to the impact event. Then we neglect the non-linear convective terms since S is small compared to p_0. This effectively linearises the formulation: the inclusion of these nonlinear convective terms by Cooker (1996), who uses S as a small parameter in order to obtain a perturbation expansion, shows that these terms are influential only near the free surface, helping to quantify the singularity in the gradient of P where the free surface meets the vertical wall. Similarly, we neglect the viscous terms (N small) and gravity. Thus we consider inviscid flow. Since the duration of the impact (Δt) is small, this is a reasonable approximation because there is insufficient time for viscous effects to develop at the solid boundaries: Rosenhead (1963, p.60) gives the following formula for the displacement thickness of the boundary layer, δ, at small times, t':

$$\delta \sim 2\sqrt{\frac{\nu t'}{\pi}}.$$

If $t' = \Delta t = 0.01$ sec then $\delta \sim 1.13 \times 10^{-4}$ m which is indeed small compared with length scales such as the depth of water at the wall, L.

Now (1.2.3) becomes (in dimensional variables)

$$\frac{\partial \underline{u}}{\partial t} = -\frac{1}{\rho}\nabla p. \tag{1.2.5}$$

Integrating with respect to time gives

$$\int_{t_b}^{t_a} \frac{\partial \underline{u}}{\partial t}\mathrm{d}t \ = \underline{u}_a - \underline{u}_b = -\frac{1}{\rho}\nabla \int_{t_b}^{t_a} p\mathrm{d}t = -\frac{1}{\rho}\nabla P,$$

that is,

$$\underline{u}_a = \underline{u}_b - \frac{1}{\rho}\nabla P \tag{1.2.6}$$

where P is pressure impulse, as defined by (1.2.1), and, using the same subscript convention as before, $\underline{u}_b$ and $\underline{u}_a$ are the fluid velocities before and after the impact. Thus the gradient of P relates how the velocity of the fluid changes over the short duration of impact. We assume that the fluid is incompressible before impact and after impact, $\nabla.\underline{u}_b = 0$ and $\nabla.\underline{u}_a = 0$, making no assumptions about its compressibility during impact. This does not extend to the bubbly mixture often present after the impact, but by this stage PIT is no longer valid. During the short impact time the impact speed is taken to be much less than the speed of sound in the fluid, and the peak pressures never exceed 2 atmospheres, so that incompressibility should be a good approximation. Then the divergence of (1.2.6) shows that

$$\nabla^2 P = 0. \tag{1.2.7}$$

That is, the Pressure Impulse satisfies Laplace's equation. Notice also that the curl of (1.2.6) implies that vorticity is conserved. Then whatever the vorticity before impact, none will be generated by the impact.

We can now formulate, and solve, mixed boundary value problems for the pressure impulse. The boundary conditions can be in one of four forms:

- $\nabla P.\underline{n} = 0$ on a fixed impermeable surface (with normal vector $\underline{n}$) which is in contact with the fluid before and after impact. That is, fluid can't pass through the boundary.

- $\partial P/\partial n = \rho\, \underline{u}_b . \underline{n}$ where fluid impacts on a solid surface with velocity $\underline{u}_b$ and remains in contact with the surface after impact (whence $\underline{u}_a = 0$). This is a consequence of (1.2.6).
- P or ∇P specified in the far field.
- $P = 0$ on a free surface. Since pressure, p, is constant on a free surface, we can define P up to an arbitrary constant, and without loss of generality this constant is zero. A consequence of this is that we can take any contour of constant pressure impulse to be a free surface for the flow.

The present method simplifies the flow equations at the instant when the fluid undergoes a large acceleration. The non-linear boundary conditions are approximated by a linear free surface condition, $P = 0$, and the deforming fluid domain is replaced by the domain at the instant at which the impulsive pressures occur. We neglect the large fluid displacements which occur at the free surface, since we are interested only in the high pressures on the wall. Indeed, since the highest pressures occur when the wave approaches parallel to the wall, two-dimensional analysis of P is often appropriate for predicting the highest impact pressures.

Given a pressure impulse distribution $P(x, y, z)$, we can calculate the impulse, $\underline{I}$, on a solid structure, B, in the fluid domain, by integrating the normal component of P over its boundary, ∂B. That is, $\underline{I} = -\int_{\partial B} P\underline{n}\, \mathrm{d}B$, where $\underline{n}$ is the normal pointing out of B and $\mathrm{d}B$ is a surface element of B. Then, given $\underline{I}$, we can approximate the force on B by assuming that the impulse is the product of a large force $\underline{F}$ and a short time Δt so that $\underline{F} = \underline{I}/\Delta t$. Since Δt is often very small, and $|\underline{I}|$ is proportional to the size of the body and the peak pressure, this can give very large forces, which anecdotal evidence suggests are so great as to overcome the forces holding objects such as caissons in place. So by finding P for some particular geometries, we intend to show how big these forces are, and that the movement of elements of breakwaters is caused by impulsive pressures due to wave breaking.

1.2.1 Applications of PIT - a Literature Review

Cooker and Peregrine (1990, 1995) use PIT to account for the high pressures and velocities involved in the impact of a body of incompressible fluid on a solid surface. They solve for the pressure impulse in a two-dimensional rectangular domain, which is an idealisation of a wave breaking against a vertical wall in shoaling water. The wave is assumed to impact with a vertical face and a flat free surface. The length of the impact zone, the upper part of the wall over which the wave breaks, is a free parameter, and their calculations show that wave breaking over the whole wall gives the highest impact pressures. The length of the domain (distance away from the wall) is also varied to allow the theory to account for wave breaking in containers (small lengths) as well as sea waves (semi-infinite approximation). We extend this analysis in the next chapter, where the model is explained in more depth. Cooker and Peregrine (1995) also use PIT to examine liquid-liquid impact.

The impact zone is extended by Topliss (1994) to a rectangular patch on the wall (in three-dimensions). She shows that as the size of the patch grows, so does the maximum pressure impulse, although it is generally less than that predicted by a two-dimensional model. In the same piece of work, the author uses PIT to find pressure impulse distributions in containers, such as lorries carrying liquid loads. In particular, for partially filled circular containers very high pressure impulse gradients are found.

Wave impact under a horizontal deck projecting out from a vertical wall is studied by Wood (1997) using PIT and conformal mapping. A numerical solution is evaluated, showing that as the depth of water under the deck decreases, the pressure impulses on the underside of the deck increase. This leads to a consideration of the filling flow of Peregrine and Kalliadasis (1996) (see earlier). Wood also models the pressure impulses in a rubble mound in front of a vertical wall by assuming it to be a uniformly porous horizontal sea bed. The pressure impulse in the rubble is relatively low and increasing porosity reduces P along the interface and on the wall.

The solution for the pressure impulse in the rectangular domain of Cooker and

Peregrine (1995) is compared with numerical computations by Cooker and Peregrine (1992). They show that there is reasonably good agreement between the distribution of pressure predicted by each method and that PIT only slightly underestimates peak pressures on the wall. They also find large pressure impulse gradients along the sea bed, acting away from the wall. Hypothesising the presence of a rigid body, resting on the sea bed but free to move, they show that the pressure impulse on the object, generated by the wave breaking against the wall, may be large enough to overcome the fluid drag and friction acting and so move the body. Results are presented for a hemi-ellipsoid and for a circular cylinder, although their conclusion that the cylinder experiences a vertical impulse is incorrect, due to an error in their numerical integration. Their paper also shows that if the body is fixed to the bed it will experience a greater fluid impulse. This model is extended in Chapter 3 to enable some general formulae to be applied to the impulse on a body in this position.

Okamura (1993) employs PIT to explore the effect on the maximum pressures on a sea wall if the wall is inclined. In this wedge shaped geometry, the equations are solved using a Mellin transform. With a careful choice of impacting velocity profile, he shows that pressure impulses (and therefore peak pressures) are higher when the wall is nearly vertical. This, in part, justifies our choice of a vertical wall for most of the analysis that follows.

Agreement between PIT and experiment is found by Chan (1994). He describes his experiments concerning wave breaking against a vertical wall in deep water. In particular, choosing parameter values for the analysis of Cooker and Peregrine (1990) from his experiments, Chan shows that the profiles of peak pressure in the impact zone are similar. It is suggested that trapped air effects could account for the small discrepancy.

Chapter 2

A Comparison of Models for Fluid Impacting on a Vertical Wall

2.1 Introduction

In this chapter we model a wave entering shoaling water and impacting against a vertical wall. As the depth of water decreases towards the wall, the wave steepens and its forward face becomes vertical. Some waves will hit the wall before this happens, and others will propagate further so that a jet is formed at the forward edge, but Bagnold (1939) suggests that the largest pressure forces are caused by those waves whose face is vertical at the instant of impact. We approximate the gently sloping free surface by a flat, horizontal free surface, and assume that the sea bed is also horizontal so that we can solve a boundary value problem for the pressure impulse in this idealised rectangular domain, to model the fluid domain during the time of impact. We extend the model of Cooker and Peregrine (1990, 1995) to ascertain the sensitivity of their results to changes in the velocity profile of the impacting wave. The authors calculate the field of pressure impulse when a rectangular wave slams into a vertical wall. The sea bed is assumed to be flat and the wave impacts over a certain amount of the top of the wall, expressed as a fraction of the total water depth at the wall. For instance, Chan (1994) suggests that for deep-water plunging breakers the proportion of the wall being impacted upon is only 0.028. Cooker and Peregrine take the wave face to be vertical, since this is the shape that experiments show to be the wave profile giving the highest impact pressures. But we wish to know if other idealised profiles will give similar peak pressures, or whether this 'flat face' is unique in causing particularly high peak pressures. We shall consider three different profiles, including the flat face, which will enable us to make some comments about how important it is to choose the correct profile when using PIT.

The next section contains the details of the domain studied here. Section 2.3 describes the results of the modelling, some analytic results and a discussion concerning the number of terms required in the sum giving the solution for the pressure impulse. In §2.4 we give a method enabling $\sum_{n=1}^{\infty} \cos(2n-1)\theta/(2n-1)$ to be repeatedly summed and integrated which uses an asymptotic expansion for $\tan(\theta/2)$. Following this we draw some conclusions.

2.2 Formulation

At the instant of impact the shape of the fluid domain is idealised, as in figure 2.2.1. Consider this simple domain in which the free surface is flat and lies along $y = 0$. The sea bed is at $y = -H$ and the domain extends to $x = B$, for some $B > 0$. The vertical wall is at $x = 0$ and the fraction of the wall in the impact is denoted by μ - the impact occurs over the part of the wall $y \in [-\mu H, 0]$. It may seem perverse to hypothesise a flat free surface, when so many people spend so much time trying to deduce the free surface profile during wave impact. However we justify this choice on two counts: (i) after solving the problem we can choose any of the lines of constant P to be the free surface, since P is only specified up to an additive constant and (ii) during the very short time of impact, $\Delta t \sim 0.01$ seconds, the free surface profile changes little.

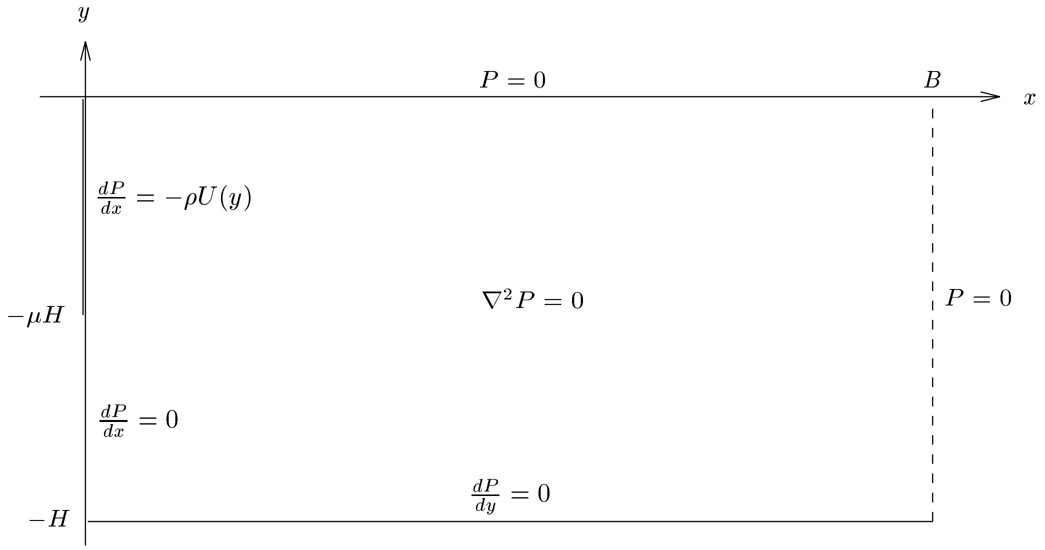

Figure 2.2.1: The boundary value problem for P, which satisfies Laplace's equation throughout the fluid. It is zero on both the free surface, $y = 0$, and the line $x = B > 0$. On the sea bed, $y = -H$, and on the lower part of the vertical wall at $x = 0$ we have $\partial P/\partial n = 0$ (where n is the normal to the specified surface). On the remainder of the wall (the fraction μH over which the wave impacts) $\partial P/\partial x = -\rho U(y)$ for a specified impact velocity profile, $U(y)$. ρ is the density of the fluid and we choose $U(y)$ to be one of three profiles.

The four boundary conditions on the pressure impulse $P(x, y)$ are derived according to the rules in §1.2, and are summarised in figure 2.2.1. P is zero on the free surface and also on $x = B$. The normal derivative of P is zero on the part of the wall below the impact zone and on the sea bed. In the impact zone itself, the normal derivative of P is given by (1.2.6) with $u_a = 0$ and $u_b = U(y)$. Thus

- $P(x, 0) = 0,$ for $x \in [0, B]$
- $\partial P/\partial y\ (x, -H) = 0,$ for $x \in [0, B]$
- $P(B, y) = 0,$ for $y \in [-H, 0]$ or, as $B \to \infty$, $P(x, y) \to 0$ as $x \to \infty$
- $\partial P/\partial x\ (0, y) = \begin{cases} -\rho U(y) \text{ for } y \in [-\mu H, 0) \\ 0 \qquad\quad \text{otherwise} \end{cases}$

where $\mu \in [0, 1]$ and $U(y)$ is the given normal (horizontal) component of the velocity profile of the impacting wave.

A solution of (1.2.7) satisfying the first three conditions is

$$P(x, y) = \sum_{n=1}^{\infty} a_n \sin\left(\lambda_n \frac{y}{H}\right) \frac{\sinh(\lambda_n (x - B)/H)}{\cosh(-\lambda_n B/H)} \tag{2.2.1}$$

where $\lambda_n = (n - \frac{1}{2})\pi$ and the a_n are Fourier coefficients. The set of functions $\sin(\lambda_n y/H), n \in \mathbb{N}$ are orthogonal for $y \in [-H, 0]$, so substitution of (2.2.1) into the fourth boundary condition, together with Fourier analysis gives

$$a_n = -\frac{2\rho}{\lambda_n} \int_{-\mu H}^{0} U(y) \sin(\lambda_n \frac{y}{H})\, \mathrm{d}y. \tag{2.2.2}$$

We consider three impact velocity profiles, each representing a wave impinging with maximum velocity u_0.

- A: $U(y) = u_1 = u_0$.

  u_1 represents the limiting case of a thin lens shape that Bagnold (1939) cites as responsible for the highest peak pressures, where the forward face of the wave is vertical at the moment of impact. This case is treated by Cooker and Peregrine (1990, 1995) and it is included here for comparison of results.

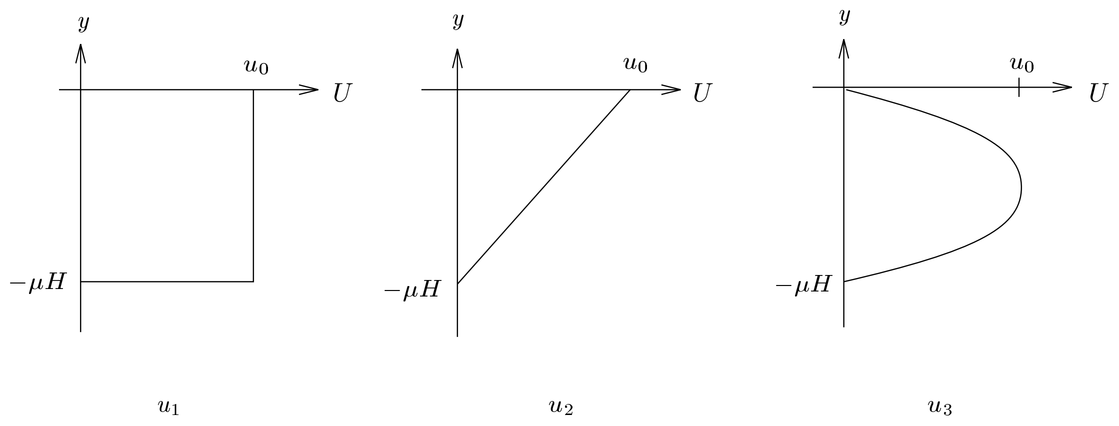

Figure 2.2.2: The impinging velocity profiles, u_1, u_2 and u_3. Each hits the wall over the range $[-\mu H, 0]$ with maximum velocity u_0.

- B: $U(y) = u_2 = \begin{cases} u_0 \frac{(y+\mu H)}{\mu H} & \text{for } y \in [-\mu H, 0) \\ 0 & \text{otherwise.} \end{cases}$

  u_2 exhibits a 'trapdoor' type mechanism where the fluid speeds increase towards the top of the wave.

- C: $U(y) = u_3 = \begin{cases} -4u_0 y \frac{(y+\mu H)}{(\mu H)^2} & \text{for } y \in [-\mu H, 0) \\ 0 & \text{otherwise.} \end{cases}$

  u_3 is parabolic in shape, with faster fluid at the centre compared to the fluid at the top and bottom of the impact zone.

These profiles are illustrated in figure 2.2.2, where u_0 is constant but there is no rule as to how it should be prescribed. Hattori *et al* (1994) find forward velocities of $1 - 2$ m sec^{-1}, but the jets which are often formed move much faster than this. Since there is so much variability between waves, even those classed together as either plunging, upward deflected or spilling, it is hard to relate our three chosen profiles to particular wave types: they are perhaps better left as mathematical constructs.

The corresponding Fourier coefficients, from (2.2.2), are

$$\begin{aligned} &\bullet\ A: a_{1n} = 2\rho u_0 H \frac{1-\cos(\mu\lambda_n)}{\lambda_n^2} \\ &\bullet\ B: a_{2n} = \frac{2\rho u_0 H}{\mu}\frac{\mu\lambda_n - \sin(\mu\lambda_n)}{\lambda_n^3} \\ &\bullet\ C: a_{3n} = \frac{8\rho u_0 H}{\mu^2}\frac{2(1-\cos(\mu\lambda_n)) - \mu\lambda_n\sin(\mu\lambda_n)}{\lambda_n^4} \end{aligned} \qquad (2.2.3)$$

Thus far a rectangle of finite length B has been considered, but in the limiting case of a semi-infinite rectangle as $B \to \infty$, each term of (2.2.1) simplifies since

$$\lim_{B\to\infty} \frac{\sinh(\lambda_n(x-B)/H)}{\cosh(-\lambda_n B/H)} = \lim_{B\to\infty} \mathrm{e}^{-\lambda_n x/H}\,\frac{\mathrm{e}^{2\lambda_n(x-B)/H}-1}{\mathrm{e}^{-2\lambda_n B/H}+1} = -\mathrm{e}^{-\lambda_n x/H}.$$

Writing the hyperbolic functions in terms of their constituent exponentials also increases the rate of convergence, and eases the computation, reducing rounding errors. In the following, the semi-infinite domain is considered, where

$$P_i = -\sum_{n=1}^{\infty} a_{in}\sin\left(\lambda_n\frac{y}{H}\right)\mathrm{e}^{-\lambda_n x/H} \qquad i = 1,2,3. \qquad (2.2.4)$$

2.3 Results

Use of the semi-infinite approximation ($B \to \infty$) is justified by referring to figure 2.3.1, which shows $P_3|_{x=0}$ (which we write as P_3^0) for different values of the length of the domain, B. For $B/H < 0.5$ the pressure impulse on the wall is relatively small and decays to zero towards the sea bed. However, once $B/H > 0.5$, $P|_{x=0}$ changes very little as $B \to \infty$, showing significant pressure impulses everywhere, including the base of the wall. For $B/H \geq 2$ the profile is virtually indistinguishable from $B/H \to \infty$ showing that for $B > H$ the pressure impulse distribution doesn't depend significantly on B and the assumption $B \to \infty$ is valid. $B < H$ is not considered further here since this geometry is of a different nature. In particular it is useful for analysing waves breaking in containers, and perhaps for impulsive pressure propagation in cracks in breakwaters: see Cooker and Peregrine (1995) and also Chapter 5.

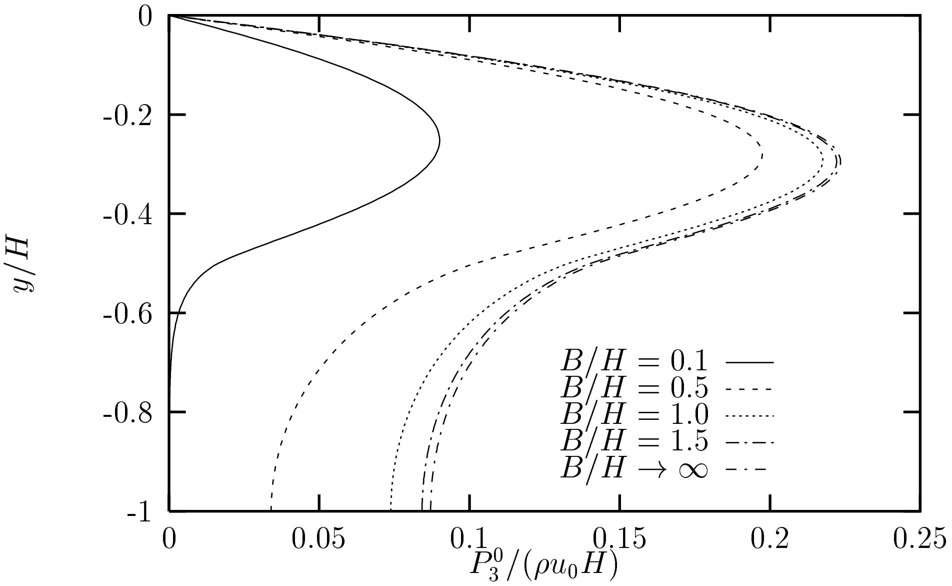

Figure 2.3.1: The pressure impulse on the wall, $x = 0$, for different values of the length of the domain, $B/H = 0.1, 0.5, 1.0, 1.5, \infty$. Case C, with velocity profile $U(y) = u_3$ and $\mu = 0.5$ is shown; the other cases give similar results, as do different values of either x or μ. Notice how close the two lines for $B/H = 1.5$ and $B/H \to \infty$ are, showing how quickly the semi infinite approximation becomes effective.

2.3.1 Varying impact zone length

Figure 2.3.2 indicates that, in each of the three cases, the pressure impulses increase as μ increases. It shows plots of the pressure impulse at the wall, P_i^0, in each of the three cases ($i = 1, 2, 3$), for $\mu = 0.2, 0.5$ and 0.8 respectively. In fact, purely physical considerations lead to the same conclusion - a larger impact zone has a larger body of fluid hitting it (providing all other factors remain constant, as they do here) and so the impulsive pressure is greater. Case B gives the smallest pressure impulses, except near to the surface where, for all μ, it shows higher values than Case C. Case A gives the largest pressure impulses on the wall. Note that the point on the wall at which the maximum pressure impulse occurs, $y_{\max}$, moves down the wall as μ increases.

2.3.2 Comparison of the three velocity profiles

Figures 2.3.3 to 2.3.5 show lines of constant pressure impulse in the domain $x \in [0, H], y \in [-H, 0]$. $P_i = 0$ on the x-axis and P_i increases into the fluid, with increments between the contours of $2 \times 10^{-3} \rho u_0 H$ for $\mu = 0.2$ and $1 \times 10^{-2} \rho u_0 H$ for $\mu = 0.5$ and $\mu = 0.8$.

With μ constant at 0.2 (figure 2.3.3) there is a trend of decreasing maximum pressure impulse from Case A, through Case C, to Case B. That is, $P_1^{\max} = 0.112 \rho u_0 H$, $P_2^{\max} = 0.045 \rho u_0 H$ and $P_3^{\max} = 0.087 \rho u_0 H$. Whilst the impact occurs in the same place on each occasion, the pressure gradients around this area steepen dramatically in Case A. The maxima occur at positions on the wall given by $y_{\max}/H = -0.12, -0.09$ and -0.12 respectively.

As μ increases to 0.5 (figure 2.3.4), an increase in the pressure gradients is observed through the tighter spacing of the contours. In particular, the pressure impulse gradients are very large around the impact zones in Cases A and C. The maximum pressure impulses in each case are $P_1^{\max} = 0.294 \rho u_0 H$, $P_2^{\max} = 0.123 \rho u_0 H$ and $P_3^{\max} = 0.223 \rho u_0 H$. The points at which the maximum pressure occurs on the wall are less close together: respectively $y_{\max}/H = -0.35, -0.22, -0.30$. This effect is due to the

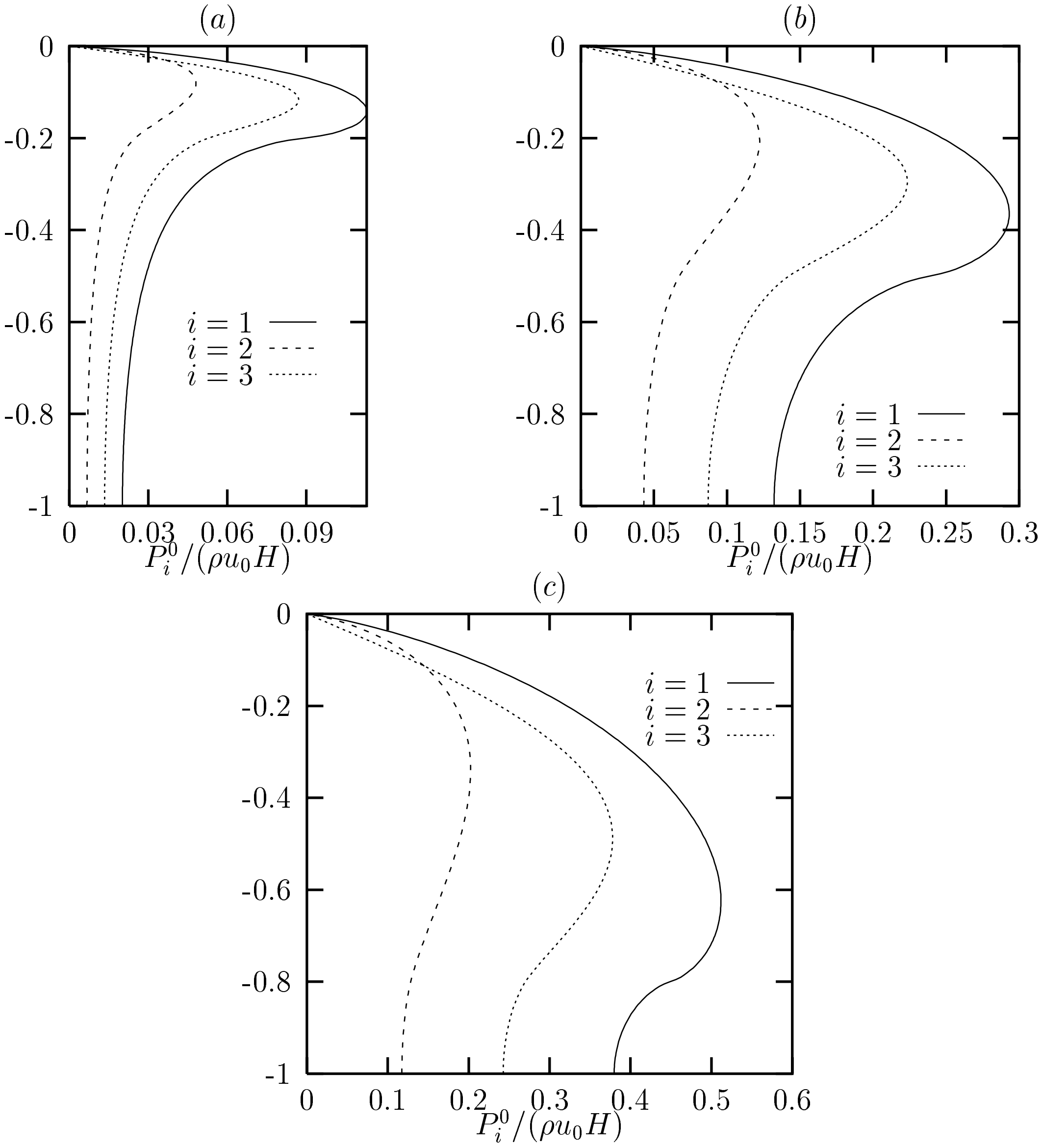

Figure 2.3.2: The pressure impulse on the wall, $x = 0$, for (a) $\mu = 0.2$, (b) $\mu = 0.5$ and (c) $\mu = 0.8$ in each of the three cases. The vertical axis represents distance down the wall, y/H, so that the base of the wall is $y/H = -1$. Case A ($i = 1$) gives the highest pressures. Case B ($i = 2$) gives the lowest pressure impulses, except near the surface, where Case C ($i = 3$) is lower. Recall that the velocity profiles show Case B to have a larger velocity at the surface than Case C, which explains this phenomenon.

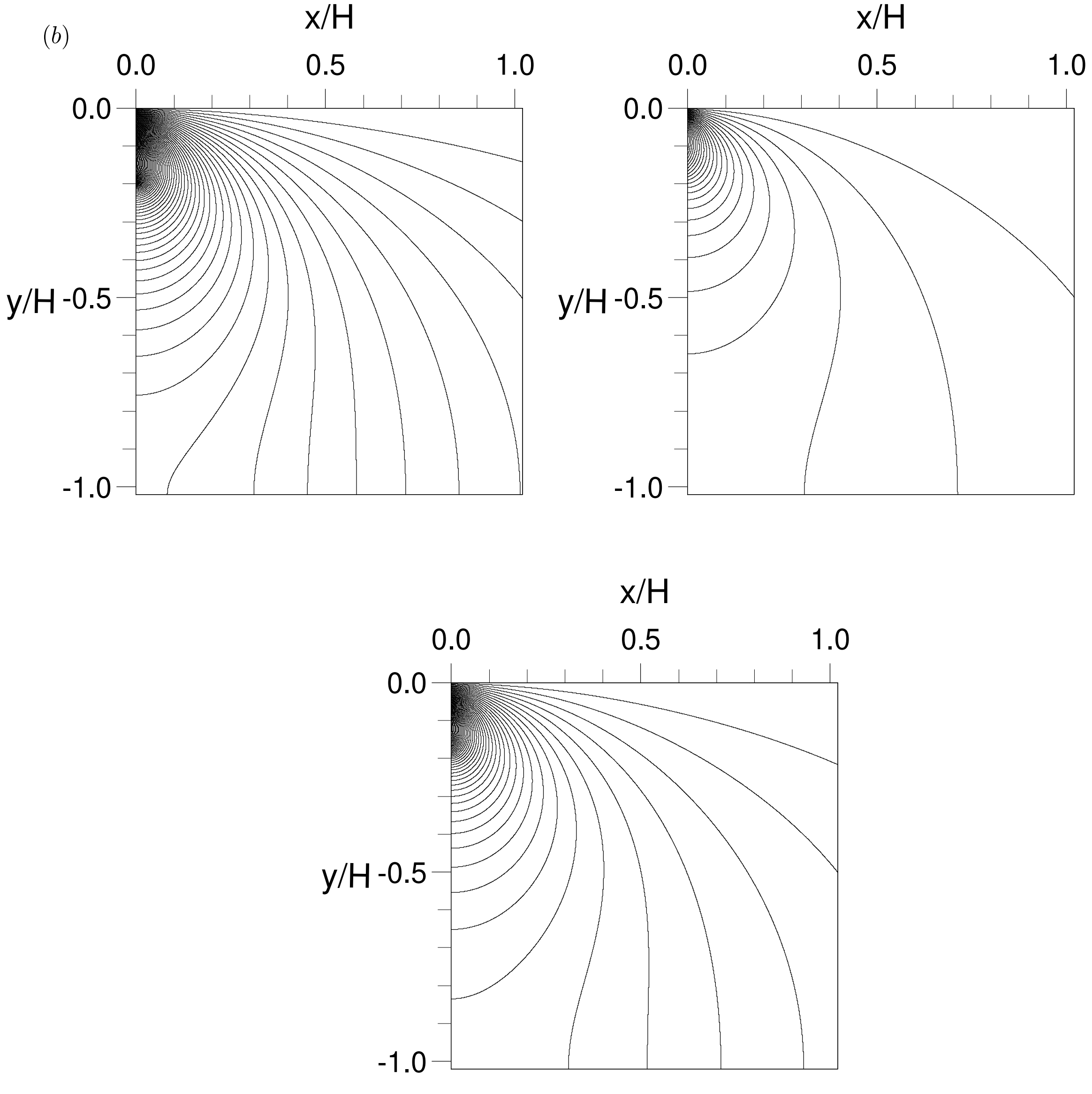
(b)
x/H
0.0
0.5
1.0
0.0
y/H
-0.5
-1.0
x/H
0.0
0.5
1.0
0.0
y/H
-0.5
-1.0
x/H
0.0
0.5
1.0
0.0
y/H
-0.5
-1.0

(c)

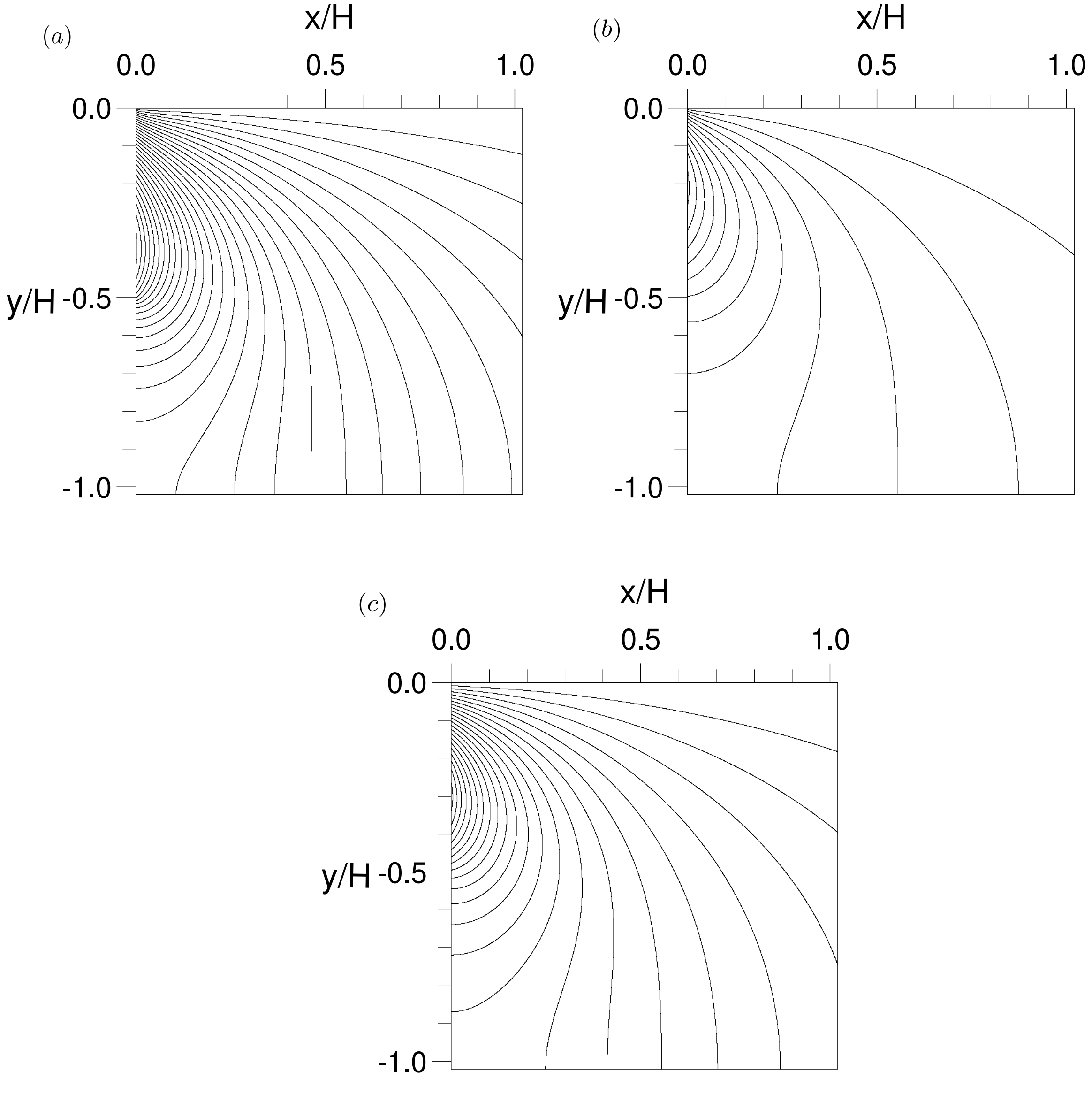

Figure 2.3.4: Lines of constant pressure impulse for $\mu = 0.5, H = 1$. Contour separation is $0.01\rho u_0 H$. (a) Case A: $U(y) = u_1$. (b) Case B: $U(y) = u_2$. (c) Case C: $U(y) = u_3$.

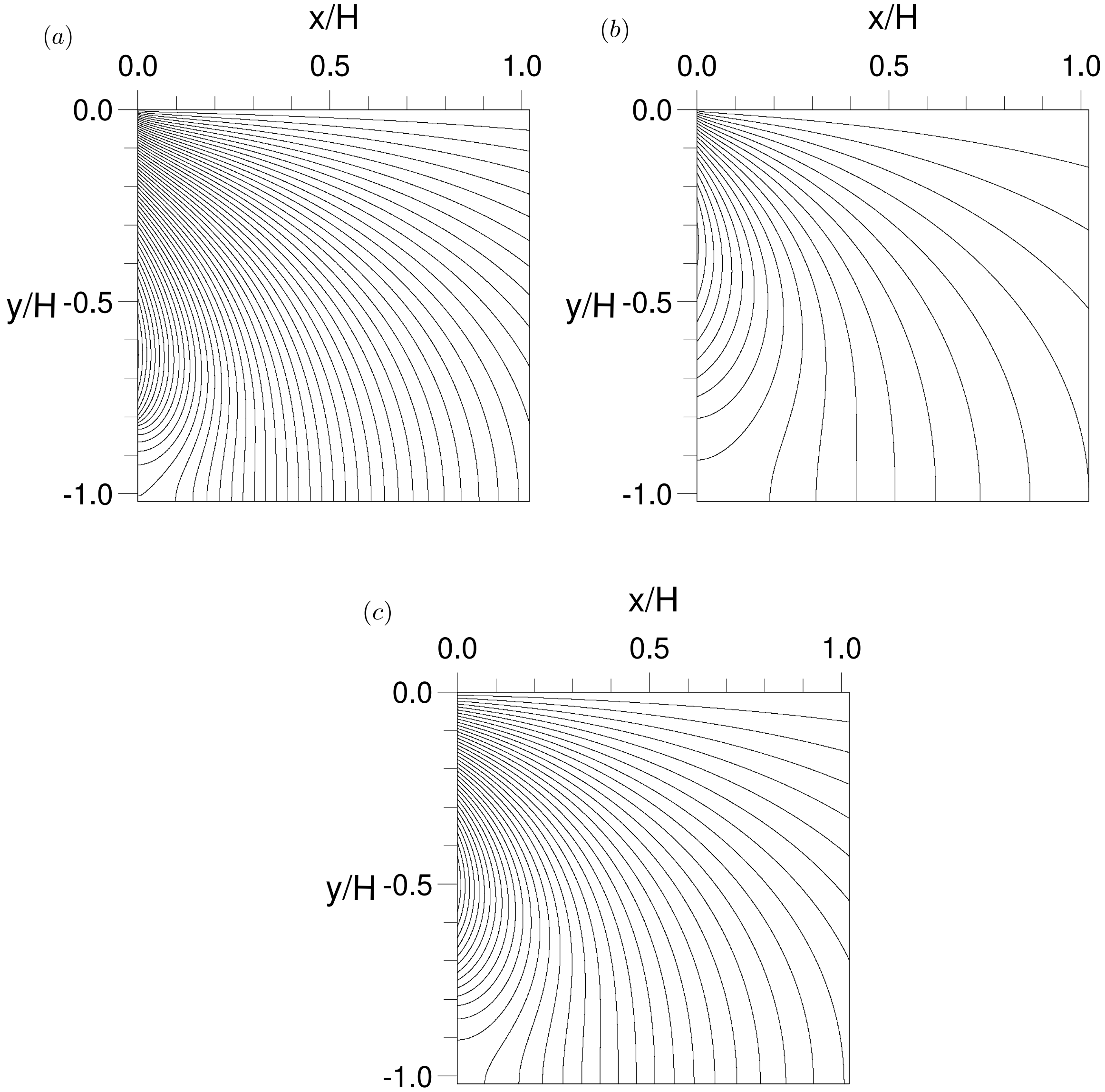

Figure 2.3.5: Lines of constant pressure impulse for $\mu = 0.8, H = 1$. Contour separation is $0.01\rho u_0 H$. (a) Case A: $U(y) = u_1$. (b) Case B: $U(y) = u_2$. (c) Case C: $U(y) = u_3$.

shape of the initial velocity profile, where the shape of u_2 is ‘top-heavy’.

The same trends are noticed with μ at a value of 0.8 (figure 2.3.5). In particular the positions of the maxima are well separated between the cases: $y_{\max}/H = -0.62, -0.34, -0.50$. Notice that the separation between the contours for Case A and Case C is roughly the same now - in fact Case A still gives the highest pressure impulse and Case B the smallest ($P_1^{\max} = 0.520\rho u_0 H$, $P_2^{\max} = 0.203\rho u_0 H$ and $P_3^{\max} = 0.378\rho u_0 H$).

Thus, in summary, there is a trend in increasing magnitude of pressure impulses and pressure impulse gradients from Case B, through Case C, to Case A. The distances between the points on the wall at which the maximum pressure impulse occurs in each case, for the same μ, become greater, in proportion to the size of the impact zone. The pressure impulse gradients are particularly high on the wall above the point of maximum pressure impulse.

As noted in §1.2, we can choose any of the contours of constant pressure impulse to be the free surface. Often the most realistic free surface is the one immediately below the line $y = 0$, which shows the wave elevation decreasing as x/H tends to infinity and rising near the wall at $x = 0$.

2.3.3 Maximum pressure impulses

Figure 2.3.6 shows the maximum pressure impulse, $P_i^{\max}$, as a function of μ for each of the cases A, B and C. As discussed above, Case A always has larger maximum impulses, yet this figure shows that the difference between the cases is not remarkably great. The maximum impulse as a function of μ is remarkably linear for Case B and fairly linear for Case C. When $\mu = 1$, the pressure impulse maxima are $P_i^{\max}/\rho u_0 H = 0.742, 0.262, 0.504$ respectively. In general, there is a factor of about 2.5 in the values between Case A and Case B, which can best be explained by the factor 2 difference in fluid flux approaching the impact zone specified by the wave velocity profiles.

In order to make conservative estimates of pressure impulse maxima when the

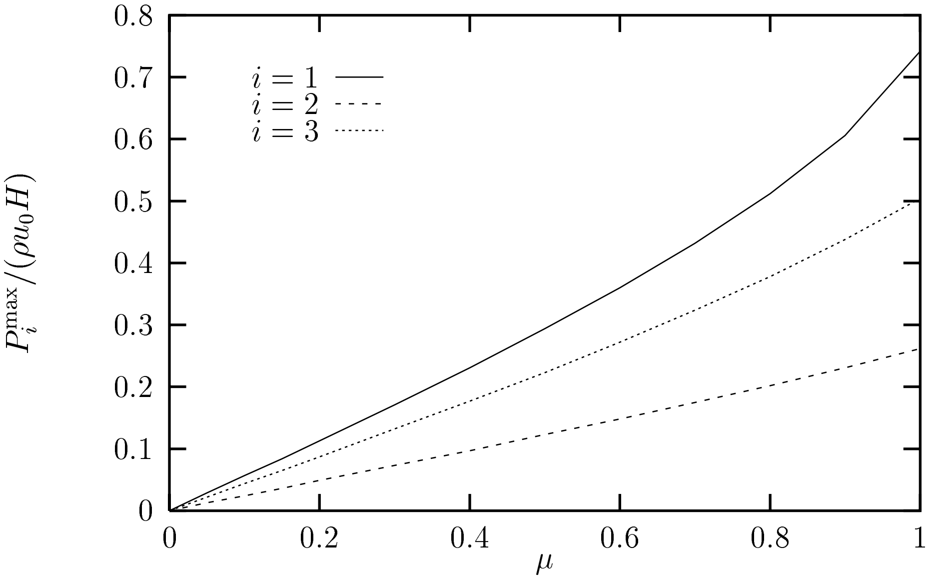

Figure 2.3.6: The maximum value of P_i, $i = 1, 2, 3$, as a function of μ, the impact zone length. The maxima occur on the wall, $x = 0$, and are greatest for Case A and smallest for Case B.

wave velocity profile is uncertain, it is possible to use Case A with $\mu = 1$. This gives the largest expected maximum pressure impulse of about $0.75\rho u_0 H$ under a wide range of wave impacts.

Cooker and Peregrine (1992) compare their numerical routine with the values given by PIT and this procedure is extended here. Their computations suggest $u_0 = 2.6(gh)^{1/2}$, $H = 2.8h$ and $\Delta t = 0.04(h/g)^{1/2}$ for $\mu = 0.1$ (where g is gravitational acceleration and h is the initial water depth at the wall). For the cases described here, this gives maximum peak pressures, according to (1.2.2), of

- $A : p_{peak} = 20.8\rho gh$
- $B : p_{peak} = 8.92\rho gh$
- $C : p_{peak} = 15.8\rho gh.$

(Note that the peak pressure predicted by the pressure impulse calculations of Cooker and Peregrine (1992) is $22\rho gh$ for Case A, due to rounding errors in the values of P obtained.) The computations in Cooker and Peregrine (1992) give a pressure of $26\rho gh$, which the above values underestimate, but not significantly. In his experiments detailing plunging waves breaking against a vertical wall, Chan (1994) finds a mean peak pressure of $9\rho {u_0}^2$. For the waves he studies, $u_0 \approx 1.7(gh)^{1/2}$ so that $p_{peak} \approx 26.1\rho gh$. This is remarkably close to the value predicted theoretically by Cooker and Peregrine (1992) and is just slightly larger than the peak pressure which PIT suggests for a vertical impacting wave face.

2.3.4 Impulse and momentum length

The impulse I on the wall is the integral of the pressure (2.2.4) at $x = 0$ over the wall, that is

$$I = \int_{-H}^{0} P_i(0, y)\,\mathrm{d}y = -\int_{-H}^{0} \sum_{n=1}^{\infty} a_{in} \sin\left(\lambda_n \frac{y}{H}\right)\,\mathrm{d}y = H \sum_{n=1}^{\infty} \frac{a_{in}}{\lambda_n}, \qquad (2.3.1)$$

where $\lambda_n = \left(n - \frac{1}{2}\right)\pi$. The concept of momentum length is then used, which is the significant thickness of fluid involved in the impact. We equate the impulse with the momentum of a notional rectangle of fluid of height μH, speed u_0, density ρ and length L_m, then

$$L_m = \frac{I}{\rho u_0 \mu H} = \frac{1}{\rho u_0 \mu} \sum_{n=1}^{\infty} \frac{a_{in}}{\lambda_n}. \tag{2.3.2}$$

The maximum occurs when $\mu = 1$, giving (to 3 d.p.)

- $A : L_m = 0.542\ H$
- $B : L_m = 0.217\ H$
- $C : L_m = 0.381\ H$

This is a measure of the amount of fluid contributing to the total impulse on the wall - the largest amount being involved in Case A, which is not surprising considering the shape of the profile. Bagnold (1939) estimates this thickness (empirically) to be one-fifth of the wave amplitude, which only makes sense for Case B here.

2.3.5 Number of terms required in sum for computation

The sum in the expression for the pressure impulse, (2.2.4), is infinite, but this is not computationally usable. An idea of how quickly the sum converges is required. Obviously the sums do converge, since a_{in} is proportional to $1/\lambda_n^{i+1}$ for each $i = 1, 2, 3$ (from 2.2.3), but the decrease is not always monotone. Due to the trigonometrical terms, a_{in} oscillates about zero so that for certain non-zero values of μ, $a_{1n} = 0$ and $a_{3n} = 0$. For instance, when $i = 1$,

$$\mu = \frac{4k}{2n-1} \Leftrightarrow 1 - \cos(\mu\lambda_n) = 0 \tag{2.3.3}$$

for all $n \in \mathbb{N}$ and some $k \in \mathbb{N}$ such that $0 < \mu \leq 1$. Then $a_{1n} = 0$ and so $P_1 = 0$. When $i = 3$, we make the substitution $t = \tan(\mu\lambda_n/2)$ to show that

$$\mu = \frac{2\gamma}{(2n-1)\pi} \Leftrightarrow 2(1 - \cos(\mu\lambda_n)) - \mu\lambda_n \sin(\mu\lambda_n) = 0,$$

where γ is a root of the equation $\tan\left(\frac{\gamma}{2}\right) - \frac{\gamma}{2} = 0$

so that $a_{3n} = 0$ and so $P_3 = 0$. Thus a criterion for halting the summation when the series first contains small a_{in} is inadequate; a different approach is needed. We estimate a_{in} as $n \to \infty$:

$$a_{1n} \sim \frac{4}{\lambda_n^2}, \qquad a_{2n} \sim \frac{2}{\lambda_n^2}, \qquad a_{3n} \sim \frac{8}{\lambda_n^3}$$

and then the number of terms required before $a_{in} < 10^{-6}$ is estimated as

$$n - \frac{1}{2} > \frac{2000}{\pi}, \quad \sqrt{2}\frac{1000}{\pi} \text{ and } \frac{200}{\pi}$$

respectively. Thus, we require 637/451/64 terms respectively as the cut off for the summation when calculating P. In practice only 30 to 50 terms appear to be necessary in each case, although this criterion stems purely from trial and error in getting figures 2.3.3 to 2.3.5 to look smooth.

2.4 An Alternative Representation for the Pressure Impulse on the Wall

The maximum pressure impulse on the wall occurs at the point $y = y_{\max}$, where

$$\frac{\partial P_i}{\partial y}(0, y_{\max}) = 0. \tag{2.4.1}$$

Cooker and Peregrine (1995) use an integral representation of (2.2.4) to show that $y_{\max} \sim \mu H/\sqrt{2}$ in Case A. But their method only works when the denominator contains λ_n squared: one has to integrate $f(z) = \operatorname{cosech}(\pi z/2)$ twice. In the expressions for the pressure impulse in Cases B and C we have λ_n^{-k} for $k = 3, 4$ and so would have to integrate $f(z)$ k times. But we still wish to find $y_{\max}(\mu)$ for each of the velocity profiles in cases B and C. In an attempt to do this we rearrange (2.2.4), at $x = 0$, using standard trigonometric identities in order to speed up the convergence of these otherwise slowly convergent series. Writing $P_i|_{x=0} = P_i^0$ and $\theta_\pm = y/H \pm \mu$ gives

$$\begin{aligned}
P_1^0 &= \rho u_0 H \left[\sum_{n=1}^{\infty} \frac{\sin(\lambda_n \theta_+)}{\lambda_n^2} + \sum_{n=1}^{\infty} \frac{\sin(\lambda_n \theta_-)}{\lambda_n^2} - 2 \sum_{n=1}^{\infty} \frac{\sin(\lambda_n y/H)}{\lambda_n^2} \right], \\
P_2^0 &= \frac{\rho u_0 H}{\mu} \left[\sum_{n=1}^{\infty} \frac{\cos(\lambda_n \theta_-)}{\lambda_n^3} - \sum_{n=1}^{\infty} \frac{\cos(\lambda_n \theta_+)}{\lambda_n^3} - 2\mu \sum_{n=1}^{\infty} \frac{\sin(\lambda_n y/H)}{\lambda_n^2} \right], \\
P_3^0 &= \frac{8 \rho u_0 H}{\mu^2} \left[\mu \left(\sum_{n=1}^{\infty} \frac{\cos(\lambda_n \theta_-)}{\lambda_n^3} - \sum_{n=1}^{\infty} \frac{\cos(\lambda_n \theta_+)}{\lambda_n^3} \right) + \right. \\
&\quad \left. + \sum_{n=1}^{\infty} \frac{\sin(\lambda_n \theta_+)}{\lambda_n^4} + \sum_{n=1}^{\infty} \frac{\sin(\lambda_n \theta_-)}{\lambda_n^4} - 2 \sum_{n=1}^{\infty} \frac{\sin(\lambda_n y/H)}{\lambda_n^4} \right].
\end{aligned} \tag{2.4.2}$$

It seems that these individual series are not easily summable. With $\lambda_n = (2n - 1)\pi/2$, Bromwich (1926, §121,122) shows that the intermediate cases are well behaved; that is

$$\sum_{n=1}^{\infty} \frac{\sin(2n-1)\theta}{(2n-1)}, \sum_{n=1}^{\infty} \frac{\cos(2n-1)\theta}{(2n-1)^2}, \sum_{n=1}^{\infty} \frac{\sin(2n-1)\theta}{(2n-1)^3}, \sum_{n=1}^{\infty} \frac{\cos(2n-1)\theta}{(2n-1)^4} \tag{2.4.3}$$

are all straightforward polynomials. Note that these polynomials can all be obtained by repeated integration of the first sum. However,

$$\sum_{n=1}^{\infty} \frac{\sin(2n-1)\theta}{(2n-1)^2}, \sum_{n=1}^{\infty} \frac{\cos(2n-1)\theta}{(2n-1)^3}, \sum_{n=1}^{\infty} \frac{\sin(2n-1)\theta}{(2n-1)^4} \tag{2.4.4}$$

do not sum quite so straightforwardly.

2.4.1 The summation of some awkward series

To sum the awkward series in (2.4.4), the known sum

$$\sum_{n=1}^{\infty} \frac{\cos(2n-1)\theta}{2n-1} = \frac{1}{2} \log \left| \cot \frac{\theta}{2} \right| = -\frac{1}{2} \log \left| \tan \frac{\theta}{2} \right| \tag{2.4.5}$$

must be integrated repeatedly.

To do this integration, we replace the right-hand side of (2.4.5) with an accurate expression which is valid throughout the interval $\theta \in (-\pi, \pi)$, which is appropriate for

$\theta = \frac{1}{2}\pi(\mu \pm y/H)$. In fact we need only consider $0 < \theta < \pi/2$, since $\cos(-\theta) = \cos(\theta)$ and $\sin(-\theta) = -\sin(\theta)$, and

$$\sin(2n-1)(\pi - \theta) = \sin(2n-1)\theta \text{ and } \cos(2n-1)(\pi-\theta) = -\cos(2n-1)\theta.$$

If $\theta = 0$ or $\pi/2$, the sums in (2.4.4) become series of reciprocals of positive odd integers, which are tabulated (eg. Jolley 1961) and will act as a check on the accuracy of the following method. An approximation for $\tan(\theta/2)$ that accurately describes the singular behaviour at $\theta = \pm\pi$ and that has roughly the correct slope at the origin is needed, in a similar way to that described by Cooker (1998). It must also be repeatedly integrable, preferably with a general formula. We use

$$\tan\left(\frac{\theta}{2}\right) \approx \frac{\pi^2}{4}\frac{\theta/2}{(\pi/2 - \theta/2)(\pi/2+\theta/2)} = \frac{\pi^2}{2}\frac{\theta}{\pi^2-\theta^2} := f(\theta)$$

which is the quotient of the first terms of the product expansions for $\sin(\theta/2)$ and $\cos(\theta/2)$ (from Abramowitz and Stegun 1965, eq.4.3.89/90). Note that not only is f singular in the right places, but $f(0) = \tan(0) = 0$ and $f'(0) = \frac{1}{2}\sec^2(0) = \frac{1}{2}$. Then, since $\tan(\theta/2)/f(\theta) \approx 1$, the function h, defined by

$$h(\theta) = \log\left[\frac{\tan(\theta/2)}{\theta/2}\left(1 - \left(\frac{\theta}{\pi}\right)^2\right)\right] = \log\left|\tan\frac{\theta}{2}\right| - \log\left|\frac{\theta}{2}\right| + \log\left(1-\left(\frac{\theta}{\pi}\right)^2\right) \tag{2.4.6}$$

is small throughout the interval. In fact, the maximum error occurs when $\theta = \pi/2$ which gives $h(\pi/2) = \log(3/\pi) = -0.046$. We therefore expect h to have a rapidly convergent Maclaurin series. This series is

$$\bar{h}(\theta) = \sum_{n=1}^{\infty}\left((-1)^{n+1}\frac{2^{2n-1}-1}{n(2n)!}B_{2n} - \frac{1}{n\pi^{2n}}\right)\theta^{2n} := -\sum_{n=1}^{\infty} b_n\theta^{2n} \tag{2.4.7}$$

where the B_n are Bernoulli numbers (Abramowitz and Stegun 1965, §23 & eq.4.3.73). The first four terms of the series are

$$\begin{aligned} b_1 &= \left(\frac{1}{\pi^2} - \frac{1}{12}\right) \approx 1.799 \times 10^{-2}, \\ b_2 &= \left(\frac{1}{2\pi^4} - \frac{7}{1440}\right) \approx 2.719 \times 10^{-4}, \\ b_3 &= \left(\frac{1}{3\pi^6} - \frac{31}{90720}\right) \approx 5.010 \times 10^{-6}, \\ b_4 &= \left(\frac{1}{4\pi^8} - \frac{127}{4838400}\right) \approx 9.925 \times 10^{-8}. \end{aligned}$$

Note the rapid decrease in magnitude of these terms. The first term in each of the b_n's comes from the last log term in (2.4.6) - the two would cancel when we substitute the expansion into (2.4.5), but we leave these terms in because they help to keep the b_n small, whilst the log term can be integrated exactly and repeatedly.

Now, substituting (2.4.6) and (2.4.7) in (2.4.5),

$$\sum_{n=1}^{\infty} \frac{\cos(2n-1)\theta}{2n-1} = \frac{1}{2}\left\{\sum_{n=1}^{\infty} b_n \theta^{2n} - \log\left|\frac{\theta}{2}\right| + \log\left(1-\left(\frac{\theta}{\pi}\right)^2\right)\right\}. \tag{2.4.8}$$

We can decompose the last logarithm to ease the following analysis. Upon integrating (2.4.8), and tidying, the remaining trigonometric sums of (2.4.4) become

$$\begin{aligned}
\sum_{n=1}^{\infty} \frac{\sin(2n-1)\theta}{(2n-1)^2} &= \frac{1}{2}\sum_{n=1}^{\infty} \frac{b_n}{2n+1}\theta^{2n+1} - \frac{\theta}{2}\left(1+\log\left|\frac{\theta}{2}\right| - h_1(\theta)\right) - \frac{\pi}{2}h_2(\theta), && (2.4.9)\\
\sum_{n=1}^{\infty} \frac{\cos(2n-1)\theta}{(2n-1)^3} &= \lambda(3) - \frac{1}{2}\sum_{n=1}^{\infty} \frac{b_n}{(2n+1)(2n+2)}\theta^{2n+2} + \\
&\quad + \frac{\theta^2}{4}\left(\frac{3}{2}+\log\left|\frac{\theta}{2}\right| - h_1(\theta)\right) + \frac{\pi\theta}{2}h_2(\theta) - \frac{\pi^2}{4}h_1(\theta), && (2.4.10)\\
\sum_{n=1}^{\infty} \frac{\sin(2n-1)\theta}{(2n-1)^4} &= \left(\lambda(3)+\frac{\pi^2}{6}\right)\theta - \frac{1}{2}\sum_{n=1}^{\infty} \frac{b_n}{(2n+1)(2n+2)(2n+3)}\theta^{2n+3} + \\
&\quad + \frac{\theta^3}{12}\left(\frac{11}{6} + \log\left|\frac{\theta}{2}\right| - h_1(\theta)\right) + \frac{\pi^2}{4}\left(\theta^2+\frac{\pi^2}{3}\right)h_2(\theta) - \frac{\pi^2\theta}{4}h_1(\theta) && (2.4.11)
\end{aligned}$$

where

$$\begin{aligned}
h_1(\theta) &= \log\left(1-\left(\frac{\theta}{\pi}\right)^2\right),\\
h_2(\theta) &= \log\left(\frac{\pi-\theta}{\pi+\theta}\right)
\end{aligned}$$

and

$$\lambda(3) = \sum_{n=0}^{\infty} \frac{1}{(2n+1)^3} = 1.0517997902$$

(from Abramowitz and Stegun 1965, p812). With this notation, (2.4.8) becomes

$$\sum_{n=1}^{\infty} \frac{\cos(2n-1)\theta}{2n-1} = \frac{1}{2}\left\{\bar{h}(\theta) - \log\left|\frac{\theta}{2}\right| + h_1(\theta)\right\}$$

although it is of course more accurate to use (2.4.5).

To demonstrate how accurate this method is, we insert in (2.4.9) the value of θ that gives the maximum error, $\theta = \pi/2$, with just four terms (shown above) in the Maclaurin expansion, to get

$$\sum_{n=1}^{\infty} \frac{(-1)^{n+1}}{(2n-1)^2} = 0.9159655816$$

which is correct to 7 decimal places (Abramowitz and Stegun 1965, p812). Similarly, (2.4.11) with $\theta = \pi/2$ gives

$$\sum_{n=1}^{\infty} \frac{(-1)^{n+1}}{(2n-1)^4} = 0.9889445529,$$

correct to 8 decimal places. When $\theta = \pi/2$ in (2.4.10), instead of zero we get -3.042×10^{-10}, which is the error.

Replacing θ with $\pi/2 - \theta$ shows that we can also now sum

$$\sum_{n=1}^{\infty} (-1)^{n+1} \frac{\sin(2n-1)\theta}{(2n-1)}, \quad \sum_{n=1}^{\infty} (-1)^{n+1} \frac{\cos(2n-1)\theta}{(2n-1)^2},$$
$$\sum_{n=1}^{\infty} (-1)^{n+1} \frac{\sin(2n-1)\theta}{(2n-1)^3}, \quad \sum_{n=1}^{\infty} (-1)^{n+1} \frac{\cos(2n-1)\theta}{(2n-1)^4}.$$

In principle this method extends to higher exponents of the denominator; a general formula relies only on expressing successive integrals of

$$\log\left(\frac{1-(\theta/\pi)^2}{\theta}\right)$$

neatly. The expressions in (2.4.2) can now be rewritten and will be significantly faster to compute.

2.5 Summary

PIT has enabled a comparison to be made of three velocity profiles impacting on a vertical wall. At the wall, situated at $x = 0$, the normal component of fluid velocity,

$U(y)$, immediately before impact is chosen in one of three ways in order to compare the influence on the pressure impulse, P, of varying $\partial P/\partial x|_{x=0} = \rho U(y)$.

We have shown that there is less than an order of magnitude difference between the maximum pressure impulses measured in each case, which leads to the conclusion that the shape of the impacting velocity profile is relatively unimportant (compared to quantities such as the wave impact speed, u_0) in the modelling of water wave impacts on vertical walls. Also, any value of pressure impulse, P, can be taken and used to estimate a corresponding peak pressure $p_{peak} = 2P/\Delta t$, where Δt is the duration of the impact, of the order of milliseconds.

An asymptotic expansion is constructed to simplify the infinite sums involved in the series representation of the pressure impulse at the wall. This expansion converges very quickly: four terms are sufficient to give accuracy to at least seven decimal places.

Given the distribution of pressure impulse caused by a wave breaking against the vertical wall, we can now examine the effect of this pressure impulse field on objects in the vicinity of the wall. In Chapter 3 we consider a body which is at rest on the sea floor, whose length scale is much less than the lengths associated with the model here, such as the height of the wall. We are interested in whether or not a body in this region is moved by the force of the impact. Near the free surface of the model presented above there is a pressure impulse gradient acting upwards which could cause a surface-piercing body to move. We quantify the impulse acting on a body in this position in Chapter 4 with an analysis that is similar to the work of Chapter 3.

Whereas in this chapter we have considered a plane impermeable wall at $x = 0$, in Chapter 5 we will derive an approximate theory for calculating the pressure impulse in a thin crack in the wall. We will then be able to find the impulse on the roof of the crack and compare its magnitude with the other forces acting on the roof, such as the weight of the overlying structure. This analysis leads on to a consideration of the pressure impulse in a narrow crack between an axisymmetric body and a flat plane, such as a sphere at rest on the sea bed. Using this approximation around the point of contact of the sphere, we generate a fully three-dimensional numerical solution for the pressure impulse around the sphere, so that we can find the impulse on it as we did for some two-dimensional shapes in Chapter 3.

Chapter 3

The Pressure Impulse on a Body on the Sea Floor

3.1 Introduction

We wish to explain how wave impacts are able to remove blocks from seawalls and breakwaters and move large boulders and armour protection units in the vicinity of these structures. In particular, to explain the observations of Stevenson (1864), quoted in §1.1, of huge boulders being moved by the force of the waves.

In Chapter 2 we calculated the pressure impulse in a fluid domain, D, whose shape resembles a sea wave at its moment of impact against a vertical wall. D is the region $x \geq 0, -H \leq y \leq 0$, with the wall at $x = 0$ and the horizontal sea bed at $y = -H$. Given the maximum value of the velocity impact profile, u_0, which is kept constant, and a fixed impact zone (the interval over which the velocity, $U(y)$, is non-zero) the results show that alterations of the distribution of impact speed have little influence on the maximum pressure impulse, P_{max}, exerted on the wall. However the gradients $\partial P/\partial x$ and $\partial P/\partial y$ are strongly influenced by $U(y)$. They are directly proportional to the finite change in flow velocity which occurs throughout the fluid domain during the impact. We can see this by comparing the results within each of the figures 2.3.3 to 2.3.5 where, for constant μ, these pressure impulse gradients change dramatically depending on which of the impacting velocity profiles we choose. Moreover, the gradients acting down the wall, away from the impact zone, and along the sea bed, away from the wall, are often large. These pressure impulse gradients are going to exert impulsive forces on objects in these areas, which could be great enough to move them.

As far as we are aware, only two sets of experiments have measured the pressure gradient along the bed, near to the wall. Grilli, Losada, and Martin (1993) inserted eight pressure sensors on the bed of a laboratory tank, close to the base of a vertical wall against which waves were made to break. They found that large impact pressures were recorded at a considerable distance from the wall and that these pressures propagated very rapidly. Moreover, the pressure gradients had magnitudes of up to about $2\rho g$. Müller (1995) performed small-scale experiments on waves breaking against a vertical wall and showed pressure gradients of up to almost $8\rho g$. This translates into pressure impulse gradients of approximately $0.04\rho u_0$ which are several times larger than those in the experiments of Grilli *et al.* We estimate a pressure impulse gradient along the bed, G, from Chapter 2 for Case A with $\mu = 0.5$ (see figure 2.3.4(a)). At $x/H = 0.5$, the pressure impulse gradient is $G = 0.1\rho u_0$. This is about twice as large as the pressure impulse gradients which Müller (1995) found experimentally, and could therefore be a reasonable estimate for storm waves.

Cooker and Peregrine (1992) show that a rigid body, B, placed in a field of pressure impulse experiences a net impulse $\underline{I}$ which is significant even when the body is on the sea bed. $\underline{I}$ depends on (i) the shape and volume of B, (ii) the pressure impulse gradient $\underline{G} = \nabla P$, (iii) the presence of a solid boundary such as the sea bed or other bodies and (iv) whether B is free to move. Their calculations suggest that these impulses can move or maybe even lift them.

The impulse can be thought of as the product of a force, $\underline{F}_I$, of large modulus and a short time Δt, $\underline{I} = \underline{F}_I \Delta t$. During the brief time of impact, Δt, the force may be so great as to overcome the restraining or frictional forces which usually hold a body in place, $\underline{F}_F$, with $|\underline{F}_F| = \mu(\rho_B - \rho)\mathcal{V} g$, where μ is the coefficient of friction between B and the bed, ρ_B the density and $\mathcal{V}$ the volume of B. In contrast, a fluid force $\underline{F}_D$ is exerted by the liquid flowing over the body, due to the passage of waves of period T. $\underline{F}_D$ can be modelled as due to a relatively slowly varying flow of speed $u_0(t)$ away from the body, where $u_0(t)$ is periodic of period T, which is of order 10 seconds at the coast. Because the flow varies relatively slowly ($T \gg \Delta t$), the expression $|\underline{F}_D| = \frac{1}{2}\rho C_D \mathcal{A} {u_0}^2$ is valid, pulling B towards the wall. C_D is a drag coefficient at approximately constant flow speed (appropriate to the body and Reynolds number) and $\mathcal{A}$ is the cross-sectional area of the body in the direction of motion. Batchelor (1973, §5.11) discusses the drag on a circular cylinder and a sphere, and, for flows with Reynolds number 10^6, gives $C_D \approx 0.5$ for a cylinder and $C_D \approx 0.2$ for a sphere. We will compare these forces to see if the impulsive force is large enough to move a body.

This chapter proceeds by taking a field of pressure impulse, P_1, which has already been calculated (in Chapter 2 for instance) and finding the change in P_1 brought about by the presence of a body, B, at rest in the fluid domain, D. By considering B much smaller than the significant length scale in D, it is reasonable to suppose that the effect of B on P_1 is confined to a region near B. For example, a semicircle, B, of radius a can be placed on the bed of the rectangular domain described above provided $a \ll H$. The centre of B is at $x = X, y = -H$, and then $\partial P_1/\partial x|_{x=X,y=-H} = -G$ is evaluated. From now on, G is treated as a constant for the purposes of the flow in the neighbourhood of B. Also constant is $P_1|_{x=X,y=-H} = P_0$. These two conditions can be combined to give an expression for the distorted pressure impulse field

$$P(x, y) \sim P_0 - Gx \tag{3.1.1}$$

which is applied in the far field of the model for flow around B. Usually, (3.1.1) is achieved within a few radii of B, and so the whole of the model near B lies in a region whose dimensions are small compared with H. The pressure impulse, P, near B satisfies the boundary value problem shown in figure 3.1.1. New coordinates $x' = x - X, y' = y - (-H)$ are introduced and the bed boundary condition changes to $\partial P/\partial n = 0$ on both the boundary of B and the remainder of the bed. P continues to satisfy Laplace's equation and the far field boundary condition (3.1.1). More

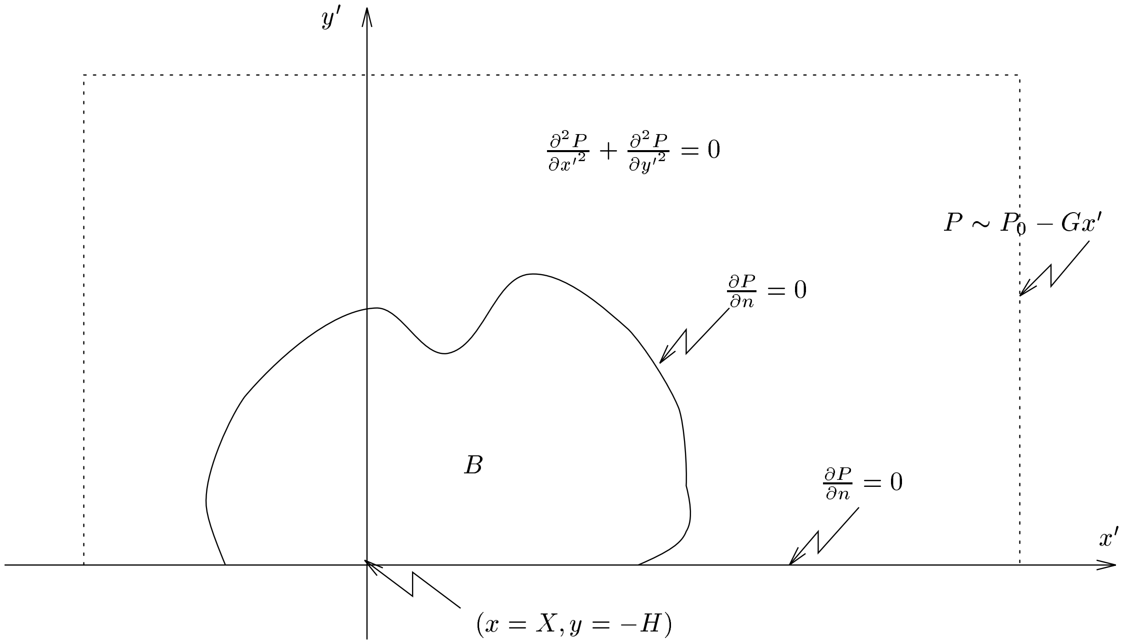

Figure 3.1.1: The boundary value problem for the pressure impulse around B. The free surface lies in the y' direction and the base of the wall in the negative x' direction. The dotted line represents infinity as viewed by this local model. The pressure impulse satisfies Laplace's equation and the far field condition is that $P \sim P_0 - Gx'$. The normal velocity is zero on both B and the sea bed, $y = -H$.

generally, x' could be a coordinate indicating arc length along a solid surface and y' normal to the surface. (The far field condition might also be directly proportional to y' if B lay inside an impact zone. Approximations of order higher than those in (3.1.1) can be calculated, but the term proportional to the square of x' has no net effect on the impulse for a left-right symmetric body.) The boundary condition on B significantly changes the pressure impulse contours, usually attracting them towards B and thereby increasing the impulse on the body.

The method is readily extended to small three-dimensional bodies placed in fields of pressure impulse, $P_1 = P_1(x, y, z)$. With a suitable change of axes, the x-axis can be placed parallel to ∇P_1 so that $P_1 = P_1(x', y')$ and then the three-dimensional distortion, P, of a locally two-dimensional field, P_1, may be considered.

In the following sections, P is calculated for several two-dimensional bodies fixed to the sea bed, including semicircles, semi-ellipses, sinusoidal lumps and rectangular boxes. The impulse on each of these shapes is also found and is shown to be calculable even when P is too complex to find, using the techniques of complex function theory and Fourier series analysis.

3.2 Mathematical Formulation

Given P_0 and G, we assume that the presence of B causes a distortion to P, in (3.1.1), which we write as $F(x, y)$ (dropping primes). Thus

$$P = P_0 - Gx + GF(x, y)$$

where F is of order ϵx for $\epsilon \ll 1.0$.

A method of representing the change in the sea bed due to B is required; in particular, one which doesn't affect the sea floor away from B. The first idea considered is that of a Fourier Series: we can use the series to represent a periodically undulating bed or, by choosing those series that have a periodic elevation surrounded by a profile coinciding with the axis, we can represent a single body (and assume that the distance to the next elevation is large enough that it doesn't affect the pressure impulse around the one in which we are interested). There is already a large collection of series defining particular shapes, which are all built from a simple basis of trigonometric functions.

Secondly, an exact method is to conformally map the real axis of a w plane to a physical sea bed in a z plane. These maps will generate bodies in the form of simple geometric shapes on a horizontal base with explicit transformations in the form $z = z(w)$, from either the upper half-plane or the exterior of the unit circle. Examples of such maps can be found in Kober (1957).

3.3 Fourier Series Approach

The bed is given by $y(x) = \epsilon h(x)$, with normal $\underline{n} = (-\epsilon \mathrm{d}h/\mathrm{d}x, 1)$. Since P is a solution of Laplace's equation, F must satisfy:

$$\nabla^2 F = 0 \text{ in } y \geq \epsilon h(x) \tag{3.3.1}$$

with boundary conditions

$$\frac{\partial F}{\partial x} \to 0 \text{ as } y \to \infty \tag{3.3.2}$$

and

$$0 = \frac{\partial P}{\partial n}(x, y(x)) = \nabla P.\underline{n} = \left(-G + G\frac{\partial F}{\partial x}, G\frac{\partial F}{\partial y}\right).\underline{n} \quad \text{on } y = \epsilon h(x).$$

The second can be rewritten

$$\frac{\partial F}{\partial y} = \left(\frac{\partial F}{\partial x} - 1\right)\epsilon\frac{\mathrm{d}h}{\mathrm{d}x} \quad \text{on } y = \epsilon h(x). \tag{3.3.3}$$

Then we try a solution of the form

$$F(x,y) = F_0(x,y) + \epsilon F_1(x,y) + \epsilon^2 F_2(x,y) + ... = \sum_{j=0}^{\infty} \epsilon^j F_j(x,y) \tag{3.3.4}$$

and use perturbation techniques (Van Dyke 1964) in order to find the unknown functions F_j. As $\epsilon \to 0, P \to P_0 - Gx + GF_0$. But $\epsilon = 0$ implies a flat sea bed, and thus $F_0 = 0$. A Taylor series expansion of the derivatives is now used,

$$\frac{\partial F}{\partial x}(x, \epsilon h(x)) = \sum_{k=0}^{\infty} \frac{(\epsilon h(x))^k}{k!} \frac{\partial^{k+1} F}{\partial x \partial y^k}(x, 0) \tag{3.3.5}$$

$$\frac{\partial F}{\partial y}(x, \epsilon h(x)) = \sum_{k=0}^{\infty} \frac{(\epsilon h(x))^k}{k!} \frac{\partial^{k+1} F}{\partial y^{k+1}}(x, 0) \tag{3.3.6}$$

together with the expansion for F from (3.3.4), in the boundary condition (3.3.3) to give

$$h'\epsilon - h'\epsilon \sum_{k=0}^{\infty} \frac{(\epsilon h)^k}{k!} \frac{\partial^{k+1}}{\partial x \partial y^k}\left(\sum_{j=1}^{\infty} \epsilon^j F_j\right) + \sum_{k=0}^{\infty} \frac{(\epsilon h)^k}{k!} \frac{\partial^{k+1}}{\partial y^{k+1}}\left(\sum_{j=1}^{\infty} \epsilon^j F_j\right) = 0, \tag{3.3.7}$$

where $h' = \mathrm{d}h(x)/\mathrm{d}x$. This can be written as

$$h'\epsilon - \sum_{k=0}^{\infty} h' \frac{h^k}{k!} \frac{\partial^{k+1}}{\partial x \partial y^k} \left(\sum_{j=1}^{\infty} \epsilon^{j+k+1} F_j \right) + \sum_{k=0}^{\infty} \frac{h^k}{k!} \frac{\partial^{k+1}}{\partial y^{k+1}} \left(\sum_{j=1}^{\infty} \epsilon^{j+k} F_j \right) = 0. \tag{3.3.8}$$

For $i \geq 2$, the coefficient of ϵ^i is

$$-\sum_{k=0}^{i-2} h' \frac{h^k}{k!} \frac{\partial^{k+1}}{\partial x \partial y^k} F_{i-k+1} + \sum_{k=0}^{i-1} \frac{h^k}{k!} \frac{\partial^{k+1}}{\partial y^{k+1}} F_{i-k},$$

so

$$-\sum_{k=0}^{i-2} h' \frac{h^k}{k!} \frac{\partial^{k+1}}{\partial x \partial y^k} F_{i-k+1} + \sum_{k=1}^{i-1} \frac{h^k}{k!} \frac{\partial^{k+1}}{\partial y^{k+1}} F_{i-k} + \frac{\partial F_i}{\partial y} = 0.$$

Rearranging implies

$$\begin{aligned}
\frac{\partial F_i}{\partial y} &= -\left(-\sum_{k=0}^{i-2} h' \frac{h^k}{k!} \frac{\partial^{k+1}}{\partial x \partial y^k} F_{i-k+1} + \sum_{k=1}^{i-1} \frac{h^k}{k!} \frac{\partial^{k+1}}{\partial y^{k+1}} F_{i-k} \right) \\
&= \sum_{k=0}^{i-2} h' \frac{h^k}{k!} \frac{\partial^{k+1}}{\partial x \partial y^k} F_{i-k+1} - \sum_{k=0}^{i-2} \frac{h^{k+1}}{(k+1)!} \frac{\partial^{k+2}}{\partial y^{k+2}} F_{i-k-1} \\
&= \sum_{k=0}^{i-2} \left(h' \frac{h^k}{k!} \frac{\partial^{k+1}}{\partial x \partial y^k} - \frac{h^{k+1}}{(k+1)!} \frac{\partial^{k+2}}{\partial y^{k+2}} \right) F_{i-k-1}
\end{aligned}$$

giving a recursive formula for the bed boundary condition for the F_j's :

$$\frac{\partial F_1}{\partial y}(x, 0) = -h' \tag{3.3.9}$$

and, for $j \geq 2$,

$$\frac{\partial F_j}{\partial y}(x, 0) = \sum_{k=0}^{j-2} \left(h' \frac{h^k}{k!} \frac{\partial^{k+1}}{\partial x \partial y^k} - \frac{h^{k+1}}{(k+1)!} \frac{\partial^{k+2}}{\partial y^{k+2}} \right) F_{j-1-k}(x, 0). \tag{3.3.10}$$

F_1 satisfies $\nabla^2 F_1 = 0$ and the far field boundary condition (3.3.2), so once (3.3.9) is solved, (3.3.10) generates the boundary data on $y = 0$ from known data. Each F_j is subject to the same conditions as F_1. Finding all the $F_j(x, y)$ gives the pressure impulse P in the neighbourhood of the object.

As $h(x)$ becomes more complicated, the manipulations become very hard. Notice however that for small $\epsilon, \epsilon^2 \ll \epsilon$, so that for a gently sloping body (where the Fourier

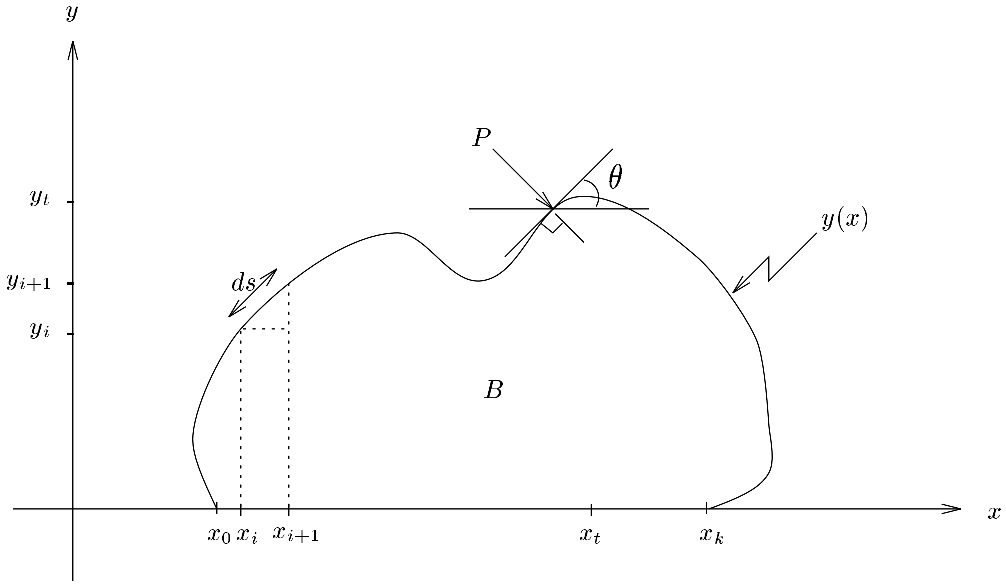

Figure 3.3.1: Describing notation: the pressure impulse P acts normally to the body B which is defined by the equation $y(x)$. The tangent to B is at an angle θ to the positive x direction and a small segment of the boundary of B is denoted $\mathrm{d}s$.

series converges quickly) only one term in the expansion of F may be necessary. So to find $F = \epsilon F_1$, suppose $h(x)$ is given by

$$h(x) = \sum_{n=1}^{\infty} a_n \sin(nx) + \sum_{m=1}^{\infty} b_m \cos(mx)$$

then a solution of (3.3.1) which satisfies (3.3.2) and (3.3.9) is

$$F_1 = \sum_{n=1}^{\infty} a_n \cos(nx)\, \mathrm{e}^{-ny} - \sum_{m=1}^{\infty} b_m \sin(mx)\, \mathrm{e}^{-my}. \tag{3.3.11}$$

3.3.1 Impulses

Once the pressure impulse field throughout the fluid has been obtained, the next step is to find the impulse on the body in directions parallel to the x and y axes, $\underline{I} = I_x\underline{\hat{x}} + I_y\underline{\hat{y}}$. We define an angle θ between the tangent to the body and the positive x-axis as shown in figure 3.3.1. The boundary of B, denoted ∂B and given by $y(x)$, intersects the x-axis at $x = x_0$ and $x = x_k$. The arc length between two points $(x_i, y_i = y(x_i))$ and (x_j, y_j) on ∂B is $\mathrm{d}s$. Then

$$\begin{aligned} \underline{I} &= \int_{y(x)} P(\sin\theta\ \underline{\hat{x}} - \cos\theta\ \underline{\hat{y}})\ \mathrm{d}s & (3.3.12)\\ &= \int_{x_0}^{x_k} P\tan\theta\,\mathrm{d}x\ \underline{\hat{x}} - \int_{x_0}^{x_k} P\ \mathrm{d}x\ \underline{\hat{y}} \\ &= \int_{x_0}^{x_k} P\ \frac{\mathrm{d}y}{\mathrm{d}x}\ \mathrm{d}x\ \underline{\hat{x}} - \int_{x_0}^{x_k} P\ \mathrm{d}x\ \underline{\hat{y}}. & (3.3.13) \end{aligned}$$

Calculation of the impulse on a body is often possible, but rarely straightforward, so an easier, computational, method is to approximate the arc length, $\mathrm{d}s$, between two points on ∂B by

$$\mathrm{d}s = \sqrt{(x_j - x_i)^2 + (y_j - y_i)^2}.$$

Thus

$$\underline{I} = \sum_{\forall x_i, y_i \in \partial B} \mathrm{d}s.P(x_i, y_i)(\sin\theta\ \underline{\hat{x}} - \cos\theta\ \underline{\hat{y}}).$$

Since $\sin\theta = (y_{i+1} - y_i)/\mathrm{d}s$ and $\cos\theta = (x_{i+1} - x_i)/\mathrm{d}s$, the impulse is

$$\underline{I} = \sum_{\forall x_i, y_i \in \partial B} P(x_i, y_i)\left[(y_{i+1} - y_i)\ \underline{\hat{x}} - (x_{i+1} - x_i)\ \underline{\hat{y}}\right]. \qquad (3.3.14)$$

3.4 Examples using Fourier Series

3.4.1 Sinusoidal Sea Bed

As an example of how this method works, consider initially the basic sinusoid, $h(x) = \sin(px)$ for some integer p, since this is the basic 'building block' of the Fourier series concept. (The following procedure is very similar for $h(x) = \cos(px)$.) The boundary condition (3.3.3) becomes

$$\frac{\partial F}{\partial y}(x, \epsilon\sin(px)) = \epsilon p\cos(px)\left(\frac{\partial F}{\partial x}(x, \epsilon\sin(px)) - 1\right). \qquad (3.4.1)$$

Substitution of $h(x)$ and h' in (3.3.9) and (3.3.10), for $j = 1$ to 3 gives

$$\frac{\partial F_1}{\partial y}(x, 0) = -p\cos(px)$$

$$
\begin{aligned}
\frac{\partial F_2}{\partial y}(x,0) &= h'\frac{\partial F_1}{\partial x}(x,0) - h\frac{\partial^2 F_1}{\partial y^2}(x,0)\\
&= p\cos(px)\frac{\partial F_1}{\partial x}(x,0) - \sin(px)\frac{\partial^2 F_1}{\partial y^2}(x,0)\\
\frac{\partial F_3}{\partial y}(x,0) &= h'\frac{\partial F_2}{\partial x}(x,0) - h\frac{\partial^2 F_2}{\partial y^2}(x,0) + h'h\frac{\partial^2 F_1}{\partial x\partial y}(x,0) - \frac{h^2}{2}\frac{\partial^3 F_1}{\partial y^3}(x,0)\\
&= p\cos(px)\frac{\partial F_2}{\partial x}(x,0) - \sin(px)\frac{\partial^2 F_2}{\partial y^2}(x,0)\\
&\quad + \frac{p\sin(2px)}{2}\frac{\partial^2 F_1}{\partial x\partial y}(x,0) - \frac{p^2\cos^2(px)}{2}\frac{\partial^3 F_1}{\partial y^3}(x,0).
\end{aligned}
$$

Application of the remaining boundary condition (3.3.2) to each equation in turn gives the solution (after manipulation)

$$
\begin{aligned}
F(x,y) &= \epsilon\cos(px)\mathrm{e}^{-py} + \frac{1}{2}\epsilon^2 p\sin(2px)\mathrm{e}^{-2py}\\
&\quad + \frac{1}{8}\epsilon^3 p^2\left(\cos(px)\mathrm{e}^{-py} - 3\cos(3px)\mathrm{e}^{-3py}\right) + O(\epsilon^4) \qquad (3.4.2)
\end{aligned}
$$

which satisfies Laplace's equation (3.3.1). This solution is very similar to that deduced by Whitley (1984) for flow past a sinusoidal bed given by $y = \epsilon\cos x$. We note that he uses 50 terms in the series to obtain accuracy to ten significant figures. An example of the pressure impulse contours around a sinusoid is shown in figure 3.4.1.

Comparison of the first and second terms in (3.4.2) gives a measure of how small ϵ must be for this method to work. Thus

$$
\epsilon \ll \left|\frac{\mathrm{e}^{py}}{p\sin(px)}\right| \quad \text{for all } x \text{ and } y.\ \text{Hence } \epsilon \ll \frac{1}{p}.
$$

Boundary condition (3.3.3) implies that the pressure impulse contours should be perpendicular to the curve at the boundary, so as a measure of the error involved, the angle θ between the exact normal and the contour line is found. Here

$$
\sin\theta = \frac{\nabla P.\underline{n}}{|\nabla P|} = \frac{\epsilon^3 p^3}{8}\left(\cos(px) - 9\cos(3px)\right),
$$

as shown in figure 3.4.2. For the example given there, with $\epsilon = 0.05$ and $p = 10$, the angle θ is at most about 9°. This is fairly large because ϵ is not considerably less than $1/p$, the condition for the solution to be valid, given above. The value of

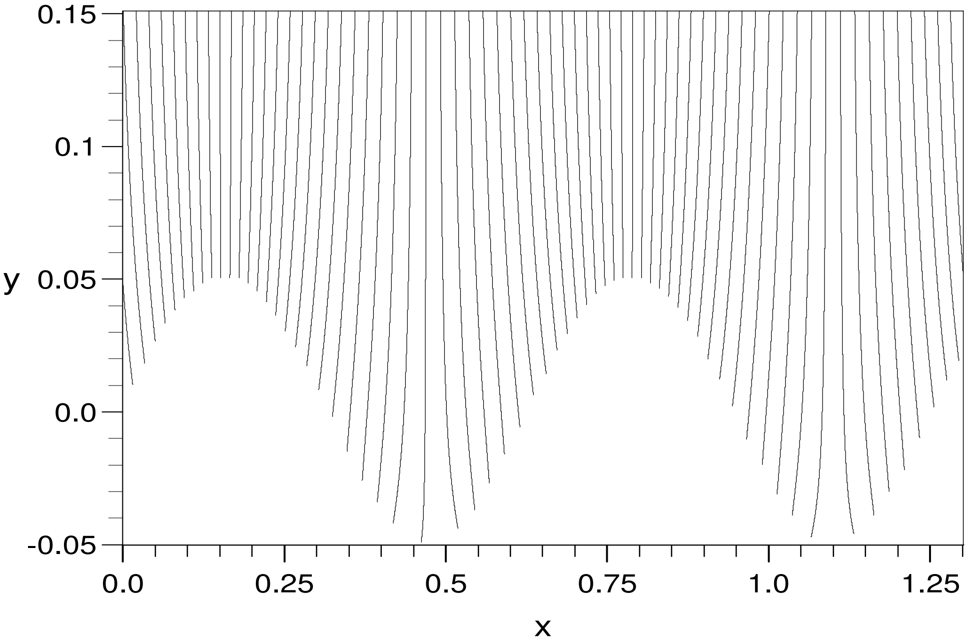

Figure 3.4.1: The pressure impulse contours for $y(x) = \epsilon \sin(px)$. Here $\epsilon = 0.05, p = 10.0$ and $P_0 = G = 1$. Notice that although the scaling of the graph distorts the plot, the contours are in fact almost perpendicular to the body on the boundary and that the distance between adjacent contour lines changes relative to the curvature of the sine curve. Contour separation is $0.02G/p$.

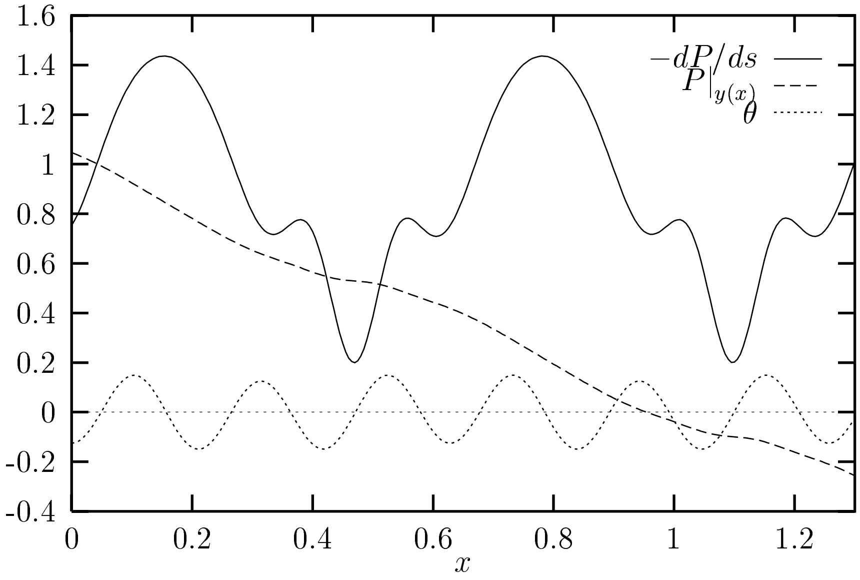

Figure 3.4.2: The graph shows the angle θ, in radians, between the exact normal and the pressure impulse contour lines in figure 3.4.1, for which $\epsilon = 0.05, p = 10.0$ and $P_0 = G = 1$. This demonstrates the error involved in using the Fourier series. The maximum deviation from the perpendicular is $0.15^{rad} \approx 8.6^\circ$. Also shown is the pressure impulse on the boundary, which decreases from a maximum on the left-hand side of the sine curve (nearest the impact). The curve showing the variation of P with arc length along the body, $-\mathrm{d}P/\mathrm{d}s$, implies that the pressure impulse changes most quickly at the top of the sinusoid, so that this is where the highest pressure impulse gradients act.

the pressure impulse on the boundary of the sinusoid and the variation of $\mathrm{d}P/\mathrm{d}s$, for arc length s along the boundary, are also both graphed in figure 3.4.2. The former decreases away from the wall (and the impacting wave) while the latter oscillates with the same period as the sinusoid - the peaks of $\mathrm{d}P/\mathrm{d}s$ are associated with the higher pressure impulse gradients which occur at the top of the sinusoid, and the troughs with low pressure impulse gradients, and therefore small changes in fluid velocities, in the troughs of the sinusoid.

To find the impulse on a body B that is a single sinusoid in the interval $[x_0, x_0 + 2\pi/p]$, we use $P|_{y=0} = P_0 - Gx + \epsilon G\cos(px) + O(\epsilon^2)$ with (3.3.13). Then, since $\mathrm{d}y/\mathrm{d}x = \epsilon p\cos(px)$, the horizontal impulse (in the $\underline{\hat{x}}$ direction) is

$$\begin{aligned}
I_x &= \int_{x_0}^{x_0+2\pi/p} \left[P_0 - Gx + \epsilon G\cos(px)\right]\frac{\mathrm{d}y}{\mathrm{d}x}\mathrm{d}x + O(\epsilon^3)\\
&= -\epsilon Gp\int_{x_0}^{x_0+2\pi/p} x\cos(px)\ \mathrm{d}x + \epsilon^2 Gp\int_{x_0}^{x_0+2\pi/p}\cos^2(px)\ \mathrm{d}x + O(\epsilon^3)\\
&= -\epsilon G\left[x\sin(px)\right]_{x_0}^{x_0+2\pi/p} + \frac{1}{2}\epsilon^2 Gp\left[x\right]_{x_0}^{x_0+2\pi/p} + O(\epsilon^3)\\
&= -2\pi\epsilon G\frac{\sin(px_0)}{p} + \pi\epsilon^2 G + O(\epsilon^3)\\
&= \pi G\epsilon\left(-2\frac{\sin(px_0)}{p} + \epsilon\right) + O(\epsilon^3).
\end{aligned}$$

The first term of this expression is equal to $G\sin(px_0)$ multiplied by the area under one period of the sinusoid. For the body associated with the pressure impulse P_0 at $x = 0$, we require $x_0 = -\pi/p$ and then $I_x = \pi G\epsilon^2$. To calculate the vertical impulse (in the $\underline{\hat{y}}$ direction), we take an extra term, proportional to ϵ^2, in the expansion for P. Then

$$\begin{aligned}
I_y &= -\int_{x_0}^{x_0+2\pi/p} P_0 - Gx + \epsilon G\cos(px) + \frac{1}{2}\epsilon^2 pG\sin(2px)\ \mathrm{d}x + O(\epsilon^3)\\
&= -\frac{2\pi P_0}{p} + \frac{2\pi G}{p}\left(x_0 + \frac{\pi}{p}\right) + O(\epsilon^3).
\end{aligned}$$

The first term is P_0 multiplied by the length of the base of the sinusoid and corresponds to an impulse downwards, pushing the sinusoid against the sea bed. The second term increases with translation along the x-axis, so that if we consider the sinusoid in the interval $x \in [-\pi/p, \pi/p]$, which is associated with $P = P_0$ on $x = 0$, the contribution is zero and $I_y = -2\pi P_0/p + O(\epsilon^3)$. Notice that the contribution to the vertical impulse from the distortion term in P, $F(x)$, is at most of order ϵ^3. So the total impulse is dominated by the downward impulse proportional to the length of the base of the sinusoid, with a small horizontal impulse pushing away from the wall.

3.4.2 Rectangle

A particularly interesting case is where B is a rectangle of height ϵ and length $2k$ on the bed, for which the Fourier Series can be written $y(x) = \epsilon h(x)$ with

$$h(x) = k + \frac{2}{\pi} \sum_{n=1}^{\infty} \frac{\sin(n\pi k)}{n} \cos(n\pi x) \tag{3.4.3}$$

on $x \in (-1, 1)$ with $k < 1$. The periodicity of the Fourier Series implies that the next rectangle occurs a distance $2k$ away in either direction. Then (3.3.11) gives

$$F(x, y) = -\frac{2\epsilon}{\pi} \sum_{n=1}^{\infty} \frac{\sin(n\pi k)}{n} \sin(n\pi x) \mathrm{e}^{-n\pi y}$$

and $P = P_0 - Gx + GF$. Figure 3.4.3 shows the pressure impulse contours around a rectangle. With 300 terms this series gives a fairly good representation of the rectangle, but there is some rounding off or overshooting at corners; this error in representing a step function by a Fourier series is due to the well-known Gibb's phenomenon (see, for example, Lanczos 1966). The corners are also the areas which are under the influence of the highest local pressure impulse gradients. An expression for the errors, as a function of θ, as in the case of a sinusoid, is not derived here - but the figure shows how large the error is, and the case of the rectangle is left until we have developed the theory for a conformal mapping technique.

3.5 Conformal Mapping Approach

With a conformal map from a small area of the flat sea bed of Chapter 2 to the exterior of a small body, the errors in the Fourier series are avoided, especially around sharp

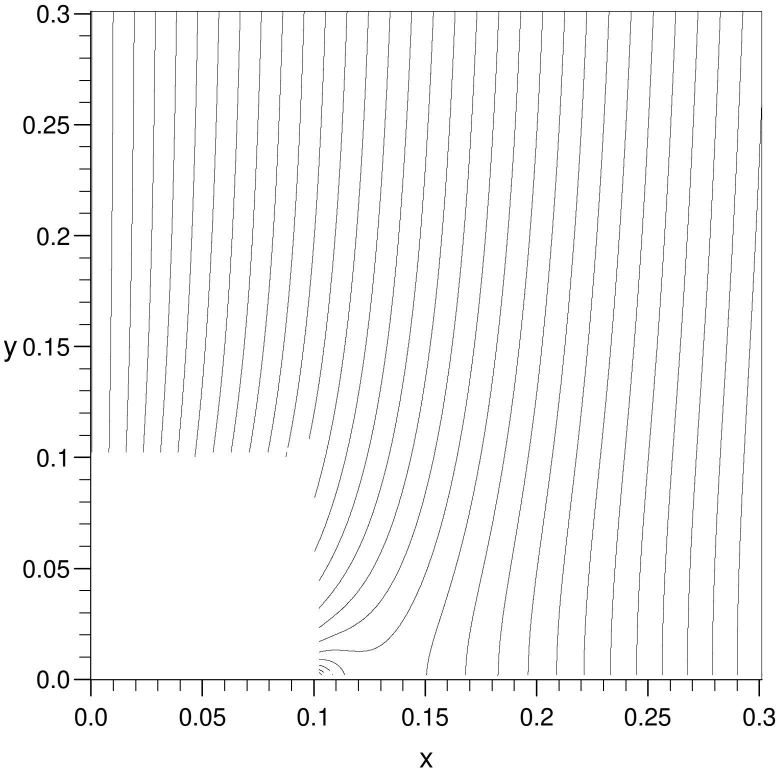

Figure 3.4.3: The pressure impulse contours around a rectangle with $\epsilon = 0.1$ and $k = 0.1$ and 300 terms in the series. Only half of the domain is drawn since the pressure impulse contours are symmetric about the line $x = 0$. There is a region around the base of each side where the Fourier series is a particularly poor approximation, due to Gibb's phenomenon. In fact, the contours are far from being perpendicular to the side of the rectangle. Contour separation is $0.01Gk$.

corners. Also, since a Fourier series cannot represent a multivalued function, we can use a conformal map to define a body with an overhang. This enables the pressure impulse gradients acting on a single body on this flat sea bed to be modelled and the impulse on the body to be found.

Consider first an arbitrary body $\bar{B}$ with boundary $\partial\bar{B}$ in an infinite fluid. We define a 'complex pressure impulse' (CPI), $\Phi : \mathbb{C} \to \mathbb{C}$ by $\Phi(z) = P(x,y) + iQ(x,y)$, where $z = x + iy$, P is pressure impulse and Q is defined, up to an arbitrary constant, by the Cauchy-Riemann equations:

$$\frac{\partial P}{\partial x} = \frac{\partial Q}{\partial y}\,,\ \frac{\partial P}{\partial y} = -\frac{\partial Q}{\partial x}.$$

Since the lines of constant Q are perpendicular to the lines of constant pressure impulse, Q is constant on $\partial\bar{B}$ (without loss of generality $Q = 0$).

The conformal transformation, $z = z(w)$, maps the complex $w = u + iv$ plane to the complex z plane containing the body $\bar{B}$. The real axis in the w plane, $v = 0$, is mapped to the union of the sea bed on either side of $\bar{B}$, $y = 0$, and $\partial\bar{B}$. The pre-image of $\partial\bar{B}$ is denoted $\partial\bar{B}'$, lying along the real w-axis between $u = u_1$ and $u = u_2$. Pressure impulse contours in the w plane (lines of constant u) are mapped to pressure impulse contours around $\bar{B}$. If the map is such that $z \sim dw$ as $|z| \to \infty$, for some constant $d > 0$, then in the w plane the CPI is $\Phi(w) = P_0 - Gdw$. The corresponding CPI after mapping is $\Phi(z(w)) = \Phi(w) = P_0 - Gz(w) + GF(z)$ where $F(z)$ is a correction term due to the presence of the body as hypothesised in §3.2. It follows that $F(z) \to 0$ as $|z| \to \infty$. Then $F(z) \sim z(w) - dw$ as $|z| \to \infty$.

3.5.1 Impulses

Let a small segment of $\partial\bar{B}$ be denoted ds and the angle between the tangent to $\bar{B}$ and the positive real axis be ϕ. The impulse on $\bar{B}$ has horizontal and vertical components given by $\underline{\bar{I}} = (\bar{I}_x, \bar{I}_y)$ where

$$\bar{I}_x + i\bar{I}_y = \int_{\partial\bar{B}} P(z)\sin\phi\,\mathrm{d}s - i\int_{\partial\bar{B}} P(z)\cos\phi\,\mathrm{d}s \qquad (3.5.1)$$

$$
\begin{aligned}
&= -i \int_{\partial \bar{B}} (P + iQ)\,(\cos\phi + i \sin\phi)\,\mathrm{d}s \\
&= -i \int_{\partial \bar{B}} \Phi(z)\,\mathrm{d}z \qquad (3.5.2)
\end{aligned}
$$

since $\mathrm{d}z = \mathrm{e}^{i\phi}\mathrm{d}s$. These formulae hold when $\partial\bar{B}$ is a closed curve. If $\bar{B}$, and therefore $\partial\bar{B}$, has the real axis as its line of symmetry then the body B in which we are interested is the top half of $\bar{B}$, projecting above the real axis. $\partial P/\partial y = 0$ on the real axis, so the horizontal impulse, I_x, on the body B projecting into the upper half-plane is half that on $\bar{B}$. We write this impulse on B as $\underline{I} = (I_x, I_y)$. In which case we can perform the integration along a path in the w plane so that (3.5.2) becomes

$$
\begin{aligned}
I_x + iI_y &= -i \int_{\partial \bar{B}'} \Phi(w) \frac{\mathrm{d}z}{\mathrm{d}w}\mathrm{d}w \qquad (3.5.3) \\
&= -i \int_{u_1}^{u_2} (P_0 - Gdu) \left.\frac{\mathrm{d}z}{\mathrm{d}w}\right|_{w=u} \mathrm{d}u \qquad (3.5.4) \\
&= -iP_0\,(z(u_2) - z(u_1)) + iGd\,(u_2 z(u_2) - u_1 z(u_1)) - iGd \int_{u_1}^{u_2} z(u)\,\mathrm{d}u. \qquad (3.5.5)
\end{aligned}
$$

The first term of (3.5.5) is a downward impulse equal to P_0 multiplied by the length of the body along the x-axis. Cooker and Peregrine (1992) suggest that a body which has a flat base and which is free to move might have a thin layer of fluid underneath it. Then the impulse generated by this fluid is also P_0 multiplied (at least in two-dimensional analysis) by the length of the base, but in an upward direction. So we conclude that this vertical impulse has no effect on the subsequent motion of the object. The second term is only non-zero for asymmetric bodies. By integrating the third term in (3.5.5) we can find the total impulse on B. Since both the u_i and $z(u_i)$ are real, for $i = 1, 2$, then this term is the only one that could possibly give a real component in (3.5.5), relating to a horizontal impulse. If the body is symmetric then $u_1 = -u_2$ and we expect the integral to be purely imaginary, corresponding to only a horizontal impulse. If the conformal map is given in the form $\mathrm{d}z/\mathrm{d}w = f(w)$ we perform the integration in (3.5.4) and take real and imaginary parts to find the horizontal and vertical components of impulse respectively.

The impulse on the body determines whether or not it will move, and if so then with what initial velocity. We next derive some methods to allow straightforward calculation of these impulses and velocities, extending the formulae of this section.

3.5.2 Laurent Expansion

An easier way of calculating the horizontal impulse is to use a Laurent series to represent the conformal map, as follows. If $\partial\bar{B}$ is a simple closed curve surrounded by fluid, with the point $z = 0$ inside $\partial\bar{B}$, and if Φ can be expressed as a power series, i.e.

$$\Phi = G \sum_{k=-1}^{\infty} \frac{a_k}{z^k} \ , \ a_k \in \mathbb{C} \tag{3.5.6}$$

then by Cauchy's residue theorem, since the contour is traversed in a clockwise manner, (3.5.2) gives

$$\bar{I}_x = -i.2\pi i \Re\left(-Ga_1\right) = -2\pi G \Re\left(a_1\right) \tag{3.5.7}$$

where $\Re$ denotes real part. The expansion of $F(z)$ gives the coefficient a_1 of $\Phi(z)$. As $|z| \to \infty$, $F(z) \sim z(w) - dw$, so the expansion of the conformal map, $z(w)$, as a Laurent series for large w, gives a_1. Thus, if

$$z(w) = dw + b_0 + \frac{b_1}{w} + \frac{b_2}{w^2} + \dots, \tag{3.5.8}$$

we substitute $w = z/d$, and then $a_1 = db_1$ and (3.5.7) becomes

$$\bar{I}_x = -2\pi G \Re\left(db_1\right). \tag{3.5.9}$$

For a conformal map from the exterior of the unit circle ($|S| = 1$ in a complex S plane) to the exterior of the body $\bar{B}$ (in the z plane), we can write

$$z(S) = d_1 S + c_0 + \frac{c_1}{S} + \frac{c_2}{S^2} + \dots \tag{3.5.10}$$

with $d_1 > 0$. The composition of a map from the unit circle to a flat plane with a map from the flat plane to $\bar{B}$, from (3.5.8), is

$$z(w(S)) = z\left(S + \frac{1}{S}\right) = dS + b_0 + \frac{d + b_1}{S} + \dots$$

Comparison with (3.5.10) shows that $d = d_1$, $b_0 = c_0$ and $b_1 = c_1 - d$. Then the horizontal impulse, given by (3.5.9), is

$$\bar{I}_x = 2\pi G d_1^2 \left[1 - \Re\left(\frac{c_1}{d_1}\right)\right]. \tag{3.5.11}$$

Pólya (1947), in his calculations of the two-dimensional motion of a solid through a fluid which is at rest at infinity, constructs the cross-section of a cylindrical body $\bar{B}$ using a conformal map, such as in (3.5.10). The body, of mass per unit length m, moves as if its mass per unit length were $m + \bar{M}_x$, where $\bar{M}_x$ is the added mass per unit length of the body for motion parallel to the x-axis. Then he derives the following formula for $\bar{M}_x$:

$$\frac{\bar{M}_x}{\rho} + \mathcal{V} = 2\pi d_1^2 \left[1 - \Re\left(\frac{c_1}{d_1}\right)\right]$$

where $\mathcal{V}$ is the volume per unit length of the body (i.e. cross-sectional area for a two-dimensional body) and ρ is the density of the fluid. (This relationship between added mass and dipole moment is also discussed by Newman 1978.) Thus

$$\bar{I}_x = G\left(\frac{\bar{M}_x}{\rho} + \mathcal{V}\right). \tag{3.5.12}$$

For the body B in which we are interested, which has its line of symmetry along the real axis, the impulse is half that on $\bar{B}$ and the results (3.5.9), (3.5.11) and (3.5.12) become $I_x = Gk$ where

$$\begin{aligned} k &= -\pi\Re\left(db_1\right) && (3.5.13)\\ &= \pi d_1^2\left[1 - \Re\left(\frac{c_1}{d_1}\right)\right] && (3.5.14)\\ &= \frac{M_x}{\rho} + \mathcal{V}. && (3.5.15) \end{aligned}$$

Here M_x is the added mass of B for motion in the x direction. If the area of B is non-zero (i.e. B is not a line segment) then the added mass is proportional to the displaced mass of water. We define an added mass coefficient, λ_x, which is dependent upon the shape of B. In fact, the value of λ_x is that for the whole body, $\bar{B}$, and then $M_x = \lambda_x \rho \mathcal{V}$ and so

$$k = \mathcal{V}\left(\lambda_x + 1\right). \tag{3.5.16}$$

The values of λ_x are tabulated for many shapes, but in those cases where they are not, we can calculate λ_x by finding k and $\mathcal{V}$. So those shapes which receive the greatest impulse per unit cross-sectional area are those with the largest added mass coefficients.

These results apply equally well to the three-dimensional work of Cooker and Peregrine (1992), who find the impulse on a body due to a uniform pressure impulse gradient acting away from a vertical wall where wave breaking has occurred. For instance, for a hemisphere of radius a, at rest ($U = 0$) but free to move, not far from the wall, they give $I_{\mathrm{hem}} = \pi G a^3$. Since $\lambda_x = \frac{1}{2}$ for a sphere, then $\mathcal{V}$ is volume and (3.5.16) correctly predicts this value.

3.5.3 A Moving Body

If B is free to move, then we assume that the pressure impulse gradient, G, will accelerate it from rest to a horizontal velocity, V. The boundary condition on the moving body is now $\partial P/\partial n = -\rho V \underset{\sim}{i}.\underset{\sim}{n}$, with the same far field condition as before, $P \sim P_0 - Gx$, and the same impermeability condition on the sea floor, $\partial P/\partial y|_{y=0} = 0$. The pressure impulse which satisfies these conditions is $P_1 = \hat{P} - \rho V x$ where $\hat{P}$ is the same as P for a fixed body but with the effective pressure impulse gradient modified from G to $G - \rho V$. Then, since the horizontal impulse on a fixed body is $I_x = Gk$, the horizontal impulse on the same body, but which is free to move, is the integral of the normal component of P_1 over its surface:

$$I_{Vx} = (G - \rho V)\, k + \rho V \mathcal{V}. \tag{3.5.17}$$

We can then use any of (3.5.13) - (3.5.16) to express k in whichever way is most natural.

Equating the impulse on the moving body B, of density ρ_B, with the change in momentum, $\rho_B \mathcal{V} V$, gives

$$V = \frac{Gk}{\rho_B \mathcal{V} + \rho\,(k - \mathcal{V})}. \tag{3.5.18}$$

This velocity is independent of the volume of B, since k is proportional to $\mathcal{V}$, and depends only on its shape and density (and the pressure impulse gradient and the density of the fluid, but these are the same for all the shapes considered). A more dense body moves less quickly. If the body moves, then the impulse on it is

$$I_{Vx} = \frac{G\rho_B \mathcal{V} k}{\rho_B \mathcal{V} + \rho\,(k - \mathcal{V})} \tag{3.5.19}$$

which is less than the impulse on a fixed body, since $k > \mathcal{V}$ by (3.5.16). (If $\lambda_x = 0$ then the impulse is zero.) We can use (3.5.15), in (3.5.18), to express k and therefore V in terms of added masses:

$$V = \frac{G}{\rho}\left(\frac{\rho\mathcal{V} + M_x}{\rho_B\mathcal{V} + M_x}\right)$$

For the hemisphere mentioned above this becomes

$$V = \frac{3G}{2\rho_B + \rho}$$

as derived by Cooker and Peregrine (1992).

The horizontal force pushing a body, B, which is free to move, away from the wall when the wave breaks is the impulsive force, $F_I = I_{Vx}/\Delta t$. In the opposite direction, friction, F_f, and the fluid drag, F_D, act to stop the motion. Then, comparing these forces acting on B shows that for B to move we must have

$$\frac{I_{Vx}}{\Delta t} > \mu(\rho_B - \rho)\mathcal{V}g + \frac{1}{2}\rho C_D \mathcal{A} {u_0}^2. \tag{3.5.20}$$

(If there is no layer of fluid beneath the body, the vertical impulse will modify the normal reaction and hence the frictional force.) Using (3.5.16) and (3.5.19) gives the condition

$$\frac{\mathcal{V}}{\mathcal{A}} > \frac{\frac{1}{2}\rho C_D {u_0}^2 \Delta t(\rho_B + \rho\lambda_x)}{G\rho_B(\lambda_x + 1) - \mu(\rho_B - \rho)g\Delta t(\rho_B + \rho\lambda_x)} \tag{3.5.21}$$

for B to move. Since $\mathcal{V}/\mathcal{A}$ is proportional to the length scale of the body, this gives a lower bound for the critical length scale at which a body will move. For instance, for a hemisphere of radius a we take $\Delta t = 0.04$ sec, $\mu = 0.5$, $\rho_B = 3\rho$, $C_D = 0.2$ and, for a water depth at the wall of $H = 10$m, $u_0 = \sqrt{gH} = 9.91$ m sec^{-1}. Our estimate of G from the analysis of Chapter 2 becomes, at $x_0 = 5$m, $G = 991$ N sec m^{-3}. (Note that at this point our model predicts a pressure impulse of $P = P_0 = 0.1\rho u_0 H =$

9910 N sec m^{-2}. This corresponds to a peak pressure $p_{peak} \approx 5 \times 10^5$ N m^{-2}.) Then (3.5.21) gives a critical radius of $a_c = 0.674$ m. So if the hemisphere has radius $a > a_c$, the impulsive forces will dominate over the frictional forces and the body will move. The value of a_c is directly proportional to the drag coefficient C_D. Here we have used $C_D = 0.2$, but for a different flow speed or a different body this could change dramatically.

3.6 Examples using Conformal Mapping

In order to demonstrate the methods shown above, we now give some examples of shapes of body, for which we can calculate the impulse on the body and, usually, the pressure impulse distribution. The only way to find the vertical impulse on a body is to integrate the conformal map directly. Otherwise, we can usually find the horizontal impulse using any of the methods described above, and this is demonstrated in some cases. Our aim is to calculate the impulses (particularly the horizontal impulses) for these different shapes of body to allow us to compare the forces acting on each body. Then using (3.5.21) we can decide how large a particular body must be to move when subjected to pressure impulses from storm waves breaking against a vertical wall. The impulse also relates to the velocity at which the object would initially move, using (3.5.18). If a body experiences a non-trivial vertical impulse, then it is conceivable that it could be thrown back towards the wall to cause further damage.

In the following section we first demonstrate that for a semicircle at rest on the bed all the methods of calculating the impulse give the same answer. We also estimate how large a semicircular cylinder must be for the impulsive forces to overcome the frictional and drag forces, using the calculated horizontal impulse. Then to find the impulse on a semi-ellipse requires only a little more work, but allows us to compare objects with different aspect ratios. The case of a circle, or a circular cylinder with its long axis parallel to the wall, provides analytic confirmation of a previously published numerical result. We then treat an inclined plate, which exhibits asymmetry, and therefore has a non-trivial vertical impulse. The effect of this plate being curved is then examined with a section of a circular arc. An aerofoil is studied as an example of a body which is asymmetric and has non-zero area. Most sea walls are made of blocks that are rectangular, so that our last body is a rectangle on the sea bed, for which we use the Schwarz-Christoffel mapping theorem. We also use an existing formula to allow us to draw the pressure impulse contours around the rectangle. Finally, in §3.7, we compare some of these results and make some general observations on the significance of our calculations for the movement of bodies by wave impact.

We envisage that the information gained from these two-dimensional calculations will be useful to coastal engineers who are interested in the relative movement of different shapes of object on the sea floor. This may seem of less worth than the three-dimensional bodies analysed by Cooker and Peregrine (1992) but, since the calculations are usually more straightforward in two-dimensions, we can cover a wider range of bodies, thus allowing more comparisons to be made. Also, these impulses are equal to the impulse per unit length on a (three-dimensional) cylindrical body whose cross-section is given by B. If this cylinder has different shaped cross-sections at different points along its length then our calculations will show on which parts of the cylinder the highest impulses act and therefore where the largest turning moments will occur.

The pressure impulse distribution around B, in the $z = x + iy$ plane, is given by

$$P(x, y) = P_0 - Gd\Re\left\{w(z)\right\}. \tag{3.6.1}$$

To plot the contours of constant P we use the conformal map $z = z(w)$ to map vertical lines of constant P in the w plane to the contours in the z plane. This avoids having to invert the conformal map.

3.6.1 Semicircle

The conformal map from the upper half of the w plane to the region above a semicircle of radius a and the real z-axis is

$$z(w) = \frac{w + \sqrt{w^2 - 4a^2}}{2}. \tag{3.6.2}$$

Then for large w,

$$\begin{aligned} z(w) &= \frac{w}{2}\left(1+\sqrt{1-\frac{4a^2}{w^2}}\right) \\ &\sim \frac{w}{2}\left(2-\frac{2a^2}{w^2}+O(w^{-4})\right) \\ &\sim w-\frac{a^2}{w}+O(w^{-3}). \end{aligned}$$

Therefore the horizontal impulse on a semicircle on a flat sea bed, given by (3.5.13), is

$$I_x = \pi G a^2. \tag{3.6.3}$$

This result can be checked by integrating around the boundary - i.e. performing the first integration in (3.3.12). As for boundaries modelled with Fourier series, (3.3.14) can be used to verify these analytical results. Since the added mass coefficient for a circle is $\lambda_x = 1$ and the area of the semicircle is $\mathcal{V} = \frac{1}{2}\pi a^2$, (3.5.16) also correctly reproduces the result. This value can be thought of as the horizontal impulse per unit length on a semicircular cylinder oriented with its axis parallel to the wall. So the above answer corrects the fallacious solution of Cooker and Peregrine (1992, eq 4.13).

In order to find out how large a semicircular cylinder must be for the impulsive force to overcome the frictional and drag forces and move it, we note that the cross-sectional area (per unit length) in the direction of motion is $\mathcal{A} = a$. If its density is $\rho_B = 3\rho = 3000$ kg m^{-3}, then (3.5.21) implies, with $C_D = 0.5$ and all other parameter values as before, that the critical value of a for the body to move is $a_c = 0.575$m. Thus, a semicircular cylinder of radius $a > a_c$ is likely to be moved by the impact of a storm wave. When it moves, B will have an initial speed given by (3.5.18): $V = 0.496$ m sec^{-1}.

We can also apply (3.5.5) to give

$$\begin{aligned} I_x &= -iG\int_{-2a}^{2a}\frac{u+\sqrt{u^2-4a^2}}{2}\mathrm{d}u \\ &= -\frac{iG}{2}\int_{-2a}^{2a}\sqrt{u^2-4a^2}\mathrm{d}u \end{aligned}$$

$$= \pi G a^2$$

$$\text{and } I_y = -2aP_0.$$

This confirms the horizontal impulse and shows that the vertical impulse on the semicircle is $2aP_0$ downwards: P_0 times the length of the base of the body. This vertical impulse comes from the first term of (3.5.5) and applies to all flat bottomed bodies resting on the sea bed. If B is free to move, then there is a thin layer of fluid beneath it, exerting an impulse equal in magnitude and opposite in direction to I_y.

3.6.2 Semi-ellipse

For a semi-ellipse of half-width $\alpha(a,b)$ and height $\beta(a,b)$ the conformal map from the upper half of the w plane to its exterior is

$$z(w) = \frac{\alpha w}{\alpha+\beta} + \beta\sqrt{\left(\frac{w}{\alpha+\beta}\right)^2 - 1}, \tag{3.6.4}$$

where $a, b \in \mathbb{R}, b^2 < a^2$ and

- Case (i) $\alpha = a - b^2/a,\ \beta = a + b^2/a$ for a semi-ellipse which is taller than it is wide ($\beta \geq \alpha$)
- Case (ii) $\alpha = a + b^2/a,\ \beta = a - b^2/a$ for a semi-ellipse which is wider than it is tall ($\beta \leq \alpha$).

In general, a and b are given by

$$a = \frac{\alpha+\beta}{2}, \qquad b = \frac{1}{2}\left|\alpha^2 - \beta^2\right|^{\frac{1}{2}}. \tag{3.6.5}$$

Expanding the conformal map and applying (3.5.13) gives

$$I_x = \frac{1}{2}\pi G\beta\left(\alpha+\beta\right). \tag{3.6.6}$$

As for the semicircle, (3.5.5) gives a vertical impulse of $-2\alpha P_0$ (since 2α is the length of the body in contact with the bed) and confirms the horizontal impulse.

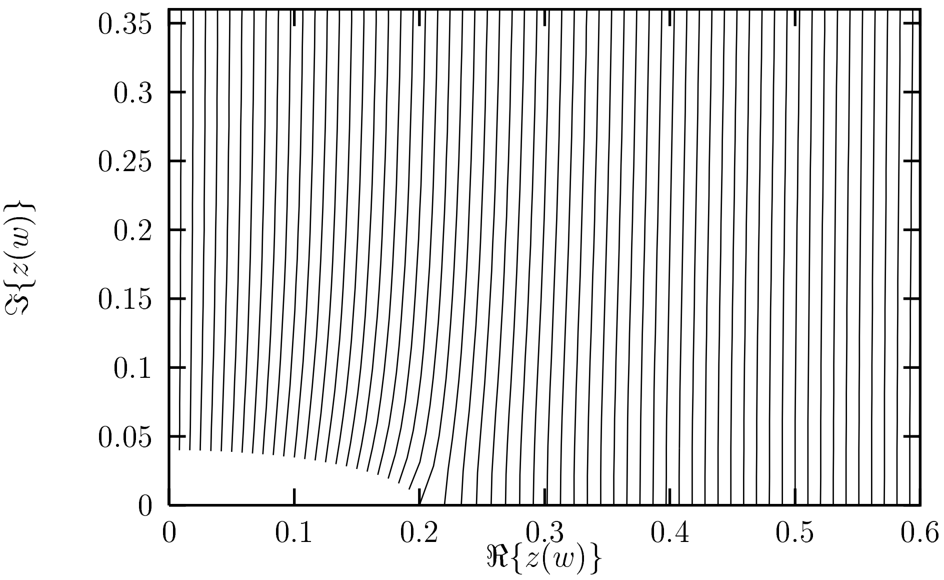

Figure 3.6.1: The pressure impulse contours around a semi-ellipse of half-width $\alpha = 0.2$ and height $\beta = 0.04$, for which $a = 0.12$, $b = 0.098$ and $P_0 = G = 1.0$. Due to symmetry about the line $x = 0$ we draw only one half of the fluid domain. The contours are always perpendicular to the body's surface, with a separation of $0.01aG$. There is a region of low flow speed around the points where the body meets the sea bed.

Alternatively, we can treat the problem by using a conformal map from the exterior of the unit circle (in the S plane) to the semi-ellipse (in the z plane). The map is given by

$$z(S) = aS \mp \frac{b^2}{aS}$$

where the $-$ refers to case (i) and the $+$ to case (ii). Then the horizontal impulse, by (3.5.14), is

$$I_x = \pi G a^2 \left[1 - \Re\left(\frac{\mp b^2}{a}\frac{1}{a}\right)\right] = \pi G \left(a^2 \pm b^2\right)$$

which is the same as (3.6.6) on substitution of a and b for α and β in each of the two cases.

In terms of added masses, the added mass coefficient for a semi-ellipse in horizontal translation is $\lambda_x = \beta/\alpha$ (Sedov 1965, p.30) so (3.5.16) implies $I_x = \frac{1}{2}\pi G\alpha\beta(\beta/\alpha + 1)$ which confirms the result already obtained. So semi-ellipses with large aspect ratio, β/α, receive a greater impulse per unit area. Note that both the conformal map and the resulting impulse reduce to the case of a semicircle of radius a when $b = 0$. If $b = a$ in case (i), the semi-ellipse becomes a vertical plate of height $h = 2a$ with $I_x = \frac{1}{2}\pi G h^2$.

For case (ii), figure 3.6.1 shows the pressure impulse contours around the body with $\alpha = 0.2$ and $\beta = 0.04$. In this case (3.6.5) gives $a = 0.12$ and $b = 0.098$.

3.6.3 Circle

Adapting the complex potential given by Batchelor (1973, §6.52) or the inverse of the conformal map in Paterson (1983, p461) for the flow past a cylindrical log on a horizontal bed gives the following conformal map from the upper half of the w plane to the exterior of a log of radius a on the real z-axis:

$$z(w) = \frac{a\pi}{\coth^{-1}(w/a\pi)}.$$

The points on the real w-axis which map to the origin in the z plane (the point of contact between the circle and the sea bed) are $u = \pm a\pi$. Figure 3.6.2 demonstrates

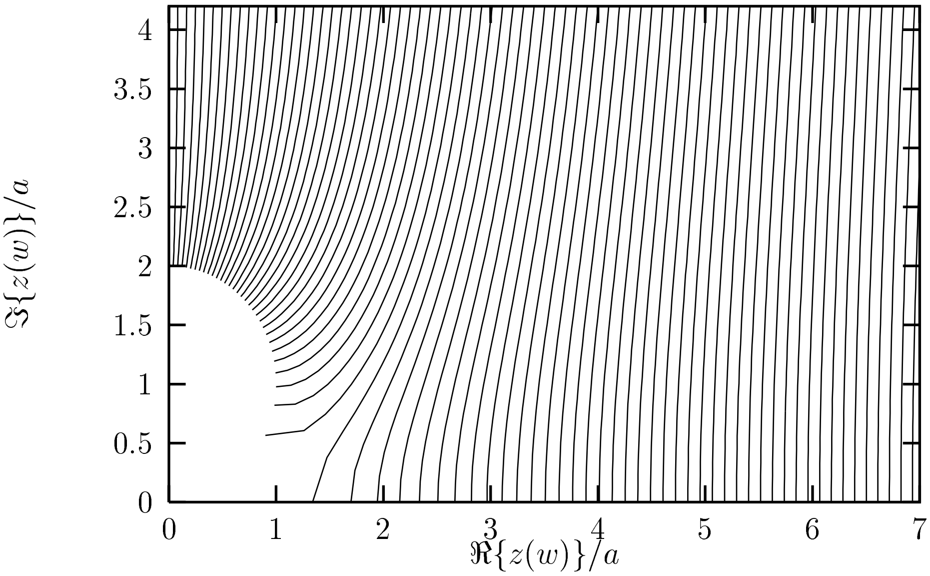

Figure 3.6.2: Lines of constant pressure impulse around a log on a flat sea bed. Here $P_0 = G = a = 1$ and the contour separation is $0.1aG$. Very few contours penetrate to the base of the log, suggesting low fluid speeds there. Again, due to symmetry we draw only half of the fluid domain.

how the contours bend around the body. Then, using Abramowitz and Stegun (1965, eq.4.6.34) for the expansion of $\coth^{-1}(w)$ for large w,

$$\begin{aligned} z(w) &\sim \frac{1}{1/w + a^2\pi^2/(3w^3) + O(w^{-5})} \\ &\sim w\left(1 + a^2\pi^2/(3w^2) + O(w^{-4})\right)^{-1} \\ &\sim w - \frac{a^2\pi^2}{3w} + O(w^{-3}) \end{aligned}$$

as $w \to \infty$. Therefore the horizontal impulse is

$$I_x = \frac{1}{3}\pi^3 Ga^2. \tag{3.6.7}$$

This compares well with Cooker and Peregrine (1992, §4.3) who give a numerical answer of $I_{\text{log}} = 3.29\pi Ga^2$. Since $\pi^2/3 \approx 3.29$, (3.6.7) confirms this earlier result.

In order to find out if the impulsive force on the circle is likely to overcome the frictional and drag forces and move it, we apply (3.5.21) with $C_D = 0.5$ and all other parameter values as before. The area of the circle is $\mathcal{V} = \pi a^2$ and the cross-sectional area (per unit length) in the direction of motion is $\mathcal{A} = 2a$. Then we find that for the body to move $a_c = 0.431$m. Thus, a circular cylinder of radius $a > a_c$ is likely to be moved by the impact of a storm wave.

Directly integrating the conformal map, as in (3.5.5), gives $I_x + iI_y = i\pi^2 G a^2 J$ where

$$J = \int_{-1}^{1} \frac{\mathrm{d}x}{\coth^{-1}(x)}.$$

Using the substitution $x = \tanh u$ and Cauchy's residue theorem, we find $J = -i\pi/3$ as shown in Appendix I. This verifies (3.6.7) and shows that the vertical impulse is zero (contradicting the calculation in Cooker and Peregrine (1992), which is flawed since a plot of their integrand shows the net area beneath it to be zero). Greenhow and Yanbao (1987) give $\lambda_x = \frac{1}{3}\pi^2 - 1$ for the added mass coefficient of a circular cylinder next to a fixed boundary, so (3.5.16) verifies the value of k.

3.6.4 Inclined Plate

The impulse on an inclined plate (a straight line segment) of length a, projecting at an arbitrary angle $\alpha \in (0, \pi)$ from the bed can be computed. The conformal map (adapted from Jeffrey 1992) is

$$z(w) = (w - a)^{\beta} \left(a + \frac{\beta w}{1 - \beta} \right)^{1-\beta} \tag{3.6.8}$$

with $\beta = \alpha/\pi$. The plate lies between $z = 0$ and $z = (-1)^{\beta} a$ (taking the principle value) to which it is mapped from the interval $[a(\beta - 1)/\beta, a]$ on the real w-axis. Figure 3.6.3 shows the pressure impulse contours around a plate with $\alpha = 72°$ $(\beta = 0.4)$.

In contrast to earlier examples, $z \sim dw$ as $|z| \to \infty$, where $d = (\beta/(1 - \beta))^{1-\beta}$. Rearranging the conformal map for large w gives

$$z(w) = dw \left(1 - \frac{a}{w}\right)^{\beta} \left(1 + \frac{a(1 - \beta)}{\beta w}\right)^{1-\beta}$$

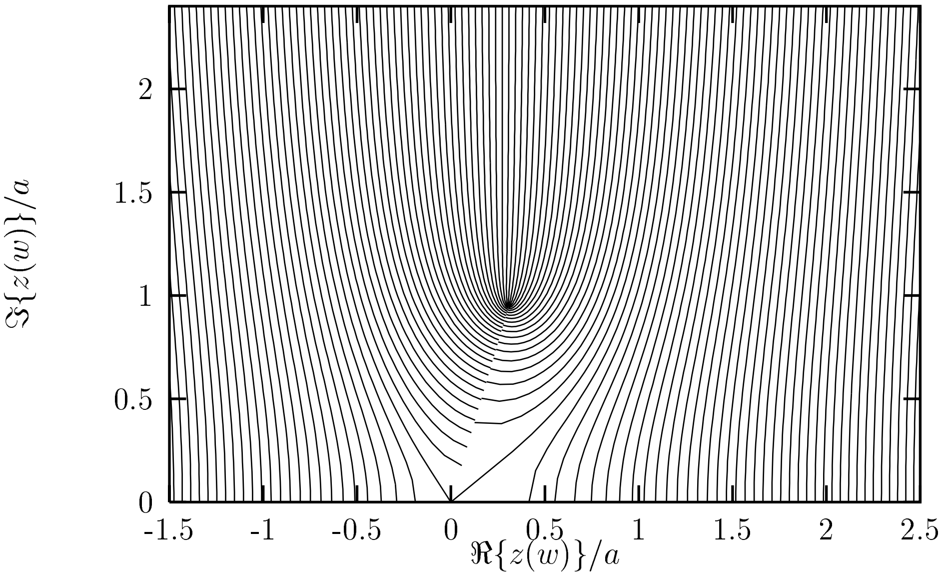

Figure 3.6.3: The pressure impulse contours around a plate inclined at an angle of $\alpha = 72^\circ$ ($\beta = 0.4$) to the positive horizontal, with $P_0 = G = a = 1.0$. Contour separation is $0.05aG$. There are very few contours on the side away from the wall where the impact occurs, and hence the pressure impulse changes less under the plate.

$$\begin{aligned}
&\sim dw\left(1-\beta\frac{a}{w}+\frac{\beta(\beta-1)}{2}\frac{a^2}{w^2}+O(w^{-3})\right)\times\\
&\qquad\left(1+\frac{(1-\beta)^2}{\beta}\frac{a}{w}-\frac{(1-\beta)^3}{2\beta}\frac{a^2}{w^2}+O(w^{-3})\right)\\
&\sim dw+\frac{ad(1-2\beta)}{\beta}-\frac{a^2d(1-\beta)}{2\beta w}+O(w^{-2}).
\end{aligned}$$

Applying (3.5.13) gives the horizontal impulse

$$I_x=\frac{\pi Ga^2d^2}{2}\left(\frac{1-\beta}{\beta}\right)=\frac{\pi Ga^2}{2}\left(\frac{1-\beta}{\beta}\right)^{2\beta-1}. \tag{3.6.9}$$

When $\beta=\frac{1}{2}$ the plate is vertical and the horizontal impulse on it is $\frac{1}{2}\pi Ga^2$ as found in §3.6.2 for the limiting case of a thin ellipse.

Equation (3.5.15) predicts that the added mass of the plate is

$$M_x=\frac{\pi\rho a^2}{2}\left(\frac{1-\beta}{\beta}\right)^{2\beta-1}.$$

When $\beta=\frac{1}{2}$, the added mass of a vertical plate is $\frac{1}{2}\pi\rho a^2$. When $\beta=0$ or 1 and the plate lies flat the prediction of zero added mass is also correct.

To find the total impulse, (3.5.5) becomes

$$\begin{aligned}
I_x+iI_y &= -iGd\int_{a(\beta-1)/\beta}^{a}z(u)\mathrm{d}u\\
&= -iGa^2d\int_{(\beta-1)/\beta}^{1}(u-1)^\beta\left(1+\frac{\beta}{1-\beta}u\right)^{1-\beta}\mathrm{d}u\\
&= -iGa^2d(-1)^\beta\left(\frac{\beta}{1-\beta}\right)^{1-\beta}\int_0^{1/\beta}x^\beta\left(\frac{1}{\beta}-x\right)^{1-\beta}\mathrm{d}x\\
&= -\frac{iGa^2d}{2}\frac{(-1)^\beta}{\beta^2}\left(\frac{\beta}{1-\beta}\right)^{1-\beta}\Gamma(2-\beta)\Gamma(1+\beta)\\
&= -\frac{i\pi Ga^2d}{2}\left(\frac{1-\beta}{\beta}\right)^{\beta}\frac{(-1)^\beta}{\sin(\pi\beta)}\\
&= \frac{\pi Ga^2d}{2}\left(\frac{1-\beta}{\beta}\right)^{\beta}(1-i\cot(\pi\beta))\\
&= \frac{\pi Ga^2}{2}\left(\frac{1-\beta}{\beta}\right)^{2\beta-1}(1-i\cot(\pi\beta)) \qquad (3.6.10)
\end{aligned}$$

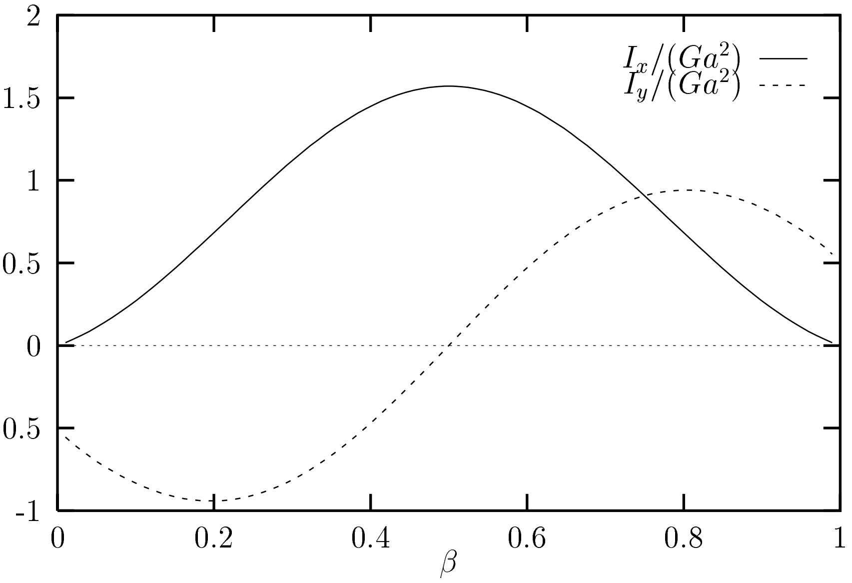

Figure 3.6.4: The horizontal and vertical impulses on the plate. Recall $I_y = -I_x \cot(\pi\beta)$.

using Abramowitz and Stegun (1965, eq.6.1.31) and Gradshteyn and Ryzhik (1965, eq.3.191). The horizontal and vertical components of the impulse on the plate are graphed in figure 3.6.4. This confirms the horizontal impulse of (3.6.9) which is the same whether the plate leans to the right or to the left at a particular angle to the bed. Also, $I_y = -I_x \cot(\pi\beta)$ which suggests that the added mass of the plate for movement in a vertical direction is

$$M_y = -M_x \cot(\pi\beta) = -\frac{\pi \rho a^2}{2\tan(\pi\beta)} \left(\frac{1-\beta}{\beta}\right)^{2\beta-1}. \tag{3.6.11}$$

We note that for small β, $I_x \propto \beta$ and for $\beta \approx 1$, $I_x \propto 1-\beta$. The maximum total horizontal impulse, $I_x = \frac{1}{2}\pi G a^2$, occurs when the plate is perpendicular to the bed ($\alpha = 90°$, $\beta = \frac{1}{2}$). Also, I_y is antisymmetric about $\alpha = 90°$, $I_y(1-\beta) = -I_y(\beta)$, with minimum and maximum values of $\mp 0.94 G a^2$ at $\alpha = 35.5°, 144.5°$ ($\beta = 0.197, 0.803$) respectively. That is, when the plate leans away from the impact zone it experiences an impulse downwards and when it leans towards the impact zone it experiences an impulse in the positive y direction, towards the free surface. Therefore when the plate is itself vertical it experiences no vertical impulse. When the plate lies flat ($\beta = 0$ or 1) the vertical impulse is $\pm\frac{1}{2}Ga^2$. This is the limiting case of a inclined plate which traps an infinitesimally small amount of fluid.

3.6.5 Circular Arc

We can examine the pressure impulse around a 'bent' plate with the conformal map

$$z(S) = \frac{a(S+2)}{1+(1/2S)} \tag{3.6.12}$$

which transforms the region exterior to the unit circle, $|S| = 1$, to the region outside an arc of a circle of radius $2a$ with centre at the origin and with symmetry about the real z-axis. We study the half of this arc in the upper half-plane, which subtends an angle $\pi/3$ at the origin and has length $\frac{2}{3}\pi a$.

The pressure impulse contours around an arc are shown in figure 3.6.5. To calculate the horizontal impulse we expand the conformal map in (3.6.12) as a power series,

$$z(w) = a(S+2)\left(1+\frac{1}{2S}\right)^{-1} \sim aS + \frac{3a}{2} - \frac{3a}{4S} + O(S^{-2}),$$

and then apply (3.5.14) to give

$$I_x = \frac{7}{4}\pi G a^2. \tag{3.6.13}$$

The conformal map from the upper half of the w plane, using (3.6.12), is

$$z(w) = \frac{a\left(2+\frac{1}{2}\left(w+\sqrt{w^2-4}\right)\right)}{1+\left(w+\sqrt{w^2-4}\right)^{-1}}$$

and then the vertical impulse is calculated by integrating (3.5.5) to give $I_y = 8Ga^2 - 2Ga^2 J$ where

$$\begin{aligned} J &= \Re\int_{-1}^{1} \frac{2+u+\sqrt{u^2-1}}{1+\frac{1}{2}(u+\sqrt{u^2-1})^{-1}}\,\mathrm{d}u \\ &= 2\int_{-1}^{1} \frac{2u^2+4u+3}{4u+5}\,\mathrm{d}u \\ &= \frac{3}{2} + \frac{9}{8}\log(3). \end{aligned}$$

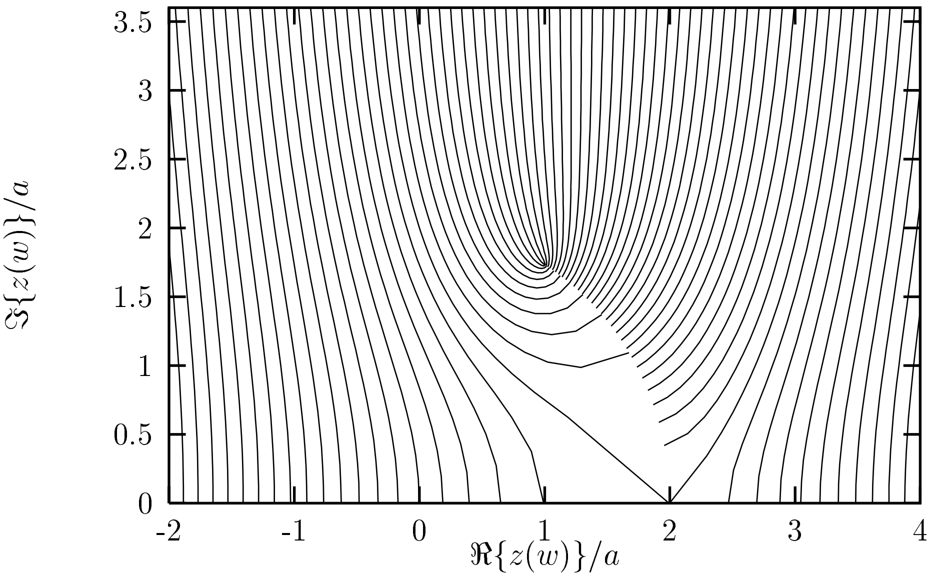

Figure 3.6.5: The pressure impulse contours around an arc of a circle of radius $2a$ on the sea bed. The arc subtends an angle of $\pi/3$ at the origin. Contour separation is $0.1aG$ and $P_0 = G = a = 1.0$. Notice how, as for the contours around a plate in figure 3.6.3, there are few contours penetrating under the arc.

So the total impulse is

$$\begin{aligned}I_x + iI_y &= \frac{7}{4}\pi Ga^2 + 8iGa^2 - 2iGa^2\left(\frac{3}{2} + \frac{9}{8}\log(3)\right)\\ &= \frac{7}{4}\pi Ga^2 + \left(5 - \frac{9}{4}\log(3)\right) iGa^2\\ &\approx (5.498 + 2.528i)\, Ga^2.\end{aligned}$$

So, there is a vertical impulse on the plate, which is smaller in magnitude than the horizontal impulse. The body is pushed up and away from the impact zone, but it is not clear whether the impulse would be large enough to allow it to break away from the bed, since no assumptions have been made about how the two are joined.

Since the arc has zero area, (3.6.13) implies that its added mass is $M_x = \frac{7}{4}\pi\rho a^2$. Recall from §3.6.4 that the horizontal impulse on a vertical plate of length L is $\frac{1}{2}\pi GL^2$. Therefore the horizontal impulse on a vertical plate of length $L = \frac{2}{3}\pi a$, equal to the length of the arc, is $I_x = 2.193\pi Ga^2$, slightly greater than the impulse on the arc in (3.6.13). If, however, we compare the horizontal impulse on the arc with the horizontal impulse on a vertical plate of the same maximum height above the sea bed, $L = \sqrt{3}a$, we find $I_x = \frac{3}{2}\pi Ga^2$, slightly less than in (3.6.13). Thus the horizontal impulse on this 'bent' plate lies between the impulse on a vertical plate with the same height and the impulse on a vertical plate with the same length.

3.6.6 Aerofoil

An aerofoil which is symmetric about the x-axis can be constructed by a composition of conformal maps. The unit circle $|S| = 1, S \in \mathbb{C}$ is shifted along the positive real axis a distance $0 < k \in \mathbb{R}$ and dilated to a circle of radius $a(1+k)$ in a complex T plane. Then the map $z(T) = T + a^2/T$ sends the region around the circle to the region around an aerofoil which has an axis of symmetry along the real line, and with its blunt end pointing away from the wall. Composing these three maps gives

$$z(S) = a(1+k)S + ak + \frac{a}{(1+k)S + k}. \tag{3.6.14}$$

The aerofoil lies in the z plane between $z = -2a$ and $z = a(1 + 2k + 1/(1 + 2k))$. As $|z| \to \infty$, $z \sim a(1 + k)S$. The lines of constant pressure impulse around the top half of the aerofoil, lying above the real axis, are shown in figure 3.6.6. These contours are calculated by mapping the real line between $-2a$ and $2a$ in a complex w plane to the unit circle in the S plane, and then composing this with (3.6.14) to give the conformal map

$$z(w) = \frac{(1+k)}{2}\left(w + \sqrt{w^2 - 4a^2}\right) + ak + \frac{2a^2}{(1+k)\left(w + \sqrt{w^2 - 4a^2}\right) + 2ak}. \quad (3.6.15)$$

As $|z| \to \infty$, $z \sim (1 + k)w$. Applying (3.5.14) to (3.6.14) gives the horizontal impulse on the body,

$$I_x = \pi G a^2 k(2 + k). \quad (3.6.16)$$

Since the aerofoil isn't symmetric about the line $x = 0$, we expect a non-zero component of vertical impulse from the last term in (3.5.5). However, using either (3.5.4) or (3.5.5) to find this proves more complicated than finding the horizontal impulse. We use (3.5.5) and quote the result here; the interested reader is referred to Appendix II. The horizontal impulse in (3.6.16) is confirmed and then the vertical impulse is

$$I_y = -4P_0 a\frac{(1+k)^2}{1+2k} - 2a^2 G\left(\frac{1+k}{k} + 2k\frac{1+k}{1+2k} - \frac{1+2k}{2k^2}\log(1+2k)\right). \quad (3.6.17)$$

This is a combination of an impulse downward equal to the length of the base multiplied by P_0, as expected, and a downward impulse proportional to G and increasing monotonically with k.

Reversing the direction in which the aerofoil points, we find that the horizontal impulse is unchanged and the part of the vertical impulse proportional to G changes sign, as for the plate. So when the blunt end of the aerofoil points towards the wall, it experiences a vertical component of impulse acting to push it away from the bed. In order to verify that the horizontal impulse is given in terms of the aerofoil's added mass and area by (3.5.15), we refer to Chapter I of Sedov (1965) who gives the added mass and area of a symmetric aerofoil as

$$M_x = \frac{1}{4}\rho\pi\bar{a}^2(l-2)(l+1), \qquad \mathcal{V} = \frac{1}{4}\pi\bar{a}^2 l^2\sqrt{1 - \frac{2}{l}}$$

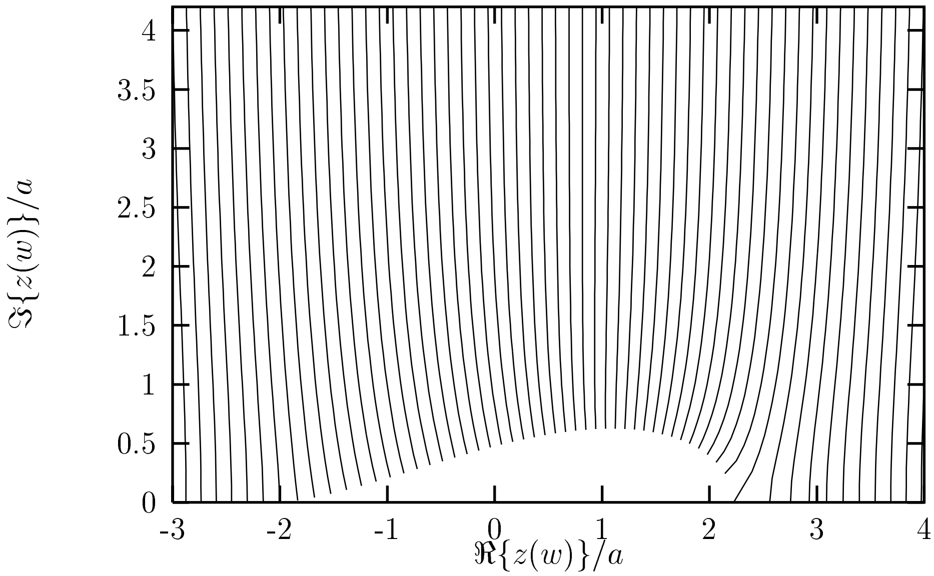

Figure 3.6.6: The pressure impulse contours around the top half of an aerofoil (with a horizontal axis of symmetry) on the sea bed. The conformal map is defined by (3.6.15). Contour separation is $0.1aG$ and $k = 0.3$, $P_0 = G = a = 1.0$.

where $l\bar{a}$ is the total length of the aerofoil. We find that $\bar{a} = 2a$ and so

$$l = \frac{1}{2}\left(3 + 2k + \frac{1}{1+2k}\right) = \frac{2(1+k)^2}{1+2k}.$$

For the top half of the aerofoil the horizontal impulse is

$$\begin{aligned} G\left(\frac{M_x}{\rho} + \mathcal{V}\right) &= \frac{\pi G a^2}{2}\left(\left(\frac{2(1+k)^2}{1+2k} - 2\right)\left(\frac{2(1+k)^2}{1+2k} + 1\right) + \left(\frac{2(1+k)^2}{1+2k}\right)^2 \frac{k}{1+k}\right) \\ &= \pi G a^2 k(2+k) \end{aligned}$$

after some algebraic manipulation. This shows that (3.5.15) is true for the aerofoil, and is an example of how this formula continues to work for a body without a vertical line of symmetry. We also see that the added mass coefficient for a (top-bottom) symmetric aerofoil is $\lambda_x = \frac{1}{2}k(2k^2 + 6k + 3)$.

3.6.7 Rectangle

The Fourier series for a rectangle on the x-axis in §3.4.2 was inaccurate and didn't yield a formula for the impulse acting on it. We therefore proceed by trying to find a conformal map from the upper half-plane to the exterior of a rectangle joined to the real axis.

It is fairly straightforward to map the real axis to a step (Kober 1957; Milne-Thompson 1962) using

$$z(w) = \sqrt{w^2 - 1} + \cosh^{-1} w. \qquad (3.6.18)$$

A possible route to representing a rectangle would be to perform the map twice, with the second map reflected in a vertical line through a point on the upper horizontal of the step. This 'combined' transformation certainly has the correct behaviour at infinity, but, as figure 3.6.7 shows, the pressure impulse contours don't become parallel as they approach the vertical line of symmetry and therefore this solution is invalid. If the rectangle were very wide then this method might be accurate.

An alternative approach is to apply the Schwarz-Christoffel mapping theorem (see,

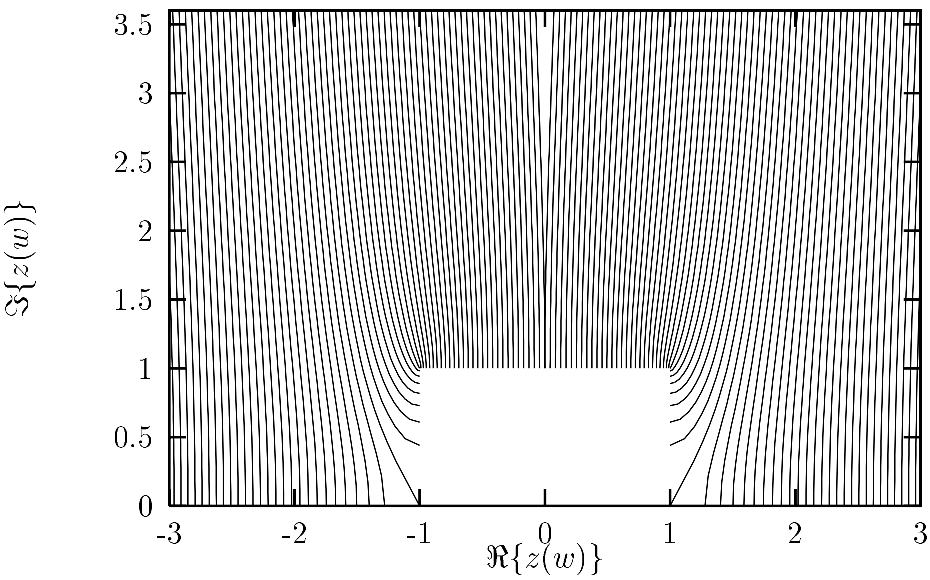

Figure 3.6.7: The pressure impulse contours around a rectangle on the sea bed, formed by reflecting the solution for a single step in a vertical axis. The deficiency of this method becomes apparent in the growing wedge between the central contours, where they should be parallel and vertical.

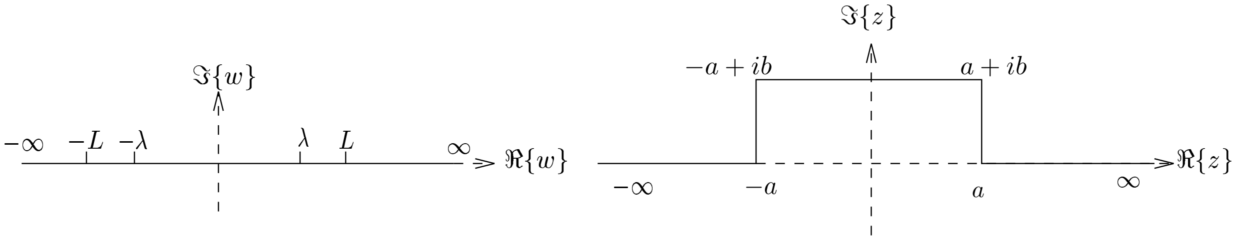

Figure 3.6.8: Illustrating the construction of the conformal map for a rectangle on the sea bed. The map sends $\pm\infty \mapsto \pm\infty, \pm L \mapsto \pm a$ and $\pm\lambda \mapsto \pm a + ib$.

for example, Copson 1935) to give the expression

$$\frac{\mathrm{d}z}{\mathrm{d}w} = \sqrt{\frac{w^2 - \lambda^2}{w^2 - L^2}} \tag{3.6.19}$$

where $\lambda \in [0, L]$ is a parameter governing the aspect ratio of the rectangle, which is at rest on the real axis with a vertical line of symmetry through the origin, as in figure 3.6.8. The map transforms the real line between $w = -L$ and L to the sides and top of a rectangle of width $2a$ and height b and transforms the remainder of the real w-axis to the real z-axis outside the rectangle. Note that $0 \leq a, b \leq L$, so that (3.6.19) can be used for any rectangle from a long flat plate, through a square, to a tall thin spike.

We let $\lambda' = \lambda/L$ then the half-width of this rectangle is given by

$$\begin{aligned} a &= \Re \int_0^L \frac{\mathrm{d}z}{\mathrm{d}w}\,\mathrm{d}w = \int_0^\lambda \frac{\mathrm{d}z}{\mathrm{d}w}\,\mathrm{d}w = L\int_0^{\lambda'} \sqrt{\frac{\lambda'^2 - w^2}{1 - w^2}}\,\mathrm{d}w \\ &= L\left\{E\left(\frac{\pi}{2}, \lambda'\right) - \left(1 - \lambda'^2\right) F\left(\frac{\pi}{2}, \lambda'\right)\right\} \end{aligned}$$

(Gradshteyn and Ryzhik 1965, eq.3.169.10) where $F(\phi, k)$ and $E(\phi, k)$ are Incomplete Legendre Elliptic integrals of the first and second kinds respectively. The height is

$$\begin{aligned} b &= \Im \int_0^L \frac{\mathrm{d}z}{\mathrm{d}w}\,\mathrm{d}w = \int_\lambda^L \frac{\mathrm{d}z}{\mathrm{d}w}\,\mathrm{d}w = L\int_{\lambda'}^1 \sqrt{\frac{w^2 - \lambda'^2}{1 - w^2}}\,\mathrm{d}w \\ &= L\left\{E\left(\frac{\pi}{2}, \sqrt{1 - \lambda'^2}\right) - \lambda'^2 F\left(\frac{\pi}{2}, \sqrt{1 - \lambda'^2}\right)\right\} \end{aligned}$$

(Gradshteyn and Ryzhik 1965, eq.3.169.12). Writing these in terms of Complete Elliptic integrals of the first and second kinds (K, E) and their associated Complete

Elliptic integrals (K', E') (see Byrd and Friedman 1971) gives

$$a(\lambda') = L\left(E(\lambda') - (1-\lambda'^2)K(\lambda')\right) \text{ and } b(\lambda') = L\left(E'(\lambda') - \lambda'^2 K'(\lambda')\right). \quad (3.6.20)$$

It is not possible to relate λ explicitly to the dimensions of the rectangle. In practice one chooses an aspect ratio for the rectangle, b/a, from which a value of λ' can be calculated using figure 3.6.9. Then figure 3.6.10 enables a/L and b/L to be found, giving the size of the rectangle. The symbolic manipulation package Maple (Vr3) was used to evaluate (3.6.20).

To find the horizontal impulse on this shape we would like to apply (3.5.13). However for the rectangle we don't have an explicit conformal map, but the derivative of the conformal map. So we differentiate (3.5.8):

$$\frac{\mathrm{d}z}{\mathrm{d}w} = d - \frac{b_1}{w^2} - \frac{2b_2}{w^3} - \dots$$

then (3.5.13) implies

$$I_x = -\pi G \Re\left(db_1\right) \quad (3.6.21)$$

where b_1 is now the coefficient of $-1/w^2$ in the expansion of $\mathrm{d}z/\mathrm{d}w$ for large w. For the rectangle, as $w \to \infty$ (3.6.19) becomes

$$\begin{aligned}\frac{\mathrm{d}z}{\mathrm{d}w} &= \left(1 - \left(\frac{\lambda}{w}\right)^2\right)^{\frac{1}{2}} \left(1 - \left(\frac{L}{w}\right)^2\right)^{-\frac{1}{2}} \\ &\sim 1 + \frac{1}{2w^2}\left(L^2 - \lambda^2\right) + O\left(\frac{1}{w^4}\right).\end{aligned}$$

Since $w \sim z$ as $|z| \to \infty$, $d = 1$ and $b_1 = -\frac{1}{2}(L^2 - \lambda^2)$, then $I_x = \frac{1}{2}\pi G(L^2 - \lambda^2)$. This correctly predicts the special cases of the vertical plate of height L ($\lambda = 0$) with horizontal impulse $\frac{1}{2}\pi G L^2$, as in §3.6.2, and the identity transformation from the flat sea bed ($\lambda = L$) which receives zero horizontal impulse. For a rectangle which is twice as wide as it is high, we have $b/a = 1$ and then $\lambda' = 1/\sqrt{2}$. Figure 3.6.10 gives $a = b = 0.423L$, so we put $L = 1/0.423 = 2.361$ to give a rectangle of width 2 and unit height. For this rectangle the horizontal impulse is $I_x = 4.378G$. This is much larger than the horizontal impulse of $I_x = 1.57G$ on a vertical plate of the same

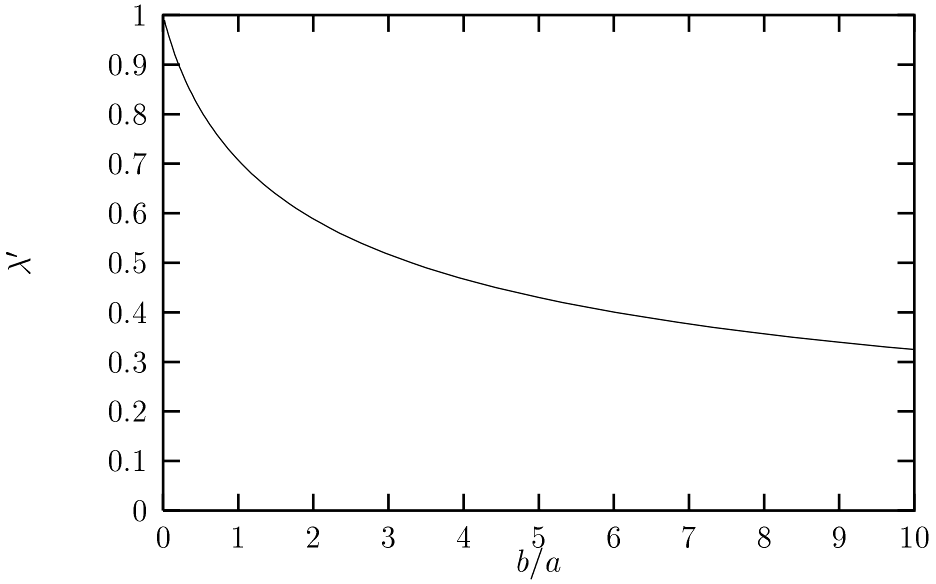

Figure 3.6.9: A graph of the aspect ratio of the rectangle, b/a, against λ'. Note that as $\lambda' \to 0$, $b/a \to \infty$, corresponding to the vertical plate. Maple was used to evaluate (3.6.20) to provide the data for these curves.

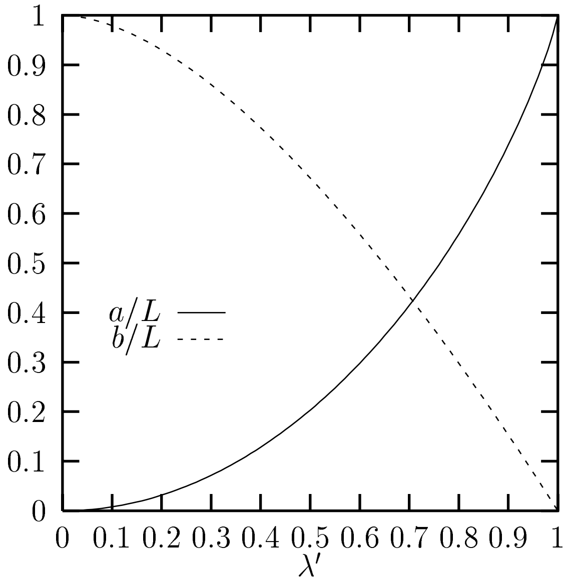

Figure 3.6.10: A graph of the lengths of the sides of the rectangle, a/L and b/L, against λ'. Maple was used to evaluate (3.6.20) to provide the data for these curves.

height, showing the effect of increasing width and area. A square, with $b/a = 2$, has $\lambda = 0.588L$ by figure 3.6.9 and then $b = 2a = 0.570L$. If $L = 3.509$ then the square has side length 2 and $I_x = 12.653G$. Comparing this with the impulse on a rectangle of width 2 and unit height shows that the effect of doubling the height, at constant width, is to almost triple the horizontal impulse on the rectangle. A square of side length $\sqrt{2}$ has a horizontal impulse $I_x = 12.653G/2 = 6.326G$ which is larger than the impulse on a rectangle with the same area but different aspect ratio. Thus for a given cross-sectional area, the tallest rectangles receive the highest horizontal impulses, and rectangles with larger areas receive higher horizontal impulses. Equation (3.5.15) predicts that the added mass of the rectangle for horizontal motion is

$$M_x = \rho\left(\frac{1}{2}\pi(L^2 - \lambda^2) - 2ab\right) \tag{3.6.22}$$

which is consistent with alternative derivations.

To find the vertical impulse, we apply (3.5.4) to get

$$\begin{aligned} I_x + iI_y &= -i\int_{-L}^{L}(P_0 - Gx)\sqrt{\frac{x^2-\lambda^2}{x^2-L^2}}\mathrm{d}x \\ &= -iP_0L\int_{-1}^{1}\sqrt{\frac{x^2-\lambda'^2}{x^2-1}}\mathrm{d}x + iGL^2\int_{-1}^{1}x\sqrt{\frac{x^2-\lambda'^2}{x^2-1}}\mathrm{d}x \end{aligned}$$

Note that the first integrand is symmetric for $x \in [-\lambda', \lambda']$ so the contributions add up, whereas for the remainder of the interval the integrand is antisymmetric and the contributions cancel. The second integral behaves in reverse because of the extra factor of x. Thus

$$\begin{aligned} I_x + iI_y &= -2iP_0L\int_{0}^{\lambda'}\sqrt{\frac{\lambda'^2-x^2}{1-x^2}}\mathrm{d}x + 2GL^2\int_{\lambda'}^{1}x\sqrt{\frac{x^2-\lambda'^2}{1-x^2}}\mathrm{d}x \\ &= -2iP_0a + 2GL^2J \end{aligned}$$

where J is the last integral, which we calculate using the substitution $x = \sin u$ and Gröbner and Hofreiter (1965, eq.241.13 b) so that, with $\lambda' = \sin(u')$,

$$J = i\lambda'\int_{u'}^{\pi/2}\sin u\sqrt{1 - \frac{1}{\lambda'^2}\sin^2 u}\,\mathrm{d}u$$

$$\begin{aligned}
&= i\lambda' \left[-\frac{\cos u}{2\lambda'}\sqrt{\lambda'^2 - \sin^2 u} + \frac{\lambda'^2 - 1}{2\lambda'} \log\left(\frac{\sqrt{\lambda'^2 - \sin^2 u} - \cos u}{\lambda' - 1} \right) \right]_{u'}^{\pi/2} \\
&= \frac{i}{2}\left(\lambda'^2 - 1\right) \left[\log\left(\frac{\sqrt{\lambda'^2 - x^2} - \sqrt{1 - x^2}}{\lambda' - 1} \right) \right]_{\lambda'}^{1} \\
&= \frac{i}{2}\left(\lambda'^2 - 1\right) \log\left(\frac{\sqrt{\lambda'^2 - 1}}{-\sqrt{1 - \lambda'^2}} \right) \\
&= \frac{i}{2}\left(\lambda'^2 - 1\right) \log\left(-i\right) \\
&= \frac{\pi}{4}(1 - \lambda'^2).
\end{aligned}$$

Then

$$I_x + iI_y = -2iP_0 a + \frac{1}{2}\pi G(L^2 - \lambda^2) \tag{3.6.23}$$

which verifies the horizontal impulse calculated above. Note that again we have a vertical impulse equal to the length of the base multiplied by P_0.

Bickley (1932) gives the transformation

$$z(S) = C\left\{ S + \sum_{n=1}^{\infty} c_n S^{(1-2n)} \right\} \tag{3.6.24}$$

which conformally maps the exterior of the unit circle ($|S| = 1$) to the exterior of a rectangle of length $2a$ and height $2b$ in the z plane. The rectangle is arranged with its sides parallel and perpendicular to the axes, and symmetrically across them, and is generated by an angle $\alpha = \cos^{-1}(\lambda/L) \in [0°, 90°]$ that Bickley uses to label the aspect ratio of the rectangle (where λ is the parameter used in (3.6.19) to generate a Schwarz-Christoffel map). Then

$$C = \frac{a}{2L_2} = \frac{b}{2L_1} \tag{3.6.25}$$

for

$$L_1(\alpha) = \frac{a(\sin\alpha)}{L} \text{ and } L_2(\alpha) = \frac{b(\sin\alpha)}{L} \tag{3.6.26}$$

by (3.6.20). The c_n are given by the recursive formula

$$\begin{aligned}
(n+1)(2n+1)c_{n+1} - (2n-1)^2\mu c_n + (2n-3)(n-2)c_{n-1} = 0 \\
\text{with } c_0 = 1, c_1 = \mu = \cos(2\alpha).
\end{aligned}$$

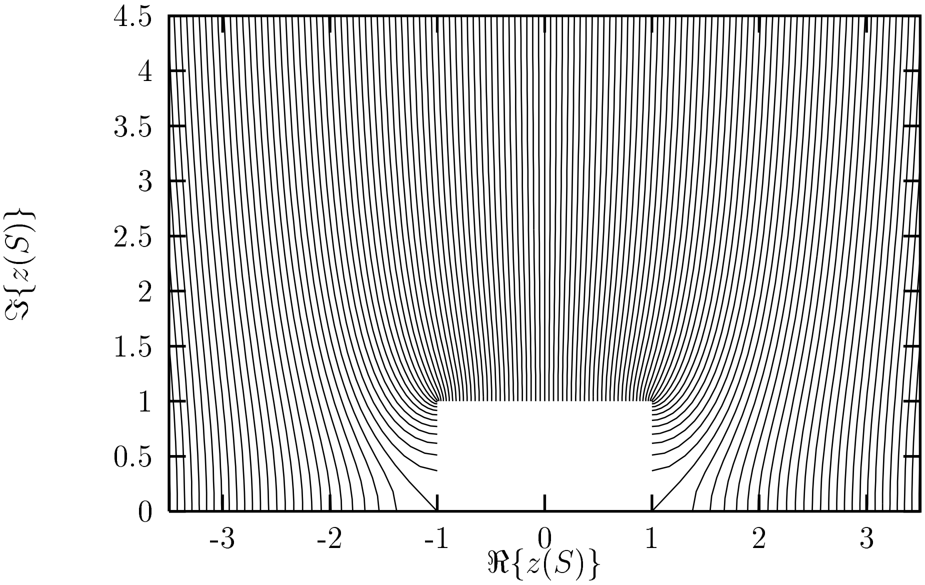

Figure 3.6.11: The pressure impulse contours around a rectangle on the sea bed, using the map in (3.6.24) with $\alpha = 45.0^\circ$ and $a = 1.0$. Contour separation is $0.05aG$. These contours should be compared with those in figure 3.4.3, for P around a rectangle constructed using a Fourier series. Here, there are no errors in satisfying the boundary condition on the rectangle.

Finding the pressure impulse contours around a circle is a problem solved in §3.6.1, and therefore this mapping can be used to generate the pressure impulse contours around the rectangle, as shown in figure 3.6.11. The contours are found by using the conformal map from the flat plane to the unit circle, (3.6.2) with $a = 1$, and then mapping to the region around a rectangle using (3.6.24).

3.7 Impulse Comparisons

We have found the impulses on numerous objects. The horizontal impulses on a selection of shapes are shown in Table 3.7.1. Also shown, where the area of the body is non-zero, is horizontal impulse per unit cross-sectional area. This latter expression has the dimensions of velocity, and doesn't depend on the size of the body, only its shape. For the asymmetric shapes considered, reflecting them in the line $x = 0$ leaves the horizontal impulse unchanged, as does translation along the x-axis. The horizontal impulse per unit area on a body increases with its aspect ratio (height over width), so that tall thin shapes receive larger impulses for a given cross-sectional area, as shown for semi-ellipses and rectangles. Thus (3.5.15) shows that the added mass coefficient relates to the aspect ratio of the body profile. Calculations for a semicircular and a circular cylinder shows that we expect objects of greater than about half a metre in radius to be moved by the effect of the wave impact.

Of the three asymmetric bodies studied, the non-vertical plate and the circular arc have only point contact, and must be held up in some way. For any movement to occur, the resultant impulse would have to be great enough to overcome whatever forces were fixing the body to the sea floor. Alternatively, the body could be in motion, and touches the sea bed instantaneously. Then the impulse causes a change in its velocity, given by (3.5.18). The other asymmetric body is the aerofoil, which experiences a vertical impulse upwards when its blunt end faces the wall. For those bodies which are not fixed, the comments at the end of §3.5.2 suggest at what speed they would initially move, although this applies only to movement in a horizontal direction.

Body, B	I_x/G	$I_x/(G\mathcal{V})$
Semicircle, radius a	πa^2	2
Semi-ellipse, with semi-axes α, β	$\frac{1}{2}\pi\beta\,(\alpha+\beta)$	$1+\beta/\alpha$
Circle, radius a	$\frac{1}{3}\pi^3 a^2$	$\frac{1}{3}\pi^2$
Rectangle, width $2a$, height b	$\frac{1}{2}\pi(L^2-\lambda^2)$	$\frac{1}{4}\pi(L^2-\lambda^2)/ab$
Vertical plate, height a	$\frac{1}{2}\pi a^2$	
Plate of length a, inclined at angle $\beta\pi$	$\frac{1}{2}\pi a^2((1-\beta)/\beta)^{2\beta-1}$	
Arc of circle, radius $2a$ subtending angle $\frac{1}{3}\pi$	$\frac{7}{4}\pi a^2$	

Table 3.7.1: Horizontal impulse, and horizontal impulse per unit cross-sectional area, on a given body lying on the sea bed. The values in the last column are equal to $1+\lambda_x$ if $\mathcal{V}>0$ and λ_x itself otherwise, where λ_x is the added mass coefficient for horizontal translation.

3.8 Conclusions

Since the normal derivative of the pressure impulse is zero on the wall, below the impact zone, this theory can also be used to find the effect of a wave impact on an object protruding from the wall. Considering again the contours of pressure impulse in figures 2.3.3 to 2.3.5, we see that a small body attached to the wall at position $(0, -y_0)$, where $y_0 > \mu H$, is subjected to a pressure impulse gradient down the wall. For a body whose size is much less than the height of the wall, we can approximate the gradient to be almost uniform, so that we are able to write the far field condition as $P \sim P_0 - Gx'$, where x' is now a coordinate pointing down the wall. Now $G = -\left.\partial P_1/\partial x'\right|_{x=0,y=-y_0}$ and $P_0 = \left.P_1\right|_{x=0,y=-y_0}$. The gradient, G, is evidently often large, since the contours are so close together, and will act in such a way as to attempt to push the body towards the sea bed. We can again use a Fourier Series or a conformal map to represent the body, B, and, since the boundary conditions are the same as for the problem considered earlier, all the results transfer to this situation. Then the impulse on this body protruding from the wall is I_x downwards (in the x' direction) and I_y pointing perpendicularly away from the wall.

We have described two methods for representing a body on the sea bed which is exposed to the effects of wave impact: using either a Fourier series or a conformal map. This latter method is found to be more useful, since we can represent truly isolated objects with a transformation from the upper half-plane or the exterior of a unit circle, in which cases there are several ways of calculating the impulse on the body. The horizontal impulse, which is proportional to the pressure impulse gradient, G, also depends on the sum of the body's volume and its added mass, which is itself a function of the aspect ratio of the body. So we see that not only do large objects receive a greater impulse (and move farther if they are free to move) but that for two bodies with equal volumes, the taller thinner one will receive the largest impulse. For a body which is free to move the impulse is reduced and then the velocity at which it is impulsively kicked into motion depends on its density, as well as its volume and added mass. Again, objects with large volume or aspect ratio will move more quickly, and heavier bodies move less fast. We find that for an object with a length scale of greater than about half a metre, the impulsive forces will overcome the frictional forces and the body will move. So this theory accounts for the movement of armour protection blocks, situated around the base of a breakwater, away from the wall against which waves are breaking. It predicts even greater displacements for larger isolated, submerged blocks, which could be constituents of a breakwater.

Our analysis also suggests that a body without a vertical line of symmetry will experience a vertical impulse proportional to G, which is, in general, difficult to calculate. However all objects, irrespective of their symmetries, experience an impulse proportional to the local pressure impulse, which is equal and opposite to the impulse that they receive from any fluid beneath them if they are free to move.

Chapter 4

The Pressure Impulse on a Surface-Piercing Body

4.1 Introduction

When a wave breaks against a vertical wall, high pressures of brief duration occur both on the wall and in the surrounding fluid. The analysis of Chapter 3 showed that objects on the sea bed in the vicinity of a wave impact can experience impulses big enough to move them, and this is a probable mechanism for the movement of concrete armour blocks near breakwaters. Our goal in this chapter is to try and quantify the effect of these violent impacts on a body piercing the surface near a sea wall when a wave breaks against the wall.

We think about three classes of problem.

- (i) A suspended body: For instance, a pipe suspended from a crane during offshore construction work is free to move upwards due to wave impact in the vicinity. This body is likely to have a density greater than that of water and will therefore experience an impulse causing it to be moved upward at some velocity dependent on its shape.

- (ii) A fixed body: Parts of offshore structures, such as oil rigs, are often partly submerged. If the body is fixed it will experience a greater vertical impulse than a similar body which is free to move. It is possible that this impulse would be great enough to separate it from a larger, immobile, structure.

- (iii) A moving body: Consider a body, which is heavier than water, that is falling through the free surface at the instant a wave breaks against a sea wall. This might be a block knocked out of the wall by a previous impact which could be thrown back towards the wall to cause further damage. Observations suggest that only the very high pressures generated by breaking waves give sufficiently large forces to damage sea walls, and perhaps this is a mechanism by which the damage occurs.

Two-dimensional non-linear calculations of the action of waves on surface-piercing bodies are widespread (see the review of Tsai and Yue 1996). Similarly, many experiments have been performed concerning wave breaking on surface-piercing bodies, in particular cylinders, such as the recent work of Chan, Cheong, and Tan (1995). The present problem is however concerned with the effect of nearby wave impact and the pressure impulse it generates. If the wave breaks at the wall to give high impact pressures then as it passes over the body prior to impact the wave will be less well developed and any motion of the body will be on a more slowly varying timescale. The geometries we consider are similar to the water entry and exit problems described in the literature. For instance, Howison, Ockendon, and Wilson (1991) describe the water entry of a wedge with a small deadrise angle (the angle between the free surface and the wedge). They calculate the effective wetted length for this 'almost flat plate' using matched asymptotic expansions, with the angle as the small parameter, improving upon the early calculations of Wagner (1932), who thought of the impacting body as a horizontal plate that grew in length as time progressed. In the case of a flat plate (when the deadrise angle is zero), Verhagen (1967) includes the effects of the air cushion trapped beneath the plate to obtain better agreement between theory and experiment. Greenhow (1988) describes the entry and exit of a circular cylinder. He calculates numerically the free surface flow as the body is dropped or pulled out and compares with experiment. The agreement is not good, due to the complexity of the flows. Again, our problem differs since the body is initially surface-piercing, and at worst will submerge slightly after the impact occurs. More likely perhaps is that the body will remain in the free surface and, since it moves more slowly than the surrounding fluid, the free surface will be effectively depressed.

We neglect the effect of the free surface displacement on the body, B, during impact. Similarly, we shall not considered the effect of the free surface motion caused by the presence of B. Greenhow and Yanbao (1987), in their investigation of the motion of circular cylinders penetrating fluid boundaries, make the observation that for high speed entry the 'free surface is considerably distorted'. However, because we pose a problem where the body is initially at rest in the free surface, we believe that in our formulation this distortion will only take effect after the initial motion induced by the impact of the wave against the wall, since the interval of time over which the impact takes place, Δt, is so small. We also ignore the effect of the jets often created at the fluid-solid interface, since the fluid of which they consist exerts relatively low pressures on B.

In the analysis below, we find the pressure impulses and velocities associated with different shapes of body. In particular, we will be in a position to decide whether a thin, horizontal body, rather than a body which projects deep into the fluid, will be less affected by the nearby impact. The profile of B above the water-line is left indeterminate and we require only its total mass. If B is not fixed then it will move with the (change of) velocity specified (as a function of its mass) for the appropriate shape underwater. In the case of large bodies, we envisage the two-dimensional calculations to be used to find the pressure impulse on a small cross-section of B. This can then be done for several different cross-sections to compare the different impulses acting on different parts of B, and therefore where stresses are likely to act (see Newman (1978), §7.7, on strip theory).

Examining the results of Chapter 2, in particular figures 2.3.3 to 2.3.5, suggests that in a small region, D, of the surface, such as that around $x = 0.25H := X$, the contours of constant P are approximately parallel to the x-axis. On the free surface itself $P = 0$ and P increases with distance into the fluid. In practice we can choose any of the pressure impulse contours to be the $P = 0$ contour, so that the free surface does not have to be horizontal. If $\underline{u}_b$ and $\underline{u}_a$ denote the velocities of the fluid before and after impact respectively, then, as in (1.2.6),

$$\underline{u}_a - \underline{u}_b = -\frac{1}{\rho}\nabla P. \qquad (4.1.1)$$

The conclusion of Chapter 2 was that the velocity profile chosen had a relatively unimportant effect on the pressure impulses generated, and that it is acceptable to use the velocity profile of Case A. Therefore we take $\underline{u}_b = (-u_0, 0)$, so that the vertical component of (4.1.1) is

$$v_a = -\frac{1}{\rho}\frac{\partial P}{\partial y}. \qquad (4.1.2)$$

The pressure impulse gradient at the surface in D, which we denote by G, is therefore associated with a vertical fluid velocity after impact. A body, B, in this region, which is free to move and of density ρ_B, will be propelled upward, with some speed V. In the absence of B the free surface would rise with speed $V_{max} = G/\rho$. We expect V to be dependent upon the shape of B with $V \leq V_{max}$. We can estimate G in one of two ways; either by examining the contour separation on the graphs produced in Chapter 2, or by obtaining empirical measurements of the vertical fluid velocity in a breaking wave and applying $G = \rho V_{max}$. It is possible to employ the latter method by examining sequential photographs such as those of Hattori *et al* (1994) but, because the time scales for which PIT is accurate are small, very high speed photography is required to obtain much accuracy. Therefore in the former case, we estimate a possible value of G: we assume a water depth of $H = 10$m and therefore a fluid speed of $u_0 = \sqrt{gH} = 9.91$ m sec^{-1}, in fluid of density $\rho = 1000$ kg m^{-3}. In figure 2.3.4(a), where $\mu = 0.5$ (the wave impacts over the top half of the wall), the pressure impulse gradient near $X = 2.5$m is $G = 0.5\rho u_0 = 4955$ N sec m^{-3}. If $H = 1$m then $u_0 = \sqrt{gH} = 3.13$ m sec^{-1} and at $X = 0.25$m we obtain $G = 1565.0$ N sec m^{-3}. Note then that $G \approx 1500\sqrt{H}$. In these cases V_{max} ranges between about 1.5 m sec^{-1} and 5 m sec^{-1}. The velocities we expect for a body B are therefore less than these values. Heuristically, halving X/H doubles G, so that V doubles. Thus, if the body is placed nearer the wall, it is lifted at a higher velocity.

If we were to choose one of the non-horizontal lines of constant pressure impulse to be the free surface then we would still find that a body experiences an impulse perpendicular to the surface. However in the following we assume that the free surface is flat to simplify the analysis. We note that the pressure impulse gradient could also be thought of as due to an explosion deep below the free surface.

4.2 Mathematical Formulation

We now consider a local model of the domain D and define a new horizontal coordinate by the shift $x' = x - X$. The origin is now on the free surface, $y = 0$, at the centre of a body B with boundary ∂B and submerged volume per unit length $\mathcal{V}$ (cross-sectional area). The normal to ∂B is $\underline{n}$, pointing into the fluid. The pressure forces acting on B are assumed to be much greater than any gravitational forces, and it is assumed to be fixed. Note that the length scale, L, of B is necessarily very much less than its distance from the wall, $L \ll X$. The body receives an impulse due to the local pressure impulse gradient, $G > 0$, in the positive y direction. The pressure impulse satisfies Laplace's equation throughout the fluid and is zero on the free surface. Since the body is fixed, the normal derivative of P on B is zero. Dropping primes, the boundary value problem for $P(x, y)$ in the lower half-plane is then

$$\begin{aligned} &\bullet\ \nabla^2 P = 0 \text{ everywhere in the fluid} \\ &\bullet\ P \sim -Gy \text{ as } y \to -\infty \text{ or } |x| \to \infty \\ &\bullet\ P = 0 \text{ on } y = 0 \text{ away from } B \\ &\bullet\ \tfrac{\partial P}{\partial n} = 0 \text{ on } \partial B \end{aligned} \qquad (4.2.1)$$

as shown in figure 4.2.1. The vertical impulse, I_y, on B is found, as before, by integrating P over the surface of the body.

Having found P around a fixed body, we can then find the pressure impulse, P_1, around a moving body. If B is initially at rest and free to move then the pressure impulse gradient, G, will accelerate it from rest to a velocity V in the positive y

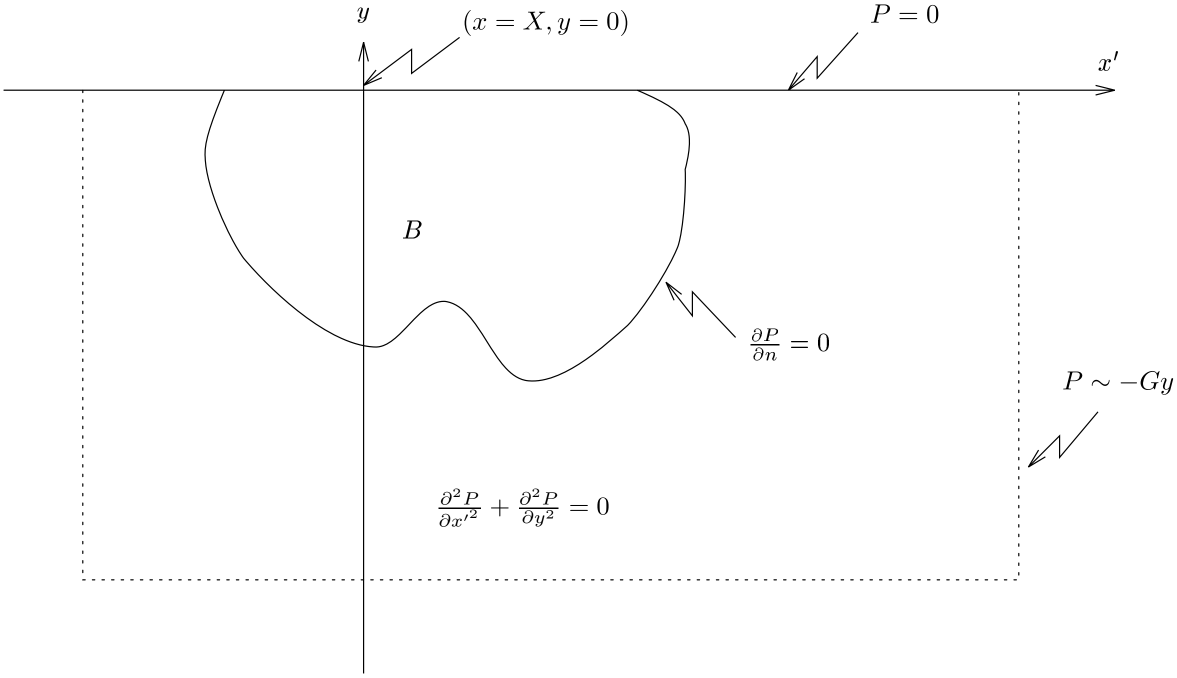

Figure 4.2.1: The boundary value problem for the pressure impulse around a fixed surface-piercing body B. P satisfies Laplace's equation with conditions of $P = 0$ on the free surface, $\partial P/\partial n = 0$ on ∂B and $P \sim -Gy$ as $y \to \infty$ or $|x'| \to \infty$.

direction. (If B is already in motion then V will be a change in the vertical component of velocity.) The body, of total mass $m \geq 0$, now has $\partial P_1/\partial y|_{\partial B} = -\rho V$, by (4.1.2). The free surface and far field boundary conditions remain the same. Then in the lower half-plane, $P_1(x, y)$ satisfies

$$\begin{aligned}
&\bullet\ \nabla^2 P_1 = 0 \text{ everywhere in the fluid}\\
&\bullet\ P_1 \sim -Gy \text{ as } y \to -\infty \text{ or } |x| \to \infty\\
&\bullet\ P_1 = 0 \text{ on } y = 0 \text{ away from } B\\
&\bullet\ \tfrac{\partial P_1}{\partial y} = -\rho V \text{ on } \partial B.
\end{aligned} \tag{4.2.2}$$

The discussion in §3.5.3 gives

$$P_1 = \hat{P} - \rho V y,$$

where $\hat{P}$ is the solution for the fixed body problem, (4.2.1), with the effective pressure impulse gradient G replaced by $G - \rho V$. Notice that we have merely to put $V = 0$ in these expressions to return P for a fixed body, so that we need only solve the problem for a body which is free to move.

If the vertical impulse on a fixed body is $I_y = Gk$, then the vertical impulse on the same body which is free to move is

$$I_{Vy} = (G - \rho V)k + \rho V \mathcal{V}. \tag{4.2.3}$$

Equating the vertical impulse on the moving body with its change in momentum, mV, gives

$$V = \frac{Gk}{m + \rho(k - \mathcal{V})} \text{ and } I_{Vy} = \frac{mGk}{m + \rho(k - \mathcal{V})}. \tag{4.2.4}$$

The limit $m \to \infty$ is equivalent to putting $V = 0$, since we obtain the expressions for a fixed body.

It remains to find P, and then k. We will do this for several different shaped bodies. Firstly, we exploit a link between this problem and the problem solved in the previous chapter for a body, at rest on the sea bed, which is exposed to a pressure impulse gradient. This enables the pressure impulses on some symmetric bodies to be found, for which we give examples of a semicircle and a rectangle. A flat plate on the surface, which is the limiting case of a thin rectangle, is considered in more detail, and then we conformally map the solution for P beneath this plate to other, not necessarily symmetric, bodies beneath the free surface. As examples of this we give a circle, a wedge, a blunt wedge and an inclined plate. In §4.5 we find the solution for P beneath a flat circular disc on the surface and then beneath a hemisphere in §4.6. We discuss these results in §4.7 and draw some conclusions about which shapes will move more quickly when subjected to wave impact. We also show how to translate some of the more general results of potential theory to give the pressure impulses beneath a moving body.

4.3 Comparison with a Body on the Sea Bed

For any left-right symmetric body on the free surface, the pressure impulse is symmetric about this line of symmetry ($x = 0$) too, with $\partial P/\partial x|_{x=0} = 0$. For a body which also has a horizontal line of symmetry along $y = 0$ we can solve these boundary value problems for the pressure impulse by referring to the analysis of Chapter 3. Figure 4.3.1 shows that for any body with these two lines of symmetry, we can put $P_0 = 0$ and then the present problem is the same, but rotated anticlockwise through 90°. The pressure impulse distribution around a body on the sea floor is given by (3.6.1):

$$P(x,y) = P_0 - Gd\Re\{w(z)\}$$

where $z = x + iy$ and $w(z)$ is the inverse of the conformal map which takes the flat sea bed in the w plane to the boundary of the body B in the z plane, with $z \sim dw$ as $|z| \to \infty$ (and $\Re$ denotes real part). The rotation by 90° is equivalent to multiplying the complex numbers by i and, since $P_0 = 0$, the pressure impulse around this body piercing the free surface is

$$P(x,y) = Gd\Re\{w(iz)\} \tag{4.3.1}$$

which satisfies (4.2.1). If the body is free to move, then this becomes

$$P_1(x,y) = (G - \rho V)d\Re\{w(iz)\} - \rho V y \tag{4.3.2}$$

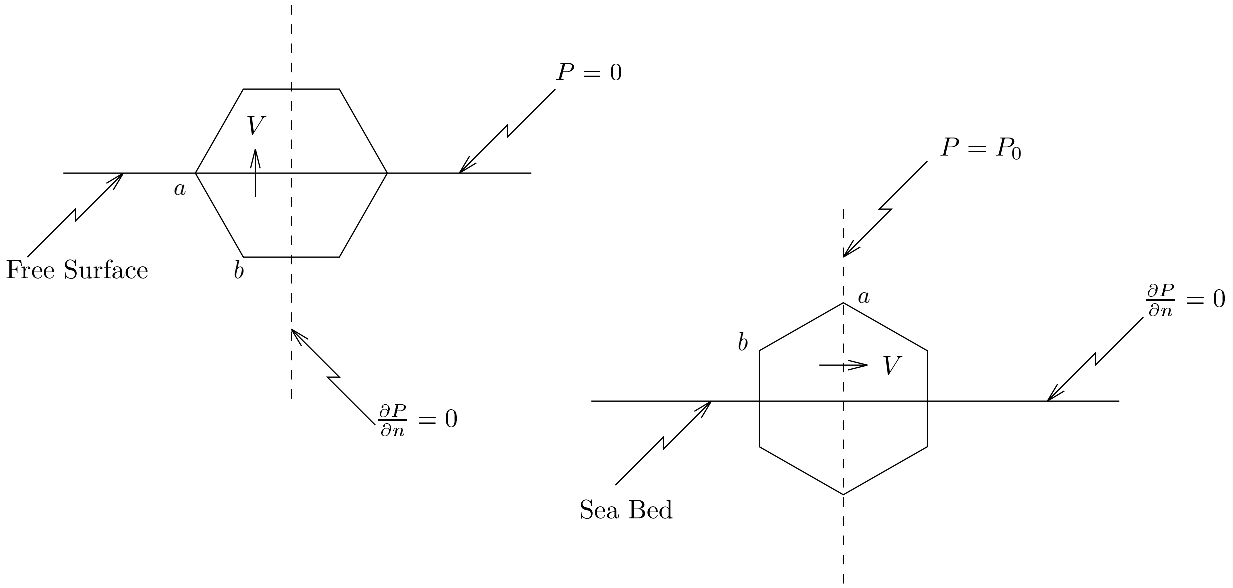

Figure 4.3.1: Showing the similarity between the problems of a body moving along the sea bed and being pushed upward at the free surface. If the body has two perpendicular lines of symmetry, then the normal derivative of P on the centre line of the surface-piercing body is zero so that the problem on the left is the same as the problem on the right, solved in Chapter 3, with $P_0 = 0$.

which satisfies (4.2.2). As for a body moving along the sea bed, the solution is a sum of two pressure impulses: the second is a multiple of the depth, $P = -\rho V y$, which satisfies the last two boundary conditions. Then the first must have $\partial P/\partial y = 0$ on the body, with far-field condition $P \sim -(G - \rho V)y$.

In the same way, for those bodies with these two lines of symmetry, the horizontal impulse on a body fixed to the sea bed, $I_x = Gk$, translates to a vertical impulse, $I_y = Gk$, on the same body fixed so as to pierce the free surface, and rotated anticlockwise by 90°. (This is not quite as straightforward as it seems: to find the horizontal impulse on a fixed body on the sea bed we halved the horizontal impulse on a fixed body surrounded by fluid, $\bar{B}$. The vertical impulse on a fixed body piercing the free surface is half the vertical impulse on the rotated body $\bar{B}$ piercing the free surface, because now $\bar{B}$ is only half surrounded by fluid. So these factors cancel out.) Then for a moving body the expressions for the velocity, (3.5.18), and impulse, (3.5.19), apply, which were found independently in (4.2.4).

In order to test the hypothesis that the velocity at which a body moves depends on its shape, we wish to find the velocities of several different shaped bodies. We can now do this using the results of Chapter 3. We found there that those bodies which are taller and thinner, for a given cross-sectional area, experience the greatest impulses. So now, for a fixed body piercing the free surface, greater impulses are exerted on flatter, wider bodies, for a given cross-sectional area. That is, the width of the body at the free surface is more significant than its depth. If the impulse on a shape is larger, then, if it is free to move, so will the velocity be larger. Thus, we find that flatter, wider bodies will move at higher speeds.

4.3.1 Semicircle

For a fixed body whose submerged shape is that of a semicircle of radius a, the inverse of the conformal map from the flat sea bed to its exterior is $w(z) = z + a^2/z$. Then (4.3.1) implies

$$P = -Gy\left(1 + \frac{a^2}{x^2+y^2}\right).$$

The vertical impulse, from (3.6.3), is

$$I_y = \pi G a^2$$

and the horizontal impulse on the semicircle is zero. If the body is free to move then

$$P_1 = -(G-\rho V)y\left(1 + \frac{a^2}{x^2+y^2}\right) - \rho V y = -Gy - (G-\rho V)\frac{a^2 y}{x^2+y^2}$$

and (4.2.4) implies that

$$V = \frac{\pi G a^2}{m + \frac{1}{2}\pi\rho a^2}. \tag{4.3.3}$$

The pressure impulse contours for a moving semicircle of radius a are shown in figure 4.3.2. As for a body on the sea bed, the contours are attracted towards the body, increasing the vertical impulse on it.

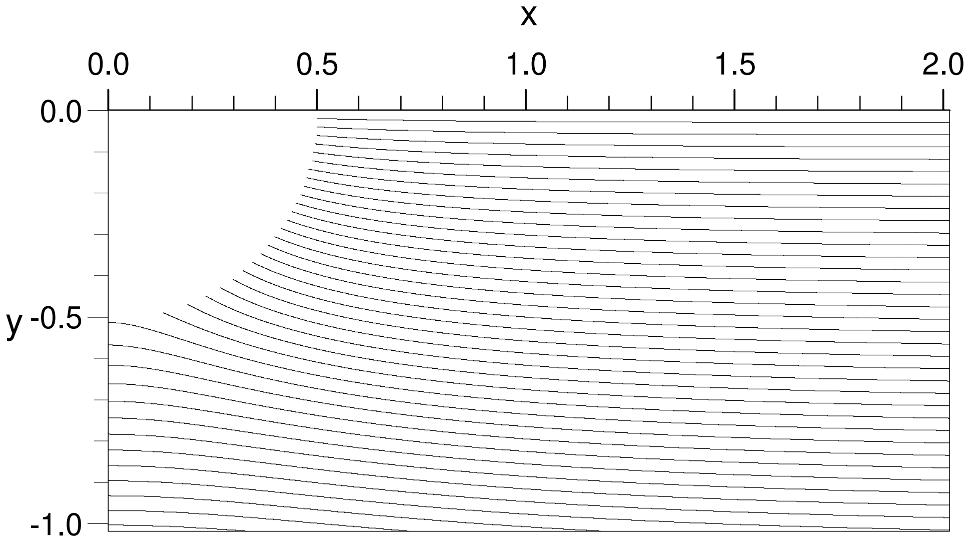

Figure 4.3.2: Pressure impulse contours below a semicircle of radius a. In this case the mass of the semicircle is $m = \frac{1}{2}\pi\rho_B a^2$ and $G = a = \rho = 1.0$, where $\rho_B = 3\rho$. The contour separation is $0.03Ga$. Only the right-hand half of the domain is shown, since the lines of constant P are symmetrical about the line $x = 0$.

4.3.2 Rectangle

We now relate the rectangle on the sea bed, from §3.6.7, to a surface-piercing rectangle. The conformal map (3.6.19):

$$\frac{\mathrm{d}z}{\mathrm{d}w} = \sqrt{\frac{w^2 - \lambda^2}{w^2 - L^2}} \tag{4.3.4}$$

is generated by introducing a parameter $\lambda \leq L$ and conformally mapping the length of sea bed between $-L$ and L to a rectangle of width $2a$ and height b. It was not possible to find the pressure impulse using this method, because we were unable to invert this conformal map, but we did find the horizontal impulse on the fixed rectangle, $I_x = \frac{1}{2}\pi G(L^2 - \lambda^2)$. Rotating this rectangle by 90° gives a rectangle below the free surface, of half-width b and depth a, where a and b are given by (3.6.20). Although we don't know the distribution of P, we apply (4.2.3) to give

$$I_{Vy} = \frac{1}{2}\pi(G - \rho V)(L^2 - \lambda^2) + 2\rho V ab. \tag{4.3.5}$$

Equating the change in momentum with the impulse on the body gives

$$V = \frac{\frac{1}{2}\pi G(L^2 - \lambda^2)}{m + (\frac{1}{2}\pi(L^2 - \lambda^2) - 2ab)\rho}. \tag{4.3.6}$$

Note that when $\lambda = L$ (which was the identity transformation of the sea bed) we have $a = L$ and $b = 0$, corresponding to a vertical surface-piercing plate of depth L and negligible thickness, for which $V = 0$. In this special case, the pressure impulse is $P = P_1 = -Gy$; this is as if there were no body present. For $\lambda = 0$, we have $a = 0$ and $b = L$, corresponding to a flat plate of length $2L$ on the free surface, which we study further in the next section. A square has $a = 2b$ which means $\lambda = 0.808L$ from figure 3.6.9. Then $a = 0.570L$, so we put $L = 1/0.570 = 1.754$ to give a square of unit side length. If $\rho_B = 3\rho$ and the square doesn't project above the free surface then $V = 0.152G/\rho$.

The other shapes studied in Chapter 3 which have the necessary two axes of symmetry for the translation of results to be valid are the class of semi-ellipses and the circle on the sea bed (since it also has a mirror image in the bed) which becomes two adjacent semicircular lumps extending below the free surface. Most useful however, will be the flat plate of length $2L$ lying on the free surface, found above as the limiting case of a rectangle. Then we can find the pressure impulse beneath this plate, and use it to find the pressure impulse around other shapes using another conformal map.

4.3.3 Flat Plate

We consider again the rectangle on the sea bed, which was transformed to a rectangle on the free surface in §4.3.2. When $\lambda = 0$, the conformal map, (4.3.4), can be integrated to give

$$z = \sqrt{w^2 - L^2}. \tag{4.3.7}$$

This maps the sea bed to a vertical plate of length L. So we rotate this by 90° anticlockwise to give a flat plate lying on the surface. The plate is of length $2L$ and lies between $x = -L$ and $x = L$, on $y = 0$. The pressure impulse solution is given by

(4.3.2) using the inverse of (4.3.7), $w(z) = \sqrt{z^2 + L^2}$:

$$P = (G - \rho V)\Re\left\{\sqrt{L^2 - z^2}\right\} - \rho V y. \tag{4.3.8}$$

In this case $k = \frac{1}{2}\pi L^2$ and, if the plate has mass m, (4.2.4) gives

$$V = \frac{\frac{1}{2}\pi G L^2}{m + \frac{1}{2}\pi \rho L^2} \tag{4.3.9}$$

since $\mathcal{V} = 0$. Then the pressure impulse is

$$P(x, y) = \frac{G}{m + \frac{1}{2}\pi\rho L^2}\left(m\Re\left\{\sqrt{L^2 - z^2}\right\} - \frac{1}{2}\pi\rho L^2 y\right). \tag{4.3.10}$$

As the mass of the plate increases, the velocity at which it is moved decreases. As $m \to 0, V \to V_{max}$, and the plate moves with the free surface, experiencing no impulse. In the same limit, the pressure impulse tends to a value of $-Gy$, which is zero on $y = 0$, consistent with there being no plate present. If the plate is constrained, so that $V = 0$, then the impulse on it is greater than if it were able to move, $I_y = \frac{1}{2}\pi G L^2$. The lines of constant pressure impulse below the plate are graphed in figure 4.3.3 for $G = 1.0, m = 1.0, \rho = 1.0$ and $L = 1.0$. Note that the contours are becoming more parallel as y becomes more negative. For a plate of unit length and density $\rho_B = 3\rho$, we find $V = 0.116G/\rho$.

The pressure impulse on the plate is given by

$$P(x, 0) = \frac{mG}{m + \frac{1}{2}L^2\pi\rho}\sqrt{L^2 - x^2}$$

with a maximum, at the centre ($x = 0$), of $mLG/(m + \frac{1}{2}L^2\pi\rho)$.

4.4 Conformal Mapping

Another way of finding the velocity at which a body will move is to represent it with a conformal map from the flat plate. Then we can further study the change in P due to a change in the shape of B. The solution for P below a flat plate, (4.3.8), in the

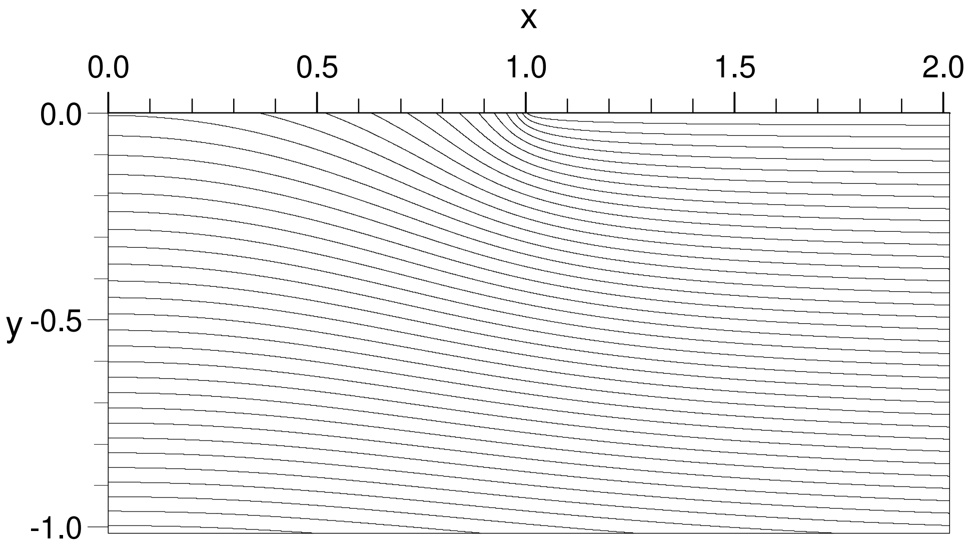

Figure 4.3.3: Pressure impulse contours below a flat plate $x \in [-L, L], y = 0$. In this case $G = m = L = \rho = 1.0$ and the contour separation is $0.03GL$. We show only half the domain since P is symmetric about $x = 0$. Note that $|\nabla P|$ is singular at $|x| = L$, corresponding to spray roots.

z plane, is mapped to the region around a body B' in a complex w plane (which is different to the w plane in Chapter 3). We write $w = u + iv$ and require that the conformal map, $w(z)$, has $w \sim z$ as $|z| \to \infty$ and also that the free surface in the z plane is mapped to the free surface in the w plane. The inverse of $w(z)$ is $z(w)$. Again, the solution is a sum of two pressure impulses: the same pressure impulse proportional to the depth below the free surface, $v = \Im\{w\}$, and a second pressure impulse, proportional to the effective pressure impulse gradient for a moving body, $G - \rho V$, which has $\partial P/\partial n = 0$ on the body so that we conformally map P around the flat plate, $\Re\{\sqrt{L^2 - z^2}\}$ to P around B'. Then (4.3.8) becomes

$$P(u, v) = (G - \rho V)\,\Re\left\{\sqrt{L^2 - z(w)^2}\right\} - \rho V v. \tag{4.4.1}$$

As in §4.3.3, V can be found by equating the momentum of B' with the impulse acting on it. Then

$$mV = I_{Vy} = \Im\left\{\int_{B'} Pi\mathrm{d}w\right\}$$

$$= \Re \int_{-L}^{L} (G - \rho V) \left[(L^2 - z(w)^2)^{1/2} \frac{\mathrm{d}w}{\mathrm{d}z} \right]_{z=x} \mathrm{d}x - \rho V \int_{w(-L)}^{w(L)} v \, \mathrm{d}u$$
$$= (G - \rho V) \, \Re \int_{-L}^{L} \sqrt{L^2 - x^2} \, \frac{\mathrm{d}w}{\mathrm{d}z}\bigg|_{z=x} \mathrm{d}x + \rho V \mathcal{V}.$$

So

$$k = \Re \int_{-L}^{L} \sqrt{L^2 - x^2} \, \frac{\mathrm{d}w}{\mathrm{d}z}\bigg|_{z=x} \mathrm{d}x \tag{4.4.2}$$

and then V and I_{Vy} are given by (4.2.4). Notice that large k implies a large velocity, V, and vertical impulse, I_{Vy}. So a body with a large value of k will move more quickly than one with the same density and area but smaller k, when subjected to the same pressure impulse gradient. As $k \to \infty$, $V \to G/\rho = V_{max}$ and $I_{Vy} \to m V_{max}$. Also, since m, $\mathcal{V}$ and k are all proportional to L^2, the velocity of the body is independent of its length scale. The same is not true of the impulse, which depends on L^2. If the body is fixed, so $V = 0$, then the impulse on it is $I_y = Gk$ as before.

To find k, rather than performing the integration in (4.4.2) explicitly, we can use a procedure analogous to that derived in §3.5.2 where Cauchy's residue theorem is applied. By writing the integrand of (4.4.2) as a Laurent series,

$$\sqrt{L^2 - x^2} \, \frac{\mathrm{d}w}{\mathrm{d}z}\bigg|_{z=x} = ix + a_0 + \frac{a_1}{x} + \frac{a_2}{x^2} + \ldots \tag{4.4.3}$$

we find that

$$k = -\pi \Im\{a_1\}. \tag{4.4.4}$$

This is generally much easier and quicker than evaluating (4.4.2).

With the concept of added mass, as in (3.5.15), we have

$$k = \frac{M_y}{\rho} + \mathcal{V} = \frac{1}{\rho} \left(M_y + M \right). \tag{4.4.5}$$

and the general expressions for the velocity and vertical impulse, (4.2.4), are then

$$V = \frac{G}{\rho} \left(\frac{M + M_y}{m + M_y} \right) \quad \text{and} \quad I_{Vy} = \frac{mG}{\rho} \left(\frac{M + M_y}{m + M_y} \right) \tag{4.4.6}$$

where $M = \rho \mathcal{V}$ is the mass of fluid displaced by the body and M_y is the added mass for vertical motion of a body half immersed in fluid. M_y will generally be different to the added mass for horizontal translation, M_x, used in Chapter 3, except for those shapes with two axes of symmetry discussed above. These results will remain true even if the body is asymmetric or three-dimensional.

Drawing on the vast literature on conformal maps (for instance Kober 1957) enables the pressure impulses on many other shapes to be calculated. All the following results are exact, mapping the real line $[-L, L]$ to a new surface-piercing object which is free to move. As in Chapter 3, we present several different calculations to enable, for instance, a coastal engineer to make a comparison between the velocity at which different bodies will move. In particular, the effect of a body having abrupt corners, as opposed to a smooth gradient around the boundary, is interesting.

Firstly, we use the conformal map from the flat plate to a circle to find the pressure impulse distribution around it, and the impulse on it, as we did for a circle on the sea bed in §3.6.3. It is not possible to find the pressure impulse around a triangular wedge beneath the free surface because this requires the inverse of the conformal map, which we cannot calculate. However we can find the impulse on this shape, which we demonstrate in §4.4.2. We do the same for a trapezoidal 'blunt' wedge; both of these can be thought of as idealisations of the keel shape of a boat. We then find the value of k for an inclined plate below the free surface, which is asymmetric. We can find the impulse for a plate inclined at any angle, but can only find P in some special cases.

4.4.1 Circle

Consider the cross-section of a cylindrical pipe just below the surface. We model this as a circle, the top of which touches the real axis at the origin, using the map

$$w = \frac{L}{\coth^{-1}(z/L)} \tag{4.4.7}$$

which has $w \sim z$ as $|z| \to \infty$. The circle has radius L/π and $\mathcal{V} = L^2/\pi$. (It would be preferable to use $w = L\pi/\coth^{-1}(z/L)$, which maps to a circle of radius L, but this map doesn't have $w \sim z$ as $|z| \to \infty$; similarly $w = L\pi/\coth^{-1}(z/L\pi)$ doesn't have the pre-image $x \in [-L, L]$.) The corresponding value of k is given by (4.4.2):

$$k = -\int_{-L}^{L} \frac{\sqrt{L^2 - x^2}}{\left[\coth^{-1}(x/L)\right]^2 \left((x/L)^2 - 1\right)}\,\mathrm{d}x \tag{4.4.8}$$

$$= -L^2 \int_{-1}^{1} \frac{\mathrm{d}x}{[\coth^{-1}(x)]^2 \sqrt{1 - x^2}}$$

$$= \frac{1}{6}\pi L^2 \tag{4.4.9}$$

where Cauchy's residue theorem is used to evaluate the integral - see Appendix I for the details. Alternatively, the Laurent series for the integrand of (4.4.8) is

$$\begin{aligned}
\frac{-\sqrt{L^2 - x^2}}{\left[\coth^{-1}(x/L)\right]^2 \left((x/L)^2 - 1\right)} &\sim \frac{L^2 i \left(x^2 - L^2\right)^{-\frac{1}{2}}}{\left(L/x + \frac{1}{3}(L/x)^3 + O(x^{-4})\right)^2} \\
&\sim ix\left(1 + \frac{1}{2}\left(\frac{L}{x}\right)^2 + O(x^{-4})\right)\left(1 - \frac{2}{3}\left(\frac{L}{x}\right)^2 + O(x^{-4})\right) \\
&\sim ix - \frac{iL^2}{6x} + O(x^{-3})
\end{aligned}$$

so applying (4.4.4) gives the same result, but more easily.

The value of k for a circle of radius a ($= L/\pi$) is $k = \frac{1}{6}\pi^3 a^2$. The added mass of a cylinder in heave motion below the free surface is $M_y = (\pi^2/6 - 1)\rho\pi a^2$ (Greenhow and Yanbao 1987, eq.13), so (4.4.5) confirms this value of k. Then, since we know the mass of the cylinder to be $\pi a^2 \rho_B$,

$$V = \frac{\frac{1}{6}\pi^3 G a^2}{\pi a^2 \rho_B + (\frac{1}{6}\pi^3 a^2 - \pi a^2)\rho} = \frac{\frac{1}{6}\pi^2 G}{\rho_B + (\frac{1}{6}\pi^2 - 1)\rho} \tag{4.4.10}$$

and

$$I_{Vy} = \frac{\frac{1}{6}\pi^3 a^2 G}{1 + (\frac{1}{6}\pi^2 - 1)\rho/\rho_B}.$$

By the symmetry exhibited in figure 4.3.1, we see that this is equivalent to the case of two semicircular cylinders lying next to each other on the sea bed. Then the horizontal impulse on this fixed object is $I_x = \frac{1}{6}\pi^3 G a^2$. The horizontal impulse per unit area is $I_x/\mathcal{V} = \frac{1}{6}\pi^2 G$ which is less than $I_x/\mathcal{V} = 2G$ for an isolated semicircular cylinder. So the effect of concatenating two semicircular cylinders is to reduce the

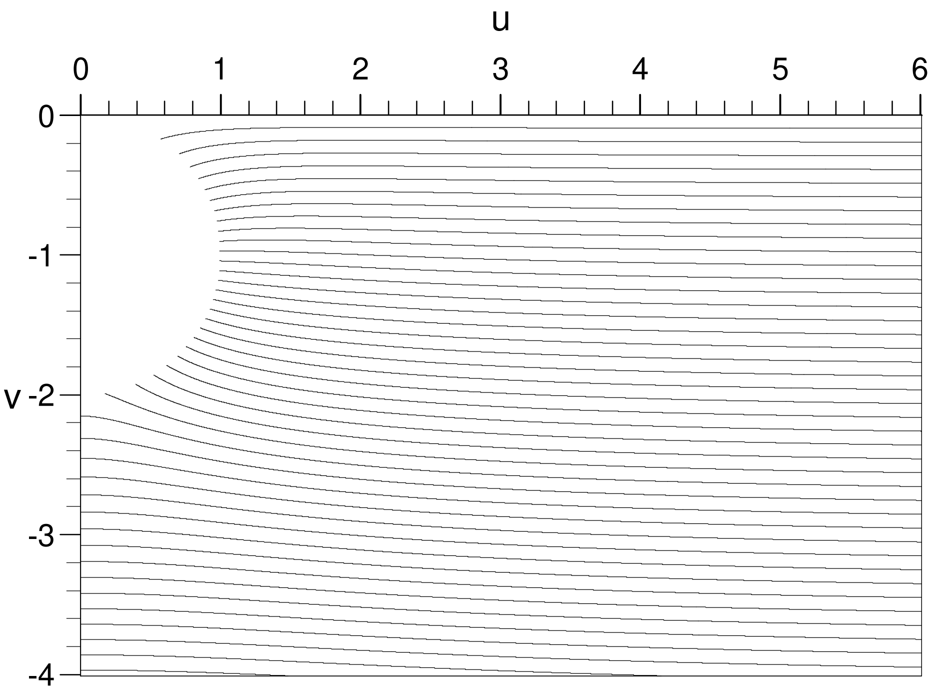

Figure 4.4.1: Pressure impulse contours around a circle of unit radius. In this case $G = a = \rho = 1.0, \rho_B = 3.0, L = \pi$ and the contour separation is $0.1Ga$. Only the right-hand half of the domain is shown and FORTRAN NAG routine S01EAF for the complex exponential function is used to calculate $\coth(L/w)$. As ρ_B decreases, the contours become straighter. Note the region around the point of contact with the surface where there are very low flow speeds.

horizontal impulse per unit area on them, and presumably with more cylinders it would decrease further, since this decreases the aspect ratio.

The contours of pressure impulse around a circle of unit radius and density $\rho_B = 3\rho$ are shown in figure 4.4.1, using the inverse of (4.4.7), $z = L\coth(L/w)$, in (4.4.1). The velocity of this circle is, by (4.4.10),

$$V = \frac{\frac{1}{6}\pi^2}{3 + \frac{1}{6}\pi^2 - 1}\frac{G}{\rho} = 0.451\frac{G}{\rho} \tag{4.4.11}$$

and the vertical impulse on it is $I_{Vy} = 4.253G$. A circle of radius $1/\sqrt{\pi} \approx 0.564$ has unit area, the same velocity, and vertical impulse

$$I_{Vy} = \frac{\frac{1}{6}\pi^2 G}{1 + (\frac{1}{6}\pi^2 - 1)\rho/\rho_B} = 1.354G.$$

These impulses differ, of course, by a factor of $a^2 = 1/\pi$.

4.4.2 Wedge

The effect of wave impact near a wedge with a vertical axis of symmetry can be examined using the Schwarz-Christoffel conformal mapping theorem to construct the transformation:

$$\frac{\mathrm{d}w}{\mathrm{d}z} = \frac{z^{2\theta/\pi}}{(z^2 - L^2)^{\theta/\pi}} \tag{4.4.12}$$

where θ is the internal angle between the side of the wedge and the line $v = 0$. The wedge is symmetrical about the line $u = 0$. Consider figure 4.4.3 with $\alpha' = 0$ to visualise the wedge. Note that $\mathrm{d}w/\mathrm{d}z \to 1$ as $|z| \to \infty$, so that $z \sim w$ as $|z| \to \infty$. We define $\sigma = \theta/\pi \leq \frac{1}{2}$ and then $\phi = \frac{1}{2}\pi - \theta$ to be the half-angle in the apex of the wedge. The half-width of the wedge (on $v = 0$) is

$$\alpha = \frac{L}{2}B\left(\frac{1}{2} + \sigma, 1 - \sigma\right)\cos\theta,$$

and $B(x, y)$ is Euler's beta function (Abramowitz and Stegun 1965, §6). The maximum depth of the submerged part of the wedge (at $u = 0$) is $\beta = \alpha\tan\theta$. Figure

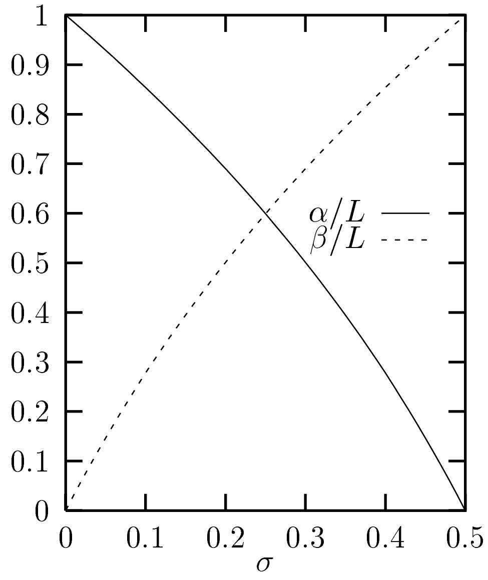

Figure 4.4.2: The half-width, α/L, and the depth, β/L, of the wedge plotted against $\sigma = \theta/\pi$. When $\sigma = 0.25$, $\alpha = \beta = 0.599L$ and when $\sigma = \tan^{-1}(2)/\pi = 0.352$, $\beta = 2\alpha = 0.778L$, and the wedge has its total width at the surface equal to its depth.

4.4.2 shows α/L and β/L plotted against σ. Then we can write

$$L = \frac{2\alpha \sec\theta}{B\left(\frac{1}{2}+\sigma, 1-\sigma\right)} = \frac{2\alpha \csc\phi}{B\left(\frac{1}{2}+\sigma, 1-\sigma\right)} = \frac{2\sqrt{\alpha^2+\beta^2}}{B\left(\frac{1}{2}+\sigma, 1-\sigma\right)}. \tag{4.4.13}$$

Note that $\sqrt{\alpha^2+\beta^2}$ is the length of the hypotenuse of the wedge.

The conformal map is given in the form of a differential, making the equation for k easy to write down:

$$\begin{aligned} k &= \int_{-L}^{L} \sqrt{L^2-x^2}\frac{x^{2\sigma}}{(x^2-L^2)^\sigma}\,\mathrm{d}x & (4.4.14)\\ &= (-1)^{-\sigma}L^2\int_{-1}^{1} x^{2\sigma}(1-x^2)^{(1/2-\sigma)}\,\mathrm{d}x \\ &= \left[(-1)^{-\sigma}+(-1)^{\sigma}\right]L^2\int_0^1 x^{2\sigma}(1-x^2)^{(1/2-\sigma)}\,\mathrm{d}x \\ &= \cos(\sigma\pi)L^2 B\left(\sigma+\frac{1}{2}, \frac{3}{2}-\sigma\right) \\ &= L^2\pi\left(\frac{1}{2}-\sigma\right) & (4.4.15) \end{aligned}$$

$$= \phi L^2 \tag{4.4.16}$$

using the results of Abramowitz and Stegun (1965, §6). More straightforwardly,

$$\begin{aligned}\sqrt{L^2 - x^2}\frac{x^{2\sigma}}{(x^2 - L^2)^\sigma} &= ix^{2\sigma}\left(x^2 - L^2\right)^{\frac{1}{2}-\sigma} \\ &\sim ix\left(1 - \left(\frac{1}{2} - \sigma\right)\left(\frac{L}{x}\right)^2 + O(x^{-4})\right)\end{aligned}$$

so (4.4.4) provides confirmation of (4.4.15).

The area of the wedge can be written $\mathcal{V} = \alpha^2 \cot\phi$ so that

$$V = \frac{\phi G L^2}{m + (\phi L^2 - \alpha^2 \cot\phi)\,\rho} \tag{4.4.17}$$

and $I_{Vy} = mV$ as usual. The added mass of the wedge, by (4.4.5), is

$$M_y = \rho\left(\phi L^2 - \alpha^2 \cot\phi\right) = \rho\left(\frac{4\phi\left(\alpha^2 + \beta^2\right)}{\left(B\left(\frac{1}{2} + \sigma, 1 - \sigma\right)\right)^2} - \alpha^2 \cot\phi\right)$$

(see also Wagner 1932). We are unable to calculate the pressure impulse around the wedge because the conformal map in (4.4.12) is not, in general, invertible.

Examples

When $\sigma = 0$ we confirm the result for the flat plate. When $\sigma = \frac{1}{2}$ we see that a vertical spike experiences no movement. As a non-trivial example we choose $\sigma = \frac{1}{4}$, corresponding to a wedge with a right-angled apex. Then $\alpha = \beta = 0.599L$ and $k = \frac{1}{4}\pi L^2$. Putting $L = 1/0.599 = 1.669$ gives a right-angled triangle of unit half-width and unit depth ($\alpha = \beta = 1$) for which $k = 0.697\pi = 2.189$. Then

$$V = \frac{2.189G}{m + 1.189\rho}.$$

Assuming that this wedge of unit area doesn't project out of the fluid, and that $\rho_B = 3\rho$, gives $m = 3\rho$ and therefore $V = 0.523G/\rho$. The vertical impulse is then $I_{Vy} = 1.568G$.

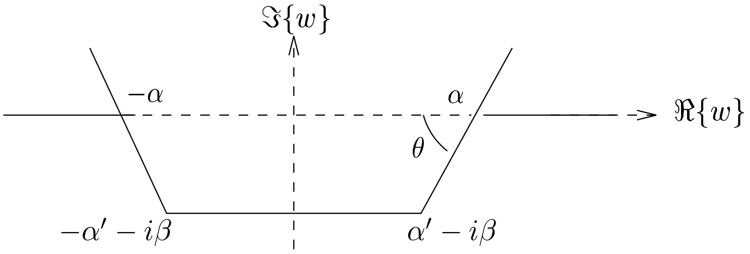

Figure 4.4.3: Illustrating the nature of the blunt wedge. The internal angle is θ and the length of the body along the free surface is 2α. The width of the blunt 'nose' is $2\alpha'$ and the depth is β. When $\alpha' = 0$ this represents the wedge of §4.4.2.

For a wedge of total width 1 and depth 2 ($\alpha = \frac{1}{2}$, $\beta = 2$) we take $\theta = \tan^{-1} 4$ so $\phi = 14.0°$, $\sigma = 0.422$, $\beta = 4\alpha = 0.887L$ and $k = 0.078\pi L^2$. Putting $L = 1/0.887 = 1.127$ gives $k = 0.311$ for this wedge of unit area. Thus

$$V = \frac{0.311G}{m - 0.689\rho}.$$

With the same assumptions as above, we get $V = 0.135G/\rho$ and $I_{Vy} = 0.404G$. For given G and ρ, comparison of these two shapes shows that for constant area (and mass) the wider triangle receives a significantly greater impulse and moves at a higher velocity.

4.4.3 Blunt Wedge

We can use the Schwarz-Christoffel conformal mapping theorem to provide a map from the flat plate on the free surface to a trapeze piercing the free surface. We define $\sigma = \theta/\pi$ where $0 \leq \sigma < \frac{1}{2}$ and θ is the angle that the side of the trapeze makes with the free surface (see figure 4.4.3). As for the rectangle in §3.6.7, we use a parameter $0 \leq \lambda \leq L$ to define the conformal map. Then

$$\frac{\mathrm{d}w}{\mathrm{d}z} = \left(\frac{z^2 - \lambda^2}{z^2 - L^2}\right)^{\sigma}. \tag{4.4.18}$$

Note that again $\mathrm{d}w/\mathrm{d}z \sim 1$ as $z \to \infty$. We put $\lambda' = \lambda/L$ and denote the half-width of this blunt wedge at the surface by α. The wedge is submerged to a depth β and the horizontal ‘nose’ has half-width α', as illustrated in figure 4.4.3. Then $\alpha = \alpha' + \beta \cot\theta$, but from the conformal map we have that

$$\begin{aligned}
\alpha &= \Re \int_0^L \left(\frac{x^2-\lambda^2}{x^2-L^2}\right)^{\sigma} \mathrm{d}x = L\Re \int_0^1 \left(\frac{x^2-\lambda'^2}{x^2-1}\right)^{\sigma} \mathrm{d}x \\
\Rightarrow \alpha/L &= \int_0^{\lambda'} \left(\frac{\lambda'^2-x^2}{1-x^2}\right)^{\sigma} \mathrm{d}x + \cos\theta \int_{\lambda'}^1 \left(\frac{x^2-\lambda'^2}{1-x^2}\right)^{\sigma} \mathrm{d}x \\
&= \frac{\lambda'^{1+2\sigma}}{2} B\left(\frac{1}{2}, 1+\sigma\right) {}_2F_1\left(\frac{1}{2}, \sigma; \frac{3}{2}+\sigma; \lambda'^2\right) + \\
&\qquad \cot\theta\, \frac{\theta}{2}\left(1-\lambda'^2\right) {}_2F_1\left(\frac{1}{2}, 1-\sigma; 2; 1-\lambda'^2\right)
\end{aligned}$$

where ${}_2F_1$ is the hypergeometric function, using Gradshteyn and Ryzhik (1965, eq.3.197.3) and Abramowitz and Stegun (1965, eq.15.3.4 & 6.1.31). We then see that

$$\begin{aligned}
\beta/L &= \frac{\theta}{2}(1-\lambda'^2)\, {}_2F_1\left(\frac{1}{2}, 1-\sigma; 2; 1-\lambda'^2\right) \\
\text{and } \alpha'/L &= \frac{\lambda'^{1+2\sigma}}{2} B\left(\frac{1}{2}, 1+\sigma\right) {}_2F_1\left(\frac{1}{2}, \sigma; \frac{3}{2}+\sigma; \lambda'^2\right).
\end{aligned}$$

The area of the blunt wedge is

$$\mathcal{V} = 2\alpha'\beta + \beta^2\cot\theta = 2\alpha\beta - \beta^2\cot\theta$$

and the lengths of the sides, as functions of λ', are shown in figure 4.4.4, in the case $\sigma = 0.25$. Note that $\sigma < \frac{1}{2} \Rightarrow \alpha' < \alpha$.

The value of k is calculated by applying (4.4.2) to (4.4.18),

$$\begin{aligned}
k &= \Re \int_{-L}^{L} \sqrt{L^2-x^2} \left(\frac{x^2-\lambda^2}{x^2-L^2}\right)^{\sigma} \mathrm{d}x \\
&= 2L^2 \left[\int_0^{\lambda'} (1-x^2)^{1/2-\sigma}(\lambda'^2-x^2)^{\sigma}\mathrm{d}x + \cos(\sigma\pi)\int_{\lambda'}^1 (1-x^2)^{1/2-\sigma}(x^2-\lambda'^2)^{\sigma}\mathrm{d}x\right] \\
&= L^2 \left[\lambda'^{1+2\sigma} B\left(\frac{1}{2}, 1+\sigma\right) {}_2F_1\left(\sigma-\frac{1}{2}, \frac{1}{2}; \frac{3}{2}+\sigma; \lambda'^2\right) + \right. \\
&\qquad \left. \cos(\sigma\pi)\left(1-\lambda'^2\right)^{\frac{3}{2}} B\left(\frac{3}{2}-\sigma, 1+\sigma\right) {}_2F_1\left(\frac{1}{2}, \frac{3}{2}-\sigma; \frac{5}{2}; 1-\lambda'^2\right)\right]. \qquad (4.4.19)
\end{aligned}$$

However, using a Laurent expansion for the integrand gives

$$\sqrt{L^2-x^2}\left(\frac{x^2-\lambda^2}{x^2-L^2}\right)^{\sigma} = i\left(x^2-L^2\right)^{\frac{1}{2}-\sigma}\left(x^2-\lambda^2\right)^{\sigma}$$

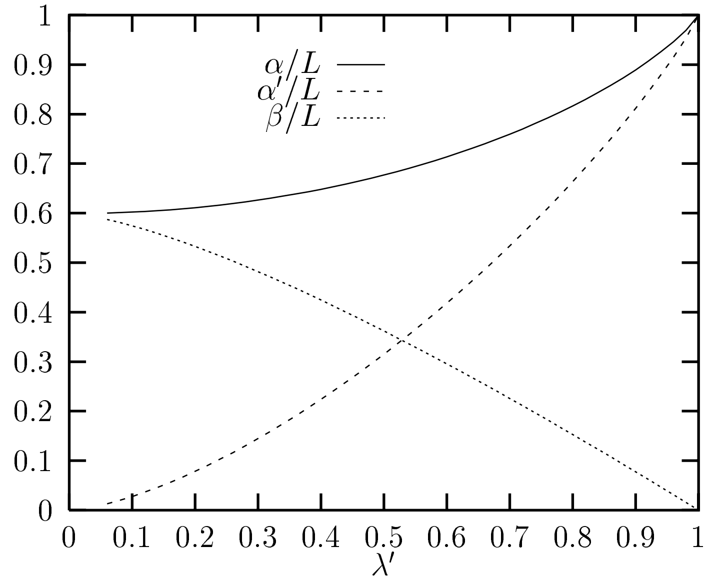

Figure 4.4.4: A graph showing the half-width and depth of the wedge, α/L and β/L, and the half-width of the submerged 'nose', α'/L, against λ' in the case $\sigma = 0.25$. Other values of σ give similar results.

$$\begin{aligned}
&\sim ix\left(1-\left(\frac{1}{2}-\sigma\right)\left(\frac{L}{x}\right)^2-\sigma\left(\frac{\lambda}{x}\right)^2+O(x^{-4})\right)\\
&\sim ix-\frac{i}{x}\left(\left(\frac{1}{2}-\sigma\right)L^2+\sigma\lambda^2\right)+O(x^{-3})
\end{aligned}$$

so, by (4.4.4), we find

$$k=\pi\left(\frac{1}{2}L^2-\sigma\left(L^2-\lambda^2\right)\right)=\frac{\pi}{2}L^2-\theta\left(L^2-\lambda^2\right). \tag{4.4.20}$$

Equations (4.4.19) and (4.4.20) are numerically equivalent for all σ, λ and L. This demonstrates that it is relatively easy to find k, but often considerably harder to find the lengths of the sides of the body and therefore its area. For this blunt wedge, the area is $\mathcal{V} = 2\alpha\beta - \beta^2 \cot\theta$ so the added mass is

$$M_y=\rho\left(\frac{1}{2}\pi L^2-\theta\left(L^2-\lambda^2\right)-2\alpha\beta+\beta^2\cot\theta\right)$$

and thus

$$V=\frac{G\left(\frac{1}{2}\pi L^2-\theta\left(L^2-\lambda^2\right)\right)}{m+\rho\left(\frac{1}{2}\pi L^2-\theta\left(L^2-\lambda^2\right)-2\alpha\beta+\beta^2\cot\theta\right)}$$

and the impulse is mV.

We note that the map reduces to the identity map when either $\sigma = 0$ or $\lambda = L$. If $\sigma = \frac{1}{2}$ we obtain a rectangle which should be compared with the rectangle in §4.3: using the conformal map from the flat plate on the surface we have now generated the 'complement' of the rectangle generated with a conformal map from the flat sea floor and rotated by 90° to pierce the free surface. That is, we identify the width of this new rectangle with the depth of the one in §4.3 and vice versa. The value of k, which was previously $\frac{1}{2}\pi(L^2 - \lambda^2)$, becomes $k = \frac{1}{2}\pi\lambda^2$.

If $\lambda = 0$ we revert to the case of the wedge in §4.4.2 whence comparing (4.4.19) with (4.4.15) implies that

$$B\left(\sigma + \frac{1}{2}, \frac{3}{2} - \sigma\right) = B\left(\sigma + 1, \frac{3}{2} - \sigma\right) {}_2F_1\left(\frac{1}{2}, \frac{3}{2} - \sigma; \frac{5}{2}; 1\right)$$

which appears to be a non-trivial identity.

For example, if $\theta = \pi/4$ and if we choose $\lambda = 0.529L$ (from figure 4.4.4) then $\sigma = \frac{1}{4}$, $\alpha = 0.686L$ and $\beta = \alpha' = \frac{1}{2}\alpha = 0.343L$. The value of k for this blunt wedge with $\mathcal{V} = 2\alpha\beta - \beta^2 = 0.353L^2$ is $k = 1.005L^2$. We put $L = 1/0.343 = 2.915$ then this body has surface half-width 2, depth and submerged half-width 1, $\mathcal{V} = 3$, $k = 8.542$ and the impulse on it is

$$I_{Vy} = \frac{8.542mG}{m + 5.542\rho}. \tag{4.4.21}$$

If we assume that the body doesn't project out of the fluid and that $\rho_B = 3\rho$ then we can calculate the mass to give $I_{Vy} = 5.287G$. Comparing this with the impulse on a wedge of surface half-width 2 and depth 1.5, so that $\mathcal{V} = 3$, which is $I_{Vy} = 3G$, shows that the change of shape from a wedge to a blunt wedge increases the impulses. This is due to the flat submerged surface which, like the flat plate, presents a larger horizontal cross-section for the fluid to act on.

4.4.4 Inclined Plate

A relatively simple example of an asymmetric body projecting below the free surface is a plate inclined at an angle $\alpha = \beta\pi$ to the positive x-axis, $\beta \in [0, 1]$. We use the conformal map (3.6.8):

$$w(z) = (z-L)^{\beta}\left(L + \frac{\beta z}{1-\beta}\right)^{1-\beta}$$

which maps the interval $x \in [L(\beta-1)/\beta, L]$ to a plate of length L. The map must be adapted so that it takes the flat plate, $x \in [-L, L]$, to an inclined plate, whilst preserving its conformality. We first scale the interval over which it takes x values to be of length $2L$:

$$w(z) = \left(\frac{z}{2\beta} - L\right)^{\beta}\left(L + \frac{z}{2(1-\beta)}\right)^{1-\beta}$$

and then shift this so as to take values $x \in [-L, L]$:

$$w(z) = \frac{1}{2\beta^{\beta}(1-\beta)^{1-\beta}}\,(z-L)^{\beta}\,(z+L)^{1-\beta}\,. \tag{4.4.22}$$

It can be shown that with the map in this form, the results of §3.6.4 are duplicated. As $|z| \to \infty$, we have $w \sim dz$ where $d = 1/2\beta^{\beta}(1-\beta)^{1-\beta}$, so that the earlier results for finding P and V are not immediately applicable.

To find a value of k for this body, we expand the derivative of (4.4.22) as a Laurent series. Then for large z,

$$\begin{aligned}
\frac{\mathrm{d}w}{\mathrm{d}z} &= d\beta\left(\frac{z+L}{z-L}\right)^{1-\beta} + d(1-\beta)\left(\frac{z-L}{z+L}\right)^{\beta} \\
&= d\left(\frac{z-L}{z+L}\right)^{\beta}\frac{z+(2\beta-1)L}{z-L} \\
&= \frac{d(z+(2\beta-1)L)}{(z+L)^{\beta}(z-L)^{1-\beta}} \\
&= d\left(1-(1-2\beta)\left(\frac{L}{z}\right)\right)\left(1+\frac{L}{z}\right)^{-\beta}\left(1-\frac{L}{z}\right)^{\beta-1} \\
&\sim d\left(1-(1-2\beta)\left(\frac{L}{z}\right)\right)\left(1-\beta\left(\frac{L}{z}\right)+\frac{\beta(\beta+1)}{2}\left(\frac{L}{z}\right)^{2}+O(z^{-3})\right)\times \\
&\qquad\qquad \left(1+(1-\beta)\left(\frac{L}{z}\right)+\frac{(\beta-1)(\beta-2)}{2}\left(\frac{L}{z}\right)^{2}+O(z^{-3})\right) \\
&\sim d\left(1+2\beta(1-\beta)\left(\frac{L}{z}\right)^{2}+O(z^{-3})\right).
\end{aligned}$$

The coefficient of x^{-2} in $\sqrt{L^2-x^2}\,\mathrm{d}w/\mathrm{d}z|_{z=x}$ is then $a_1 = id(2\beta(1-\beta)-\frac{1}{2})L^2$. We wish to apply (4.4.4), but now $w \sim dz$ as $|w| \to \infty$, for $d \neq 1$, so that, as in Chapter 3, (4.4.4) becomes

$$k = -\pi \Im\{da_1\}. \tag{4.4.23}$$

Then for the inclined plate we have

$$k = d^2\left(\frac{1}{2}-2\beta(1-\beta)\right)\pi L^2 = \frac{(1-2\beta)^2}{8\beta^{2\beta}(1-\beta)^{2(1-\beta)}}\pi L^2. \tag{4.4.24}$$

The volume of the inclined plate is zero, $\mathcal{V}=0$, so then (4.2.4) gives

$$V = \frac{\frac{1}{2}\pi G d^2(1-2\beta)^2L^2}{m+\frac{1}{2}\pi\rho d^2(1-2\beta)^2L^2}. \tag{4.4.25}$$

When $\beta = \frac{1}{2}$, corresponding to a vertical plate, $k=0$ (its minimum), confirming that this body experiences no vertical impulse or velocity. When $\beta = 0$ or 1, which represents a horizontal plate of length L, we find $k = \frac{1}{8}\pi L^2$ (its maximum). This agrees with the value of k for a flat plate of length L in §4.3.3, by putting $L = L/2$. In these cases we can invert the conformal map, (4.4.22) to give $z = 2w \mp L$ for $\beta = 0, 1$ respectively and

$$V = \frac{\frac{1}{8}\pi G L^2}{m+\frac{1}{8}\pi\rho L^2}.$$

The pressure impulse is then given by (4.4.1) with a factor of $d=\frac{1}{2}$ in the first term (compare (4.3.2)),

$$\begin{aligned} P(u,v) &= (G-\rho V)\, d\Re\left\{\sqrt{L^2-(2w\mp L)^2}\right\} - \rho V v \\ &= \frac{G}{m+\frac{1}{8}\pi\rho L^2}\left(m\Re\left\{\sqrt{\pm wL - w^2}\right\} - \frac{1}{8}\pi\rho L^2 v\right), \end{aligned}$$

which is directly comparable to the expression for P beneath a plate of length $2L$, (4.3.10), with the factor $\frac{1}{2}$ replaced by $\frac{1}{8}$, due to the change in length of the plate. These contours of pressure impulse are shown, in the case $\beta = 0$, in figure 4.4.5.

However, when the vane is neither horizontal or vertical, we might expect a horizontal component of impulse, pushing the plate to one side. Performing the integration in (4.4.2), but not taking the real part gives

$$k = \frac{1}{2}\pi d^2\left(1-2\beta\right)^2 L^2\left(1+i\tan\alpha\right) \tag{4.4.26}$$

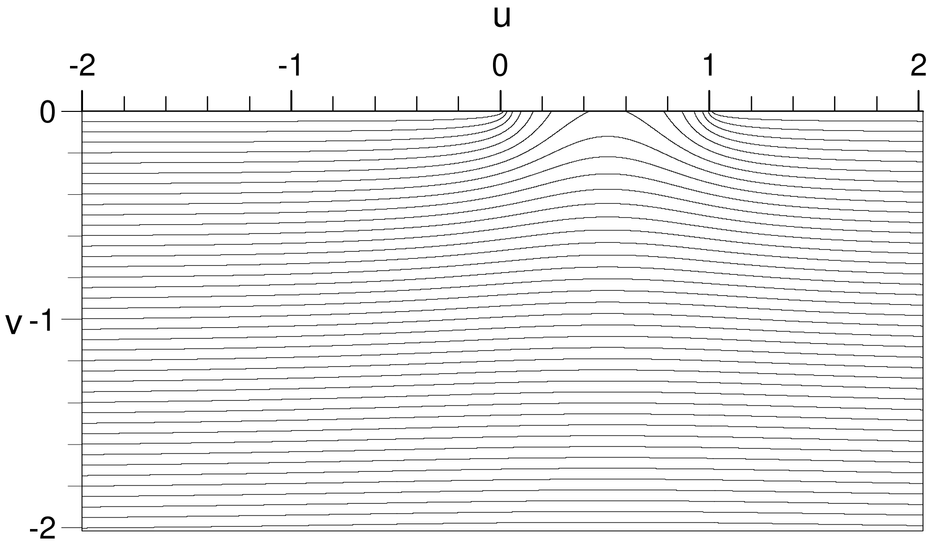

Figure 4.4.5: Pressure impulse contours below a flat plate $x \in [0, L], y = 0$ using the conformal map for an inclined plate with $\beta = 0$. In this case $G = m = L = \rho = 1.0$ and the contour separation is $0.05GL$. This figure should be compared with figure 4.3.3 for a plate of length $2L$ - the two are very similar, with the axis of symmetry at the centre of the plate and $|\nabla P|$ singular at the ends. Reflecting the contours in $x = 0$ gives the contours for the case $\beta = 1$, when the plate is $x \in [-L, 0]$.

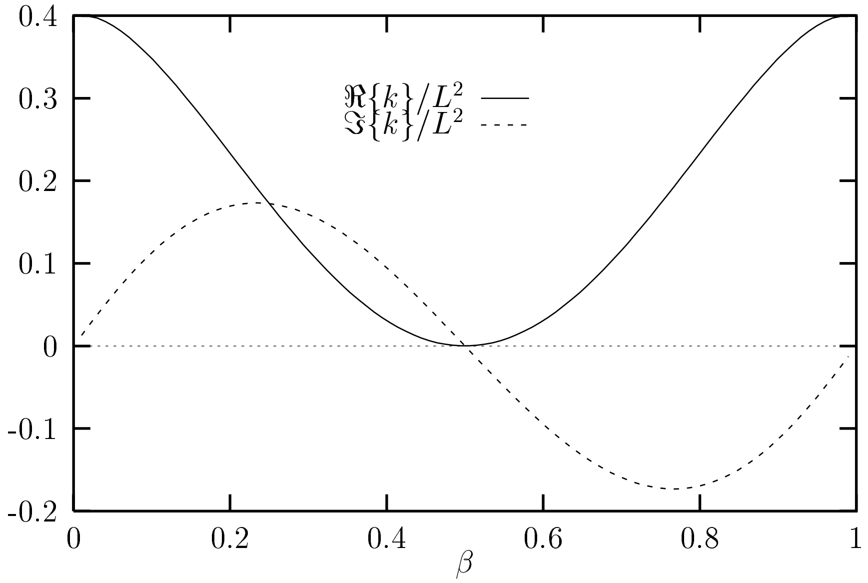

Figure 4.4.6: A graph of the real and imaginary parts of k/L^2 against β for an inclined plate of length L inclined at an angle $\alpha = \beta\pi$ below the positive x-axis. $\Re\{k\}$, corresponding to a vertical impulse, has its minimum at $\beta = 0.5$ when the plate is vertical and experiences no lift. The maxima of $\Re\{k\}$ occur when the plate lies flat along the axis, $\beta = 0$ or 1, where $\Re\{k\}/L^2 = \pi/8$. The imaginary part of k, corresponding to the horizontal impulse on the plate, is zero when the plate is either horizontal or vertical. If the plate leans to the left ($\beta > 0.5$) then $\Im\{k\}$ is equal in magnitude and opposite in sign to the value for a plate inclined at the complementary angle, $1 - \beta$.

where we have used Abramowitz and Stegun (1965, eq.6.1.30) and Gradshteyn and Ryzhik (1965, eq.3.196.3) in much the same way as for the calculation in (3.6.10). Indeed, the form of the result is very similar to that result for a plate inclined at an angle α to the horizontal sea bed. The real part of (4.4.26) is in agreement with (4.4.24) and the real and imaginary parts of k are shown in figure 4.4.6. When $\beta < 0.5$, the imaginary part of k is positive, which relates to a horizontal impulse in the positive x direction, and when $\beta > 0.5$ and the vane leans to the left, this impulse is in the negative x direction. The maximum value of $\Im\{k\}$ occurs when $\beta = 0.25$, i.e. $\alpha = 45°$.

In terms of added masses, we have $M_y + iM_x = \rho k$, since $\mathcal{V} = 0$. Note then that

$M_x = M_y \tan\alpha$, which should be compared with the similar relationship, (3.6.11), found for the inclined plate on the sea bed, although the values are generally different.

So the pressure impulse gradient in the y direction at infinity, G, gives rise to movement of this asymmetric shape in the x direction, perpendicular to G. This is qualitatively similar to the results for a body on the sea floor. The horizontal component of velocity, U, is

$$U = \frac{\frac{1}{2}\pi G d^2(1-2\beta)^2 \tan\alpha L^2}{m + \frac{1}{2}\pi\rho\, d^2(1-2\beta)^2 \tan\alpha L^2}$$

which should be compared with the vertical velocity V in (4.4.25).

4.5 Horizontal Circular Disc

In an attempt to find some truly three-dimensional solutions, we calculate the pressure impulse around and beneath a flat, horizontal, circular disc, which exhibits axisymmetry. The disc has radius a, is free to move, and rests initially on the fluid free surface. We assume that the pressure impulse field calculated in Chapter 2 is uniform in a direction parallel to the wall. Following Fabrikant (1991, p87), but see also Batchelor (1973, §6.10), we use cylindrical polar coordinates (r, θ, y) to solve the system

- $\nabla^2 P = 0$ for $y \leq 0$
- $P \sim -Gy$ as $y \to -\infty$ or $r \to \infty$
- $P = 0$ on $r > a, y = 0$
- $\frac{\partial P}{\partial y} = -\rho V$ on $r \leq a, y = 0$.

(4.5.1)

Then

$$P(r, y) = -Gy + \frac{2}{\pi}(G - \rho V)\left(\sqrt{a^2 - l_-^2} + y \sin^{-1}\left(\frac{a}{l_+}\right)\right) \tag{4.5.2}$$

where

$$l_\pm = \frac{1}{2}\left\{\left[(r+a)^2 + y^2\right]^{\frac{1}{2}} \pm \left[(r-a)^2 + y^2\right]^{\frac{1}{2}}\right\}.$$

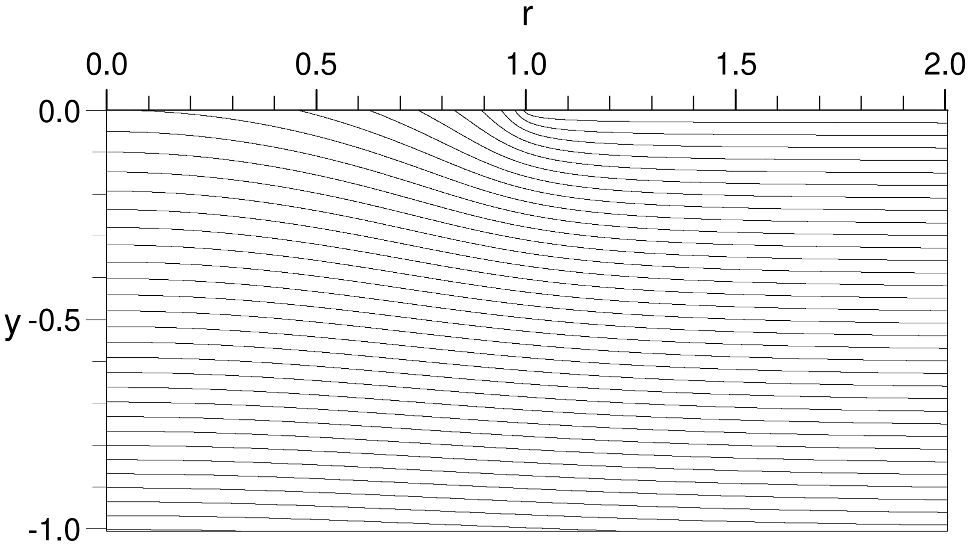

Figure 4.5.1: Pressure impulse contours below a flat horizontal disc, $r \in [0, a], y = 0$. In this case $G = m = a = \rho = 1.0$ and the contour separation is $0.03Ga$. These contours should be compared with those in figure 4.3.3.

Equating the momentum of the disc with the impulse on it gives

$$\begin{aligned} mV = I_{Vy} &= \int_0^{2\pi} \mathrm{d}\theta \int_0^a r \left. P\right|_{y=0} \mathrm{d}r \\ &= 4(G - \rho V) \int_0^a r\sqrt{a^2 - r^2}\mathrm{d}r \\ &= \frac{4}{3}(G - \rho V)a^3 \end{aligned}$$

and then

$$V = \frac{\frac{4}{3}a^3 G}{m + \frac{4}{3}a^3\rho} \text{ and } I_{Vy} = \frac{\frac{4}{3}a^3 mG}{m + \frac{4}{3}a^3\rho}. \tag{4.5.3}$$

For a three-dimensional body, these quantities retain the same form as for a two-dimensional body, compare (4.3.9), where an increase in mass, m, reduces the speed at which the disc moves. Note that $k = mV/(G - \rho V) = \frac{4}{3}a^3$ is now proportional to the radius of the disc cubed, rather than squared as for the two-dimensional flat plate. Since the submerged volume of the disc is zero, it is again true that $k = M_y/\rho$ (Batchelor 1973, eq.6.10.7). So (4.4.5) generalises to three-dimensions. The lines of constant pressure impulse below the disc are shown in figure 4.5.1 and are very similar to the contours of P below the flat plate in figure 4.3.3.

For a disc of unit area, we have $a = 1/\sqrt{\pi}$. Then, if $\rho_B = 3\rho$, we find $V = 0.074G/\rho$, which is much less than the velocity of any of the two-dimensional bodies considered, even the flat plate. This is an effect of the three-dimensionality but is also because the disc doesn't penetrate into the fluid.

4.6 Hemisphere

For a body which, below the free surface, is a hemisphere of radius a we can still use the axisymmetry of the problem. We define spherical polar coordinates: r is radial, θ is the angle from the vertical y-axis in the (x, y)-plane and ϕ is the angle made with the positive z-axis in the horizontal (x, z)-plane. Then $x = r\sin\theta\sin\phi, y = r\cos\theta$ and $z = r\sin\theta\cos\phi$. The boundary value problem for P becomes

- $\nabla^2 P = 0$ for $r \geq a, \theta \in [\frac{\pi}{2}, \pi]$
- $P \sim -Gy$ as $y \to -\infty$ or $P \sim -Gr\cos\theta$ as $r \to \infty, \theta \in [\frac{\pi}{2}, \pi]$ (4.6.1)
- $P = 0$ on $r > a, \theta = \frac{\pi}{2}$
- $\frac{\partial P}{\partial r} = -\rho V \cos\theta$ on $r = a, \theta \in [\frac{\pi}{2}, \pi]$

all for $\phi \in [0, 2\pi]$. We find

$$P(r, \theta) = -\rho V r\cos\theta - (G - \rho V)\left(r + \frac{a^3}{2r^2}\right)\cos\theta. \tag{4.6.2}$$

Notice that, as before, the first term is like $-\rho V y$ and the second term has zero normal derivative on the surface of the hemisphere.

To find the vertical impulse on the hemisphere, we calculate the integral of the (vertical component of) pressure impulse over its surface. Then

$$\begin{aligned} mV = I_{Vy} &= \int_0^{2\pi}\int_{\pi/2}^{\pi} P|_{r=a} .a^2\sin\theta.\,(-\cos\theta)\ \mathrm{d}\theta\,\mathrm{d}\phi \\ &= \pi a^3(3G - \rho V)\int_{\pi/2}^{\pi}\cos^2\theta\ \sin\theta\,\mathrm{d}\theta \\ &= \pi a^3(G - \frac{1}{3}\rho V) \end{aligned}$$

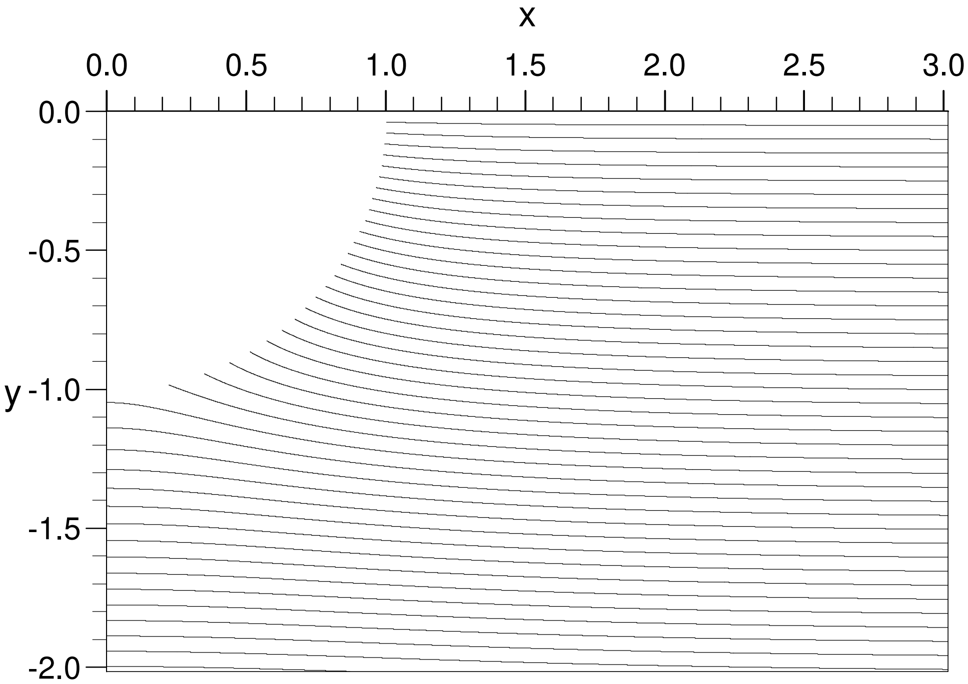

Figure 4.6.1: Pressure impulse contours below a hemisphere of radius a. In this case $G = a = \rho = 1.0$, $\rho_b = 3\rho$ and the mass is $m = \frac{2}{3}\pi a^3 \rho_B$. The contour separation is $0.05Ga$. These contours should be compared with those around a semicircle of radius a, shown in figure 4.3.2, to which they are very similar.

and

$$V = \frac{\pi a^3 G}{m + \frac{1}{3}\pi a^3 \rho} \text{ and } I_{Vy} = \frac{\pi a^3 m G}{m + \frac{1}{3}\pi a^3 \rho}$$

which is the same as for a hemisphere of mass m moving horizontally along the sea bed due to the influence of an impulsive pressure gradient G (Cooker and Peregrine 1992). The added mass coefficient for a sphere is a half, so (4.4.5) predicts that the value of k for a hemisphere is $k = \pi a^3$. Then the expressions for the velocity and impulse from (4.2.4) or (4.4.6) agree with those found above for this three-dimensional example. The pressure impulse contours around a hemisphere which has a flat top, level with the free surface, and density $\rho_B = 3\rho$ are shown in figure 4.6.1. If $a = \sqrt[3]{3/(2\pi)}$ then the hemisphere has unit volume and velocity $V = \frac{3}{7}G/\rho$ which is similar in magnitude to the velocity of a two-dimensional body with unit area.

B	Width	Depth	$\mathcal{V}$	k
Flat Plate	$2a$	0	0	$\frac{1}{2}\pi a^2$
Horizontal circular disc	$2a$	0	πa^2	$\frac{4}{3}a^3$
Semicircle	$2a$	a	$\frac{1}{2}\pi a^2$	πa^2
Circle	$2a$	$2a$	πa^2	$\frac{1}{6}\pi^3 a^2$
Rectangle	$2a$	b	$2ab$	$\frac{1}{2}\pi\lambda^2$
Wedge	$2a$	b	ab	$\tan^{-1}(a/b)L^2$
Blunt Wedge	$2a$	b	$2ab - b^2\cot\theta$	$\frac{1}{2}\pi L^2 - \theta\,(L^2 - \lambda^2)$
Hemisphere	$2a$	a	$\frac{2}{3}\pi a^3$	πa^3

Table 4.7.1: Values of width, depth, area and k for some of the shapes considered. Large k implies higher velocities, V, and vertical impulses, I_{Vy}.

4.7 Discussion

The velocity, V, at which a body, B, will move, and the vertical impulse, I_{Vy}, on it, as a function of shape, are governed by the equations

$$\begin{aligned} V &= \frac{Gk}{m + \rho(k - \mathcal{V})} = \frac{G}{\rho}\left(\frac{M + M_y}{m + M_y}\right) \\ I_{Vy} &= \frac{mGk}{m + \rho(k - \mathcal{V})} = \frac{mG}{\rho}\left(\frac{M + M_y}{m + M_y}\right) \end{aligned}$$

where $\mathcal{V}$ is its submerged volume, $M = \rho\mathcal{V}$, and M_y is the added mass of B for vertical movement when half surrounded by fluid. If the body is fixed, so that $V = 0$, then the impulse is $I_y = Gk$. Values of

$$k = \Re \int_{-L}^{L} \sqrt{L^2 - x^2}\, \left.\frac{\mathrm{d}w}{\mathrm{d}z}\right|_{z=x} \mathrm{d}x = \frac{M_y}{\rho} + \mathcal{V}$$

for several different bodies are shown in Table 4.7.1.

B	Width	$\bar{V}(\rho/G)$
Semicircle of radius $\sqrt{2/\pi}$	1.596	0.500
Circle of radius $1/\sqrt{\pi}$	1.128	0.451
Square of unit side length	1	0.152
Wedge of unit depth and unit half-width	2	0.523
Wedge of depth 2 and total width 1	1	0.135

Table 4.7.2: Values of width and $\bar{V}$ for a selection of the two-dimensional shapes considered. $\bar{V}$ is the vertical velocity of a body with density $\rho_B = 3\rho$ which rests with its top surface continuous with the free surface, $\bar{V}(\rho/G) = k/(2+k)$. It is a restriction of the theory presented in this chapter, to a body which has no 'superstructure' - i.e. no mass above the water line.

In Table 4.7.2 we present the velocity of a body that doesn't project above the free surface and has density equal to three times that of water. The greatest velocity is that of the right-angled wedge, which is the widest body at the surface. Conversely, the smallest velocities are those of the square and the tall thin wedge, which both have the same, relatively small, width. The velocity of the square is slightly greater than the velocity of this wedge, because the wedge is less easy for the fluid to 'grip'. So it is not that objects with sharper corners move more quickly, but that objects with flat surfaces perpendicular to the pressure impulse gradient move more quickly.

We compare the different velocities of a circle when it is half submerged or fully submerged: for a semicircle (of any radius) with mass equal to that of a complete circle, (4.3.3) with $\rho_B = 3\rho$ gives

$$V = \frac{\pi G}{\pi\rho_B + \frac{1}{2}\pi\rho} = \frac{2}{7}\frac{G}{\rho} \tag{4.7.1}$$

whilst a submerged circle has $V = 0.451G/\rho$ by (4.4.11). Therefore the velocity of a circle is almost twice as great when it is submerged. The, perhaps unsurprising, conclusion is therefore that the less a body penetrates into the water, the less will be the impulse on it. The exception to this is when a body is vanishingly thin, for instance a vertical plate, which receives no impulse however far into the fluid it penetrates.

We can also compare the velocities of two semicircles, one of which has twice the mass. The value of $V = \frac{2}{7}G/\rho$ from (4.7.1) for a semicircle with mass $m = \rho_B \pi a^2$ is less than the value in Table 4.7.2 for a semicircle of mass $m = \frac{1}{2}\rho_B \pi a^2$ with $V = \frac{1}{2}G/\rho$. Therefore an increase in mass causes a decreased velocity - doubling the mass almost halves the velocity, at least for a semicircle. So a heavier semicircle will move at a slower speed, despite the impulse on it being about 14% greater.

In §4.1 we estimated a value of $G \approx 5 \times 10^3$ N sec m^{-3} for a water depth at the wall of 10 m. Then $G/\rho = 5$ m sec^{-1} and so the initial velocity of a semicircle of mass $m = 3$ kg, from Table 4.7.2, is 2.5 m sec^{-1}. If no other forces except gravity acted on the body then it would rise to a height of 30 cm - these displacements are not large.

An area where much work has been done is that of a body falling vertically onto a flat free surface. If the velocity potential, Φ, describing the impact of the body onto the fluid at unit speed is known, then we can write the pressure impulse for a surface-piercing body of the same shape which is caused to move with velocity V by an impulsive pressure gradient G as

$$P = -(G - \rho V)\Phi - \rho V y \qquad (4.7.2)$$

where y is a coordinate pointing upwards, perpendicular to the free surface. We could then integrate P to find the impulse, and hence V. But if we know the added mass of the body, we can apply (4.4.6) to find V, so that P is completely specified in terms of G, and also the impulse on the body. For instance, consider a flat elliptic plate impacting on the free surface, with a minor axis of unit length and a major axis of length c (when $c = 1$ this reduces to the disc in §4.5 with unit radius). Wood (1997, §3.10) finds that the velocity potential for the subsequent flow is

$$\Phi = Cy \int_{\lambda}^{\infty} \frac{\mathrm{d}\lambda'}{\lambda' \sqrt{\lambda'(1+\lambda')(c^2+\lambda')}} \qquad (4.7.3)$$

where

$$C = 1 \Big/ \int_0^\infty \frac{2u + 1 + c^2}{\sqrt{u(1+u)^3(c^2+u)^3}}$$

$$\text{and } \lambda = \frac{1}{2}\left(x^2 + y^2 - 1 + \sqrt{4y^2 + (1 - x^2 - y^2)^2}\right).$$

Then we apply (4.7.2) to construct P. To find the impulse on the plate, one would normally integrate (4.7.3) once more, but since this looks distinctly difficult, we find that the added mass of the elliptic plate is given by Lamb (1932, §114) as

$$M_y = \frac{2}{3}\pi\rho c^2 \Bigg/ \int_0^{\pi/2} \sqrt{\sin^2\theta + c^2\cos^2\theta}\,\mathrm{d}\theta$$

(where we have halved Lamb's result since it is for a body surrounded by fluid) which is a much easier calculation. Then the pressure impulse and velocity is completely defined by applying (4.4.6).

4.8 Conclusions

We have shown that any body (with non-negligible width) near the surface, in the vicinity of a sea wall when a wave breaks against it, experiences an impulsive lift. The velocity at which it moves initially is independent of the length scale of the body and inversely proportional to its mass. The vertical impulse is, however, proportional to the mass and size of the body. Both the impulse on a body, and its velocity, depend more upon its width, particularly close to the surface, than its depth. These can be calculated from a combination of the added mass of the body and its submerged volume/area. We expect vertical velocities of the order of $1 - 3$ m sec^{-1}. If the body does not have a vertical line of symmetry, then it will experience an impulse which has a horizontal component as well as the vertical component associated with symmetric bodies.

Using the Schwarz-Christoffel conformal mapping theorem makes it possible to find the velocity of any straight sided body, although it is probable that numerical techniques would be required to perform the integrations to find the shape and size of the body. Almost all of the shapes considered have a vertical axis of symmetry and on these shapes no resultant horizontal impulses act. However, the asymmetric inclined plate experiences an impulse in a direction perpendicular to the direction of G. It may therefore be useful to extend the work of this chapter by studying some more asymmetric bodies.

Chapter 5

The Pressure Impulse in a Thin Crack in the Wall

5.1 Introduction

Sea walls constructed of blocks or caissons fail when one of these constituent parts is loosened from the structure. One mechanism for this to happen is that the impact of a wave causes fluid to rush into the crack between two blocks, gradually wearing away the cement between the blocks, until it can get behind the block and exert a force on it, pushing seaward. Of relevance here is the observation of Gaillard (1904), quoted earlier, concerning constituent parts of a wall being pushed towards the direction from which the waves are impacting. Fluid in the crack can also exert an impulse upwards, which could cause a block to move in that direction, against gravity.

Müller (1997) has instigated the most important experimental study into pressure propagation into cracks in sea walls. He measured the impact pressures on a vertical wall and then in a vertical crack in the wall with its top at still water level. The crack had width 0.5 mm, height 25 mm and a depth (into the wall) of 100.4 mm and contained two pressure transducers, one near the back of the crack and the other towards the front (near the face of the wall). Three different wave heights were used, and the crack remained saturated with fluid throughout the experiments. Müller found that impact pressures on the wall propagated into the crack and were higher at the back of the crack. (If the crack was open to the atmosphere at the back, then the pressures were reduced on the rear transducer, and were less than those on the front transducer.) The recorded pressures were, in general, only slightly less than those on the wall. He suggests that these are due to compression waves caused by entrained air, and that the impact pressures in these thin cracks cause large lateral pressures which can exert high splitting stresses on the surrounding walls.

In this chapter we model the effect of wave impact against a sea wall containing a fluid filled crack between two of its constituent blocks. Our aim is to give a description of the splitting stresses acting within the crack. The crack is assumed to be below the impact zone, so that we need not consider the filling flows of Peregrine and Kalliadasis (1996) with a free surface inside the crack. Indeed, we suggest that the highest impulses in cracks are experienced by those cracks in which no return flow is possible. Thus we consider a crack in a wall which is saturated with fluid, and assume that a wave breaks against the wall, causing high pressures to propagate into the crack. Also, since the fluid is incompressible, we expect the pressures in the crack to be higher than the theoretical results of Peregrine and Thais (1996) and the experimental results of Müller (1997).

Consider, in a vertical sea wall, a horizontal seam between two rectangular blocks from which the mortar has been excavated by erosion in some way. Then there is a thin gap whose height is much smaller than both its width and depth. We define the open, or seaward, end to be that face of the crack which is visible, and the back of the crack to be the points of the crack furthest away from the wall face. We say a crack is closed if the top (or roof) and base (or floor) of the crack meet at the back. Since we have neglected gravity in constructing the equations for the pressure impulse, the crack could also be lying in a vertical plane (i.e. the vertical seam between the sides of two adjacent rectangular blocks).

We wish to find the impulse on the floor, roof and walls of the crack from the impact of a wave that hits the wall surrounding its open end. This impulse will depend not only on the size of the crack, but also on the severity of the impact. Therefore we assume knowledge of the pressure impulse caused by the wave impact at the open end of the crack. For instance, for a crack in a vertical plane, the analysis of Chapter 2 would give the pressure impulse down the sea wall, from which we can take a distribution of P for our seaward boundary condition. From figure 2.3.2(a), with $\mu = 0.2$ and $i = 1$, the pressure impulse is almost constant near the base of the wall, so the boundary condition would be $P = 0.02(\rho u_0 H)$. Further up the wall the pressure impulse increases as the distance to the free surface decreases, so on the small interval $y/H \in [-0.43, -0.4]$ we have that $P \approx 0.06(1 + y)(\rho u_0 H)$. This information will allow us to completely specify the pressure impulse in the crack. Further, given P, we can find the velocity field in the crack, so that information will be available on how loose material in the crack will be moved around.

Having found the pressure impulse in the crack we then integrate the normal component of P over each of the bounding surfaces of the crack to find the impulse, I, on each one. We intend to compare the impulsive force, $F_I = I/\Delta t$, with the gravitational force acting on the blocks surrounding the crack to see if it is significant enough to cause the blocks to move.

If the pressure impulse at the seaward end of a simple, one-dimensional, crack is constant ($P = P_0$), then because the walls are impermeable, the pressure impulse is (the same) constant throughout the crack. However, if the crack is uniform in height and open to the atmosphere at the back ($P = 0$), then the solution for P decreases linearly from the front of the crack to the back, $P = P_0(1 + x/L)$, where L is the length of the crack and $x \in [-L, 0]$ a coordinate along the base of the crack. Note that x could also be the arc length along the base of some more complicated crack, in which case P would be the same, provided that the crack was still uniform in height. We find P in some more complicated one dimensional cracks in §5.3.

We commence by assuming that the crack is thin, so that the pressure impulse changes little over the depth of the crack. Then we can derive a new field equation for the pressure impulse in the crack by simplifying Laplace's equation. We solve this for several different geometries. The cracks between constituent blocks of breakwaters,

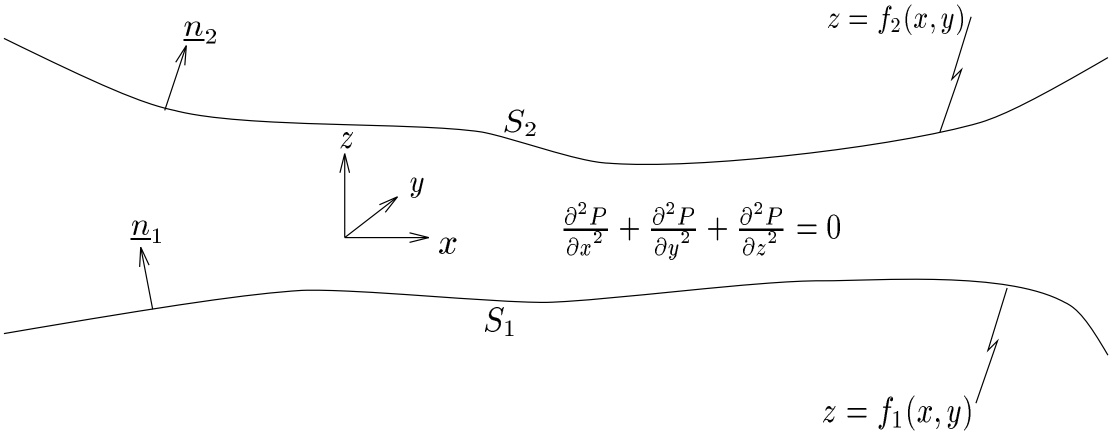

Figure 5.2.1: Notation for calculating the pressure impulse in a crack. S_1 and S_2 are impermeable surfaces confining incompressible fluid and $\underline{n}_1$ and $\underline{n}_2$ are the respective normals. S_1 is given by $z = f_1(x,y)$ and S_2 by $z = f_2(x,y)$. The pressure impulse, P, satisfies the three-dimensional Laplace's equation with zero normal derivative on the bounding surfaces.

which are likely to be linear, can be well approximated by a collection of small straight segments, so in §5.4 we find P in a crack which is closed at one end and whose roof is made up of a continuous collection of piecewise linear segments. The pressure impulse in the thin crack between a flat plane and an axisymmetric body is found in §5.5, and then in §5.6 we perturb the solution found for P beneath a sphere, to give the pressure impulse distribution under an ellipsoid of small eccentricity. The method of conformal mapping, as derived in Chapter 3, is then used in §5.7 to generate some different crack shapes on which we find the impulses acting.

5.2 An Equation for the Pressure Impulse in a Crack

For a crack which is small in height, and whose bounding surfaces are impermeable and nearly parallel, there is little flow across its height. Fluid tends to move parallel to the roof and floor. We define two almost parallel, impermeable, surfaces, S_1 and S_2, the gap between which is filled with fluid, as in figure 5.2.1. In the fluid domain P satisfies the three-dimensional Laplace's equation, $\nabla^2 P = 0$. The boundary conditions are

$$\nabla P.\underline{n}_i|_{S_i} = 0, \qquad i = 1, 2 \tag{5.2.1}$$

where $\underline{n}_i$ is the normal to the surface. If S_i is defined by the equation $z = f_i(x, y)$ then $\underline{n}_i = (-\partial f_i/\partial x, -\partial f_i/\partial y, 1)$ and (5.2.1) becomes

$$\left.\frac{\partial P}{\partial z}\right|_{S_i} = \left.\frac{\partial P}{\partial x}\right|_{S_i} \frac{\partial f_i}{\partial x} + \left.\frac{\partial P}{\partial y}\right|_{S_i} \frac{\partial f_i}{\partial y}, \qquad i = 1, 2. \tag{5.2.2}$$

Integrating Laplace's equation across the height of the crack, from $z = f_1$ to $z = f_2$, for fixed x and y gives (where x, y and z subscripts denote derivatives)

$$\int_{f_1}^{f_2} P_{xx} + P_{yy} + P_{zz}\,\mathrm{d}z = \int_{f_1}^{f_2} P_{xx}\,\mathrm{d}z + \int_{f_1}^{f_2} P_{yy}\,\mathrm{d}z + \left.\frac{\partial P}{\partial z}\right|_{S_2} - \left.\frac{\partial P}{\partial z}\right|_{S_1} = 0. \tag{5.2.3}$$

If the S_i deviate little from the (x, y)-plane then both of the derivatives of each of the f_i are small: $f_{1x}, f_{1y}, f_{2x}, f_{2y} \ll 1$. Thus (5.2.2) implies $\partial P/\partial z$ is small on each of the bounding surfaces. But then P must vary little across the gap, and so the x and y derivatives of P vary little across the gap, and can be treated as independent of z. Thus (5.2.3) becomes

$$P_{xx}(f_2 - f_1) + P_{yy}(f_2 - f_1) + P_x \frac{\partial f_2}{\partial x} + P_y \frac{\partial f_2}{\partial y} - P_x \frac{\partial f_1}{\partial x} - P_y \frac{\partial f_1}{\partial y} = 0.$$

Defining $h(x, y) = f_2 - f_1 > 0$ gives

$$hP_{xx} + hP_{yy} + h_x P_x + h_y P_y = \nabla.(h\nabla P) = 0. \tag{5.2.4}$$

where now ∇ is the two-dimensional differential operator. Equation (5.2.4) reduces to a two-dimensional Laplace's equation when h is constant, and in general, when either P or $\partial P/\partial n$ is specified on the boundary, the solution of (5.2.4) enables the pressure impulse in the crack to be found, so we can use it to find the impulse on the roof of the crack.

5.3 One-dimensional Cracks

Initially we consider a one-dimensional crack where the height is $h = h(x)$ and the pressure impulse is $P = P(x)$. If the crack were closed at the back end ($h(x) = 0$ for

Figure 5.3.1: Notation for a one-dimensional crack. The crack has length $L = -x_M$ with a flat base and a roof given by $z = h(x) > 0$. The boundary conditions are that $P(x = 0) = P_0$ and $P(x = x_M) = P_M$.

some $x < 0$) then, since $\partial P/\partial n = 0$ on each of the bounding surfaces, the pressure impulse is constant and equal to the pressure impulse specified at the open boundary. Therefore in this short section we consider only cracks where $h(x)$ is non-zero for all x and the crack is open at the back. The crack has length $L = -x_M$ with the boundary conditions that P is specified at each end of the crack. See figure 5.3.1: $P(x = 0) = P_0$ and $P(x = x_M) = P_M < P_0$. We assume that the base of the crack is flat ($f_1 \equiv 0$), then $h(x) = f_2(x)$. Equation (5.2.4) becomes

$$\frac{\mathrm{d}}{\mathrm{d}x}\left(h\frac{\mathrm{d}P}{\mathrm{d}x}\right) = 0,$$

since P is a function of x only, and then a solution is

$$P(x) = P_0 + (P_M - P_0)\int_x^0 \frac{\mathrm{d}x}{h(x)} \bigg/ \int_{x_M}^0 \frac{\mathrm{d}x}{h(x)}. \tag{5.3.1}$$

Then $h(x)$ can be any function for which h is non-zero on the interval $x \in [0, L]$, $1/h$ is integrable, and $\mathrm{d}h/\mathrm{d}x$ is small. The impulse on the roof of the crack is

$$I = P_0 L + (P_M - P_0)\int_{x_M}^0 \int_x^0 \frac{\mathrm{d}x'}{h(x')}\mathrm{d}x \bigg/ \int_{x_M}^0 \frac{\mathrm{d}x}{h(x)}. \tag{5.3.2}$$

For example, if $h(x) = \alpha_0 + \alpha_1 x$, where $\alpha_0 > 0$ and $\alpha_0 + \alpha_1 x_M > 0$, then

$$P(x) = P_0 + (P_M - P_0)\frac{\log(1 + \alpha_1 x/\alpha_0)}{\log(1 + \alpha_1 x_M/\alpha_0)}.$$

The gradient of pressure impulse is highest at $x = x_M$ and decreases as x becomes less negative if $\alpha_1 > 0$. If $\alpha_1 < 0$ then the pressure impulse gradient is higher at the seaward end, where the crack is thinner. Notice that as $\alpha_1 \to 0$ we get the solution for a crack of constant depth, $P = P_0 + (P_M - P_0)x/x_M$. In this case the pressure impulse varies linearly between the two ends of the crack. By (5.3.2) the impulse on the roof of this crack is

$$I = P_M L + (P_0 - P_M)\left(\frac{L}{\log\left(1 + \alpha_1 x_M/\alpha_0\right)} + \frac{\alpha_0}{\alpha_1}\right).$$

It is also possible to find the pressure impulse in a crack with a roof which is defined as a continuous collection of segments for which we can find P from (5.3.1). To construct a solution we solve for P beneath each part of the roof and then match P and $\mathrm{d}P/\mathrm{d}x$ across the joins, to find the pressure impulses at the ends of each segment. This is demonstrated in the next section for a crack in which $P = P(x, y)$.

5.4 Piecewise Linear, Closed Cracks

The theory of the previous section is now extended to cracks in which P depends on both the width and length of the crack. The crack is closed at the back, the floor is flat, and the roof is made up of piecewise linear segments. To simplify the analysis, the crack is assumed to be uniform in the y direction and to lie between impermeable walls at $y = 0$ and $y = \pi$. The only other information required is the pressure impulse at the seaward end of the crack, specified as a function of y at $x = 0$. We make the stipulation that this data be expressed as a Fourier cosine series in y. So although $h = h(x)$ only, $P = P(x, y)$.

5.4.1 Formulation

Our starting point is (5.2.4):

$$\nabla.\,(h\nabla P) = 0$$

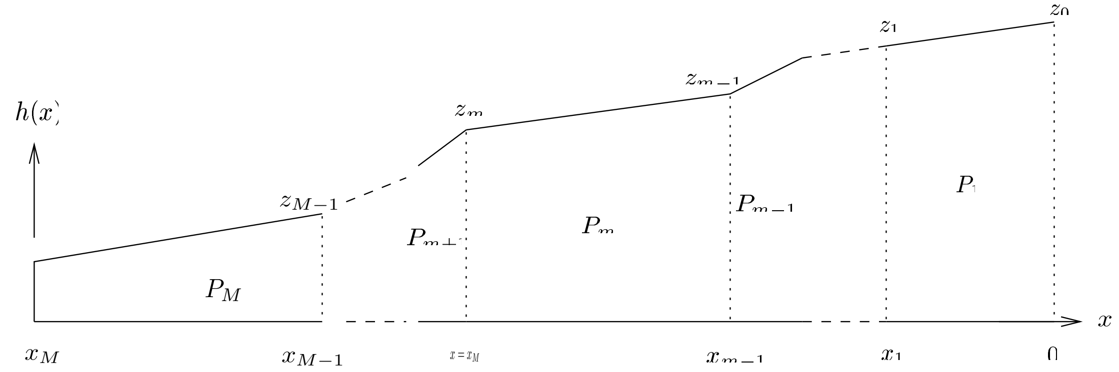

Figure 5.4.1: Notation for piecewise linear cracks. The crack is divided into M sections, each of which is such that $h_m(x)$ is linear. The crack is uniform in the y direction (into the page) and in the m^{th} section $P = P_m(x, y)$.

where $h = h(x) = f_2(x)$ is the non-negative height of the crack, $f_1 \equiv 0$ and $P = P(x, y)$ is the pressure impulse in the crack. Recall that this is only valid for small $\mathrm{d}h/\mathrm{d}x$. The base of the crack is the plane $x \in [x_M, 0],\ y \in [0, \pi]$ and so the crack has a front to back length of $L = -x_M$. The height, h, is a continuous collection of segments of the form $h_m(x) = \alpha_{0m} + \alpha_{1m}x$, each defined on the interval $[x_m, x_{m-1}]$, where $\alpha_{0m} \geq 0$ and $m = 1, \ldots, M$, as in figure 5.4.1. Note also that $h_m(x) > 0\ \forall x > x_M$. Then P is a differentiable function on each of the M segments and on the m^{th} segment, $P = P_m(x, y)$, where each P_m satisfies (5.2.4).

The crack is closed at $x = x_M < 0$ so that

$$\frac{\partial P_M}{\partial x}(x_M, y) = 0. \tag{5.4.1}$$

It is impermeable on the flat sides $y = 0$ and $y = \pi$ so

$$\frac{\partial P_m}{\partial y}(x, 0) = \frac{\partial P_m}{\partial y}(x, \pi) = 0 \text{ for } m = 1, \ldots, M. \tag{5.4.2}$$

The open (seaward) end at $x = 0$ has a specified value for P_1, given as a Fourier cosine series,

$$P_1(0, y) = P_0 + \sum_{j=1}^{\infty} S_j \cos(jy). \tag{5.4.3}$$

for some constant P_0. Notice that if the seaward condition is constant, $P_1(0, y) = P_0$, then the pressure impulse solution in the crack is P_0 everywhere. To satisfy (5.4.2) we look for solutions for P_m of the form

$$P_m = P_0 + \sum_{n=1}^{\infty} f_{mn}(x)\cos(ny) \text{ for } m = 1, \dots, M. \tag{5.4.4}$$

So for each h_m we must solve

$$\frac{\mathrm{d}^2 f_{mn}}{\mathrm{d}x^2} + \frac{h_m'}{h_m}\frac{\mathrm{d}f_{mn}}{\mathrm{d}x} - n^2 f_{mn} = 0. \tag{5.4.5}$$

For an arbitrary segment ($m \neq M$), there are two possibilities:

- (i) h_m is an increasing function of x,

  $$h_m(x) = z_{m-1} + \left(\frac{x_{m-1} - x}{x_{m-1} - x_m}\right)(z_m - z_{m-1})$$

  whence we define

  $$\xi_m(x) = \frac{h_m}{h_m'} = x + \frac{x_{m-1}z_m - x_m z_{m-1}}{z_{m-1} - z_m}.$$

  With this change of variable, (5.4.5) becomes

  $$\frac{\mathrm{d}^2 f_{mn}}{\mathrm{d}\xi_m^2} + \frac{1}{\xi_m}\frac{\mathrm{d}f_{mn}}{\mathrm{d}\xi_m} - n^2 f_{mn} = 0$$

  with solutions

  $$f_{mn}(x) = A_{mn}\frac{I_0\left(n\xi_m(x)\right)}{I_0\left(n\xi_m(x_m)\right)} + B_{mn}\frac{K_0\left(n\xi_m(x)\right)}{K_0\left(n\xi_m(x_m)\right)}$$

  where I_0 and K_0 are modified Bessel functions of order zero. Then

  $$P_m(x,y) = P_0 + \sum_{n=1}^{\infty}\cos(ny)\left[A_{mn}\frac{I_0\left(n\xi_m(x)\right)}{I_0\left(n\xi_m(x_m)\right)} + B_{mn}\frac{K_0\left(n\xi_m(x)\right)}{K_0\left(n\xi_m(x_m)\right)}\right]. \tag{5.4.6}$$

- (ii) h_m is constant,

  $$h_m(x) = z_{m-1},$$

  in which case (5.4.5) becomes

  $$\frac{\mathrm{d}^2 f_{mn}}{\mathrm{d}x^2} - n^2 f_{mn} = 0$$

with solutions

$$f_{mn}(x) = A_{mn}\frac{\cosh(nx)}{\cosh(nx_m)} + B_{mn}\frac{\sinh(nx)}{\sinh(nx_m)}.$$

Then

$$P_m(x,y) = P_0 + \sum_{n=1}^{\infty} \cos(ny)\left[A_{mn}\frac{\cosh(nx)}{\cosh(nx_m)} + B_{mn}\frac{\sinh(nx)}{\sinh(nx_m)}\right]. \qquad (5.4.7)$$

For the closed segment, $h = h_M$, we apply (5.4.1), the zero-flux condition at $x = x_M$, on a vertical wall. There are again two possibilities:

- (i) h_M is an increasing function of x, whence (5.4.1) applied to (5.4.6) at $x = x_M$ gives $B_{Mn} = 0$ and

  $$P_M(x,y) = P_0 + \sum_{n=1}^{\infty} \cos(ny) A_{Mn}\frac{I_0\left(n\xi_M(x)\right)}{I_0\left(n\xi_M(x_M)\right)}. \qquad (5.4.8)$$

  A special case of this solution is when h_M increases from zero at $x = x_M$. Then

  $$h_M(x) = z_{M-1}\frac{x - x_M}{x_{M-1} - x_M}.$$

  and $\xi_M(x) = h_M/h'_M = x - x_M$ so

  $$P_M(x,y) = P_0 + \sum_{n=1}^{\infty} \cos(ny) A_{Mn} I_0\left(n(x - x_M)\right). \qquad (5.4.9)$$

- (ii) h_M is constant. Then the solution for P_M is given by (5.4.7), and applying (5.4.1) gives

  $$\begin{aligned} P_M(x,y) &= P_0 + \sum_{n=1}^{\infty} \frac{\cos(ny)}{\cosh(nx_M)} A_{Mn}\left[\cosh(nx) - \sinh(nx)\tanh(nx_M)\right] \\ &= P_0 + \sum_{n=1}^{\infty} A_{Mn}\cos(ny)\frac{\cosh(n(x - x_M))}{\cosh^2(nx_M)}. \qquad (5.4.10) \end{aligned}$$

The solution is completed by applying (5.4.3) to P_1 at $x = x_0 = 0$ and by matching P_m and $\partial P_m/\partial x$ at each x_m, $m = 1, \ldots, M-1$; that is

$$P_m(x_m) = P_{m+1}(x_m),\ \frac{\partial P_m}{\partial x}(x_m) = \frac{\partial P_{m+1}}{\partial x}(x_m) \text{ for } m = 1, \ldots, M-1. \qquad (5.4.11)$$

	Case (i) h_m increasing	Case (ii) h_m constant
$p(m)$	$\dfrac{I_0\left(n\xi_{m+1}(x_m)\right)}{I_0\left(n\xi_{m+1}(x_{m+1})\right)}$	$\dfrac{\cosh(nx_m)}{\cosh(nx_{m+1})}$
$s(m)$	$\dfrac{K_0\left(n\xi_{m+1}(x_m)\right)}{K_0\left(n\xi_{m+1}(x_{m+1})\right)}$	$\dfrac{\sinh(nx_m)}{\sinh(nx_{m+1})}$
$\overline{p}(m)$	$\dfrac{I_1\left(n\xi_m(x_m)\right)}{I_0\left(n\xi_m(x_m)\right)}$	$\tanh(nx_m)$
$\overline{s}(m)$	$-\dfrac{K_1\left(n\xi_m(x_m)\right)}{K_0\left(n\xi_m(x_m)\right)}$	$\coth(nx_m)$
$\overline{\overline{p}}(m)$	$\dfrac{I_1\left(n\xi_{m+1}(x_m)\right)}{I_0\left(n\xi_{m+1}(x_{m+1})\right)}$	$\dfrac{\sinh(nx_m)}{\cosh(nx_{m+1})}$
$\overline{\overline{s}}(m)$	$-\dfrac{K_1\left(n\xi_{m+1}(x_m)\right)}{K_0\left(n\xi_{m+1}(x_{m+1})\right)}$	$\dfrac{\cosh(nx_m)}{\sinh(nx_{m+1})}$
B_{Mn}	0	$-\tanh^2(nx_M)$

Table 5.4.1: Values of the constants for the system (5.4.12) in each of the two cases, where $h_m(x)$ either increases with x or is constant.

This gives a system of $2M-1$ equations for each $n > 0$,

$$\begin{aligned} A_{1n}p(0) + B_{1n}s(0) &= S_n \\ A_{mn} + B_{mn} &= A_{(m+1)n}p(m) + B_{(m+1)n}s(m) \text{ for } m = 1,\ldots,M-1 \quad (5.4.12) \\ A_{mn}\overline{p}(m) + B_{mn}\overline{s}(m) &= A_{(m+1)n}\overline{\overline{p}}(m) + B_{(m+1)n}\overline{\overline{s}}(m) \text{ for } m = 1,\ldots,M-1. \end{aligned}$$

The expressions for $p(m), s(m), \ldots$ and B_{Mn} are chosen according to the choice of h_m and h_M respectively, as given in Table 5.4.1.

We solve the system (5.4.12) using the computer algebra package Maple (Vr3). See Appendix III for a script solving the system for each n in the cases $M \geq 2$. Then, with all the A_{mn}, B_{mn} in terms of the S_m, we find the P_m as required.

It is also possible to generalise this procedure for segments of piecewise generated cracks whose roofs are given by $h(x) = \alpha x^N$, where a general solution for P is

$$P(x,y) = P_0 + \sum_{n=1}^{\infty} \frac{\cos(ny)}{(nx)^{\nu}} \left[A_n I_\nu(nx) + B_n K_\nu(nx)\right], \qquad \nu = \frac{N-1}{2}.$$

Similarly, if $h(x) = \alpha \mathrm{e}^{Nx}$ then

$$P(x,y) = P_0 + \sum_{n=1}^{\infty} \cos(ny)\left[A_n \mathrm{e}^{m_+ x} + B_n \mathrm{e}^{m_- x}\right]$$
$$\text{where } m_\pm = \frac{1}{2}\left(-N \pm \sqrt{N^2+4n^2}\right).$$

However it must be noted that these roofs become high very quickly for $N > 1$, so that the approximation that $\mathrm{d}h/\mathrm{d}x$ is small is invalid.

5.4.2 The impulses on a piecewise linear crack

In attempting to find the nett fluid impulse, $\underline{I}$, on each segment of the roof and the back of the crack, we first remark that, due to the presence of the cosine terms in the solutions for P, the only contribution to $\underline{I}$ comes from the constant term, P_0. We define unit vectors $(\underline{i}, \underline{j}, \underline{k})$ in the x, y and z directions respectively, then the impulse from the seaward face of the crack is $-P_0\pi z_0\underline{i}$. (z_0 is the height of the crack at the wall face.) The impulse on the m^{th} segment of the horizontal floor is $P_0\pi(x_m - x_{m-1})\underline{k}$. Resolving components horizontally and vertically gives the impulse on the roof of each of the m segments:

$$\underline{I}_m = P_0\pi\left(-(z_{m-1} - z_m)\underline{i} + (x_{m-1} - x_m)\underline{k}\right). \tag{5.4.13}$$

If the crack has the roof of its M^{th} segment horizontal then the $\underline{i}$ component of $\underline{I}_M$ is $-P_0\pi z_{m-1}$ and it acts on the back wall rather than the roof. Notice then that any other segment with a horizontal roof has no horizontal component of impulse acting on it.

The total impulse on the roof and back of the crack is

$$\underline{I} = \sum_{m=1}^{M} \underline{I}_m = P_0\pi\left(-z_0\underline{i} + L\underline{k}\right). \tag{5.4.14}$$

So the horizontal impulse on the roof of a crack of length L, width W and height H (at the open end) is $-P_0WH$ and the vertical impulse is P_0LW. Moreover, the variation of P about P_0 contributes only to the scouring effect of the impact pressures.

Example 1

Consider a crack with a flat horizontal roof from the back to where it meets the seaward face of the wall in which it is situated. The height of the crack is arbitrary, though small, and we have just a single segment, $m = M = 1$. So the crack looks like a thin rectangular box. Then (5.4.10) is applicable:

$$P(x, y) = P_0 + \sum_{n=1}^{\infty} A_n \cos(ny) \frac{\cosh(n(x - x_1))}{\cosh^2(nx_1)}.$$

We choose the condition at the seaward end of $P(0, y) = 1 + y$ which, as a Fourier cosine series, can be written

$$P(0, y) = 1 + y = 1 + \frac{\pi}{2} - \frac{4}{\pi} \sum_{j=0}^{\infty} \frac{\cos(2j + 1)y}{(2j + 1)^2}.$$

Comparing coefficients gives $A_n/\cosh(nx_1) = S_n$, where

$$S_{2n} = 0 \text{ and } S_{2n+1} = -\frac{4}{\pi} \frac{1}{(2n + 1)^2}, \tag{5.4.15}$$

and $P_0 = 1 + \pi/2$. Then

$$P(x, y) = 1 + \frac{\pi}{2} - \frac{4}{\pi} \sum_{n=0}^{\infty} \frac{\cos(2n + 1)y}{(2n + 1)^2} \frac{\cosh((2n + 1)(x - x_1))}{\cosh((2n + 1)x_1)}.$$

This pressure impulse solution is shown in figure 5.4.2. The figure suggests that there are significant pressure impulse gradients generated around the edges of the crack at $x = 0$. $P = 1$, its lowest value, at $(0, 0)$ and $P = 1 + \pi$, its highest value, at $(0, \pi)$ so that fluid, and any debris scoured from the walls, is taken in at the top corner and pushed into the crack by the pressure impulse gradient. Because this gradient is large at the open end of the crack, this is therefore where most wearing away of the edges of the crack will occur. The pressure gradient which acts down the back wall of the crack ($x = x_1$) is relatively small, so that the fluid velocities are small in this region.

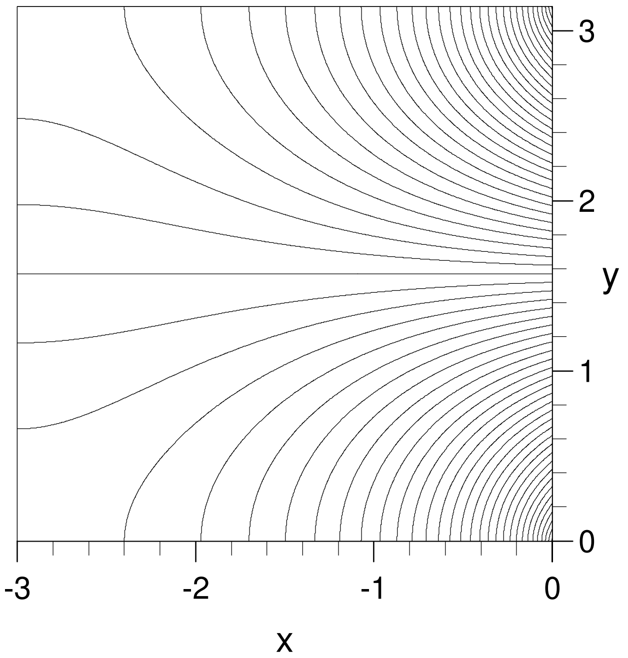

Figure 5.4.2: Contours of constant pressure impulse in a rectangular crack with a flat horizontal roof and $P(0, y) = 1 + y$. This is a plan view of the crack with contour separation $0.05\rho u_0 H$ and $x_1 = -3.0$. The sum was truncated at $n = 100$. The contours are symmetric about the centreline of the crack, $y = \pi/2$, (which follows from the cosine dependence) and show the variation of P away from P_0, the pressure impulse at the open end.

Example 2

We consider a crack with two sections

$$h_1 = \alpha_{01} \text{ on } x \in [x_1, 0] \text{ and } h_2 = \alpha_{01}\frac{x - x_2}{x_1 - x_2} \text{ on } x \in [x_2, x_1].$$

At the open end of the crack, (5.4.7) implies

$$P_1(x,y) = P_0 + \sum_{n=1}^{\infty} \cos(ny)\left[A_{1n}\frac{\cosh(nx)}{\cosh(nx_1)} + B_{1n}\frac{\sinh(nx)}{\sinh(nx_1)}\right]$$

and at the sloping, back, end, (5.4.9) implies

$$P_2(x,y) = P_0 + \sum_{n=1}^{\infty} \cos(ny) A_{2n} I_0\left(n(x - x_2)\right).$$

As in the previous example we use the seaward boundary condition that $P(0,y) = 1+y$ so $P_0 = 1 + \pi/2$. Applying the matching system from (5.4.12) means we must solve

$$\begin{aligned} A_{1n} &= S_n \cosh(nx_1) \\ A_{1n} + B_{1n} &= A_{2n} I_0\left(n(x_1 - x_2)\right) \\ A_{1n}\tanh(nx_1) + B_{1n}\coth(nx_1) &= A_{2n} I_1\left(n(x_1 - x_2)\right) \end{aligned}$$

where the S_n are given by (5.4.15). We use the Maple program in Appendix III to find B_{1n} and A_{2n}:

$$\begin{aligned} A_{2n} &= \frac{S_n}{I_0\left(n(x_1 - x_2)\right)\cosh(nx_1) - I_1\left(n(x_1 - x_2)\right)\sinh(nx_1)} \\ B_{1n} &= S_n \cosh(nx_1)\frac{I_1\left(n(x_1 - x_2)\right) - I_0\left(n(x_1 - x_2)\right)\tanh(nx_1)}{I_0\left(n(x_1 - x_2)\right)\coth(nx_1) - I_1\left(n(x_1 - x_2)\right)}. \end{aligned}$$

Then

$$\begin{aligned} P_1(x,y) = 1 + \frac{\pi}{2} - \frac{4}{\pi}\sum_{n=0}^{\infty} \frac{\cos(2n+1)y}{(2n+1)^2} \times \\ \left[\cosh(2n+1)x + \sinh(2n+1)x\frac{I_1\left(n(x_1 - x_2)\right)\coth(nx_1) - I_0\left(n(x_1 - x_2)\right)}{I_0\left(n(x_1 - x_2)\right)\coth(nx_1) - I_1\left(n(x_1 - x_2)\right)}\right], \\ P_2(x,y) = 1 + \frac{\pi}{2} - \frac{4}{\pi}\sum_{n=0}^{\infty} \frac{\cos(2n+1)y}{(2n+1)^2} \times \\ \frac{I_0\left((2n+1)(x - x_2)\right)}{I_0\left(n(x_1 - x_2)\right)\cosh(nx_1) - I_1\left(n(x_1 - x_2)\right)\sinh(nx_1)}. \end{aligned}$$

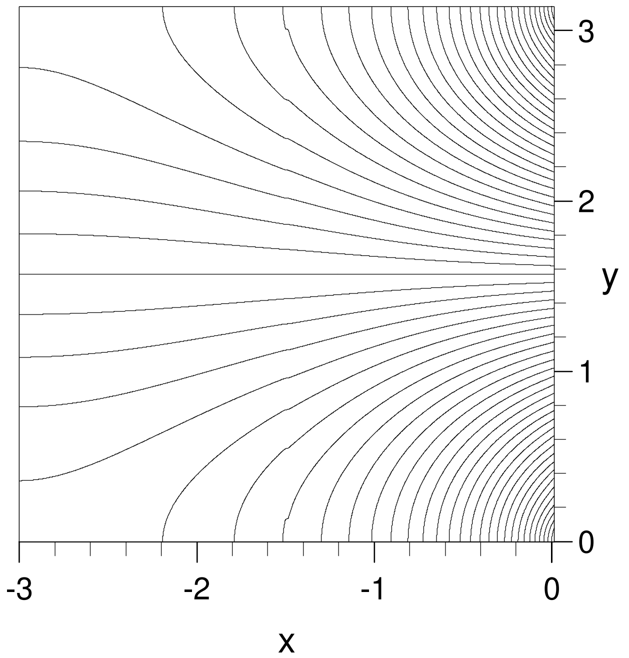

Figure 5.4.3: Contours of constant pressure impulse in a crack which has one flat roofed (seaward) segment, and a sloping segment in the closed back at $x = x_2 = -3.0$. The contour separation is $0.05\rho u_0 H$ and note how the matching isn't quite exact across the join at $x_1 = -1.5$. The figure is drawn using FORTRAN NAG routines S18AEF and S18AFF for the Bessel Functions I_0 and I_1. The number of terms in the sum is small ($n = 10$) because of the unwieldy behaviour of the constant B_{1n} at large n, which explains the slight matching errors. This figure should be compared with figure 5.4.2.

$P(x, y) = P_1 \cup P_2$ is plotted in figure 5.4.3. Comparing the contours with those in figure 5.4.2, we see that the effect of the sloping part of the roof is to slightly increase the pressure impulse at the back (closed end) of the crack. Further, the pressure impulse gradient along this back wall is almost twice that for the crack with a flat roof. The pressure impulse is independent of α_{01}, the maximum height of the crack, which is to be expected because of the supposition that P doesn't vary much across the crack. The impulses on the roofs of each of the cracks in these two examples are the same.

5.4.3 Order of magnitude analysis

We therefore have a method for determining the pressure impulse in a crack, given its dimensions and a boundary condition for the pressure impulse at the open end of the crack, expressed as a Fourier cosine series. We can also find the impulse on the roof and back of the crack: the horizontal impulse will be small, since it is a multiple of the height of the crack, but the vertical impulse on the roof of a crack of width W and length L will be $I_{roof} = P_0 LW$. This impulse generates a vertical force given by $F_I = I_{roof}/\Delta t$, where Δt is the time taken for the wave impact to occur. In §5.1 we suggested a value of $P_0 = 0.036 \rho u_0 H$. If we take a water depth at the wall of $H = 10$m, we expect $u_0 = \sqrt{gH} = 9.91$ m sec^{-1} and so $P_0 = 3.57 \times 10^3$ N sec m^{-2}. Further, we choose $\Delta t = 0.04$ sec and consider two cubic blocks of side length lm and density $\rho_B = 3\rho$, separated by a horizontal crack whose maximum height is small. The weight of the top block is $2.94 \times 10^4 l^3$ N acting downwards and the impulsive force from the pressure impulse in the crack, acting upwards, is $F_I = P_0 l^2/\Delta t = 8.92 \times 10^4 l^2$ N. We compare these two quantities in order to find out whether the impulsive force in the crack is large enough to lift the upper block at all. They are of a similar magnitude if l is of the order of 3 m (much less than the depth of water at the wall), but for any smaller blocks, our analysis suggests that the effect of the wave impacting near the crack will be to separate the blocks and widen the crack. Although the values chosen represent probably the biggest possible loading, it is advisable to make breakwater caissons of well over 3 m in height.

5.5 Crack between an Axisymmetric Body and a Plane

We wish now to use this theory that we have developed to give information about the pressure impulse distribution underneath a body next to a plane surface, where the gap between the two is small in height. Reference to the pressure impulse contours under a circular log resting on the sea bed when a wave breaks against a wall in its vicinity, figure 3.6.2, shows low fluid speeds. However, the three-dimensional case of point contact is not necessarily similar. Using (5.2.4) we can find out more about the distribution of P in the small gap beneath some more complicated shapes resting on the sea bed, for which the complete solution for P is unknown. In particular, we aim to find the pressure impulse distribution around the base of an axisymmetric body, such as a sphere, and an ellipsoid.

To model flow in a crack between an axisymmetric body and a flat surface, we transform (5.2.4) into plane polar coordinates (r, θ) and let h be a function of r only,

$$P_{rr} + \left(\frac{h_r}{h} + \frac{1}{r}\right) P_r + \frac{P_{\theta\theta}}{r^2} = 0 \tag{5.5.1}$$

where the subscripts denote partial derivatives. If $h(r) = f_2 = kr^n$, for $k > 0$ and $n \geq 1$, and $f_1 \equiv 0$ as before, then $h_r/h = n/r$ and P admits separable solutions of the form

$$P = \sum_{m=1}^{\infty} r^{\lambda_\pm} \left[A_m \cos(m\theta) + B_m \sin(m\theta)\right]$$

where

$$\lambda_\pm = -\frac{n}{2} \pm \left(\left(\frac{n}{2}\right)^2 + m^2\right)^{\frac{1}{2}}.$$

To remove the singularity at $r = 0$ we discard the negative root, obtaining

$$P(r, \theta) = \sum_{m=1}^{\infty} r^{\lambda_+} \left[A_m \cos(m\theta) + B_m \sin(m\theta)\right]. \tag{5.5.2}$$

For example, if $n = 2$ we have fluid in a crack under a paraboloid touching the (x, y)-plane at the origin. Then for uniform flow parallel to the x-axis at infinity we need solutions proportional to $\cos\theta$, so $m = 1$ and thus

$$P(r, \theta) = Ar^{2^{1/2}-1} \cos\theta. \tag{5.5.3}$$

In particular, (5.5.3) is appropriate for a sphere near the point of contact, in which case it matches the solution found by Solomentsev *et al* (1997, eq.21). Note that the change in velocity, $\underline{u} \propto \nabla P$, is singular here. This solution is shown in figure 5.6.1, where the lines of constant P in one quarter of the domain are shown (since P is the same, up to a change of sign, in the other quarters).

5.6 Crack between an Ellipsoid and a Plane

Consider the ellipsoid

$$\frac{x^2}{a^2} + \frac{y^2}{b^2} + \frac{(z-c)^2}{c^2} = 1$$

with $c > 0$. It is tangent to the (x, y)-plane at the origin and the height of the gap between this plane and the ellipsoid is approximately

$$h(r, \theta) = \frac{cr^2}{2} \left(\frac{\cos^2 \theta}{a^2} + \frac{\sin^2 \theta}{b^2} \right)$$

for $r \ll c$. For this more general class of height functions h, (5.2.4) becomes

$$P_{rr} + \left(\frac{h_r}{h} + \frac{1}{r} \right) P_r + \frac{h_\theta}{h} \frac{P_\theta}{r^2} + \frac{P_{\theta\theta}}{r^2} = 0. \tag{5.6.1}$$

We have $h_r/h = 2/r$, as for the sphere, and

$$\frac{h_\theta}{h} = \frac{(a^2 - b^2)\sin(2\theta)}{(b^2 \cos^2 \theta + a^2 \sin^2 \theta)}.$$

If $a \approx b$ then we can make the approximation $h_\theta/h = \epsilon \sin(2\theta)$ where the small parameter $\epsilon = 2(a^2 - b^2)/(a^2 + b^2)$ so

$$b = a \left(\frac{1 - \frac{1}{2}\epsilon}{1 + \frac{1}{2}\epsilon} \right)^{\frac{1}{2}}.$$

Equation (5.6.1) becomes

$$P_{rr} + \frac{3}{r} P_r + \frac{\epsilon}{r^2} \sin(2\theta) P_\theta + \frac{P_{\theta\theta}}{r^2} = 0$$

for which we find a perturbation solution, $P = P^0 + \epsilon P^1 + O(\epsilon^2)$. Then

$$P^0 = \sum_{m=1}^{\infty} r^{(1+m^2)^{1/2}-1} \left[A_m \cos(m\theta) + B_m \sin(m\theta) \right]$$

and

$$P^1 = \sum_{m=1}^{\infty} r^{(1+m^2)^{1/2}-1} g_m(\theta)$$

where g_m is the solution of

$$\frac{\mathrm{d}^2 g_m}{\mathrm{d}\theta^2} + m^2 g_m + m \sin(2\theta) \left[B_m \cos(m\theta) - A_m \sin(m\theta) \right] = 0. \tag{5.6.2}$$

Thus

$$P(r,\theta) = \sum_{m=1}^{\infty} r^{(1+m^2)^{1/2}-1} \left[A_m \cos(m\theta) + B_m \sin(m\theta) + \epsilon g_m(\theta) \right]. \tag{5.6.3}$$

Note that the same power of r persists into $O(\epsilon)$ and that the $O(1)$ solution is the same as that for a sphere.

To solve (5.6.2) we find a solution of the homogeneous equation, $g_m'' + m^2 g_m = 0$, which is

$$g_m(\theta) = C_1 \sin(m\theta) + C_2 \cos(m\theta),$$

and then try a particular integral of the form

$$D_1 \sin(m+2)\theta + D_2 \sin(m-2)\theta + D_3 \cos(m+2)\theta + D_4 \cos(m-2)\theta$$

giving

$$g_1(\theta) = \frac{A_1}{4}\left(\cos^3\theta - \cos\theta + \theta\sin\theta\right) - \frac{B_1}{4}\left(\sin^3\theta + \sin\theta - \theta\cos\theta\right) \tag{5.6.4}$$

and, when $m \geq 2$,

$$\begin{aligned} g_m(\theta) = {} & \frac{mA_m}{8}\left(\frac{\cos(m+2)\theta}{m+1} + \frac{\cos(m-2)\theta}{m-1}\right) \\ & + \frac{mB_m}{8}\left(\frac{\sin(m+2)\theta}{m+1} + \frac{\sin(m-2)\theta}{m-1}\right). \end{aligned} \tag{5.6.5}$$

Substituting these solutions, (5.6.4) and (5.6.5), in (5.6.3) gives the pressure impulse distribution around an ellipsoid which is almost spherical. Looking again for solutions proportional to $\cos\theta$ at leading order gives $m = 1$ and

$$P = A_1 r^{2^{1/2}-1}\left[\cos\theta + \frac{\epsilon}{4}\left(\cos^3\theta - \cos\theta + \theta\sin\theta\right)\right]. \tag{5.6.6}$$

The contours of constant P are shown in figure 5.6.2 and should be compared with those for a sphere in figure 5.6.1. We again present only one quarter of the domain. When $y = 0$, P is the same beneath both bodies, then as y increases the two solutions become slightly different. On the line $x = 0$, while $P = 0$ under the sphere, $P = \frac{1}{8}\pi\epsilon r^{2^{1/2}-1}$ for the ellipsoid. This occurs under the shorter axis of the ellipsoid and

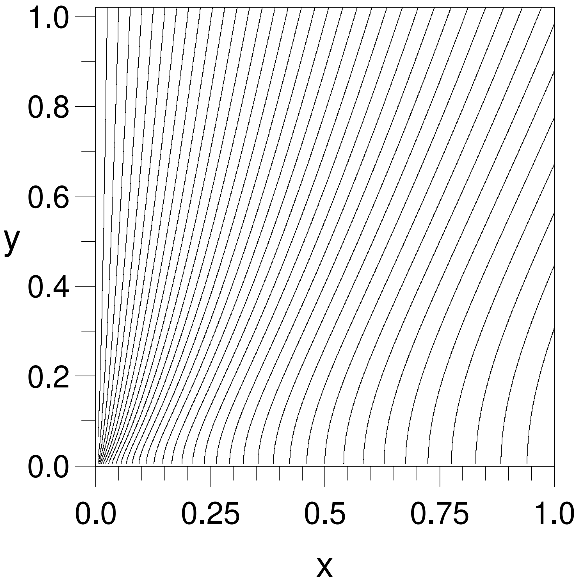

Figure 5.6.1: Contours of constant pressure impulse in the crack beneath a sphere, calculated from (5.5.3). The contour separation is $0.025A$. ∇P is singular at the origin.

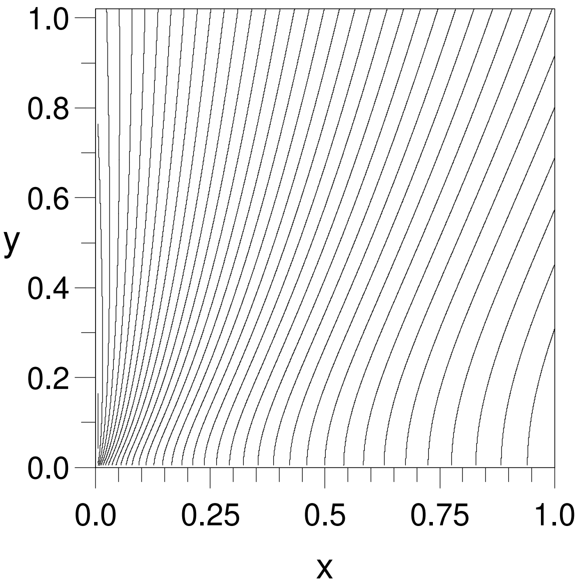

Figure 5.6.2: Contours of constant pressure impulse in the crack beneath an ellipsoid of small eccentricity, from (5.6.6). The parameter $\epsilon = 0.2$ so $b \approx 0.82a$ and the contour separation is $0.025A_1$. There is very little difference from the solution for the crack under a sphere. Note that the singular behaviour at the origin is retained.

means that the contours for the ellipsoid are all sheared towards this axis compared to those for the sphere.

The constants A (in (5.5.3)) and A_m, B_m can be found by matching the solution around the contact point with a solution for P around the rest of the body. This is demonstrated for a sphere in Chapter 6.

5.7 A Conformal Mapping Technique

It is also possible to use the conformal mapping method of Chapter 3 to find the pressure impulse distribution in a two-dimensional crack on a vertical wall. Referring to figure 3.1.1 shows that if the body B were a hollow instead of an elevation, a conformal map could transform the horizontal sea floor into a two-dimensional crack in the sea floor. The normal derivative of P is zero on the crack and the sea floor and the far field boundary condition is $P \sim P_0 - Gx$, where x is the coordinate along the sea floor, away from the wall, with its origin in the body. By the theory of §3.5, if the conformal map from the flat w plane to the physical z plane containing the crack is

$$z(w) = dw + b_0 + \frac{b_1}{w} + \frac{b_2}{w^2} + \ldots, \tag{5.7.1}$$

then the horizontal impulse on the crack is

$$I_x = -\pi G \Re\left(db_1\right). \tag{5.7.2}$$

Now, we consider what happens if the crack is in the wall: if the crack is below the impact zone then the normal derivative of P on the wall is zero. We define an orthogonal coordinate system (x', y') with origin on the wall at $(0, -y_0)$, where $y_0 > \mu H$, in which x' points down the wall towards the sea bed. The crack is situated near the origin of this coordinate system, as shown in figure 5.7.1. Along a small part of the wall, the condition $P \sim P_0 - Gx'$ is a good approximation, since the pressure impulse gradients in, for instance, figure 2.3.3 are almost constant over short distances down the wall. As before, P_0 and G can be calculated from a model such as those given in Chapter 2. So we use the conformal map (5.7.1) to map the flat sea

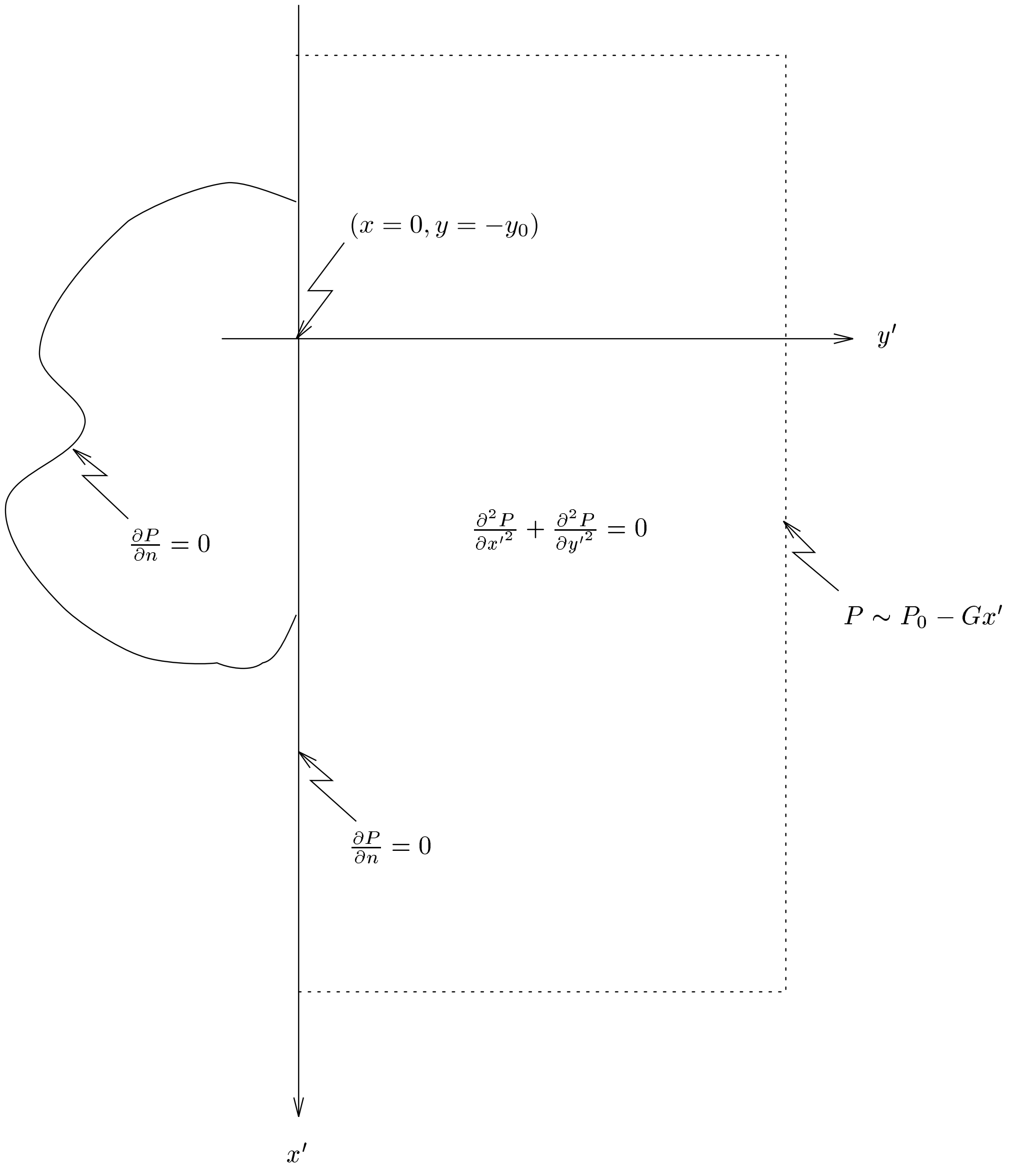

Figure 5.7.1: The boundary value problem for a crack in a vertical wall, below the impact zone. The free surface lies in the $-x'$ direction and the dotted line represents infinity as viewed by this local model. The pressure impulse satisfies Laplace's equation and the far field condition is that $P \sim P_0 + Gx'$. The normal velocity is zero on both the boundary of the crack and the wall $y' = 0$.

wall in the w plane to a sea wall containing a crack in the $z = x' + iy'$ plane. Then, providing the height of the crack is small compared with the depth of fluid at the wall, the vertical impulse on the crack, $I_{x'}$, (acting downwards, towards the base of the wall) is given by (5.7.2).

We construct a class of cracks using a conformal map given by Milne-Thompson (1962, §6.51):

$$z(w) = a \coth\left(\frac{n}{2}\coth^{-1}\left(\frac{nw}{2a}\right)\right) = ai \cot\left(\frac{n}{2}\cot^{-1}\left(\frac{nw}{2ai}\right)\right). \qquad (5.7.3)$$

When $n = 3$ this maps the region exterior to the wall to the interior of a semicircular 'trough' in the wall as well as the region exterior to the wall. In general, for $2 < n < 4$ ($n \in \mathbb{R}$) we obtain a progressively larger arc of a circle indented into the wall. The deepest point of the crack is $a \cot(n\pi/4)$. Figure 5.7.2 shows the pressure impulse contours in the case $n = 3$, where the crack is semicircular. They are symmetric about the centre line of the semicircle, but notice how little the contours more than a radius away from the wall are affected by the presence of the crack. So while the pressure impulse gradient acts to scour out the crack from top to bottom, the presence of the crack itself changes the flow in that neighbourhood very little. There is a high pressure impulse gradient around the areas where the edge of the crack meets the vertical wall. These correspond to large changes in fluid velocity, so we would expect increased scour here, widening the crack. Note also how the contours are qualitatively similar to those shown in figures 5.4.2 and 5.4.3 for thin cracks with a rectangular cross-section. We can imagine that the solution shown there is for a crack on its side, so that the two are directly comparable. That solution was found by assuming that P changed very little in a direction perpendicular to the z plane, so is essentially two-dimensional, and the agreement between the models is reassuring.

Using expansions for $\cot(w)$ (for small w) and $\cot^{-1}(w)$ (for large w) we can write the conformal map (5.7.3) as a power series, valid as $w \to \infty$:

$$z(w) \sim w + \left(1 - \frac{4}{n^2}\right)\frac{a^2}{3w} + O(w^{-3}).$$

Then comparison with (5.7.1) and (5.7.2) gives the impulse on the crack, in the x'

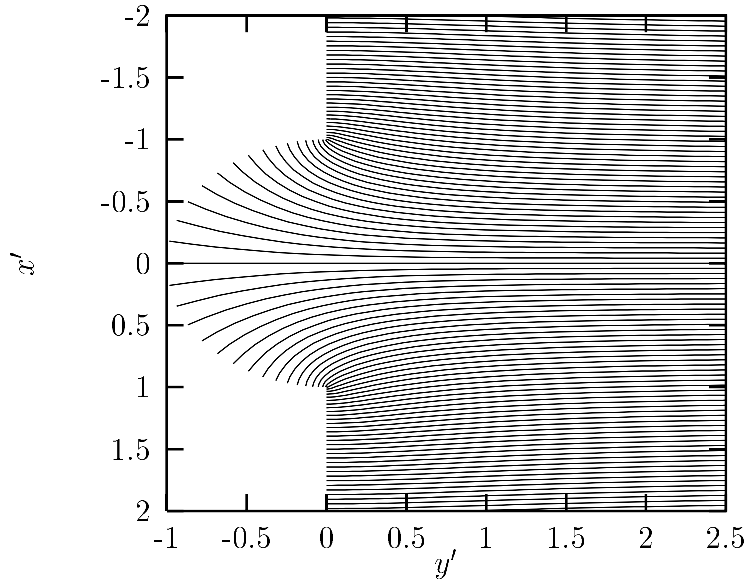

Figure 5.7.2: The pressure impulse contours around and inside a semicircular crack of unit radius in a vertical wall, below the impact zone. $P_0 = G = a = 1.0$ and contour separation is $0.04aG$. The gradient of P is singular at the points where the crack meets the vertical wall ($x' = \pm a$), corresponding to an infinite fluid velocity. However, the flow is affected little by the presence of the crack more than a radius away (the contours are almost straight there). To draw the graph, the cotangent was written in terms of exponentials and the inverse cotangent was written as a logarithm.

direction, for each n,

$$I_{x'} = \frac{1}{3}\pi G_2 a^2 \left(\frac{4}{n^2} - 1\right). \tag{5.7.4}$$

When $n = 3$, the vertical impulse in the semicircular crack is $\frac{5}{27}\pi Ga^2$ upward, against its roof. Note that this is a significantly smaller impulse than the one on a semicircle protruding from the wall, $I_{x'} = \pi Ga^2$ - there is not just a change of sign. This is because a crack changes the distribution of P much less than a lump sticking out. For any $n > 2$ we can calculate the impulse on the roof of the crack, $-I_{x'}$, which becomes greater as n increases, although the size of the crack increases too.

A similar procedure is necessary to calculate the pressure impulse distributions and impulses on different shapes of crack. However, there are fewer examples in the literature of conformal maps which transform the upper half-plane to include an indentation. Note that the impulse is comparable in magnitude to the fluid impulse in (1.1.1), calculated by Peregrine and Kalliadasis (1996), being proportional to the length of the crack squared and a velocity ($V_1 \sim G/\rho$).

5.8 Summary

We have demonstrated several methods for finding the pressure impulse in thin cracks by deriving an equation for the pressure impulse,

$$\nabla . (h \nabla P) = 0.$$

In particular, with a view to discovering what happens when waves impact against sea walls containing water saturated cracks, we can find the pressure impulse distribution and the total impulse on a crack of constant width whose roof is piecewise linear. The variation of the pressure impulse in the crack causes scouring, and the impulse is proportional purely to the local pressure impulse, P_0. We find that if the block which forms the roof is a cube with side length less than about 3 m then the force of a wave breaking against the wall, of height 10 m, in which the crack is situated could be large enough to overcome the gravitational force acting downwards and lift this block. Also, the wave forces in cracks could cause considerable lateral stresses on the constituents of a sea wall. Qualitatively similar distributions for the pressure impulse are found if we use a conformal map to generate a two-dimensional crack in the wall, using the theory of Chapter 3.

This method also makes it possible to find P around the base of an axisymmetric object (or an ellipsoid which is only a slight perturbation of a sphere, in which case the same radial dependence persists) at rest on the sea bed, when it has point contact, so that in the neighbourhood of the contact point the gap between the body and the bed is small. We will use the solution for P around the base of a sphere in the next chapter.

Chapter 6

Potential Flow Past a Sphere Touching a Tangent Plane

6.1 Introduction

We wish to extend the calculations of Chapter 3 to more general three-dimensional bodies, particularly those which have a contact point. The simplest example of a body in point contact is a sphere on a horizontal plane.

In this chapter we calculate the pressure impulse, P, in the region around a sphere and the horizontal tangent plane, or sea bed, on which it sits. On the surface of the sphere and on the tangent plane, the normal derivative of P is zero and at infinity the gradient of P is a prescribed constant vector parallel to the plane. So P is the pressure impulse in the fluid which occurs when the fluid is suddenly accelerated from one velocity field to another. But we can also think of P as the potential for uniform flow past a fixed sphere touching a tangent plane.

If we suppose that $u_b = 0$ and $u_a = \nabla\Phi$ is the necessarily irrotational flow after an impulsive start, then we may take

$$P = -\rho\Phi.$$

We are then led to consider the artificial problem of the ideal flow past a sphere on a tangent plane, and can compare the boundary value problem for P with the literature which uses the, perhaps more familiar, language of the velocity potential, Φ. We reduce the flow at infinity to rest and consider the sphere to move with constant velocity $\underline{G}/\rho$ parallel to and touching the plane. Φ is also the velocity potential for uniform flow perpendicular to the line joining the centres of two, equally sized, touching spheres.

This problem is distinct from that of finding the potential around two touching spheres in axisymmetric flow solved by Collins (1960). Lamb (1932, §98, 99) uses an image system to construct a series solution for the potential for flows perpendicular to, or in line with, the centres of the spheres. His series are expansions in powers of non-zero gap width between the two spheres. These solutions converge too slowly to be accurate as the gap width tends to zero, although they are valid for separated spheres (see also Eames, Hunt, and Belcher 1996). Li, Schultz, and Merte (1993) use spherical harmonics to show that the impermeability boundary condition is approximated with greatest error in the neighbourhood of the point of contact. Laplace's equation is solved by Solomentsev, Velegol, and Anderson (1997) to find the conductivity around two touching spheres. Near the contact point they apply matched asymptotic expansions to the problem of a sphere separated by a small distance h from the plane and they show that, in effect, as $h \to 0$ there is a singularity in the fluid velocity here. This is because, as we showed in §5.5, for small r, $P \propto r^{\sqrt{2}-1} \cos\theta$.

Latta and Hess (1973) also tackle the small gap problem in the context of critical velocity phenomena in superfluid helium. They find the same singularity in the velocity at the contact point. Davis (1977), whose work we most closely follow, considers two spheres heaving in phase on the surface of a liquid half-space. When the spheres touch, he is led to consider the present problem. The added mass of the sphere on a tangent plane, for movement parallel to the plane, is reported by Davis (1977) to be 0.621 and we confirm this value.

In §6.2 we consider the full three-dimensional problem of flow past a sphere in contact with a plane. The solution is expressed as an integral over functions which are separable solutions in tangent sphere coordinates. The integral contains an unknown function $\alpha(q)$ which satisfies an ordinary differential equation. A numerical solution for $\alpha(q)$ is found in §6.2.1 and compared with an asymptotic solution reported by Davis (1977). The field of pressure impulse around the sphere is discussed in §6.3.1 and compared with the crack theory, derived in §5.5, near the point of contact. The errors in the results are reported in §6.3.2. The impulse on a stationary sphere and its added mass are computed in §6.3.3. We use this information to model the movement of a spherical boulder on a plane sloping beach in §6.4 and draw some conclusions in §6.5.

6.2 Formulation

The problem is posed as a sphere moving along its tangent plane with the fluid at rest at infinity. The instantaneous point of contact is at the origin and the tangent plane is the (x, y)-plane. The sphere moves at unit speed ($\underline{G} = \underline{i}$) in the direction of the positive x-axis and the z-axis pierces the sphere along a diameter.

We use tangent sphere coordinates (Moon and Spencer 1961, p104)

$$x = \frac{2\mu\cos\theta}{\mu^2+\nu^2},\ y = \frac{2\mu\sin\theta}{\mu^2+\nu^2},\ z = \frac{2\nu}{\mu^2+\nu^2}$$

or

$$\mu = \frac{2\left(x^2+y^2\right)^{\frac{1}{2}}}{x^2+y^2+z^2},\ \nu = \frac{2z}{x^2+y^2+z^2},\ \tan\theta = \left(\frac{y}{x}\right).$$

The origin corresponds to $\mu = \infty$ and $\mu = 0$ lies at infinity. Surfaces of constant μ are toroids without centre opening, and surfaces of constant ν are spheres tangent to the (x, y)-plane at the origin. The (x, y)-plane is defined by $\nu = 0$ and we choose the sphere $\nu = 1$ which has unit radius.

For any scalar function $\mathcal{E}$, Moon and Spencer (1961) give

$$\nabla\mathcal{E} = \frac{\mu^2+\nu^2}{2}\left(\frac{\partial\mathcal{E}}{\partial\mu}\underline{\hat{\mu}} + \frac{\partial\mathcal{E}}{\partial\nu}\underline{\hat{\nu}} + \frac{1}{\mu}\frac{\partial\mathcal{E}}{\partial\theta}\underline{\hat{\theta}}\right)$$

where $\underline{\hat{\mu}}, \underline{\hat{\nu}}, \underline{\hat{\theta}}$ are unit vectors normal to the level surfaces of μ, ν, θ. Separation of variables gives solutions of Laplace's equation of the form

$$\bar{P}(\mu,\nu,\theta) = \left(\mu^2+\nu^2\right)^{\frac{1}{2}} M(\mu)N(\nu)\Theta(\theta) \tag{6.2.1}$$

where

$$\begin{aligned} M(\mu) &= A_1 J_p(\mu q) + B_1 J_{-p}(\mu q) \\ N(\nu) &= A_2 \cosh(\nu q) + B_2 \sinh(\nu q) \\ \Theta(\theta) &= A_3 \cos(p\theta) + B_3 \sin(p\theta) \end{aligned}$$

and p is an integer. $J_{\pm p}(\mu q)$ is a Bessel function of the first kind of order $\pm p$. The boundary condition on the moving sphere, $\nu = 1$, is

$$\left.\frac{\partial P}{\partial n}\right|_{\nu=1} = -\underline{i}.\underline{n} = -\nabla(x).\underline{\hat{\nu}} = -\frac{(\mu^2+1)}{2}\left.\frac{\partial x}{\partial \nu}\right|_{\nu=1} = \frac{2\mu\cos\theta}{(\mu^2+1)}$$

and since

$$\frac{\partial n}{\partial \nu} = \frac{2}{\mu^2+\nu^2}$$

we have

$$\left.\frac{\partial P}{\partial \nu}\right|_{\nu=1} = \left.\frac{\partial P}{\partial n}\right|_{\nu=1}\frac{\partial n}{\partial \nu} = \frac{4\mu\cos\theta}{(\mu^2+1)^2}. \tag{6.2.2}$$

The velocity component normal to the plane is zero, so

$$\left.\frac{\partial P}{\partial \nu}\right|_{\nu=0} = 0\,. \tag{6.2.3}$$

Finally, we require no singularity in P. The $\cos\theta$ dependence in (6.2.2) gives $p = 1$ and this, with (6.2.3), in (6.2.1) gives us that P is of the form

$$\bar{P} = C(q)\left(\mu^2+\nu^2\right)^{\frac{1}{2}} J_1(\mu q)\cosh(\nu q)\cos\theta.$$

Since q is a free parameter, we integrate $\bar{P}$ over all positive q to obtain the following expression for the pressure impulse:

$$P(\mu,\nu,\theta) = \left(\mu^2+\nu^2\right)^{\frac{1}{2}}\cos\theta\int_0^\infty C(q)J_1(\mu q)\cosh(\nu q)\,\mathrm{d}q. \tag{6.2.4}$$

To find $C(q)$, the boundary condition (6.2.2) is applied to (6.2.4),

$$\begin{aligned}&\left(\mu^2+1\right)^{\frac{1}{2}}\cos\theta\int_0^\infty C(q)J_1(\mu q)q\sinh(q)\,\mathrm{d}q\\&+\left(\mu^2+1\right)^{-\frac{1}{2}}\cos\theta\int_0^\infty C(q)J_1(\mu q)\cosh(\nu q)\,\mathrm{d}q=\frac{4\mu}{\left(\mu^2+1\right)^2}.\end{aligned}$$

Thus

$$\int_0^\infty C(q)J_1(\mu q)q\sinh(q)\left(\mu^2+1+\frac{\coth(q)}{q}\right)\mathrm{d}q=\frac{4\mu}{(\mu^2+1)^{\frac{3}{2}}}.$$

Let $\alpha(q)=C(q)q\sinh(q)$. Then

$$\int_0^\infty \alpha(q)J_1(\mu q)\left(\mu^2+1+\frac{\coth(q)}{q}\right)\mathrm{d}q=\frac{4\mu}{(\mu^2+1)^{\frac{3}{2}}}\tag{6.2.5}$$

and (6.2.4) becomes

$$P(\mu,\nu,\theta)=\left(\mu^2+\nu^2\right)^{\frac{1}{2}}\cos\theta\int_0^\infty \alpha(q)J_1(\mu q)\frac{\cosh(\nu q)}{q\sinh(q)}\mathrm{d}q.\tag{6.2.6}$$

Then the pressure impulse around a stationary sphere, situated at the origin with uniform flow at infinity, is $P_s=P+x$.

6.2.1 Solution for $\alpha(q)$

Following Davis (1977), the transform in (6.2.5) can be inverted, and then $\alpha(q)$ can be shown to satisfy

$$\frac{\mathrm{d}^2\alpha}{\mathrm{d}q^2}-\frac{1}{q}\frac{\mathrm{d}\alpha}{\mathrm{d}q}-\left(1+\frac{\coth(q)}{q}\right)\alpha=-4q\mathrm{e}^{-q}.\tag{6.2.7}$$

In order that the integral in (6.2.4) converges, the boundary conditions on (6.2.7) are $\alpha(0)=0$ and as $q\to\infty$, $\alpha(q)\to 0$. The equation is solved by writing it as a system of two first order ordinary differential equations:

$$\frac{\mathrm{d}\alpha}{\mathrm{d}q}=\beta q,\qquad \frac{\mathrm{d}\beta}{\mathrm{d}q}=\frac{\alpha}{q}\left(1+\frac{\coth(q)}{q}\right)-4\mathrm{e}^{-q}$$

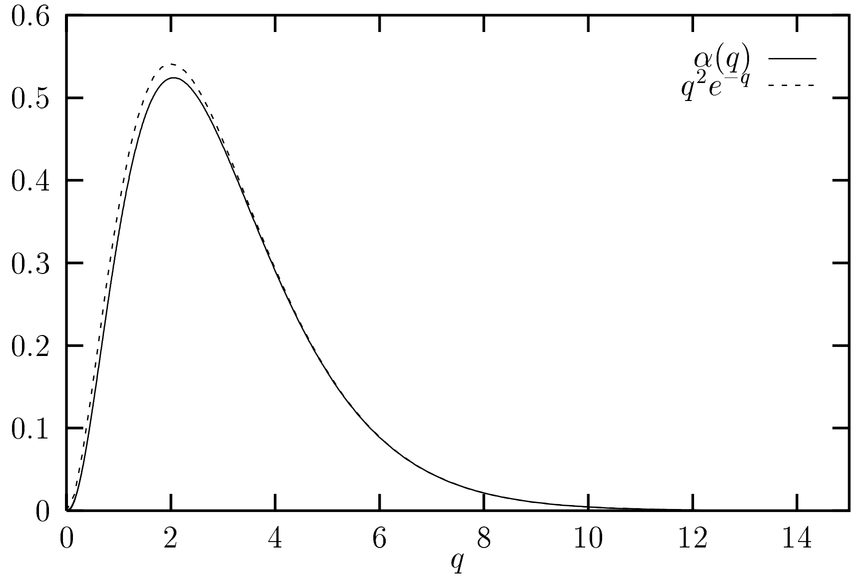

Figure 6.2.1: $\alpha(q)$, the solution of (6.2.7), compared with $q^2\mathrm{e}^{-q}$. An Euler scheme was used, with step size $h = 1 \times 10^{-5}$ and $\alpha'(0) = 0.05665895795721$.

and then making the transformation $t = q/(1+q)$ (so $q = t/(1-t)$). An Euler shooting method with constant step size h (a fourth order Runge-Kutta scheme works equally well) gives the numerical scheme:

$$\begin{aligned} \alpha_{n+1} &= \alpha_n + \frac{th\beta_n}{(1-t)^3}, \\ \beta_{n+1} &= \beta_n + \frac{h\alpha_n}{t(1-t)}\left(1 + \frac{\coth(q(t))}{q(t)}\right) - \frac{4h}{(1-t)^2}\mathrm{e}^{-q(t)} \end{aligned}$$

for $t \in [0,1]$, $n = 1, \ldots, [1/h]$ (where [ ] denotes integer part) and $\alpha_1 = 0$. The solution is shown in figure 6.2.1, with $\coth(q)$ written in terms of exponentials. The scheme requires that $\beta_1 = \alpha'(0)$ be specified, which depends critically upon the step size. The value of $\alpha'(0)$ is unique - all other initial values of α' lead to $\alpha \to \pm\infty$ as $q \to \infty$. An initial guess for $\alpha'(0)$ is refined by trial and error, any inaccuracy showing itself in the divergence to $\pm\infty$ beyond some large value of q. ($h = 1.0 \times 10^{-5}$ and $q = 15$ provided acceptable accuracy, for which $\alpha'(0) = 0.05665895795721$.)

Once $\alpha(q)$ has been found, P is calculated by numerical integration of (6.2.6). This was carried out using a simple trapezoidal rule with intervals of width $h = 2 \times 10^{-6}$ and the upper limit was truncated at $q = 15.0$. The Bessel function, $J_1(\mu q)$, was calculated using FORTRAN NAG routine S17AFF. Davis found that for large q, $\alpha(q) \approx q^2 \mathrm{e}^{-q}$ and in figure 6.2.1 we see that this is a good approximation for all q. When μ and ν are small (corresponding to points in the fluid far from the sphere) the greatest contribution to the integral in (6.2.6) comes from large q. So replacing the numerically computed $\alpha(q)$ with $\bar{\alpha}(q) = q^2 \mathrm{e}^{-q}$ led to similar values of P - compare figures 6.3.4 (a) and 6.3.4 (b).

6.3 Results

6.3.1 Pressure Impulse around the Sphere

In §5.5 we derived an expression for the pressure impulse around the point of contact between the sphere and its tangent plane. This is useful since the point of contact corresponds to $\mu = \infty$, at which point the full three-dimensional expression for P is hard to calculate. For a stationary sphere, the crack theory approximation (5.5.3) is

$$P_c(r, \theta) = A r^{\sqrt{2}-1} \cos\theta. \tag{6.3.1}$$

We choose A so that P_c agrees best with P_s from the three-dimensional analysis of §6.2. At $r = 0.1$ (one-tenth of the sphere's radius) we constrain P_c to equal P_s, as found from the numerical evaluation of (6.2.6), evaluated on the sphere $\nu = 1$. This gives $A = 1.402$, which is comparable to $A = 1.41$ estimated by Solomentsev *et al* (1997, eq.47) who use different criteria. This choice for P_c agrees well with P_s on the tangent plane for a wide interval of values of r as shown in figure 6.3.1. The crack theory solution, when $r \leq 0.4$, lies between the curves for P_s on the plane ($\nu = 0$) and the sphere ($\nu = 1$) obtained from the full three-dimensional solution. For slightly larger r the two-dimensional approximation becomes inadequate, this being the region where three-dimensional effects are significant. However P_c is an excellent

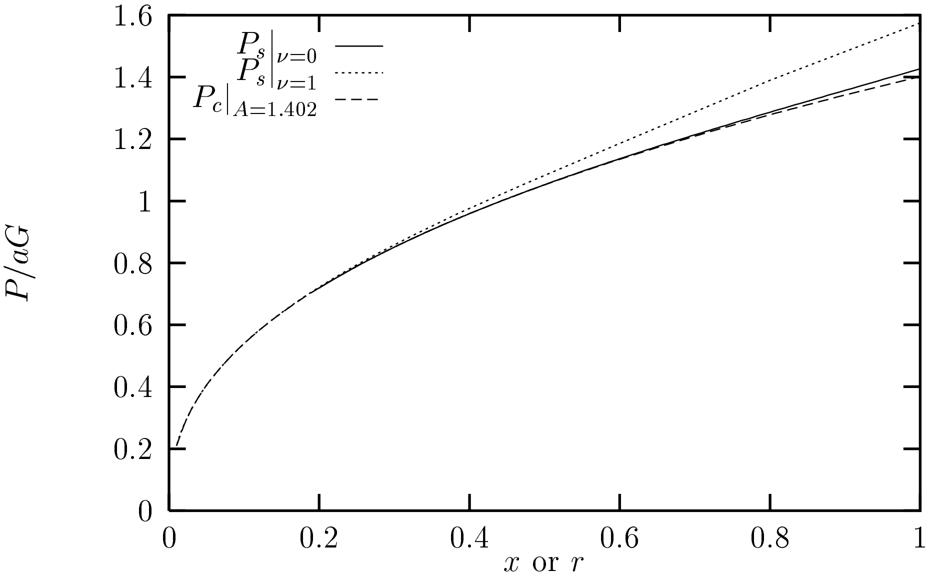

Figure 6.3.1: Comparison between the crack solution and three-dimensional theory in the plane $\theta = 0°$. P_s on the tangent plane and on the sphere bracket the crack solution $P_c = 1.402r^{2^{1/2}-1} - r$ for $r \leq 0.4$. For larger values of r, $P_c < P_s$ on both the sphere and the plane.

approximation beyond the range of r for which we would expect the theory to be valid.

Elsewhere, the maximum value of P on the sphere occurs below the equator at $\phi = 94.5°$, as shown in figure 6.3.2, where ϕ is the angle subtended at the sphere centre from the positive z-axis. This maximum coincides with the stagnation point, which can be verified graphically from a plot of $\partial P_s/\partial\mu$ against ϕ. Therefore the presence of the tangent plane moves the stagnation points down from the equator of the sphere by 4.5°. Note that the pressure impulse is zero at both $\phi = 0°$ and $\phi = 180°$.

Figures 6.3.3 – 6.3.5 show the contours of constant pressure impulse, P_s, on two-dimensional sections near the stationary sphere. These contours show how the presence of the sphere deforms uniform flow parallel to the x-axis at unit speed. On a

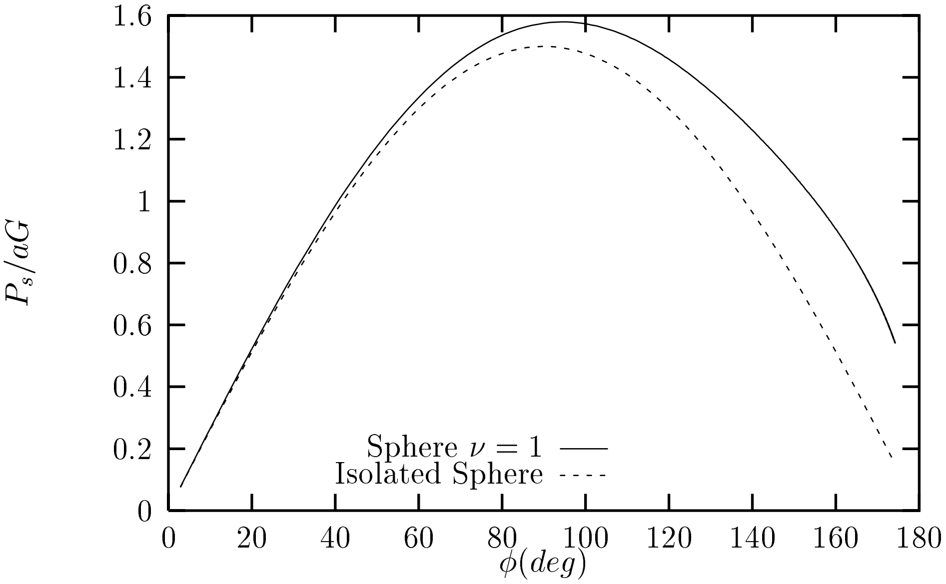

Figure 6.3.2: P_s as a function of angle ϕ on the sphere's surface, $\nu = 1$, and for an isolated sphere of unit radius ($\frac{3}{2}\sin\phi$). $\phi = 180°$ is the contact point. The maximum of P_s is $1.579aG$ and occurs at $\phi = 94.5°$. We see that the influence of the tangent plane is negligible for $\phi \in [0°, 60°]$.

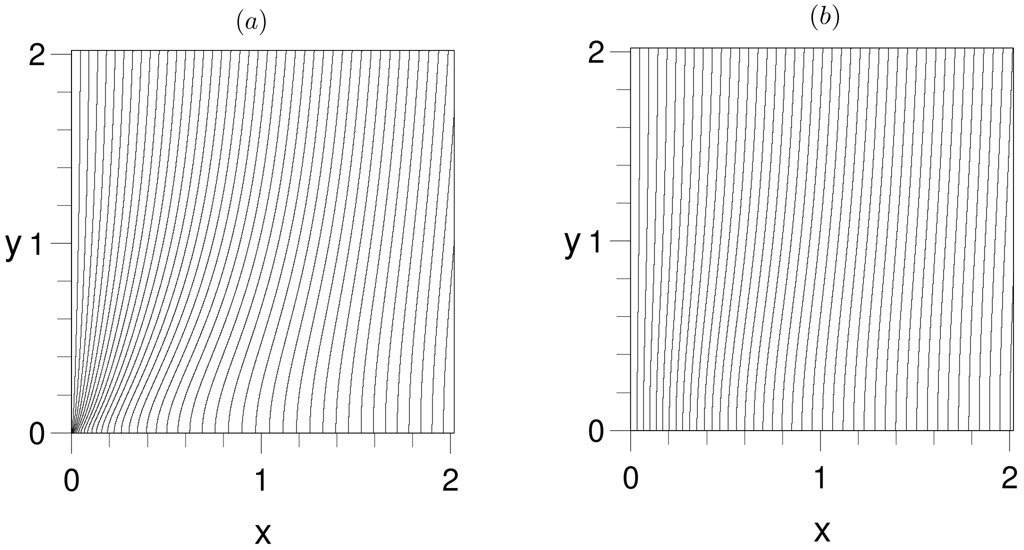

Figure 6.3.3: Constant $P_s = P + x$ contours on a horizontal plane, from (6.2.6), for uniform flow from left to right past a stationary sphere. (a) On the tangent plane $z = \nu = 0.0$. The point of contact is at the origin. This should be compared with the contours of P_c for the crack solution, shown in figure 5.6.1. Although the contour separation is different, they are qualitatively similar near the origin, where the crack solution is valid. (b) On the top plane $z = 2a$. Both have $P_s = 0.0$ on the y-axis, $a = 1.0$ and the contour separation is $0.05aG$.

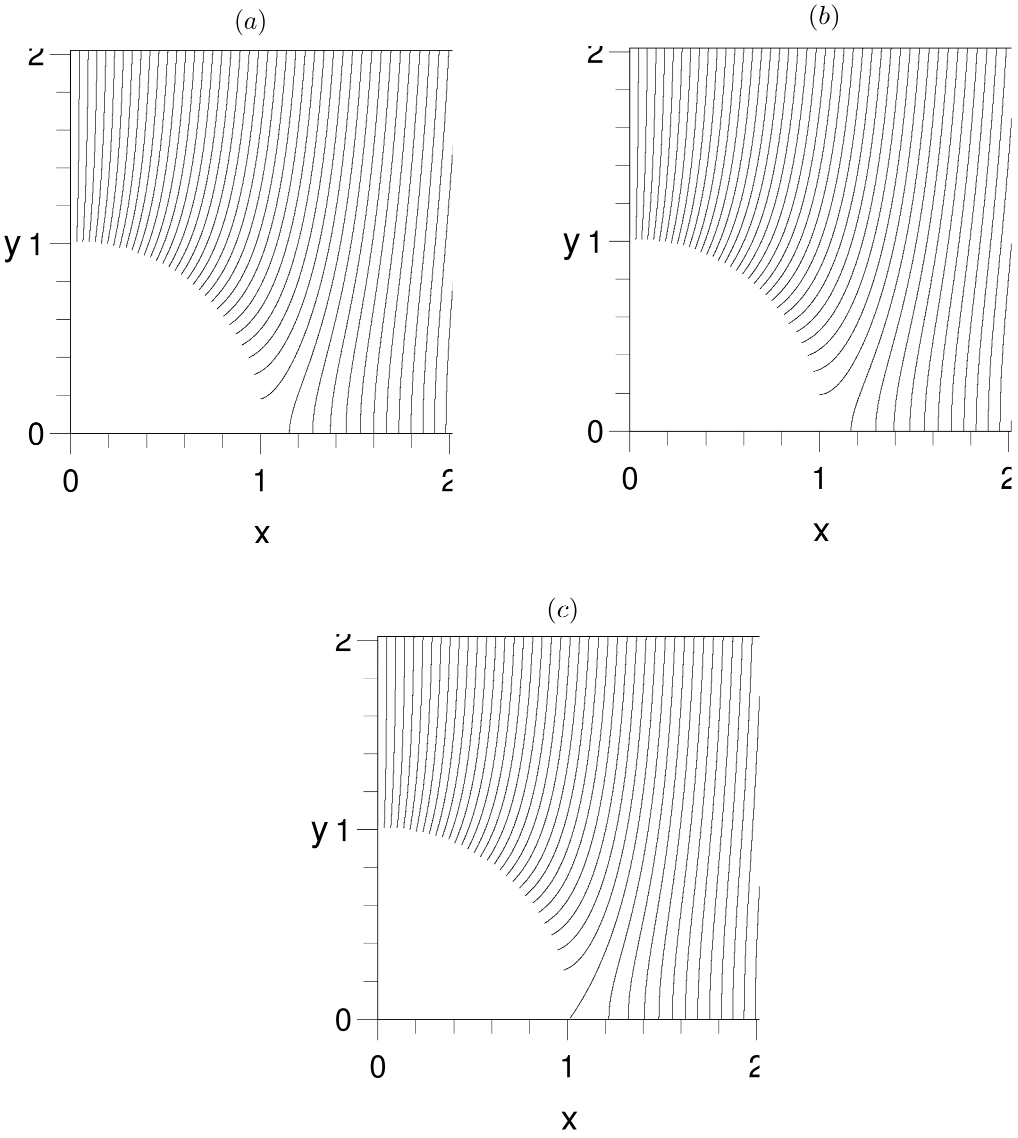

Figure 6.3.4: Constant P_s contours on the equatorial plane $z = a$ for uniform flow from left to right past a stationary sphere. $P_s = 0.0$ on the y-axis, $a = 1.0$ and the contour separation is $0.05aG$. (a) Using the numerical solution for $\alpha(q)$ to evaluate (6.2.6). (b) Using the approximation $\alpha(q) = q^2 \mathrm{e}^{-q}$ to evaluate (6.2.6). (c) Contours for an isolated sphere of radius a. Notice how similar all three figures are.

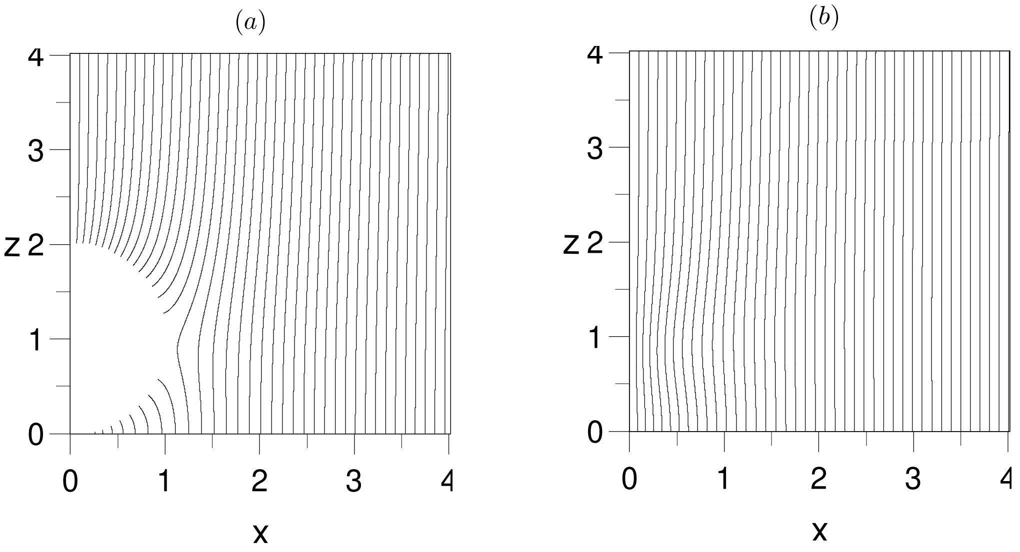

Figure 6.3.5: Constant P_s contours on a vertical plane for uniform flow from left to right past a stationary sphere. (a) On the plane $y = 0.0$. (b) On the plane $y = a$. Both figures have $a = 1.0$, $P_s = 0.0$ on the z-axis and contour separation $0.1aG$.

plane of constant z, the transformation $x \to -x$ sends $P \to -P$ and $y \to -y$ sends $P \to P$. Similar symmetries apply for planes of constant y or x and therefore only a quarter of the domain is drawn.

Figure 6.3.3 (a) gives contours of constant P_s on the tangent plane, $z = \nu = 0$. The bunching of contours near the origin corresponds to large flow speeds around the point of contact. At the top of the sphere, on the plane $z = 2a$, figure 6.3.3 (b) shows the P_s contours. Since these are almost parallel, we conclude that the sphere only slightly retards the flow near its top. Figure 6.3.4 (a) presents contours on a plane through the centre of the sphere, $z = a$, which should be compared with the contours around an isolated sphere in figure 6.3.4 (c). The two are very similar indicating that the influence of the tangent plane is small one radius away. Figure 6.3.4 (b) shows contours on the same plane, $z = a$, using the analytical approximation $\alpha(q) = q^2 e^{-q}$ to evaluate P_s. The contours are nearly the same as in figure 6.3.4 (a) – the value of the approximation to $\alpha(q)$ is evident in the significantly shorter computational time required to obtain the data. The low flow speeds around the stagnation point are evident in the low gradients of pressure impulse near the sphere on the vertical plane $y = 0$, shown in figure 6.3.5 (a). Figure 6.3.5 (b) shows the contours on the vertical plane $y = a$ where we see that the flow is only perturbed very little due to the presence of the sphere.

6.3.2 Errors in the numerical approximation

Figure 6.2.1 shows that $\alpha(q) \approx q^2 e^{-q}$, particularly for large q, which accords with Davis (1977). Very little improvement in the accuracy of $\alpha(q)$ is obtained by decreasing the step size - an Euler method with step size $h = 1 \times 10^{-5}$ is adequate. One measure of the error in our method is the difference between the calculated boundary condition on the moving sphere, $\partial P/\partial\nu|_{\nu=1}(\mu)$ and the exact value of $4\mu/(\mu^2+1)^2$ on the plane $\theta = 0°$. This is shown in figure 6.3.6 (with step size $h = 1 \times 10^{-5}$, where the approximation $\alpha(q) = q^2 e^{-q}$ is used for $q > 15.4$). This shows a maximum error of 1×10^{-4} which occurs far away from the contact point near the top of the sphere.

However, Li *et al* (1993) quantify their errors by examining the residual normal velocity component on the moving sphere, $v'(\phi)$. Here $v' = \frac{1}{2}(\mu^2+1)\,\partial P/\partial\nu|_{\nu=1}(\mu)$ and therefore the error, E, is given by

$$E(\mu) = \frac{\mu^2+1}{2}\left[\left.\frac{\partial P}{\partial \nu}\right|_{\nu=1} - \frac{4\mu}{(\mu^2+1)^2}\right].$$

This is also graphed in figure 6.3.6 (again with step size $h = 1\times10^{-5}$ and $\alpha(q) = q^2 e^{-q}$ for $q > 15.4$). This is an improvement compared with the numerical error reported by Li *et al* (1993). It is difficult to see how accurate their series representations of 10^3 terms are, especially since $\phi = 180°$ corresponds to $\mu = \infty$. However it appears that our error at $\phi = 175°$ is 5×10^{-4} compared to 1×10^{-2} for their results. We remark that if we made no allowance for the presence of the sphere the residual normal velocity would be $G \sin\phi$, an error far in excess of that present here, except *very* close to the contact point. For $\phi > 175°$, which is equivalent to $r < 0.043$, near to the point of contact, we can use the solution (6.3.1) with an error in P of less than 1×10^{-4} - notice how close the lines are in figure 6.3.1 around $r < 0.05$.

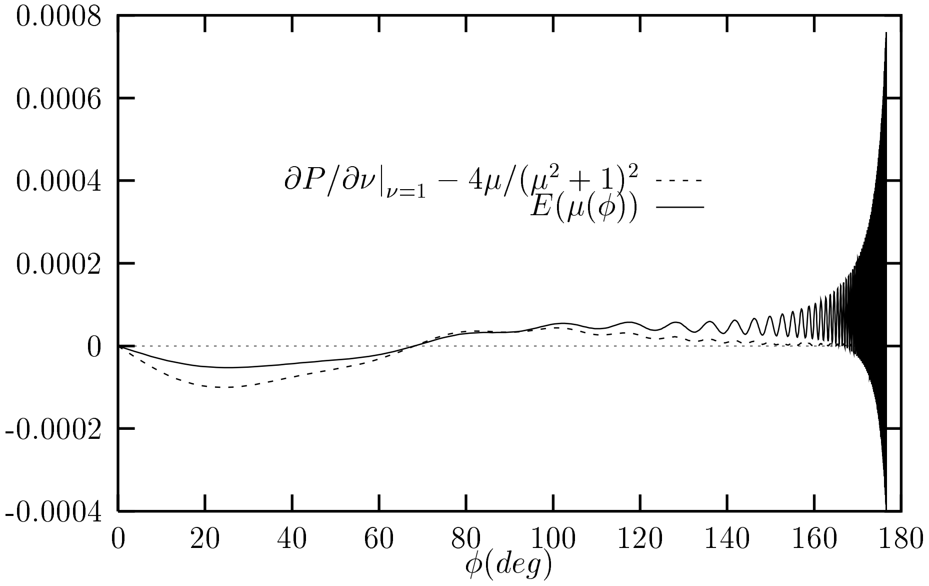

Figure 6.3.6: The error in satisfying the boundary condition on the sphere, $\partial P/\partial\nu|_{\nu=1} - 4\mu/(\mu^2+1)^2$, and $E(\mu)$, the residual normal velocity component on the sphere, on the plane $\theta = 0°$. $\phi = 180°$ is the contact point, but this is hard to attain numerically since it corresponds to $\mu = \infty$. The maximum error is about 1×10^{-4} and occurs when $\phi \approx 28°$. At $\phi = 177°$, $E \approx 7 \times 10^{-4}$.

6.3.3 Impulse and Added Mass

We calculate the impulse, I_x, on the stationary sphere due to an impulsive flow of unit speed in the x direction at infinity. The pressure impulse for a stationary sphere is $P_s = P + x$, where P is computed from (6.2.6) for a moving sphere. Using spherical polar coordinates $(r = 1, \theta, \phi)$, with origin at the centre of the sphere, we obtain

$$\begin{aligned} I_x &= \int_0^{2\pi} \int_0^{\pi} \left(P(\theta, \phi) + x\right)\big|_{\nu=1} . \cos\theta \sin\phi . \sin\phi \, \mathrm{d}\phi \, \mathrm{d}\theta \qquad (6.3.2) \\ &= \pi \int_0^{\pi} P|_{\nu=1} (\theta = 0, \phi) \sin^2\phi \, \mathrm{d}\phi + \frac{4\pi}{3}. \end{aligned}$$

Since

$$\cos\phi = \frac{1-\mu^2}{1+\mu^2}, \ \sin\phi = \frac{2\mu}{1+\mu^2} \text{ and } \sin\phi \, \mathrm{d}\phi = \frac{4\mu}{(1+\mu^2)^2} \, \mathrm{d}\mu,$$

we have

$$\begin{aligned} I_x &= 8\pi \int_0^{\infty} \frac{\mu^2}{(1+\mu^2)^3} P(\theta = 0, \mu)|_{\nu=1} \, \mathrm{d}\mu + \frac{4\pi}{3} \\ &= 8\pi \int_0^{\infty} \frac{\mu^2}{(1+\mu^2)^{5/2}} \int_0^{\infty} \frac{\coth q J_1(\mu q) \, \alpha(q)}{q} \, \mathrm{d}q \, \mathrm{d}\mu + \frac{4\pi}{3}. \end{aligned}$$

The integration was performed numerically, truncating at $\mu = 50$ (equivalent to $\phi = 177.7°$) and $q = 50$, but using the approximation $\alpha(q) = q^2 \mathrm{e}^{-q}$ for $q > 8$. Then $I_x = 0.828\pi + 4\pi/3 = 6.790$. Comparing this with (3.5.15) shows that the added mass of the sphere is $M_x = 0.828\pi$ and so the added mass coefficient is $\lambda_x = 0.621$, confirming the result of Davis (1977). Thus for a sphere of radius a the added mass is $M_x = 0.621 \left(\frac{4}{3}\pi\rho a^3\right)$ which is greater than the value $\frac{1}{2}\left(\frac{4}{3}\pi\rho a^3\right)$ for an isolated sphere.

If we denote by $s = (\pi - \phi)/2$ the arc length around the sphere from the contact point, then the contribution to the impulse, I_x, found above from the neighbourhood of the crack $175° = 3.054^{rad} = \phi_0 \le \phi \le \pi = 180°$ is

$$\begin{aligned} I_x' &= \int_0^{2\pi} \int_{\phi_0}^{\pi} 1.402 s^{\sqrt{2}-1} \cos\theta . \cos\theta \sin\phi . \sin\phi \, \mathrm{d}\phi \, \mathrm{d}\theta \\ &= 1.402\pi \int_0^{\pi - \phi_0} s^{2^{1/2}-1} \sin^2 s \, \mathrm{d}s \\ &= 1.402\pi . 7.077 \times 10^{-5} \\ &= 3.115 \times 10^{-4} \end{aligned}$$

showing that the contribution to the total impulse from the area around the crack is in the next significant figure after $I_x = 6.790$. From arguments based on symmetry, the components of the impulse in the y and z directions are zero: $I_y = I_z = 0$. So a horizontal gradient of pressure impulse, $G\underline{i}$, specified at infinity, gives a fixed sphere an impulse which is in the $\underline{i}$ direction and has magnitude $I_x = 1.621\left(\frac{4}{3}\pi a^3\right)G$.

6.4 A Spherical Boulder on a Beach

The impulse on a sphere on its tangent plane, $\underline{I} = 1.621\left(\frac{4}{3}\pi a^3\right)\underline{G}$ is only 8% larger than the impulse experienced by an isolated sphere, $1.5\left(\frac{4}{3}\pi a^3\right)\underline{G}$. This small difference suggests that we can well-approximate the impulse on a blunt randomly-shaped body by treating a sphere of the same volume. Since the impulse vector is parallel to $\underline{G}$ and to the plane, this work may help to explain the sudden movement of bodies away from a wave impact on a shingle beach.

Shingle beaches may not constitute a large part of the coastal zone on a world-wide scale, but in Britain they are particularly prevalent. During storms, shingle is often washed onshore so that beaches are steeper in winter. In the summer the generally smaller waves draw shingle away from the beach to offshore bars. Wave action on beaches also tends to grade beach material, pushing larger particles farther up the beach (landward) and finer ones toward the shoreline. Further, coarser beach material gives steeper slopes of beach. When the beach material differs greatly in size, large particles move over the fine material and are thrown up on the shore (Zenkovich 1967). Steers (1953, p.14) gives data for pebble movement in moderate weather conditions on the north Norfolk coast. This shows daily pebble displacements of up to 72 yards, although the size of the pebbles is not specified.

The pressure impulse field after a wave impacts on a shingle beach is only slightly modified, by the presence of the shingle, from that for a flat sloping wall, in the same way that P is distorted only in a small localised region around a body on the sea bed (as in Chapter 3). Typical values of beach slope are $6 - 10^\circ$ (Caldwell and Williams

1986; Palmer 1834). Okamura (1993) shows that the largest impulses occur when a wall is nearly vertical, but even for a wall at a very shallow angle we suggest that a breaking wave will still generate a large enough impulse to move a boulder on a beach. The pressure impulse gradient points up the beach above the wave impact and points down the beach below. Each boulder responds to the local applied pressure gradient - if it is free to move it acquires some initial speed from the fluid impulse and is eventually brought to rest by friction with neighbouring bodies, gravity and fluid resistance. In this way a body is displaced a short distance by each wave impact. A succession of impacts in one place can lead to the movement by many small steps of beach material both up and down the beach away from the site of impact.

To avoid the problem of the wave impact being changed by the presence of the sphere on the shore, we assume that it is some distance away from where the impact occurs. Our aim is to follow the motion of one boulder, of density ρ_B, which is free to move. We assume that the boulder is spherical so its cross-sectional area is $\mathcal{A} = \pi a^2$ and its volume is $\mathcal{V} = \frac{4}{3}\pi a^3$. The beach is at an angle α to the horizontal and we assume that $\rho_B > \rho$, so that the sphere rests initially on the beach surface, immersed in fluid. (We don't take into account the possibility of the sphere leaving the beach surface throughout its motion, although this is likely for smaller bodies and larger impact pressures - compare with mechanisms for shingle beach formation and sorting in Cornish (1898, §4,5).) This surrounding fluid moves up the beach at speed u_0, due to the wave approaching the shore before impact, but will experience a change in velocity due to the impact of the wave. We expect u_0 to be about 10 m sec^{-1}.

The complicated forces due to neighbouring boulders are modelled by a coefficient of friction, μ, between the sphere and the beach. If all the boulders on a beach were the same size, they would all be moved at similar velocities, so we assume that this one boulder is larger than the average shingle size and that it projects above the level of the beach. Therefore μ is not prohibitively large. These forces on the sphere act at its centre of mass; we ignore any overturning moments and any rolling of the sphere down the beach. Thus our attention is restricted to the translational motion. The wet weight of the boulder is $W = (\rho_B - \rho)\mathcal{V}g$ and the frictional force is $F_f = \mu(\rho_B - \rho)\mathcal{V}g\cos\alpha$, where g is the acceleration due to gravity. The drag force from the fluid flowing at speed v_w over a sphere which moves at speed V is $F_D = \frac{1}{2}\rho\mathcal{A}C_D(v_w - V)^2$, where C_D is a drag coefficient. Batchelor (1973, §5.11) suggests $C_D = 0.2$ for a sphere in water moving at 10 m sec^{-1}.

The fluid impulse generated by the pressure impulse gradient $G\underline{i}$ accelerates the sphere from rest to a velocity $V\underline{i}$, where now $\underline{i}$ is in a direction parallel to the beach. We dimensionalise P from (6.3.2) and then rewrite this expression in view of the comments in §3.5.3:

$$I_{Vx} = 0.828\pi(G - \rho V)a^3 + \frac{4}{3}\pi a^3 G = \frac{4}{3}\pi a^3\left(1.621G - 0.621\rho V\right).$$

Equating the change of momentum of the sphere, $\frac{4}{3}\pi\rho_B a^3 V$, with the impulse on it gives the speed of the sphere

$$V = \frac{1.621G}{0.621\rho + \rho_B} \tag{6.4.1}$$

and

$$I_{Vx} = \frac{4}{3}\pi a^3 G\frac{1.621\rho_B}{0.621\rho + \rho_B}. \tag{6.4.2}$$

After the impact the sphere moves with velocity V, given by (6.4.1). The velocity component of the water parallel to the beach after impact is v_w, which will be changed from u_0 by an amount equal to G/ρ. This change in fluid velocity during impact is only about twice the initial speed of the sphere but we would expect the sphere to be rapidly brought to rest by the frictional forces.

Two cases are treated, which are illustrated in figure 6.4.1.

- Case A: The wave breaks below the sphere, which is initially pushed up the slope by the impact. The fluid which moved past the sphere at speed u_0 is accelerated to move up the beach at speed $v_w = u_0 + G/\rho$, helping to continue the upslope motion of the sphere by fluid drag. Friction and the weight of the sphere oppose the motion.
- Case B: The wave impacts farther up the beach and the sphere is initially pushed down the slope by the wave impact. The water flows up the slope at

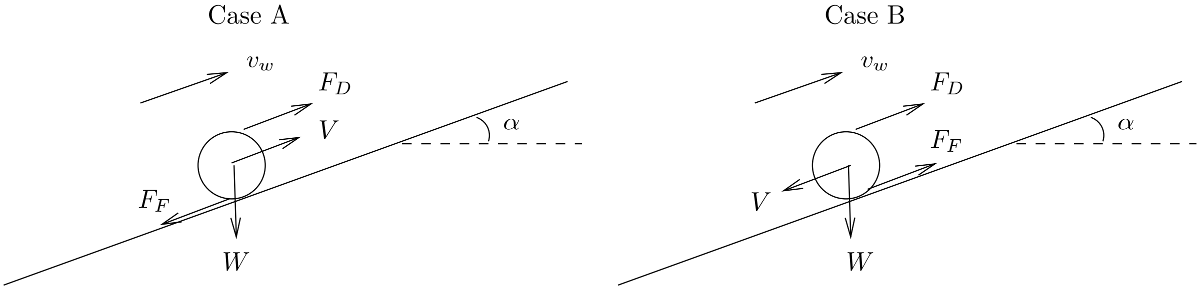

Figure 6.4.1: The geometry for cases A and B. In Case A the fluid flows up the beach, which is at an angle α to the horizontal, assisting the progress of the sphere, of weight $W = g(\rho_B - \rho)\mathcal{V}$, which moves at initial velocity V. In Case B the initial direction of motion of the sphere is down the beach rather than up. Friction opposes the motion in both cases, and the fluid drag acts up the beach.

speed $v_w = u_0 - G/\rho$, retarding the motion of the sphere by drag. In this case the weight of the boulder assists its motion down the slope.

Other combinations of the direction of the initial velocity and the water velocity can be modelled, but are almost equivalent, mathematically, to these two cases. The sphere's speed at time t is denoted by $V_i(t)$, where $i = 1, 2$ denotes case A or B. Similarly, the distance that it moves before first coming to rest at time $t_i > 0$ (i.e. $V_i(t_i) = 0$) is L_i.

6.4.1 Case A

The breaking wave impacts to seaward of the sphere so that the impulse pushes it up the slope, with initial speed $V_1 = V$, and water flows over it, up the beach, with speed, $v_w = u_0 + G/\rho$. Thus the water's motion aids the sphere's motion up the beach. This is modelled by the ODE

$$K^2 \left(v_w - V_1\right)^2 - c_+^2 = \frac{dV_1}{dt} \tag{6.4.3}$$

where

$$K^2 = \frac{1}{2}\frac{\rho \mathcal{A} C_D}{\rho_B \mathcal{V}} = \frac{3}{8}\frac{\rho C_D}{\rho_B a} \text{ and } c_+^2 = g\left(1 - \frac{\rho}{\rho_B}\right)(\mu\cos\alpha + \sin\alpha) > 0.$$

The first term on the left-hand side of (6.4.3) represents the drag forces and the second the frictional forces. Defining

$$\gamma_\pm = c_+ \pm K\left(v_w - V\right) \text{ and } \beta_\pm = c_+ \pm K v_w$$

gives the solution to (6.4.3):

$$V_1(t) = v_w + \frac{c_+}{K}\left[\frac{\gamma_- \mathrm{e}^{-2c_+Kt} - \gamma_+}{\gamma_- \mathrm{e}^{-2c_+Kt} + \gamma_+}\right]. \tag{6.4.4}$$

The sphere comes to rest after a time

$$t_1 = \frac{1}{2Kc_+}\log\left|\frac{\gamma_+\beta_-}{\gamma_-\beta_+}\right| \tag{6.4.5}$$

having travelled a distance up the beach of

$$L_1 = \frac{v_w}{2Kc_+}\log\left|\frac{\gamma_+\beta_-}{\gamma_-\beta_+}\right| + \frac{1}{2K^2}\log\left|\frac{\beta_+\beta_-}{\gamma_+\gamma_-}\right|. \tag{6.4.6}$$

6.4.2 Case B

In this case the water's motion retards the motion of the sphere. The wave has broken after passing landward of the sphere, so that the impulse acts in the seaward direction, whilst water is still passing over it up the beach with velocity $v_w = u_0 - G/\rho$. We solve

$$-K^2\left(v_w + V_2\right)^2 - c_-^2 = \frac{dV_2}{dt} \tag{6.4.7}$$

subject to $V_2(t=0) = V$ and where

$$c_-^2 = g\left(1 - \frac{\rho}{\rho_B}\right)\left(\mu\cos\alpha - \sin\alpha\right) > 0$$

i.e. $\mu > \tan(\alpha)$ so that the sphere is held at rest by friction when there are no impulsive forces ($v_w = u_0$). K is as for Case A. We redefine

$$\gamma_\pm = ic_- \pm K\left(v_w + V\right) \text{ and } \beta_\pm = ic_- \pm K v_w,$$

where $i = \sqrt{-1}$, and then the sphere's velocity down the beach is given by

$$\begin{aligned} V_2(t) &= -v_w + \frac{c_-}{K} \tan\left[-c_- Kt + \tan^{-1}\left(\frac{K\left(v_w + V\right)}{c_-}\right)\right] \\ &= -v_w - \frac{c_-}{K}\left[\frac{\gamma_- \mathrm{e}^{-2ic_- Kt} - \gamma_+}{\gamma_- \mathrm{e}^{-2ic_+ Kt} + \gamma_+}\right] \end{aligned} \tag{6.4.8}$$

and it comes to rest after a time

$$\begin{aligned} t_2 &= \frac{1}{Kc_-}\left[\tan^{-1}\left(\frac{K\left(v_w + V\right)}{c_-}\right) - \tan^{-1}\left(\frac{Kv_w}{c_-}\right)\right] \\ &= \frac{i}{2Kc_-} \log\left(\frac{\gamma_+ \beta_-}{\gamma_- \beta_+}\right) \end{aligned} \tag{6.4.9}$$

having moved a distance down the beach of

$$\begin{aligned} L_2 &= \frac{1}{K^2} \log\left(\frac{\cos\left(\tan^{-1}\left(\frac{Kv_w}{c_-}\right)\right)}{\cos\left(\tan^{-1}\left(\frac{K(v_w+V)}{c_-}\right)\right)}\right) - v_w t_2 \\ &= \frac{1}{2K^2} \log\left(\frac{c_-^2 + K^2\left(v_w + V\right)^2}{c_-^2 + K^2 v_w^2}\right) - \frac{iv_w}{2Kc_-} \log\left(\frac{\gamma_+ \beta_-}{\gamma_- \beta_+}\right) \\ &= -\frac{iv_w}{2Kc_-} \log\left(\frac{\gamma_+ \beta_-}{\gamma_- \beta_+}\right) - \frac{1}{2K^2} \log\left(\frac{\beta_+ \beta_-}{\gamma_+ \gamma_-}\right). \end{aligned} \tag{6.4.10}$$

Note that, despite the presence of the complex number i, the quantities V_2, t_2 and L_2 are all real.

6.4.3 Results

The form of the solutions for V_i, t_i and L_i are similar for $i = 1, 2$. Figure 6.4.2 shows the distance that the sphere moves for each of the two cases, L_1 and L_2, as a function of G/ρ, the change in velocity of the water flowing over the sphere due to the wave impact. The sphere of radius $a = 0.2$ m is set into motion by the wave impact. It has density $\rho_B = 3\rho$ so that its initial velocity is $V = 0.45G/\rho$. In Case A the sphere moves a large distance even for small changes in water velocity, showing how the fluid drag assists its progress. As G/ρ increases the initial velocity of the sphere is a higher fraction of the fluid velocity, so that this drag effect decreases and the

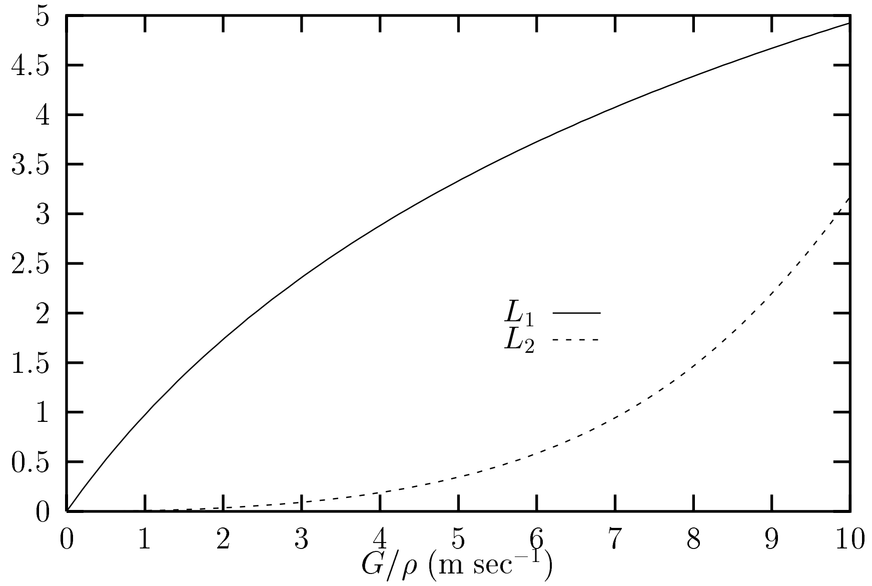

Figure 6.4.2: The distances, in metres, moved by the sphere before it first comes to rest in Case A (L_1) and Case B (L_2) as functions of the change in fluid velocity due to the wave impact, G/ρ. The parameters used are $\mu = 0.5, a = 0.2$ m, g $= 9.8$ m sec^{-2}, $\rho_{\mathrm{B}}/\rho = 3.0, \alpha = 10.0^\circ$ and $C_D = 0.2$. This gives $K = 0.353, c_+ = 2.11$ and $c_- = 1.44$. The sphere is given an initial impulsive velocity of $V = 0.45G/\rho$. The spherical boulder can move about 5 m up the beach or 3 m down the beach.

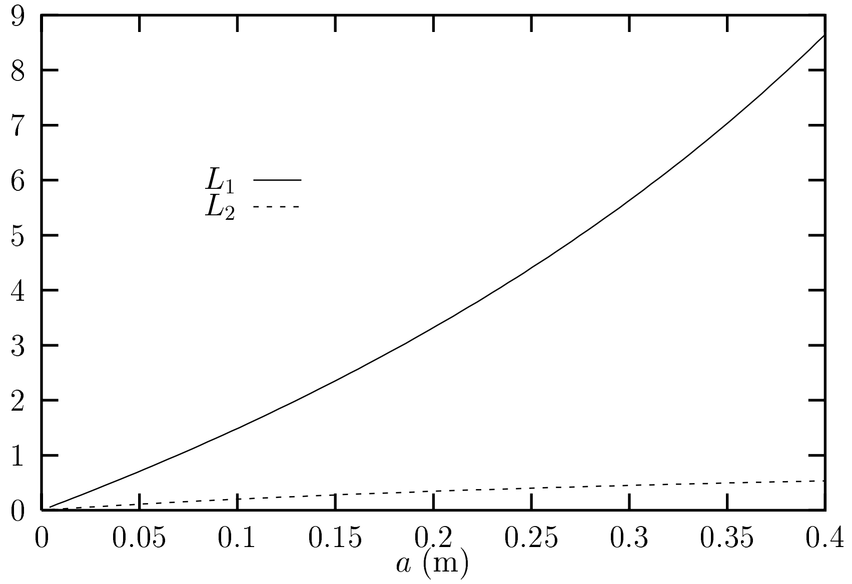

Figure 6.4.3: The distances, in metres, moved by the sphere before it first comes to rest in Case A (L_1) and Case B (L_2) as functions of its radius a. The parameters used are $\mu = 0.5, g = 9.8$ m sec^{-2}, $\rho_{\mathrm{B}}/\rho = 3.0, \alpha = 10.0°, \mathrm{G}/\rho = 5$ m sec^{-1} and $C_D = 0.2$. This gives $c_+ = 2.11$ and $c_- = 1.44$. The sphere is given an initial impulsive velocity of $V = 2.25$ m sec^{-1}.

gradient of the graph decreases. For a change in fluid speed of $G/\rho = 10$ m sec^{-1}, the boulder moves almost 5 m up the beach. This is associated with a value of the impulsive pressure gradient of $G = 10^4$ N sec m^{-3}, which is over ten times larger than the gradients predicted in Chapter 2. In Case B the boulder moves only short distances for changes in water velocity of up to 5 m sec^{-1}, due to the high fluid drag up the beach. However, at $G/\rho = 10$ m sec^{-1} the fluid is brought to rest around the sphere and it travels about 3 m down the beach. For Case A, increasing ρ_B or μ both act to decrease L_1. In contrast, increasing ρ_B or decreasing μ will increase L_2.

Figure 6.4.3 shows that as the radius of the sphere, a, increases, the distance moved either up or down the beach increases. Again, a boulder will move farther up than down the beach. This may explain the observation, stated at the beginning of

§6.4, that larger boulders collect at the top of the beach or offshore on bars. Also, boulders will move farther up the beach than down, so that a boulder is more likely to be thrown up on the shore. Note that the water only flows up the beach for a short time, then recedes before the next wave breaks, so that in practice the sphere is likely to come to rest before being moved by the next impact event. During a storm there may be hundreds of wave impacts which, collectively, will allow a body to be moved a considerable distance.

The $L_i, i = 1, 2$ represent the distance travelled by a sphere on an inclined plane beach. We define an angle β that the incoming wave makes with the line of steepest ascent up the beach, and a coordinate system $\underline{i}, \underline{j}, \underline{k}$ where $\underline{i}$ points landward, $\underline{j}$ along the shoreline and $\underline{k}$ vertically upward. Then the direction in which the sphere moves on the plane of the beach (assuming that it moves in short straight jumps) is

$$\underline{L_i} = L_i \left(\cos\beta \cos\alpha \, \underline{i} + \sin\beta \, \underline{j} + \cos\beta \sin\alpha \, \underline{k}\right), \qquad i = 1, 2.$$

Thus, given the angle of incidence of waves on a beach, it is possible to follow the process of what Palmer (1834) calls progression, where a boulder is moved up and along the beach. A boulder will be pushed in the direction of $\underline{L_i}$ until coming to rest after a distance L_i and will then be dragged seaward, down the line of steepest descent by the backwash, this latter motion generally being shorter, particularly for larger bodies.

6.5 Conclusions

The calculations outlined above provide a simple method for visualising the flow around a sphere on a tangent plane. The problem can be viewed as a stationary sphere at the origin, with ∇P a specified constant at infinity, or as a sphere moving in the direction of the positive x-axis in fluid at rest. The errors, as measured by how closely the boundary condition on the sphere is satisfied, are small compared with those of Li *et al* (1993).

The sphere experiences no impulsive lift. The impulse is parallel to the applied pressure gradient $\underline{G}$, and to the tangent plane, and is $1.621\left(\frac{4}{3}\pi\rho a^3\right)\underline{G}$ for a sphere of radius a. This is only 8% larger than the impulse experienced by an isolated sphere, $1.5\left(\frac{4}{3}\pi\rho a^3\right)\underline{G}$.

Due to this small difference in impulse, we can approximate any blunt, randomly shaped, boulder on a shingle beach by a sphere. We show that the effect of a wave impact on a beach is to move a boulder with a velocity proportional to the pressure impulse gradient. The distance the boulder moves is proportional to its size, so that large boulders will collect towards the top or bottom of a beach, rather than in the surf zone.

Chapter 7

Concluding Remarks

We have reviewed the literature concerning the modelling of wave breaking against coastal structures, and then defined Pressure Impulse Theory and discussed its uses. By solving Laplace's equation for the pressure impulse, P, in a semi-infinite domain with mixed boundary conditions, we represent a wave breaking against a vertical wall. By altering the velocity profile of this hypothetical impacting wave, it is found that a vertical wave face gives the highest peak pressures, of over $20\rho gh$, but that other profiles give peak pressures of the same order of magnitude. We therefore conclude that the choice of impact velocity profile is fairly unimportant compared to other parameters such as wave speed and height. P is given by an infinite sum, so we derive an approximate method for finding the pressure impulse distribution on the wall. This takes the form of a series solution, with some additional terms, which requires repeated integration of only four terms to give accuracy to seven decimal places.

The distribution found for P in the semi-infinite domain is then used to find the effect of wave impact (on the wall) on a body resting on the sea bed. There is often a large pressure impulse gradient, G, acting away from the wall, which causes an impulse to act on a body protruding above the flat bed. We demonstrate how to use either a Fourier series or a conformal map to represent the body, although the former is inaccurate and unwieldy. The impulse on the body is related to its added mass and its volume. Moreover, we can find the impulse even if P cannot be found explicitly. If the body has a vertical line of symmetry then the impulse is parallel to G and, for bodies with length scales of over about half a metre, this impulse is great enough to overcome the frictional forces that normally hold an object in place and move it away from the wall. For an asymmetric body, the impulse can have a component perpendicular to the direction of G. This method is also used to find information about the impulse on a body attached to the vertical wall below the zone of impact, or on a crack in the same place.

In a similar way we find from the large scale calculation that there is an impulsive pressure gradient at the surface, not far from the wall. A body which pierces the free surface will therefore gain a vertical velocity at the instant of wave impact against the wall. We can again relate this velocity (or the related impulse) to the added mass and the volume of the body. We calculate that these velocities will be about 2 m $\sec^{-1}$. Even when the pressure impulse cannot be found, we can again calculate the velocity and impulse. For an asymmetric body, an example is given showing that the body also experiences a horizontal impulse, causing a horizontal component of velocity parallel to the free surface. Previous work on the velocity potential, Φ, of the fluid around a body impacting on the surface is exploited by relating P to Φ.

In a fluid filled crack in the vertical wall, we integrate the pressure impulse over the (small) height of the crack to give a new field equation for P. We are able to solve this for several geometries; in particular when the roof of the crack is made up of piecewise linear segments and the crack is uniform in a direction parallel to the face of the wall in which it is situated. This enables a comparison of the forces acting on a constituent block to be made, showing that small blocks are likely to be pushed apart by the force of the wave impact. This equation, when transformed into polar coordinates, also applies to the crack under an axisymmetric body which is at rest on the sea bed. Close to the contact point, we can find P under objects such as a sphere, which is useful when the pressure impulse around the whole body is hard to calculate.

An interesting, and difficult, case of a body on the sea bed is the three-dimensional solution for P around a sphere on the sea bed exposed to a pressure impulse gradient. A numerical solution with small error is found and matched to the crack solution obtained earlier. This is of particular interest when considering the movement of rounded boulders on a beach subjected to wave impact. We show that these boulders are moved a distance up the beach proportional to their size, so that larger boulders collect near the top of the beach. Our analysis suggests that individual wave impacts can move a spherical boulder, of radius 20 cm, distances of the order of metres.

Much of the work described can be easily generalised to three-dimensions. It seems unlikely that PIT can be extended further in this direction (although see Cooker (1996) on including the nonlinear terms in Euler's equations) but, for instance, our analysis of pressure impulses in cracks requires much more study. The three-dimensional results presented there are all either uniform in one direction or axisymmetric. It would also be useful to have experimental results with which to compare our existing answers - in particular, measurements of pressure in cracks, having simple geometrical shapes, situated below the impact zone on a wall.

The work of Chapter 3 needs more analysis of asymmetric shapes on the sea bed, to better understand how a horizontal pressure gradient can cause a vertical impulse. We have not analysed the turning moments acting on a body: this would be particularly pertinent in the cases of the inclined plate and circular arc. It would also be instructive to construct more shapes with an overhang (as for the circle), to see if other bodies which, in a sense, trap fluid are also likely to receive a greater impulse. The work of this chapter is an area which would benefit from some comparisons with simple experiments of a small object being moved along the bed by wave impact.

In the same way the work of Chapter 4 could be extended to more axisymmetric surface-piercing bodies which may experience a horizontal impulse. However, finding the shape of an object from the conformal map is difficult and a method of visualising the pressure impulse contours is still required. It is of course possible to do many more examples using numerical techniques, though the results may be hard to interpret. For these surface-piercing bodies, the effect of the jets that may be formed when the impact occurs could be included. Our expressions for the added mass of a rectangle could be compared with the graph in Sedov (1965, fig. 3.17) which is taken from a paper written in Russian.

We believe it will be possible to find an analytical solution for $\alpha(q)$ in Chapter 6. This would give an exact expression for the added mass coefficient for touching spheres moving perpendicular to their line of centres. The work there could be extended by thinking about more spheres interacting, to model a continuum of boulders on a beach.

Appendix I

Some Definite Integrals of Functions of 1/arccoth(x)

In §3.6.3 and §4.4.1 we use a conformal map in the form

$$z(w) = \frac{1}{\coth^{-1}(w)}$$

to relate the flow in a complex half-plane to that around a circle on the real axis. In calculating fluid impulses on the circles, two integrals arise, both containing the reciprocal of $\coth^{-1}(x)$. We construct two general classes of integral, of which each of these is a member, and show how to evaluate these integrals using substitutions and Cauchy's residue theorem.

Theorem 1 *For any* $0 < a \in \mathbb{R}$*,*

$$J_1(a) = \int_{-1}^{1} \frac{\mathrm{d}x}{[\coth^{-1}(x)]^a} = 2a(i\pi)^{-a}\zeta(a+1)$$

where ζ *is the Riemann zeta function.*

Proof. We initially note that $\coth^{-1}(x)$ is purely imaginary on the interval $[-1, 1)$. Also, if a is an even integer then J_1 is real and if a is an odd integer then J_1 is purely

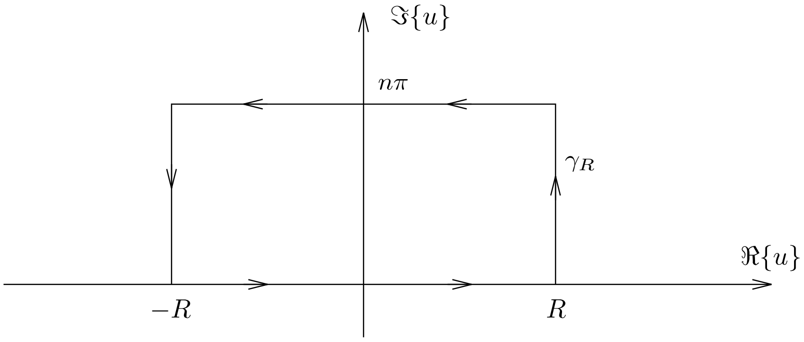

Figure I.0.1: The contour of integration, C, consisting of the real line between $-R$ and R, along with the rectangle γ_R. C is described anticlockwise. $\Re\{u\}$ and $\Im\{u\}$ denote the real and imaginary parts of u respectively.

imaginary. When a is non-integral, the principle value of the a^{th} power is assumed. Making the substitution $x = \tanh(u)$ gives

$$J_1(a) = \int_{-\infty}^{\infty} \frac{\mathrm{d}u}{(u + i\pi/2)^a \cosh^2 u}.$$

where we have taken the principle root, $m = 1$, of $\coth^{-1}(\tanh(u)) = u + i(m + \frac{1}{2})\pi$. In the upper half of the complex u plane we now construct a contour, C, described anticlockwise, made up of a rectangle, γ_R, of height $n\pi$ ($n \in \mathbb{N}$) and width $2R$, and the real axis between $-R$ and R. See figure I.0.1. We assume $R > n^{2/a}$. In the upper half-plane, the function $f(u) = 1/(u + i\pi/2)^a \cosh^2 u$ has simple poles at $u = (2k-1)i\pi/2$ ($k \in \mathbb{N}$). (Note that we can ignore the poles and the branch cut in the lower half-plane.) The Laurent expansion of f at each pole gives the coefficient of $1/(u - (2k-1)i\pi/2)$. Making the substitution $v = u - (2k-1)i\pi/2$ and expanding f about $v = 0$ gives

$$\begin{aligned} f(v) &= \frac{1}{(v + ki\pi)^a \cosh^2(v + (2k-1)i\pi/2)} \\ &= \frac{1 - av/(ki\pi) + O(v^2)}{(ki\pi)^a(1 - \cosh^2(v))} \\ &= \frac{1 - av/(ki\pi) + O(v^2)}{(ki\pi)^a(-v^2 + O(v^4))} \end{aligned}$$

so that the coefficient of $1/v$ is $a/(ki\pi)^{(a+1)}$. We have, by Cauchy's theorem, that

$$\int_C \frac{\mathrm{d}u}{(u+i\pi/2)^a \cosh^2 u} = \int_{-R}^{R} \frac{\mathrm{d}u}{(u+i\pi/2)^a \cosh^2 u} + \int_{\gamma_R} \frac{\mathrm{d}u}{(u+i\pi/2)^a \cosh^2 u}. \tag{I.0.1}$$

We need to show that this last integral around γ_R tends to zero as R and n both tend to infinity. The integral is separated into three parts, each corresponding to a straight line segment of the rectangle:

$$\begin{aligned}\int_{\gamma_R} \frac{\mathrm{d}u}{(u+i\pi/2)^a \cosh^2 u} &= \int_0^{n\pi} \frac{i\mathrm{d}y}{[R+i(y+\pi/2)]^a \cosh^2(R+iy)} && \text{(I.0.2)}\\ &+ \int_R^{-R} \frac{\mathrm{d}x}{[x+i\pi(n+\frac{1}{2})]^a \cosh^2(x+in\pi)} && \text{(I.0.3)}\\ &- \int_0^{n\pi} \frac{i\mathrm{d}y}{[-R+i(y+\pi/2)]^a \cosh^2(-R+iy)} && \text{(I.0.4)}\end{aligned}$$

and then we show that each individual integral tends to zero. Thus, for (I.0.2),

$$\begin{aligned}\left|\int_0^{n\pi} \frac{i\mathrm{d}y}{[R+i(y+\pi/2)]^a \cosh^2(R+iy)}\right| &\leq \int_0^{n\pi} \left|\frac{\mathrm{sech}^2(R+iy)}{[R+i(y+\pi/2)]^a}\right| \mathrm{d}y\\ &\leq \mathrm{sech}^2(R) \int_0^{n\pi} \frac{\mathrm{d}y}{|[R+i(y+\pi/2)]^a|}\\ &\leq \mathrm{sech}^2(R)\frac{n\pi}{R^a}\end{aligned}$$

which tends to zero as $R \to \infty$ and $n \to \infty$ for all $a > 0$, provided $R > n^{2/a}$. The same argument shows that (I.0.4) tends to zero. We note that the contour, γ_R, avoids the poles on the imaginary axis, so for (I.0.3),

$$\begin{aligned}\left|\int_R^{-R} \frac{\mathrm{d}x}{[x+i\pi(n+\frac{1}{2})]^a \cosh^2(x+in\pi)}\right| &\leq \int_{-R}^{R} \frac{\mathrm{sech}^2 x \ \mathrm{d}x}{\left|[x+i\pi(n+\frac{1}{2})]^a\right|}\\ &\leq \frac{1}{(\pi n)^a} \int_{-R}^{R} \mathrm{sech}^2 x \ \mathrm{d}x\\ &\leq \frac{2\tanh(R)}{(\pi n)^a}\end{aligned}$$

which tends to zero as $n \to \infty$ for all $a > 0$. Thus the integral around γ_R tends to zero.

Traversing C in an anticlockwise direction and applying Cauchy's residue theorem to the first term in (I.0.1) gives

$$\int_C \frac{\mathrm{d}u}{(u+i\pi/2)^a \cosh^2 u} = 2\pi i \sum_{k=1}^{n} \frac{a}{(ki\pi)^{(a+1)}} = \frac{2a}{(i\pi)^a} \sum_{k=1}^{n} \frac{1}{k^{a+1}}.$$

Thus, as $R \to \infty$ and $n \to \infty$, we obtain

$$\begin{aligned} J_1(a) &= \int_{-\infty}^{\infty} \frac{\mathrm{d}u}{(u+i\pi/2)^a \cosh^2 u} \\ &= \int_C \frac{\mathrm{d}u}{(u+i\pi/2)^a \cosh^2 u} \\ &= \frac{2a}{(i\pi)^a} \sum_{k=1}^{\infty} \frac{1}{k^{a+1}} = \frac{2a\zeta(a+1)}{(i\pi)^a}. \end{aligned}$$

This completes the proof. □

Since the Riemann zeta function is undefined at one, note that as $a \to 0$,

$$J_1(0) = 2 = \lim_{a\to 0} \frac{2}{(i\pi)^a} a\,\zeta(a+1) = \lim_{a\to 0} 2a\,\zeta(a+1). \tag{I.0.5}$$

So we see that $\zeta(1+a) \sim 1/a$ as $a \to 0$. Note also that in §3.6.3 we require $J_1(1) = -\frac{1}{3} i\pi$.

Theorem 2 *For any* $1 < a \in \mathbb{R}$,

$$\begin{aligned} J_2(a) &= \int_{-1}^{1} \frac{\mathrm{d}x}{[\coth^{-1}(x)]^a \sqrt{1-x^2}} = \int_{-\pi/2}^{\pi/2} \frac{\mathrm{d}y}{[\coth^{-1}(\sin(y))]^a} \\ &= 2i^{-a}\pi^{1-a}(1-2^{1-a})\,\zeta(a). \end{aligned}$$

Proof. Again, if a is an even integer then J_2 is real and if a is an odd integer then J_2 is purely imaginary. We substitute $x = \tanh(u)$, as before, to give

$$J_2(a) = \int_{-\infty}^{\infty} \frac{\mathrm{d}u}{(u+i\pi/2)^a \cosh u}.$$

We follow the same procedure, and use the same contour, as in Theorem 1. In the upper half-plane the integrand has simple poles at $u = (2k-1)i\pi/2$ ($k \in \mathbb{N}$) with residue $(-1)^k i/(ki\pi)^a$. The integral around the rectangle γ_R tends to zero as R and n tend to infinity and Cauchy's residue theorem gives

$$\int_C \frac{\mathrm{d}u}{(u+i\pi/2)^a \cosh u} = 2\pi i \sum_{k=1}^{\infty} \frac{(-1)^k i}{(ki\pi)^a} = \frac{2}{i^a \pi^{a-1}} \sum_{k=1}^{\infty} \frac{(-1)^{k+1}}{k^a}.$$

Then by Cauchy's theorem, in the limit as $R \to \infty$, we get

$$J_2(a) = \frac{2}{i^a \pi^{a-1}} \sum_{k=1}^{\infty} \frac{(-1)^{k+1}}{k^a} = \frac{2(1-2^{1-a})\,\zeta(a)}{i^a \pi^{a-1}} \tag{I.0.6}$$

which completes the proof. □

Since, in the limit as a tends to one, $\zeta(a)$ is undefined, we calculate $J_2(1)$ by substituting (I.0.5) in (I.0.6) to give

$$\begin{aligned}
J_2(1) &= \lim_{a\to 1} -2i(1-2^{1-a})\,\zeta(a) \\
&= \lim_{a\to 1} -2i\frac{(1-2^{1-a})}{1-a} \\
&= \lim_{a\to 1} -2i\frac{(1-\mathrm{e}^{(1-a)\log(2)})}{1-a} \\
&= \lim_{a\to 1} -2i\left(-\log(2) + O\left((1-a)^2\right)\right) \\
&= 2i\log(2)
\end{aligned}$$

where we have used the binomial expansion for the exponential, $\mathrm{e}^x = 1 + x + O(x^2)$. Note that in §4.4.1 we require $J_2(2) = -\frac{1}{6}\pi$.

It seems therefore that, in general, to calculate these ostensibly tricky integrals, we have only to make the substitution $x = \tanh(u)$ and use Cauchy's residue theorem around this particular contour C. If we can do the infinite sum, then the integral can be found in closed form (in general this is only possible when k is raised to an even integer power, see Jolley (1961)). Otherwise, the Riemann zeta function is tabulated (in, for instance, Abramowitz and Stegun 1965).

Appendix II

The Impulse on an Aerofoil

In order to calculate the impulse, $\underline{I} = (I_x, I_y)$, on an aerofoil lying on the sea bed, in Chapter 3, with an applied pressure impulse gradient, G, along the sea bed, we use (3.5.5):

$$I_x + iI_y = -iP_0\left(z(u_2) - z(u_1)\right) + iGd\left(u_2 z(u_2) - u_1 z(u_1)\right) - iGd\int_{u_1}^{u_2} z(u)\mathrm{d}u.$$

The conformal map, (3.6.15), is

$$z(w) = \frac{(1+k)}{2}\left(w + \sqrt{w^2 - 4a^2}\right) + ak + \frac{2a^2}{(1+k)\left(w + \sqrt{w^2-4a^2}\right) + 2ak}$$

and u is the real part of w. Since $z \sim (1+k)w$ as $|z| \to \infty$, we have $d = 1+k$. This map takes the real line between $u_1 = -2a$ and $u_2 = 2a$ to the top half of a symmetric aerofoil with ends at $z(u_1) = -2a$ and $z(u_2) = a[1 + 2k + 1/(1+2k)]$ on the real line.

We will need the following result: using the substitution $u = \cosh x$ and Gradshteyn and Ryzhik (1965, eq.2.451.3) we can write, for $0 \le r < 1$,

$$\begin{aligned} I_1(r) &= \int_{-1}^{1} \frac{\mathrm{d}u}{u + \sqrt{u^2-1} + r} \\ &= -\int_0^{i\pi} \frac{\sinh x \ \mathrm{d}x}{\cosh x + \sinh x + r} \\ &= \frac{1}{r} - \frac{1}{2}\left(\frac{1}{r^2} - 1\right)\log\left(\frac{1+r}{1-r}\right) - \frac{i\pi}{2}. \end{aligned}$$

Then the impulse is

$$\begin{aligned}
I_x + iI_y = {} & -iP_0 a\left(1+2k+\frac{1}{1+2k}+2\right) + 2a^2 iG(1+k)\left(1+2k+\frac{1}{1+2k}-2\right) \\
& -iG(1+k)\int_{-2a}^{2a}\left[\frac{(1+k)}{2}\left(u+\sqrt{u^2-4a^2}\right)+ak\right. \\
& \left.+\frac{2a^2}{(1+k)\left(u+\sqrt{u^2-4a^2}\right)+2ak}\right]\mathrm{d}u \\
= {} & -iP_0 a\left(3+2k+\frac{1}{1+2k}\right) + 2a^2 iG(1+k)\left(-1+2k+\frac{1}{1+2k}\right) \\
& -iG(1+k)\left[ia^2(1+k)\pi + 4a^2k + \frac{2a^2}{1+k}I_1\left(\frac{k}{1+k}\right)\right] \\
= {} & -4iP_0 a\frac{(1+k)^2}{1+2k} + 2a^2 iG(1+k)\left(-1+\frac{1}{1+2k}\right) \\
& +Ga^2(1+k)^2\pi - 2iGa^2\left[\frac{1+k}{k}-\frac{1}{2}\left(\frac{1+2k}{k^2}\right)\log(1+2k)-\frac{i\pi}{2}\right] \\
= {} & Ga^2\pi k(2+k) - 4iP_0 a\frac{(1+k)^2}{1+2k} - 4a^2 iG\frac{k(1+k)}{1+2k} \\
& -2iGa^2\left[\frac{1+k}{k}-\left(\frac{1+2k}{2k^2}\right)\log(1+2k)\right] \\
= {} & Ga^2\pi k(2+k) - 4iP_0 a\frac{(1+k)^2}{1+2k} \\
& -2a^2 iG\left[\frac{2k(1+k)}{1+2k}+\frac{1+k}{k}-\left(\frac{1+2k}{2k^2}\right)\log(1+2k)\right].
\end{aligned}$$

Taking real and imaginary parts gives

$$\begin{aligned}
I_x &= Ga^2\pi k(2+k) \\
-I_y &= 4P_0 a\frac{(1+k)^2}{1+2k} + 2a^2 G\left[\frac{2k(1+k)}{1+2k}+\frac{1+k}{k}-\left(\frac{1+2k}{2k^2}\right)\log(1+2k)\right].
\end{aligned}$$

Appendix III

A Program for Computing the Coefficients for Piecewise Linear Cracks

The following Maple (Vr3) script is used to find the unknown coefficients in the matching process described in equation (5.4.11). The notation is $A(m)$ for A_{mn} and $B(m)$ for B_{mn}. Also note that $a2(m)$ and $c(m)$ are constructs used in the iterative substitutions, that S_n is written as $A_{0n}+B_{0n}$ and that $\overline{\overline{p}}$ must be written, for instance, as *pbb* etc.

$M := 3;$ #Set number of segments

$B(M) := 0;$ #In sloping end segment, B is zero

$A(0) := S_n;$ #Set up starting conditions from seaward end

$B(0) := 0;$

$F := m \rightarrow A(m) + B(m) = A(m+1)p(m) + B(m+1)s(m);$ #Match Pressures

$G := m \rightarrow a2(m)\overline{p}(m) + B(m)\overline{s}(m) = a2(m+1)\overline{\overline{p}}(m) + B(m+1)\overline{\overline{s}}(m);$ #Match Velocities

```
for $m$ from 1 to $M$ do #Iteratively get each A as function of B's
  $A(m) := \text{solve}(F(m-1), A(m))$
od;
```

```
$a2(1) := A(1)$; #All the a2's will be put equal to A's to find the B's
```

```
for $m$ from 2 to $M$ do #Find the a2's as functions of B's
  $a2(m) := \text{solve}(G(m-1), a2(m))$
od;
```

```
for $m$ from 2 to $M-1$ do #find B's in terms of B(1), by matching A and a2 and resubstituting
  $c(m) := \text{solve}(a2(m) = A(m), B(m)):$
  for $n$ from 2 to $m$ do
    $A(m+1) := \text{subs}(B(n) = c(n), a(m+1)):$
    $a2(m+1) := \text{subs}(B(n) = c(n), a2(m+1))$
  od;
od; #Note that $c(i) = b(i)$, but need this notation to allow resubstitution
```

```
$c(1) := \text{solve}(a2(M) = A(M), B(1))$; #Now find $B(1)$
```

```
for $m$ from 1 to $M$ do # Resubstitute to get A's
  for $n$ from 2 to $m-1$ do
    $A(m) := \text{subs}(B(n) = c(n), A(m))$
  od;
```

```
  $A(m) := \mathrm{subs}(B(1) = c(1), A(m))$
od;
```

```
for $m$ from 2 to $M - 1$ do # Resubst. to get B's
  for $n$ from 1 to $m - 1$ do
    $B(m) := \mathrm{subs}(B(n) = c(n), c(m))$
  od;
  $B(m) := B(m)$
od;
```

```
$B(1) := c(1)$;
```

Bibliography

Abramowitz, M. and Stegun, I.A. 1965 *Handbook of Mathematical Functions.* Dover, New York.

Bagnold, R.A. 1939. Interim report on wave-pressure research. *J. Inst. Civil Eng.* **12**:201–226.

Baird, W.F., Caldwell, J.M., Edge, W.L., Magoon, O.T. and Treadwell, D.D. 1980. Report on the damages to the Sines Breakwater, Portugal. In *Proc. 17th Intl. Conf. Coastal Eng.* ASCE Sydney, Australia. pp. 3063–3077.

Batchelor, G.K. 1973 *An Introduction to Fluid Dynamics.* Cambridge University Press.

Bickley, W.G. 1932. Two-dimensional potential problems for the space outside a rectangle. *Proc. Lond. Math. Soc.* **37**:82–105.

Blackmore, P.A. and Hewson, P.J. 1984. Experiments on full-scale wave impact pressures. *Coastal Eng.* **8**:331–346.

Bromwich, T.J.I'A. 1926 *An Introduction to the Theory of Infinite Series.* Macmillan, London.

Byrd, P.F. and Friedman, M.D. 1971 *Handbook of Elliptic Integrals.* Springer, Berlin.

Caldwell, N.E. and Williams, A.T. 1986. Spatial and seasonal pebble beach profile characteristics. *Geol. J.* **21**(2):127–138.

Chan, E.S. 1994. Mechanics of deep water plunging-wave impacts on vertical structures. *Coastal Eng.* **22**:115–133.

Chan, E.S., Cheong, H.F. and Tan, B.C. 1995. Laboratory study of plunging wave impacts on vertical cylinders. *Coastal Eng.* **25**:87–107.

Chan, E.S. and Melville, W.K. 1988. Deep-water plunging wave pressures on a vertical plane wall. *Proc. R. Soc. Lond.* A **417**:95–131.

Collins, W.D. 1960. On the solution of some axisymmetric boundary value problems by means of integral equations III. Some electrostatic and hydrodynamic problems for two spherical caps. *Proc. Lond. Math. Soc.* **3**(10):428–460.

Cooker, M.J. 1996. Sudden changes in a potential flow with a free surface due to impact. *Q. J. Mech. Appl. Math.* **49**:581–591.

Cooker, M.J. 1997. Recent numerical calculations of two-dimensional jets induced by breaking-wave impact: a comment. *Phil. Trans. R. Soc. Lond.* A **355**(1724): 687–689.

Cooker, M.J. 1998. The accurate summation of some awkward series. *Math. Gaz.* **82** (493):48–55.

Cooker, M.J. and Peregrine, D.H. 1990. A model for breaking wave impact pressures. In *Proc. 22nd Intl. Conf. Coastal Eng.* ASCE Delft, Netherlands. pp. 1473–1486.

Cooker, M.J. and Peregrine, D.H. 1992. Wave impact pressure and its effect upon bodies lying on the sea bed. *Coastal Eng.* **18**:205–229.

Cooker, M.J. and Peregrine, D.H. 1995. Pressure-impulse theory for liquid impact problems. *J. Fluid Mech.* **297**:193–214.

Copson, E.T. 1935 *An Introduction to the Theory of Functions of a Complex Variable.* Clarendon, Oxford.

Cornish, V. 1898. On Sea-Beaches and Sandbanks. *Geogr. J.* **11**:528–543,628–651.

Cox, S.J. and Cooker, M.J. 1998. The effect of wave impact on a body in the breaker zone. In *Proc. 13th Intl. Workshop Water Waves Floating Bodies* (ISBN 90-407-1720-6). Delft, The Netherlands pp. 15–20.

Cox, S.J. and Cooker, M.J. 2000. Potential flow past a sphere touching a tangent plane. *J. Eng. Math.* **38**:355–370.

Cunningham, B. 1928 *Harbour Engineering.* C. Griffin.

Davis, A.M.J. 1977. High frequency limiting virtual-mass coefficients of heaving half-immersed spheres. *J. Fluid Mech.* **80**:305–319.

Denny, D.F. 1951. Further experiments on wave pressures. *J. Inst. Civil Eng.* **35**: 330–345.

Dold, J.W. 1992. An efficient Surface-Integral Algorithm Applied to Unsteady Gravity Waves. *J. Comput. Phys.* **103**:90–115.

Dold, J.W. and Peregrine, D.H. 1986. An efficient boundary-integral method for steep unsteady water waves. In Morton, K.W. and Baines, M.J. (eds), *Numerical Methods for Fluid Dynamics II.* Oxford University Press. pp. 671–679.

Eames, I., Hunt, J.C.R. and Belcher, S.E. 1996. Displacement of inviscid fluid by a sphere moving away from a wall. *J. Fluid Mech.* **324**:333–353.

Fabrikant, V.I. 1991 *Mixed Boundary Value Problems of Potential Theory and their Applications in Engineering.* Kluwer, Dordrecht.

Gaillard, D.D. 1904 *Wave Action in Relation to Engineering Structures.* U.S. Government Printing Office.

Gradshteyn, I.S. and Ryzhik, I.M. 1965 *Table of Integrals, Series, and Products.* Edited by Alan Jeffrey. Academic Press, New York. 5th edition.

Greenhow, M. 1988. Water-entry and -exit of a horizontal circular cylinder. *Appl. Ocean Res.* **10**(4):191–198.

Greenhow, M. and Yanbao, L. 1987. Added masses for circular cylinders near or penetrating fluid boundaries - review, extension and application to water-entry, -exit and slamming. *Ocean Engng.* **14**(4):325–348.

Grilli, S.T., Losada, M.A. and Martin, F. 1993. Wave Impact Forces on Mixed Breakwaters. In *Proc. 23rd Intl. Conf. Coastal Eng.* ASCE Venice, Italy, 1992. pp. 1161–1174.

Gröbner, W. and Hofreiter, N. 1965 *Integraltafel,* Teil I*, Unbestimmte Integrale.* Springer, Wien.

Hattori, M., Arami, A. and Yui, T. 1994. Wave impact pressure on vertical walls under breaking waves of various types. *Coastal Eng.* **22**:79–114.

Hitachi, S. 1994. Case study of breakwater damages – Mutsu-Ogawara Port. In *Proc. Intl. Workshop on Wave Barriers in Deepwaters.* Port and Harbour Research Institute, Japan. pp. 308–329.

Howison, S.D., Ockendon, J.R. and Wilson, S.K. 1991. Incompressible water-entry problems at small deadrise angles. *J. Fluid Mech.* **222**:215–230.

Jeffrey, A. 1992 *Complex Analysis and Applications.* CRC, London.

Jolley, L.B.W. 1961 *Summation of series.* Dover, New York.

Kober, H. 1957 *A Dictionary of Conformal Representations.* Dover, New York.

Kortenhaus, A., Oumeraci, H., Kohlhase, S. and Klammer, P. 1994. Wave-induced uplift loading of caisson breakwaters. In *Proc. 24th Intl. Conf. Coastal Eng.* ASCE Kobe, Japan. pp. 1298–1311.

Lamb, H. 1932 *Hydrodynamics.* Cambridge University Press. 6th edition.

Lamberti, A. and Franco, L. 1994. Italian Experience on Upright Breakwaters. In *Proc. Intl. Workshop on Wave Barriers in Deepwaters.* Port and Harbour Research Institute, Japan. pp. 25–73.

Lanczos, C. 1966 *Discourse on Fourier Series.* Oliver & Boyd, Edinburgh.

Latta, G.E. and Hess, G.B. 1973. Potential flow past a sphere tangent to a plane. *Phys. Fluids* **16**(7):974–976.

Li, L., Schultz, W.W. and Merte, H. 1993. The velocity potential and the interacting force for two spheres moving perpendicularly to the line joining their centers. *J. Eng. Maths* **27**:147–160.

Lundgren, H. 1969. Wave Shock Forces: an analysis of deformations and forces in the wave and in the foundation. In *Proc. Symp. Research on Wave Action* volume 2. Delft Hydraulic Laboratory, The Netherlands pp. 153–174.

Milne-Thompson, L.M. 1962 *Theoretical Hydrodynamics.* Macmillan, London. 4th edition.

Moon, P. and Spencer, D.E. 1961 *Field Theory Handbook.* Springer, Berlin.

Müller, G. 1995. Wave impact pressures on a vertical wall and their effect on sea bed pressures. *Proc. XXVIth IAHR Congress* **3**:275–280.

Müller, G. 1997. Wave impact pressure propagation into cracks. *Proc. Instn. Civ. Engrs Wat., Marit. & Energy* **124**:79–85.

New, A.L., McIver, P. and Peregrine, D.H. 1986. Computations of overturning waves. *J. Fluid Mech.* **150**:237–251.

Newman, J.N. 1978 *Marine Hydrodynamics.* MIT, Cambridge, Massachusetts.

Okamura, M. 1993. Impulsive pressure due to wave impact on an inclined plane wall. *Fluid Dyn. Res.* **12**(4):215–228.

Oumeraci, H., Klammer, P. and Partenscky, H.W. 1993. Classification of breaking wave loads on vertical structures. *J. Waterway Port Coastal Ocean Eng.* **119**(4): 381–397.

Palmer, H.R. 1834. Observations on the motions of shingle beaches. *Phil. Trans. R. Soc. Lond.* **124**:567–576.

Paterson, A.R. 1983 *A first course in Fluid Dynamics.* Cambridge University Press.

Peregrine, D.H. and Kalliadasis, S. 1996. Filling flows, cliff erosion and cleaning flows. *J. Fluid Mech.* **310**:365–374.

Peregrine, D.H. and Thais, L. 1996. The effect of entrained air in violent water wave impacts. *J. Fluid Mech.* **325**:377–397.

Pólya, G. 1947. A Minimum Problem about the Motion of a Solid through a Fluid. *Proc. Nat. Acad. Sci.* **33**:218–221.

Richert, G. 1968. Experimental Investigation of Shock Pressures Against Breakwaters. In *Proc. 11th Intl. Conf. Coastal Eng.* ASCE London, England. pp. 954–973.

Rosenhead, L. 1963 *Laminar Boundary Layers.* Clarendon, Oxford.

Sedov, L.I. 1965 *Two-dimensional Problems in Hydrodynamics and Aerodynamics.* Wiley, New York.

Shore Protection Manual, U.S. Army, 1973. Coastal Eng. Research Center, U.S. Government Printing Office.

Solomentsev, Y., Velegol, D. and Anderson, J.L. 1997. Conduction in the small gap between two spheres. *Phys. Fluids* **9**(5):1209–1217.

Steers, J.A. 1953 *The Sea Coast.* Collins, London.

Stevenson, T. 1849. Account of Experiments upon the Force of the Waves of the Atlantic and German Oceans. *Trans. Roy. Soc. Edinburgh* **16**:23–32.

Stevenson, T. 1864 *The Design and Construction of Harbours.* Black, Edinburgh.

Tanimoto, K. and Takahashi, S. 1994. Japanese Experiences on Composite Breakwaters. In *Proc. Intl. Workshop on Wave Barriers in Deepwaters.* Port and Harbour Research Institute, Japan. pp. 1–22.

Topliss, M.E. 1994 *Water wave impact on structures.* PhD thesis. School of Mathematics, University of Bristol.

Tsai, W. and Yue, D. 1996. Computations of Nonlinear Free-surface Flows. *Ann. Rev. Fluid Mech.* **28**:249–278.

Van Dyke, M. 1964 *Perturbation Methods in Fluid Mechanics.* Academic Press, New York & London.

Verhagen, J.H.G. 1967. The Impact of a Flat Plate on a Water Surface. *J. Ship Res.* **11**:211–223.

Wagner, H. 1932. Über Stoß- und Gleitvorgänge an der Oberfläche von Flüssigkeiten. *Z. Angew. Math. Mech.* **12**:193–215 (NACA Translation **1366**).

Walkden, M.J.A., Hewson, P.J. and Bullock, G.N. 1997. Scaling. In *Proc. Task 1 Technical Workshop on Probabilistic Design Tools for Vertical Breakwaters.* Edinburgh.

Whitley, N.L. 1984. Potential flow past a sinusoidal wall of finite amplitude. *J. Eng. Math.* **18**:207–217.

Wood, D.J. 1997 *Pressure-impulse Impact Problems and Plunging Wave Jet Impact.* PhD thesis. School of Mathematics, University of Bristol.

Zenkovich, V.P. 1967 *Processes of Coastal Development.* Oliver & Boyd, London.